

AFRL-AFOSR-UK-TR-2010-0009



Kinetics in Gas Mixtures for Problem of Plasma Assisted Combustion

**SVETLANA Starikovskaia
Ecole Polytechnique
Laboratory for Physics and Technology of Plasmas
Route de Saclay
Palaiseau Cedex, France 91128**

EOARD CRDF 06-9004

May 2010

Final Report for 01 April 2007 to 01 April 2010

Distribution Statement A: Approved for public release distribution is unlimited.

**Air Force Research Laboratory
Air Force Office of Scientific Research
European Office of Aerospace Research and Development
Unit 4515 Box 14, APO AE 09421**

REPORT DOCUMENTATION PAGE		Form Approved OMB No. 0704-0188
<p>Public reporting burden for this collection of information is estimated to average 1 hour per response, including the time for reviewing instructions, searching existing data sources, gathering and maintaining the data needed, and completing and reviewing the collection of information. Send comments regarding this burden estimate or any other aspect of this collection of information, including suggestions for reducing the burden, to Department of Defense, Washington Headquarters Services, Directorate for Information Operations and Reports (0704-0188), 1215 Jefferson Davis Highway, Suite 1204, Arlington, VA 22202-4302. Respondents should be aware that notwithstanding any other provision of law, no person shall be subject to any penalty for failing to comply with a collection of information if it does not display a currently valid OMB control number.</p> <p>PLEASE DO NOT RETURN YOUR FORM TO THE ABOVE ADDRESS.</p>		
1. REPORT DATE (DD-MM-YYYY) 14-05-2010	2. REPORT TYPE Final Report	3. DATES COVERED (From – To) 1 April 2007 - 1 April 2010
4. TITLE AND SUBTITLE Kinetics in Gas Mixtures for Problem of Plasma Assisted Combustion	5a. CONTRACT NUMBER FA8655-03-D-0001, Delivery Order 0032	
	5b. GRANT NUMBER	
	5c. PROGRAM ELEMENT NUMBER	
6. AUTHOR(S) Professor SVETLANA Starikovskaia	5d. PROJECT NUMBER	
	5d. TASK NUMBER	
	5e. WORK UNIT NUMBER	
7. PERFORMING ORGANIZATION NAME(S) AND ADDRESS(ES) Ecole Polytechnique Route de Saclay Palaiseau Cedex 91128 France		8. PERFORMING ORGANIZATION REPORT NUMBER CRDF 06-9004
9. SPONSORING/MONITORING AGENCY NAME(S) AND ADDRESS(ES) EOARD Unit 4515 BOX 14 APO AE 09421	10. SPONSOR/MONITOR'S ACRONYM(S)	
	11. SPONSOR/MONITOR'S REPORT NUMBER(S) AFRL-AFOSR-UK-TR-2010-0009	
12. DISTRIBUTION/AVAILABILITY STATEMENT Approved for public release; distribution is unlimited.		
13. SUPPLEMENTARY NOTES		
14. ABSTRACT <p>Throughout the whole period of the research we performed the following tasks:</p> <p>The current state of the art in approaches to the study of kinetics of plasma assisted combustion and ignition has been reviewed. It was demonstrated that, in spite of a large body of research in this field, up to now there had been no kinetic model describing adequately plasma assisted ignition and combustion.</p> <p>Kinetics of ignition in $C_nH_{2n+2}O_2:Ar$ mixtures for $n = 1$ to 5 has been studied experimentally and numerically under the action of a high-voltage nanosecond discharge. The experiments were carried out in a shock tube behind a reflected shock wave. Ignition delay time, shock wave velocity and discharge characteristics were measured in each experiment. The delay time for plasma-assisted ignition was compared with auto-ignition delay time, which was also measured. It was shown that the initiation of the gas discharge leads to an order of magnitude decrease in ignition delay time.</p> <p>A kinetic scheme was developed to simulate the production of active particles during the discharge and in its afterglow. Using this scheme, production of atoms, radicals and excited and charged particles was numerically simulated based on measured time-resolved discharge current and electric field in the discharge phase. The calculated densities of active particles were used as input data to simulate plasma-assisted ignition of hydrocarbons. Calculated ignition delay time agrees well with experimental data. The analysis of the simulation results showed that the composition of active particles generated by the discharge is dominated by O and H atoms and the following non-equilibrium plasma ignition mechanism occurs under the conditions considered: (i) O atom production by the non-equilibrium plasma, (ii) chemical reactions of hydrocarbon oxidation with participation of O atoms and gas heating due to net exothermal chemical hydrocarbon oxidation process, and (iii) subsequent thermal ignition.</p> <p>The role of gas temperature increase in the experiments on plasma-assisted ignition was numerically analyzed. Calculations of ignition delay time under different assumptions of the input energy distribution were made for ethane containing mixture. It has been demonstrated that the non-thermal mechanism is responsible for the decrease of ignition delay time under the conditions considered.</p>		

Microwave interferometry has been proposed as a technique to study electron density decay in the afterglow of the pulsed highvoltage nanosecond discharge with microsecond resolution. The measurement scheme has been adjusted for shock tube experiments behind the incident and behind the reflected shock waves in a synthetic air. Preliminary experimental data have been obtained for a combustible mixture.

Fast streak-camera with a broad-band spectrometer has been adapted to measure emission in the discharge phase and in the ignition one within the wavelength range between 300 and 800 nm in single-shot experiments. Preliminary experimental data on the emission intensity from the discharge and during ignition have been obtained. An experimental scheme for laser absorption measurements of OH density in the ground state has been adjusted. The calibration procedure has been proposed and realized to obtain absolute values of the density of OH radicals. Behavior of OH density during plasma-assisted ignition has been investigated. We received that the temporal evolution of OH density is in good correlation with OH* emission behavior.

To separate the effects of various active species, ignition delay was experimentally studied for N₂O-containing mixtures (i) in the auto-ignition regime, (ii) by the nanosecond discharge and (iii) by laser flash-photolysis (ArF laser). Pronounced decrease in ignition delay time was obtained both for laser flash-photolysis and for plasma assisted ignition. A kinetic scheme has been suggested to describe non-equilibrium ignition under the conditions studied. The experimental data were analyzed numerically and using additional measurements of laser beam uniformity and ozone density.

Kinetics of ignition in a CH₄:air mixture has been simulated numerically under the action of a high-voltage nanosecond discharge. Good agreement was obtained between the calculated ignition delay times and available experimental data obtained in shock tubes. The analysis of simulation results showed that presence of N₂ in combustible mixtures leads to additional channels for production of O atoms (dominant active species) in the discharge via electron impact excitation of high-energy excited states of nitrogen followed by their quenching with O₂ dissociation.

A stoichiometric C₂H₆:O₂ = 2:7 mixture was ignited in a closed chamber by a sliding nanosecond dielectric barrier discharge at room temperature and 1 atm. Using fast photography, induction delay time, inflammation volume and flame propagation were investigated. Peculiarities and preliminary results of experiments concerning ignition of a combustible mixture by a sliding nanosecond DBD are presented. Ignition parameters are compared between a nanosecond spark discharge and sliding nanosecond DBD under the same initial conditions.

15. SUBJECT TERMS

EOARD, Plasma Physics, Combustion

16. SECURITY CLASSIFICATION OF:

a. REPORT
UNCLAS

b. ABSTRACT
UNCLAS

c. THIS PAGE
UNCLAS

17. LIMITATION OF ABSTRACT

UL

18. NUMBER OF PAGES

196

19a. NAME OF RESPONSIBLE PERSON

SURYA SURAMPUDI

19b. TELEPHONE NUMBER (Include area code)
+44 (0)1895 616021

Moscow Institute of Physics and Technology
Physics of Nonequilibrium Systems Laboratory

Kinetics in Gas Mixtures for Problem of Plasma Assisted Combustion

EOARD/CRDF Project # RUP1-1513-MO-06
Final Report, April 1, 2007 — March 31, 2009

Date Submitted: *April 28, 2008*



Edited by Dr. Ilya N. Kosarev,
Moscow Institute of Physics and Technology
Physics of Nonequilibrium Systems Laboratory
Institutskii lane, 9, 141700,
Dolgoprudny, 141700, RUSSIA
Phone (+7-495)-408-6347
E-mail ilya@neq.mipt.ru
URL <http://neq.mipt.ru>

Declaration of Technical Data Conformity

The Contractor hereby declares that, to the best of its knowledge and belief, the technical data delivered herewith under this contract during the period 04/01/2007 through 04/31/2009 is complete, accurate, and complies with all material requirements of the Contract.

A handwritten signature in blue ink, appearing to be 'T.V. Kondranin', is written over a faint, light blue circular stamp or watermark.

Date: 28/04/2009

Name and Title of Authorized Official: Prof. T.V.Kondranin, Vice-Rector, Science

Contents

1	Abstract	6
2	Introduction	8
3	Preliminary Analysis and Review of Available Information	9
3.1	Theoretical description	9
3.2	Historical references: first experimental observations	11
3.3	PAI/PAC: general approach	12
4	Kinetics of Plasma-Assisted Ignition of Hydrocarbons. Methane:Oxygen Mixture Diluted with Argon	16
4.1	Experiment	16
4.1.1	Experimental setup and methods	16
4.1.2	Measurement of discharge characteristics	18
4.1.3	Measurement of ignition characteristics	20
4.2	Numerical simulation and discussion	24
4.2.1	Description of discharge and nearest afterglow	24
4.3	Description of plasma assisted ignition	32
4.4	Conclusions	35
5	Kinetics of Plasma-Assisted Ignition of Hydrocarbon. Ethane-to-Pentane: Oxygen Mixtures Diluted with Argon	36
5.1	Introduction	36
5.2	Experiment	37
5.2.1	Experimental setup and methods	37
5.2.2	Measurement of discharge characteristics	37
5.2.3	Measurement of ignition characteristics	39
5.3	Numerical simulation and discussion	44
5.3.1	Description of discharge and near afterglow	44
5.3.2	Calculated results for autoignition and plasma assisted ignition . . .	54
5.4	Conclusions	59
6	Analysis of Kinetic Behaviour of Different Components	61
6.1	Experimental analysis of dynamics of intermediates	61
6.1.1	Streak-camera imaging	62
6.1.2	Preliminary experimental data	64
6.1.3	Electron density measurements	71

6.1.4	Measurements of OH radicals	73
6.2	Conclusions	76
7	Analysis of the Results on Plasma-Assisted Ignition in Hydrocarbon-Containing Mixtures	77
7.1	Discharge development in mixtures under consideration. Influence of Ar dilution	77
7.2	Analysis of gas heating. Equilibrium and nonequilibrium energy input . . .	82
7.3	Energy efficiency of O-atoms production by nanosecond discharge	86
8	Diagnostic of Unexcited OH During Plasma Assisted Ignition	88
8.1	Introduction	88
8.2	Experimental setup	89
8.2.1	Shock tube – nanosecond discharge setup	89
8.2.2	Laser system: general description	91
8.2.3	Analysis of available diagnostic techniques	95
8.2.4	Laser system: description of doubling system	96
8.3	Analysis of the overlap of absorption and emission profiles	100
8.3.1	Analysis of absorption profile of OH radical	100
8.3.2	Analysis of spectral width of UV laser light	100
8.4	Results and discussion	103
8.4.1	Experimental data	103
8.4.2	Absolute calibration of OH density	107
8.4.3	OH density measurements for plasma assisted ignition experiments	110
8.5	Conclusions	112
9	Laser Flash-Photolysis and Gas Discharge in N₂O-Containing Mixtures: Kinetic Mechanism	113
9.1	Introduction	113
9.2	Brief description of experimental results on decrease of the ignition delay time	114
9.3	Measurements of spatial distribution of laser emission	120
9.4	Measurements of ozone density: validation of calculations of [O(¹ D)] from absorbed laser energy	122
9.5	Measurements of electrical parameters of plasma assisted ignition for N ₂ O:H ₂ :O ₂ :Ar mixture	126
9.6	Approach to numerical modelling of plasma-assisted ignition in N ₂ O:H ₂ :O ₂ :Ar mixture. Analysis of cross-sections and reactions	127
9.7	Conclusions	137
10	Kinetics of Plasma-assisted Ignition in Methane–Air Mixture	139
10.1	Introduction	139
10.2	Experimental data on plasma-assisted ignition in CH ₄ :air mixtures	139
10.2.1	Discharge characteristics	139
10.2.2	Ignition characteristics	140
10.3	Numerical simulation of plasma-assisted ignition in CH ₄ :air mixtures . . .	143
10.3.1	Kinetic model for discharge and near afterglow	143

10.3.2	Kinetic model for autoignition and plasma assisted ignition	148
10.3.3	Calculated results for discharge processes	150
10.3.4	Calculated results for autoignition and plasma assisted ignition . . .	153
10.4	Conclusions	156
11	Ignition by Nanosecond DBD and Nanosecond Spark Discharge	165
11.1	Introduction	165
11.2	Experimental setup	166
11.3	Results and discussion	168
11.4	Conclusions	169
12	Summary	173
	List of figures	182

Chapter 1

Abstract

Throughout the whole period of the research we performed the following tasks:

The current state-of-art in approaches to the study of kinetics of plasma assisted combustion and ignition has been reviewed. It was demonstrated that, in spite of a large body of research in this field, up to now there had been no kinetic model describing adequately plasma assisted ignition and combustion.

Kinetics of ignition in $C_nH_{2n+2}:O_2:Ar$ mixtures for $n = 1$ to 5 has been studied experimentally and numerically under the action of a high-voltage nanosecond discharge. The experiments were carried out in a shock tube behind a reflected shock wave. Ignition delay time, shock wave velocity and discharge characteristics were measured in each experiment. The delay time for plasma-assisted ignition was compared with autoignition delay time, which was also measured. It was shown that the initiation of the gas discharge leads to an order of magnitude decrease in ignition delay time.

A kinetic scheme was developed to simulate the production of active particles during the discharge and in its afterglow. Using this scheme, production of atoms, radicals and excited and charged particles was numerically simulated based on measured time-resolved discharge current and electric field in the discharge phase. The calculated densities of active particles were used as input data to simulate plasma-assisted ignition of hydrocarbons. Calculated ignition delay time agrees well with experimental data. The analysis of the simulation results showed that the composition of active particles generated by the discharge is dominated by O and H atoms and the following nonequilibrium plasma ignition mechanism occurs under the conditions considered: (i) O atom production by the nonequilibrium plasma, (ii) chemical reactions of hydrocarbon oxidation with participation of O atoms and gas heating due to net exothermal chemical hydrocarbon oxidation process, and (iii) subsequent thermal ignition.

The role of gas temperature increase in the experiments on plasma-assisted ignition was numerically analyzed. Calculations of ignition delay time under different assumptions of the input energy distribution were made for ethane-containing mixture. It has been demonstrated that the non-thermal mechanism is responsible for the decrease of ignition delay time under the conditions considered.

Microwave interferometry has been proposed as a technique to study electron density decay in the afterglow of the pulsed highvoltage nanosecond discharge with microsecond resolution. The measurement scheme has been adjusted for shock-tube experiments behind the incident and behind the reflected shock waves in a synthetic air. Preliminary

experimental data have been obtained for a combustible mixture.

Fast streak-camera with a broad-band spectrometer has been adapted to measure emission in the discharge phase and in the ignition one within the wavelength range between 300 and 800 nm in single-shot experiments. Preliminary experimental data on the emission intensity from the discharge and during ignition have been obtained.

An experimental scheme for laser absorption measurements of OH density in the ground state has been adjusted. The calibration procedure has been proposed and realized to obtain absolute values of the density of OH radicals. Behavior of OH density during plasma-assisted ignition has been investigated. We received that the temporal evolution of OH density is in good correlation with OH* emission behavior.

To separate the effects of various active species, ignition delay was experimentally studied for N₂O-containing mixtures (i) in the autoignition regime, (ii) by the nanosecond discharge and (iii) by laser flash-photolysis (ArF laser). Pronounced decrease in ignition delay time was obtained both for laser flash-photolysis and for plasma assisted ignition. A kinetic scheme has been suggested to describe nonequilibrium ignition under the conditions studied. The experimental data were analyzed numerically and using additional measurements of laser beam uniformity and ozone density.

Kinetics of ignition in a CH₄:air mixture has been simulated numerically under the action of a high-voltage nanosecond discharge. Good agreement was obtained between the calculated ignition delay times and available experimental data obtained in shock tubes. The analysis of simulation results showed that presence of N₂ in combustible mixtures leads to additional channels for production of O atoms (dominant active species) in the discharge via electron impact excitation of high-energy excited states of nitrogen followed by their quenching with O₂ dissociation.

A stoichiometric C₂H₆:O₂ = 2:7 mixture was ignited in a closed chamber by a sliding nanosecond dielectric barrier discharge at room temperature and 1 atm. Using fast photography, induction delay time, inflammation volume and flame propagation were investigated. Peculiarities and preliminary results of experiments concerning ignition of a combustible mixture by a sliding nanosecond DBD are presented. Ignition parameters are compared between a nanosecond spark discharge and sliding nanosecond DBD under the same initial conditions.

Chapter 2

Introduction

In recent decades, considerable progress has been made in studies of non-equilibrium plasma assisted ignition and combustion. A review of modern experimental research in this area is given in [1]. The major motivation for this work is to design more efficient systems for fuel ignition and combustion in internal combustion engines and jet engines capable of operating under various conditions (at different values of equivalence ratio, pressure, flow velocity, etc.). Plasmas created by high-voltage nanosecond discharges have a number of advantages over other types of discharge plasmas. Here, the reduced electric field, E/N (N is the gas number density), is much higher than that occurring in other sources of non-equilibrium plasmas. For this reason, most of the energy deposited into the gas is spent on ionization, dissociation and excitation of high-energy states of molecules, which could favor plasma assisted ignition. In addition, the plasmas of high-voltage nanosecond discharges are more stable at high pressures as compared to other types of electric discharges. Finally, the plasmas of high-voltage nanosecond discharges could be uniform and the discharge processes occurs on a nanosecond scale, whereas the ignition processes occur on a microsecond scale. This allows to simplify modeling of plasma assisted ignition and to compare calculated results with measurements.

It is extremely important to understand the mechanism of the effect of non-equilibrium plasma on ignition and combustion of gaseous mixtures. For this purpose experiments should be conducted under controlled conditions under which a numerical simulation could be carried out, calculated results could be verified by comparing with observations and analysis of the results could be used to clarify plasma processes important to ignition.

The purpose of this paper is to study experimentally and numerically the ignition of gaseous mixtures with saturated hydrocarbons from CH_4 to C_5H_{12} excited by a high-voltage nanosecond discharge. We have made first measurements of ignition delay time in hydrocarbon-containing mixtures as a function of initial gas temperature and pressure with simultaneous control of the temporal evolution of the discharge current and electric field in the discharge. This allowed simulation of the production of active species in the discharge and in its afterglow. A kinetic mechanism of the effect of non-equilibrium plasma was determined by calculating numerically the ignition characteristics and comparing the calculated results with the measurements.

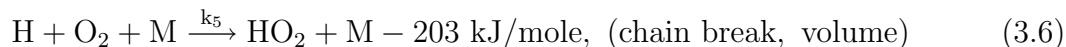
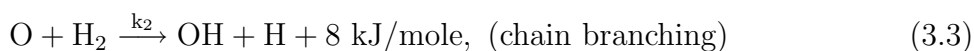
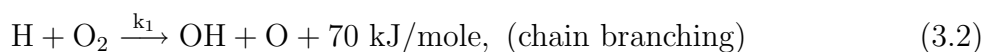
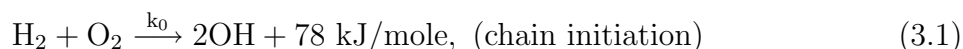
Chapter 3

Preliminary Analysis and Review of Available Information

3.1 Theoretical description

The idea to use a nonequilibrium low temperature plasma for either ignition or combustion stabilization seems to be rather promising. Indeed, a possibility to guide such a parameter as mean electron energy, provides a researcher with an opportunity to change the energy branching in plasma from mainly heating and excitation of low-energetic vibrational degrees to excitation of high-energetic electronic states and ionization.

Let us consider the mechanism of combustion for the simplest case of a hydrogen-oxygen stoichiometric mixture. In case of relatively high temperatures and pressures the kinetics of such a mixture is described by the branched chain mechanism [2, 3]:



Here reaction (3.1) is a reaction of chain initiation under conditions of autoignition. The energies necessary to break the chemical bonds are given in Table 3.1.

Table 3.1: Bond energies, kJ/mole

H-H	O=O	O-H	H-OH	H-O ₂
436	498	428	488	203

Reactions (3.2) – (3.4) are responsible for chain prolongation. Chain branching means that chemical reactions with active particles increase the number of free radicals and atoms (see reactions (3.2) – (3.3)). Both branching and chain development reactions are fast and, what is quite important, they do not lead to recombination of radicals that sustains the chain mechanism of combustion.

As follows from comparing enthalpy ΔH of reactions (3.2) – (3.4) the chain will be limited by reaction (3.2), where $\Delta H = 70$ kJ/mole. This means that the main chain break occurs through the reactions with H-atoms, that is reactions (3.5) – (3.6) lead to a chain break.

The ignition delay is usually determined as a time period between the start of the process, i.e. heating or mixing of gases, and the time of an abrupt increase in temperature, pressure, emission intensity and rate of chemical reactions.

Under induction the density of radicals increases by some orders of magnitude but the fuel is practically unconsumed and the heat release is negligibly low. When reaching a certain radical concentration, there occurs a rapid change of temperature, density of the main and intermediate chemical components that leads to ignition of the gas mixture.

Under conditions of ordinary thermal ignition (or autoignition) the ignition delay depends upon the rate of the dissociation reaction which is endothermic. Generally the induction delay time is greatly affected by temperature. Normally, the ignition delay depends exponentially on temperature that exhibits the temperature dependence of reaction rate constants:

$$\tau = A \exp(B/T), \quad A, B = \text{const} \quad (3.7)$$

There may be two scenarios under chain branched reactions. In case of the first one the rate of branching is lower than the rate of the chain break. Then a quasy-stationary concentration of free radicals is observed in the system and the reaction proceeds with a constant, or even very low reaction rate. In the second case the branching rate exceeds that of the chain break. Here the radicals are accumulated exponentially and the reaction rate increases similarly that brings about chain ignition of the reacting mixture. Transition from low to fast type of reaction occurs abruptly that corresponds to appearing of a certain explosion region in the “pressure–temperature” coordinates.

Fig. 3.1 taken from [4] gives an idea of ignition critical parameters. The so called limits of autoignition, or explosion limits, are determined by mechanisms of reactions (I, II) or heat balance in the system (III). The first limit (I) occurs when active species responsible for the chain prolongation diffuse to the walls that leads to species recombination and restricts the chain development. The second, or kinetic, limit (II) is bound to a direct gas–phase competition between reactions (3.2) – (3.4) and reaction (3.6). And, finally, the third limit (III) is determined by the balance of heat release due to chemical reactions and heat dissipation in the system.

Let us consider the equation deduced for explosion limits (I) and (II). While defining the classical explosion limit according to Semenov’s theory [3], the concentration of certain radicals ($[O]$ and $[OH]$ for hydrogen–oxygen combustion) is considered to be stationary, that is $d[O]/dt = d[OH]/dt = 0$. Then the condition of the positive derivative of H radical density, written after reactions (3.2) – (3.6), will be the following:

$$\frac{d[H]}{dt} = 2k_2[H_2][O] - k_4[H] - k_5[H][O_2][M] > 0 \quad (3.8)$$

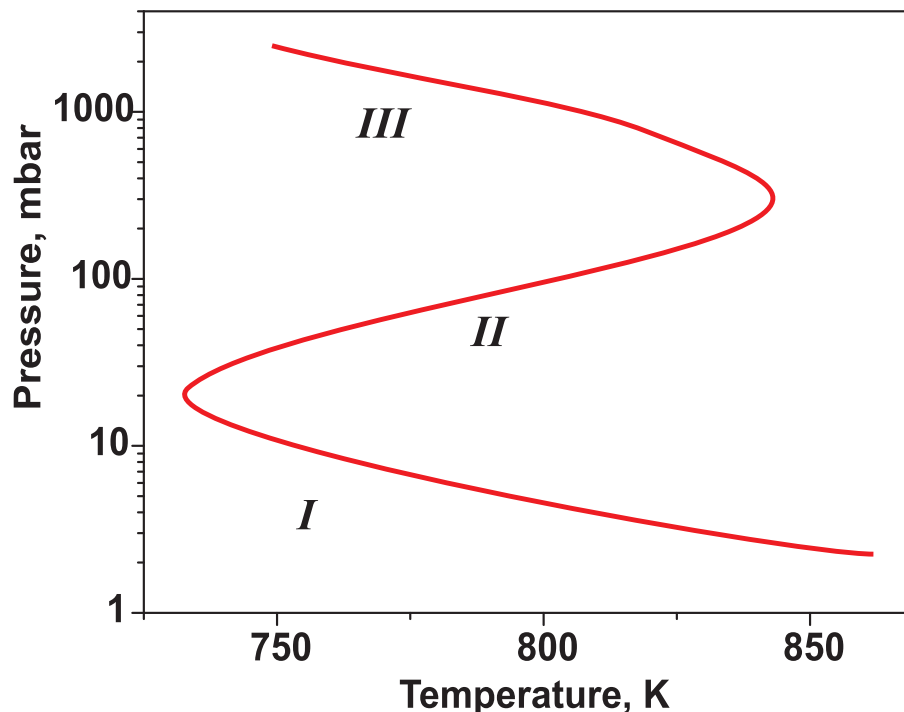


Figure 3.1: Limits of explosion for hydrogen–oxygen mixture (according to [4]).

When considering this equation in more detail, one can obtain equations describing explosion limits (I) and (II). And here, three-body reaction (3.6) is neglected at low pressures, while diffusion losses on the wall are disregarded at high pressures. Thus, the rate of chains initiation does not affect the position of the explosion limit in traditional consideration (3.8). Indeed, both the chain break and chain branching are believed to be linear respective to free radicals density. Non-linear processes, such as interaction between free radicals, are deliberately excluded. Every chain is supposed to develop independently, that means that the chain length is determined only by the ratio between the constant rates of different stages of chain process but not by the number of chains and their additional interaction with each other. Nevertheless, it is easy to imagine an essentially non-linear situation, when additional production of radicals, excited atoms and molecules as well as ions, may cause acceleration of the chain reaction and spreading of the explosion region.

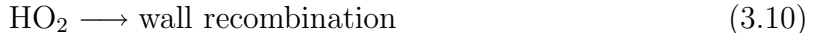
3.2 Historical references: first experimental observations

Such examples of chemically active systems have been known for years. The subsection in the textbook [5] published in 1958 is entitled “Spreading of Boundaries of H_2+O_2 Mixture Ignition under the Action of Short Wavelength radiation or under the Admixture of O-atoms” (see pages 554–566 of [5]). This book was translated into English by Pergamon Press at the same time [6]; unfortunately, the version was shortened from 685 to 305 pages and the author is not sure that the mentioned subsection was translated. It is pointed

out [5] that the ignition limits spread significantly under artificial additions of radicals. This subject is considered theoretically adding reactions



and



after reaction (3.6). Consideration of these processes together with an additional source of O atoms leads to a shift of the explosion limit to lower temperatures. The theoretical conclusions are supported by the results of the experiments [7, 8, 9]. An example of the experimental data obtained for the discharge is given in Fig. 3.2. The authors [9] used a pyrex vessel placed in a thermostat to control the temperature. The temperature was measured by a thermocouple. Slow gas flow was organized through the vessel. The discharge was initiated by switching the primary transformer circuit with a telegraph key, and different ignition curves were obtained by regulating the current in the primary circuit by means of a rheostat. The ignition was observed visually.

The kind of the discharge developed in the experiments can be hardly established without detailed analysis of the electric circuit and, unfortunately, these data are not presented in the paper. The authors called this discharge a “spark” and postulated that the discharge provided additional dissociation but probably it was an arc. On the other hand, if the secondary electric circuit was designed so that the current in the discharge zone was relatively low, they could obtain a nonequilibrium plasma close to the plasma of the glow discharge.

3.3 PAI/PAC: general approach

It should be taken into account that there are two mechanisms to affect a gas by a discharge when using a discharge to initiate combustion.

The first mechanism implies that a discharge leads to formation of an equilibrium or nearly equilibrium plasma (e.g., sparks and arcs). In this case the main factor that reduces the delay time of ignition is local heating of gas and, hence, the increase in rate of thermal dissociation and reactions of chain prolongation and development.

For example, the ignition caused by local heating of a fuel-oxidizer mixture under the action of a spark discharge is typical for ordinary internal combustion engines. Here a spark discharge produces an equilibrium plasma with a high translational temperature. After that the mixture ignites by this plasma forcing flame propagation over non-treated mixture.

It is worth mentioning that the mankind would hardly discard using internal combustion engines, especially in car producing industry. It was as far back as in the XIXth century when the principles of internal combustion engine were introduced. So, the spark ignition cycle is called the Otto Cycle after Dr N.A.Otto who patented the stationary gas engine in 1876, and in 1892 Rudolf Diesel patented the compression ignition “diesel” engine. Until today engines based on these principles are still successfully in use and constitute the major part of engines for light duty vehicles, that is cars or light trucks. A detailed review of the recent studies to evaluate the environmental, performance, and cost

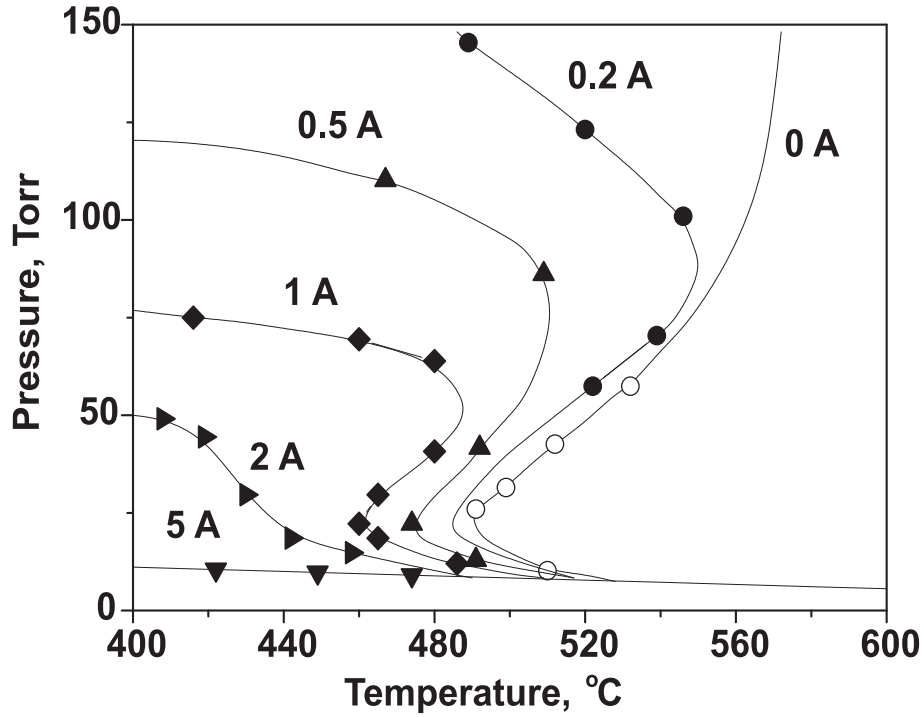


Figure 3.2: Extension of explosion limits of $\text{H}_2\text{:O}_2$ mixture under the action of a discharge. Different curves correspond to different current in a primary electric circuit (according to [9]).

characteristics of fuel/propulsion technology combinations that are currently available or will be available in the next few decades is given in [10]. According to the authors, the investigations here are primarily carried out not due to the flaws of the engines proper, but because of much higher ecological requirements to regulate emissions. At the same time, modern kinds of engines are more technically advanced as compared to those developed more than a century ago and their optimization, optimization of mixture ignition in particular, is of great importance.

The second mechanism to affect a gas is creation of nonequilibrium plasma. At a first glance, the use of nonequilibrium plasma seems to give a unique opportunity to guide the energy input into a gas. Consequently, the direct energy input to certain gas degrees of freedom that are responsible for ignition or combustion, is to extremely stimulate the ignition process. Indeed, even relatively small amounts of atoms and radicals ($\sim 10^{-5}$ – 10^{-3} of the total number of the gas particles) can shift equilibria in the system and initiate combustion. Moreover, if such a concentration of active particles is produced uniformly over the entire volume of gas, the combustion will certainly be non-detonation in character. On the other hand, a proper arranging of a discharge to obtain a given energy branching is not always an easy task for engineers and physicists. Does it seem promising to replace focused in space thermal heating caused by equilibrium plasma by uniform or focused production of active reactive species? It is fundamental knowledge on the behavior of combustible systems under the action of nonequilibrium plasma that is needed to answer this question.

Let us assume that we trigger the ignition artificially, replacing reaction (3.1) by

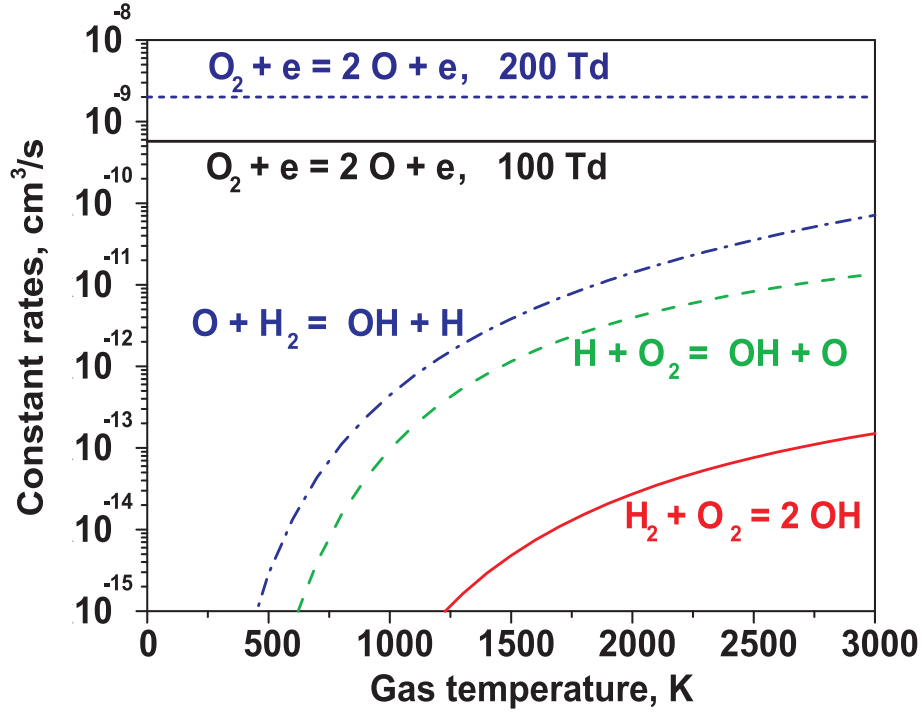
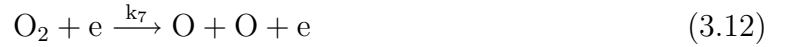


Figure 3.3: Rate constants for reactions responsible for autoignition, and for dissociation by electron impact at electric field values equal to 100 Td and 200 Td (horizontal lines).

reactions of dissociation by electron impact (3.11–3.12) that is common for gas discharges. For a hydrogen molecule, dissociation occurs [11] via $b^3\Sigma_u^+$ and $a^3\Sigma_g^+$ electronically excited states, while for oxygen it happens via $A^3\Sigma_u^+$ and $B^3\Sigma_u^-$ states with the thresholds in the region of 6–12 eV.



The mean electron energy in a discharge is determined by a reduced electric field E/N , where E is electric field and N is gas density [12]. At a reduced electric field of $E/N = 100 - 300$ Td ('Td', or Townsend, is commonly used in gas discharge physics, and $1 \text{ Td} = 0.33 \text{ V}/(\text{cm Torr}) = 10^{-17} \text{ V}\cdot\text{cm}^2$ at 20°C), the dissociation rate will be within the range of $10^{-10} - 10^{-8} \text{ cm}^3/\text{s}$, which is, at least, two orders of magnitude higher than the constant rate for reaction (3.1). Under these conditions, the main energy input is directed to excitation of electronic levels and dissociation. Fig. 3.3 demonstrates the difference between reaction constant rates for the temperature range typical for ignition. Such a great difference means that artificial initiation of a chain reaction must be more efficient than the thermal one.

Further development depends on the initial state of the system. If the pressure and temperature in the system are close to an explosion limit, then an additional injection of radicals will lead to substantial shift of the ignition threshold even if the radicals density is rather low. If the system is far behind the explosion limit (for example, at room pressure and temperature), then some concurrence between heating and development of chains will

be observed. Here, the heating will be caused by recombination of radicals produced by the discharge and the chain processes will be generated by the same radicals, as well as excited species and ions.

The problem of plasma assisted ignition can be conventionally subdivided into several stages. They are: (i) studying the discharges proper that will provide higher effectiveness of ignition and combustion; (ii) obtaining unambiguous experimental data testifying the increase in efficiency of ignition/combustion under non-equilibrium plasma; (iii) analyzing the kinetic mechanisms responsible for PAI/PAC, that include numerical modeling and experiments carried out for this particular kinetic analysis.

Chapter 4

Kinetics of Plasma-Assisted Ignition of Hydrocarbons. Methane:Oxygen Mixture Diluted with Argon

The present part of the report is devoted to the detailed treatment of experimental data obtained within the framework of previous EOARD supported Project [13]. The purpose of this part is to study experimentally and numerically the ignition of a stoichiometric methane–oxygen mixture diluted with Ar under the action of a high-voltage nanosecond discharge on the basis of the experimental data on the discharge development. We have made first systematical measurements of ignition delay time in hydrocarbon-containing mixture as a function of gas temperature and pressure with simultaneous control of the temporal evolution of the discharge current and electric field. This allowed to calculate the production of active particles in the discharge and in its afterglow. The densities of active particles were used as input parameters to simulate the ignition process. A kinetic mechanism of the effect of nonequilibrium plasma was determined by calculating numerically the ignition characteristics and comparing calculated results with measurements for various gas temperatures and pressures.

4.1 Experiment

4.1.1 Experimental setup and methods

We studied a stoichiometric $\text{CH}_4:\text{O}_2$ mixture (10 %) diluted with Ar (90 %). The required gas pressures and temperatures were obtained using a shock tube. Experiments were carried out behind a reflected shock wave, as in classic experiments on the autoignition of combustible mixtures [14]. The experimental setup (see Fig. 4.1) consisted of a shock tube (ShT) with a discharge cell (DC), a gas evacuation and supply system, a system for ignition with discharge, and a diagnostic system. The shock tube ((25×25)-mm square cross section) had a 1.6-m-long working channel. The length of the high-pressure cell (HPC) was 60 cm. The last section of the shock tube with a (25×25)-mm square cross section was made from 40-mm-thick Plexiglas. There were two pairs of windows for optical diagnostics along the stainless steel working channel and six optical windows, each 20 mm in diameter, in the dielectric section. The metal end plate (EP) of the tube served as

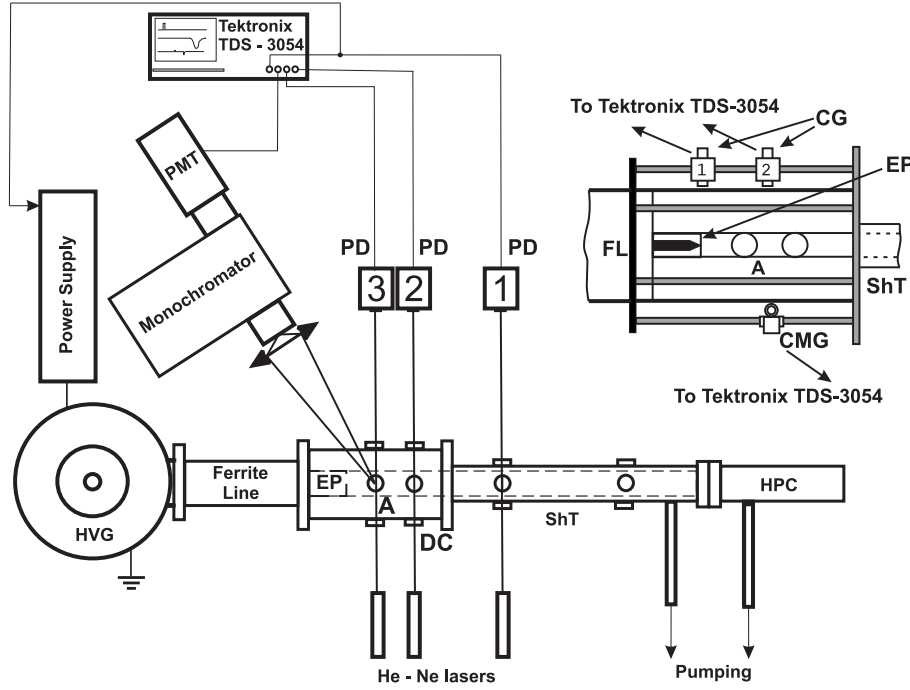


Figure 4.1: Scheme of the experimental setup: DC, discharge cell; A, cross-section of measurement; EP, end plate; HPC, high pressure cell; HVG, high voltage generator; ShT, shock tube; PD, photodiodes; PMT, photomultiplier; CG, capacitive gauge; MCG, magnetic current gauge. The insert gives the discharge cell on an enlarged scale.

a high-voltage electrode. Another electrode was the grounded steel section of the shock tube.

The nanosecond discharge was initiated at the instant at which the reflected shock wave arrived at the observation point (point A in Fig. 4.1). High-voltage pulses were produced with a ten-stage GIN-9 Marx high-voltage generator (HVG). The generator was filled with nitrogen at a pressure of 3 atm, which provided a starting voltage in the range 100–160 kV. To sharpen the high-voltage pulse applied to the discharge gap, a forming ferrite line with a wave impedance of $Z = 40 \Omega$ was used. At the output of the forming line, the voltage growth rate was several kilovolts per nanosecond, which enabled the operation of the gas discharge in the form of a fast ionization wave in the dielectric section of the shock tube. The propagation velocity of the ionization wave front was 10^9 – 10^{10} cm/s, depending on the experimental parameters.

The system for monitoring the shock-wave parameters included a system for measuring the velocities of the incident and reflected shock waves by means of the laser schlieren technique and a system for controlling initial pressure. The schlieren system consisted of three He-Ne lasers mounted at different points along the shock tube and three photodiodes (PD). The gas density (ρ_5), pressure (P_5), and temperature (T_5) behind the reflected shock wave were determined from the known initial gas mixture composition, the initial pressure, and the velocity of the incident shock wave, using conservation laws and assuming that relaxation was complete and chemical reactions frozen. Thermodynamic data were taken from [15].

The combustion process was investigated using emission spectroscopy. Emission gen-

erated in the course of combustion was monitored in the direction perpendicular to the shock tube axis at a distance of 55 mm from the end plate (point *A*) with the help of an MDR-23 monochromator (1.2 nm/mm, 1.2-m focal length, 1200 groove/mm, manufactured by LOMO), an FEU-100 photomultiplier (PMT) manufactured by MELZ, and a Tektronix TDS 3054 oscilloscope. A vertical 2×20-mm slit was installed on the optical window.

To decrease the effect of boundary layers, the kinetic measurements were usually performed in the vicinity of the end plate. In our case, however, the observation point was located rather far from the end plate. Such a position of the observation point was chosen to prevent electric field disturbances caused by the high voltage electrode. An additional series of experiments on autoignition was carried out in the discharge cell in which the end plate was located at a distance of 5 mm from the cross-section of measurements. It was shown that ignition delay times measured at a distance of 55 mm agree with those measured at a distance of 5 mm within the limits of experimental error.

Ignition delay time was determined using the OH emission ($\lambda = 306.4$ nm, $A^2\Sigma(v' = 0) \rightarrow X^2\Pi(v'' = 0)$ transition) or CH emission ($\lambda = 431$ nm, $B^1\Sigma(v' = 0) \rightarrow A^1\Pi(v'' = 0)$ transition). It turned out that the results obtained for the OH emission agree with those obtained for the CH emission to within the experimental error. In the ignition phase, the intensities of the OH and CH emission increased in a similar way and peaked at the same instant. After that the behaviour of these intensities was also similar, the only distinction was that the CH emission decayed to zero with the rate comparable to the rate of rise, whereas the OH emission decayed fast by 70–80 % and then decreased much slower. Most of experimental results was extracted from the CH emission. The delay time was determined as the time between the schlieren signal, which corresponds to the arrival of the reflected shock wave at the diagnostic cross section, and the onset of the leading front of the emission. The onset was defined as the tangent to the emission intensity–time curve at its maximum slope.

The system for monitoring the electric parameters of the nanosecond discharge includes a magnetic current gauge measuring the discharge current and capacitance gauges located at two different points along the discharge section, and measuring the shape and amplitude of the high-voltage pulse. The gauges were calibrated with a high-voltage signal of known amplitude and duration. The signals from the gauges were displayed using a Tektronix TDS 3054 oscilloscope. All the cables were extra shielded and the oscilloscopes were placed in a Faraday cage to reduce high-frequency electric noise.

The development of the high-voltage pulsed discharge in the dielectric section of the shock tube caused excitation, dissociation and ionization of the gas. A peculiarity of this experiment was that the discharge processes and ignition ones were separated in time; the discharge phase lasted only for tens of nanoseconds, whereas the duration of ignition phase was generally in the range between one and hundreds of microseconds. This allowed a consideration of the discharge processes and ignition separately.

4.1.2 Measurement of discharge characteristics

Figure 4.2 shows typical signals from electric gauges on a nanosecond scale. Curve (1) corresponds to the arrival of incident electric pulse at the high voltage electrode in the interval 0 – 100 ns. For the sake of convenience, curve (2) is shifted in Figure 4.2 from

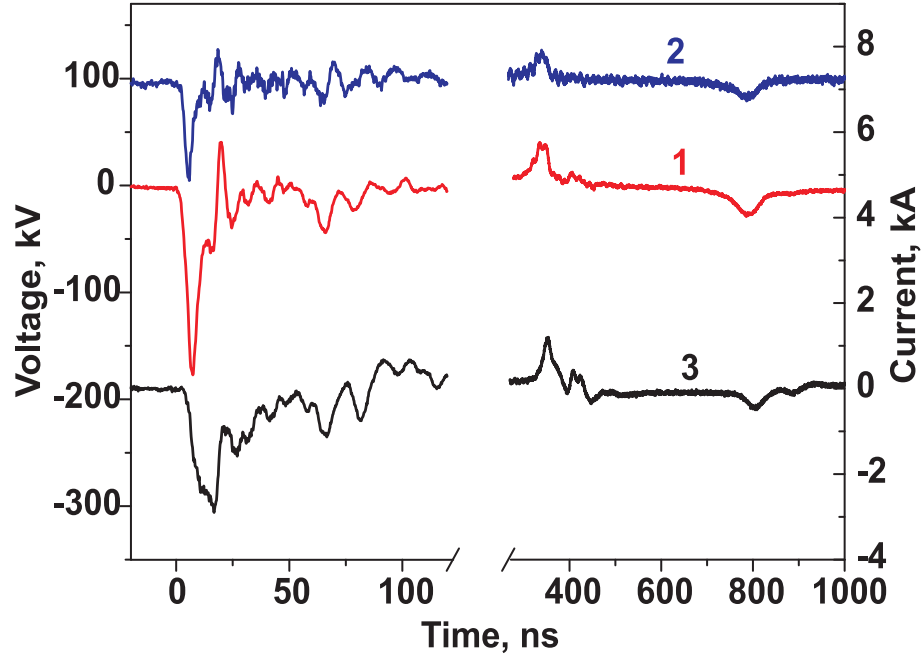


Figure 4.2: Typical signals on a nanosecond scale from (1) the capacitive gauge No 1 (see Figure 4.1), (2) capacitive gauge No 2 and (3) magnetic current gauge. The gas parameters are $T_5=1275$ K, $P_5 = 0.68$ bar and $n_5 = 3.9 \times 10^{18}$ cm $^{-3}$. The voltage amplitude is 175 kV.

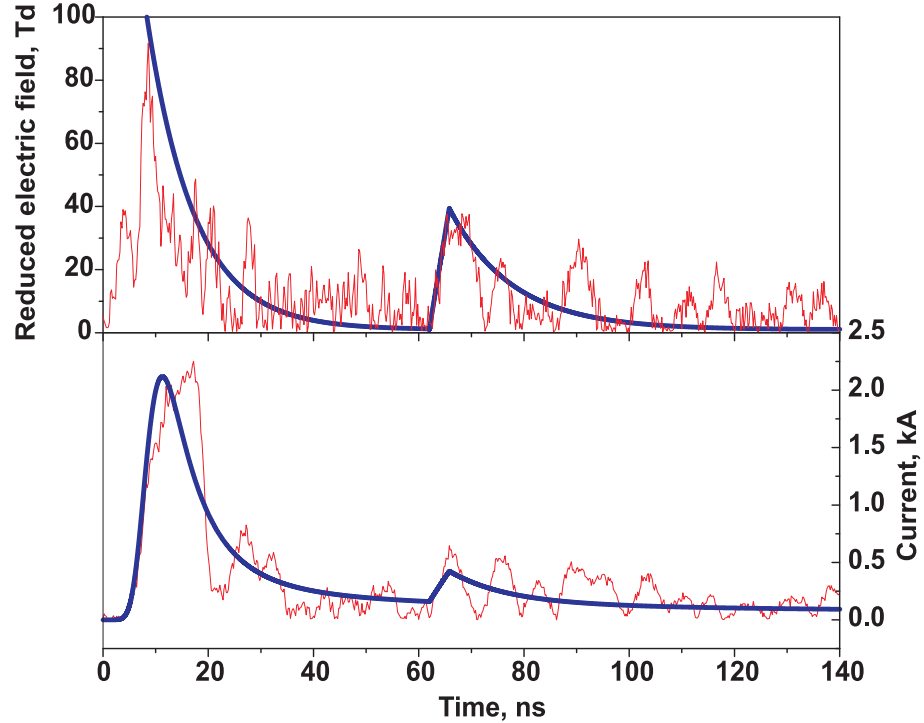


Figure 4.3: The temporal evolution of (a) the reduced electric field E/n and (b) discharge current for 1450 K and 1.2 bar. The red curves correspond to measurements, the blue curve in Fig. 4.3(a) corresponds to an approximation of the experimental data and the dash curve in Fig. 4.3(b) corresponds to calculations. 1 Td= 10^{-17} V cm 2

curve (1) for 100 V. The amplitude of the signal from the second capacitive gauge (curve (2)) is half that of the signal from the first gauge (curve (1)) due to the voltage drop along the discharge gap during the discharge development. Curve 3 shows a delay for several nanoseconds between the onset of the discharge current and instant at which the voltage arrives at the high voltage electrode. To determine time-resolved electric field in the gap, we divided the difference between magnitudes obtained from curves (1) and (2) by 10 cm, the distance between the capacitive gauges. Sometimes high-voltage pulse was followed by additional two pulses induced due to a partial reflection of the wave from the discharge cell and generator. In Figure 4.2, these additional pulses are seen at around 350 and 800 ns. During these pulses, although the amplitude of electric field is much smaller, the electron density is sufficiently high. Therefore, we took them into account when considering the production of active particles by the discharge.

Fig. 4.3 shows the typical evolution in time of the reduced electric field E/n and discharge current. In the discharge phase, the electric field rises fast, peaks and then decreases slowly. The discharge current evolves in time in a similar way; however, it peaks with some delay relative to the electric field. The peak value of E/n decreases with increasing gas number density (see Fig. 4.4). It should be noted that three closed triangle symbols are located somewhat higher than other similar symbols because these three measurements were made at higher (150–175 kV) voltage amplitude, whereas other measurements correspond to a voltage amplitude of 115 kV. Fig. 4.4 shows also the values of E/n at the instant at which the discharge current peaks. These values of E/n also decrease as the gas number density increases.

The discharge behaviour depended strongly on the gas density behind a reflected shock wave, n_5 , and was not sensitive to gas temperature under the conditions considered. To demonstrate this, Figure 4.5 shows the temporal evolution of the specific energy deposited in the discharge for various gas densities. The deposited power was determined from simultaneous measurements of the discharge current, $I(t)$, and voltage drop along the distance between the capacitive gauges, $\Delta U(t)$: $W(t) = \Delta U(t)I(t)$. The specific energy deposited in the gas was determined by integrating $W(t)$ over time on the assumption that the discharge is spatially uniform over the volume $V = LS$, where L is the distance between the gauges and S is the area of the cross section of the discharge cell: $w = W/V = \int_0^T W(t)dt/V$. Doubling the gas density from $n_5 = 3 \times 10^{18} \text{ cm}^{-3}$ to $6 \times 10^{18} \text{ cm}^{-3}$ led to a great change in discharge properties: the energy input decreased by 50 % in the first pulse and subsequent pulses became much less profound. As the gas density increased further, the uniform discharge developing between the electrodes gave way to a low-current corona discharge initiated near the high-voltage electrode. This led to a drastic decrease in the efficiency of production of active particles by the discharge plasma. It should be noted that half the energy was deposited in the first pulse at $n_5 = 3 \times 10^{18} \text{ cm}^{-3}$. Doubling the density led to a decrease in the energy deposited in the first pulse by one half, the characteristics of the voltage pulse being the same in the cable, whereas the energy deposited in the subsequent pulses decreased by an order of magnitude.

4.1.3 Measurement of ignition characteristics

Figure 4.6 shows typical primary experimental data on a microsecond scale. They are signals from schlieren gauges and those of CH emission at 431 nm. In the autoignition

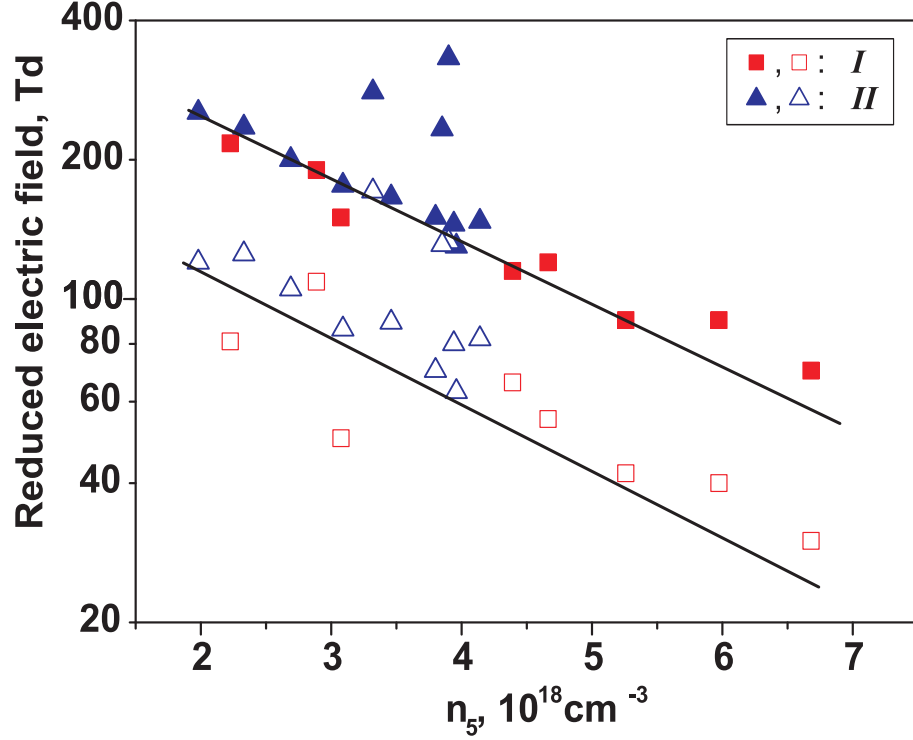


Figure 4.4: The peak values of the reduced electric field (closed symbols) and their values at the instant at which the discharge current peaks (open symbols) as a function of the gas number density. Series *I* and *II* correspond to measurements at different values of T_5 , the values of n_5 being the same. Solid lines correspond to approximations of the experimental data.

regime, the temporal evolution of the gas temperature behind a reflected shock wave, T_5 , was additionally controlled using IR radiation of CO_2 , a small (1 %) addition in the mixture under consideration. The intensity of the radiation selected by an interference filter around $4.2 \mu\text{m}$ was compared with the radiation from a specially prepared $\text{Ar}:\text{CO}_2 = 99 : 1$ mixture. It was shown that, under the conditions considered, the error in measurement of gas temperature behind a reflected shock wave did not exceed $\pm 30 \text{ K}$. The schlieren-gauge curves in Figure 4.6 have peaks corresponding to the arrival of an incident shock wave (the positive peaks in curves 1 and 2) and those corresponding to the arrival of a reflected shock wave (the negative peak in curve 2). Curve 2 shows the signal from the schlieren gauge that is located in the diagnostic cross section. Autoignition delay time was determined as the difference in time between emission signal and schlieren one corresponding to the arrival of a reflected shock wave to the diagnostic cross section. When igniting the mixture excited by the discharge, the initiation of the high-voltage generator was synchronized with the arrival of the shock wave to the diagnostic cross section and ignition delay time was determined as the difference in time between emission signal and initiation of the discharge. The instant of discharge initiation was easy to determine due to the peak of electrical noise that was located at $t = 0 \mu\text{s}$ and registered by all the measuring instruments (Figure 4.6(b)). Some contribution to the first negative narrow peak of radiation signal (curve (3) in Figure 4.6(b)) was also due to OH radiation emitted in the discharge phase, whereas the second peak in this curve was totally due to the radi-

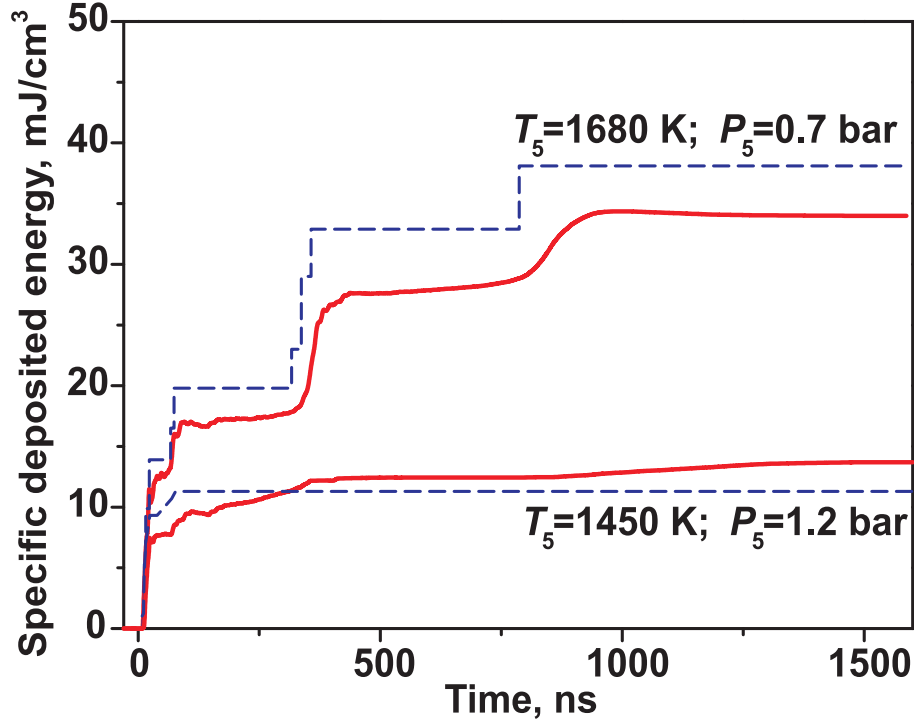


Figure 4.5: The typical temporal evolution of the specific deposited energy for various gas temperatures and pressures. Solid curves correspond to measurements and dash curves correspond to calculations.

ation in the ignition phase. In most cases synchronization was such that the time interval between the arrival of a reflected shock wave to the diagnostic cross section and discharge initiation did not exceed 10 % of measured ignition delay time. A comparison between the photomultiplier signals given in Figure 4.6(a) and Figure 4.6(b) shows that ignition delay time decreases drastically due to the action of the non-equilibrium discharge plasma.

Table 4.1 presents the initial parameters measured behind the reflected shock wave and calculated mole fractions of OH, CH₃ and H, the dominant species of active particles produced in the discharge phase, for every experiment. Initial gas number density is essentially higher in autoignition experiments (experiments No 1–6). For densities at which experiments were carried out with the discharge (experiments No 7–24), the autoignition delay time was almost an order of magnitude longer than the operation time of the shock tube; therefore, measured data were verified by comparing with calculated results. Series *I* (experiments No 7–12) and *II* (experiments No 13–24) correspond to measurements at different values of T_5 , the values of n_5 being the same. A plot of time delay of ignition versus temperature based on data from Table 4.1 is shown in Figure 4.7. We carried out two series of experiments with the discharge, each corresponding to a distinct ratio between initial pressure in the low-pressure chamber, P_1 , and that in the high-pressure chamber, P_5 . Results of these series are shown in Figure 4.7 separately. The effect of gas discharge leads to ignition of the mixture under consideration at noticeably lower temperatures and gas number densities. Under the action of the discharge, ignition delay time at 0.4–0.6 bar is comparable to autoignition delay time for the same mixture at 1.8 bar and yet much lower temperatures.

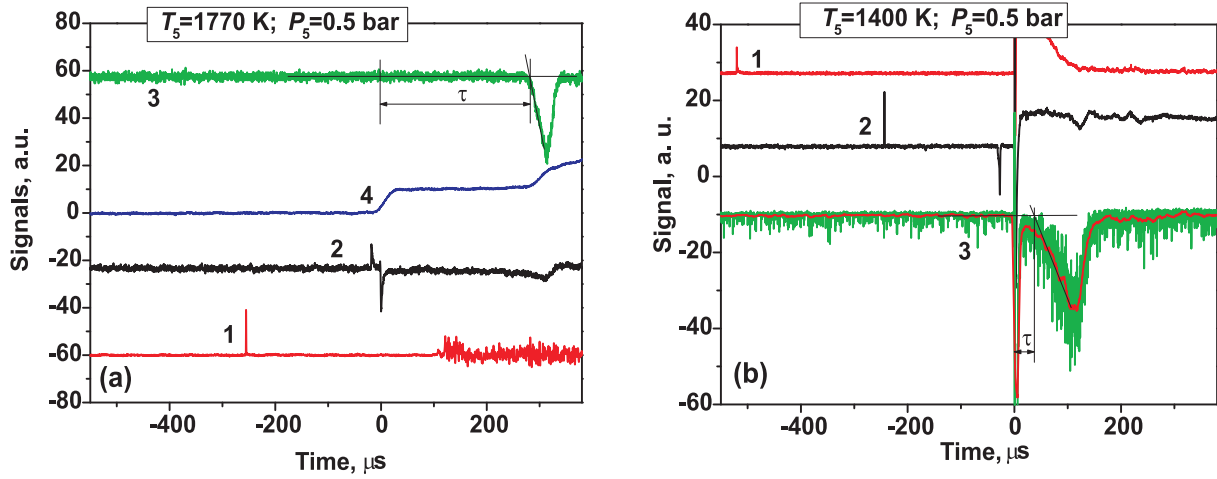


Figure 4.6: Typical behaviour of synchronized signals from (1)–(2) schlieren gauges, (3) photomultiplier, and (4) IR detector on a microsecond scale for (a) autoignition and (b) ignition by the discharge. Distance between the schlieren gauges is 226 mm. Amplitude of voltage pulse is $U = -115 \text{ kV}$.

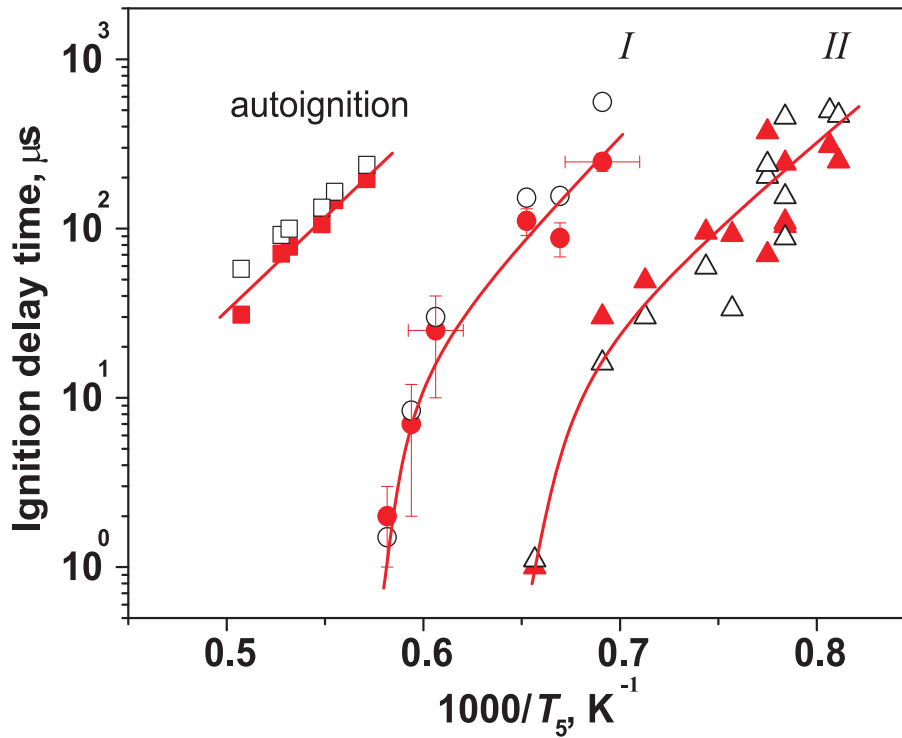


Figure 4.7: Ignition delay time in a stoichiometric $\text{CH}_4:\text{O}_2$ mixture (10 %) diluted with Ar (90%) as a function of temperature for autoignition and (I)–(II) ignition with discharge. Closed symbols correspond to measurements and open symbols correspond to calculations. Solid curves approximate experimental data.

Table 4.1: Initial parameters of the gas mixture behind the reflected shock wave, measured delay time for autoignition and ignition by the discharge and calculated mole fractions of OH, CH₃ and H.

No	T_5 , K	P_5 , bar	n_5 , 10^{18} cm ⁻³	* τ_a , μ s	τ_d , μ s	[O]	[H]	[CH ₃]
1	1895	2.03	7.86	71	-	-	-	-
2	1802	1.99	8.12	147	-	-	-	-
3	1971	2.12	7.89	31	-	-	-	-
4	1751	1.96	8.23	196	-	-	-	-
5	1823	2.18	8.77	106	-	-	-	-
6	1880	2.03	7.94	78	-	-	-	-
7	1683	0.66	2.89	-	< 10	0.0118	0.00291	0.0024
8	1649	0.69	3.08	-	< 10	0.0076	0.00187	0.00148
9	1719	0.52	2.23	-	< 20	0.0144	0.00369	0.003
10	1493	0.95	4.67	-	88	0.0036	0.00107	0.0009
11	1532	1.10	5.27	-	111	0.00291	0.00077	0.00061
12	1447	1.18	5.99	-	248	0.00175	0.0005	0.00037
13	1447	0.46	2.33	-	30	0.0146	0.00371	0.00301
14	1522	0.41	1.98	-	< 10	0.0176	0.00456	0.00396
15	1402	0.51	2.69	-	49	0.0128	0.00342	0.00382
16	1344	0.56	3.09	-	95	0.0114	0.00298	0.00249
17	1290	0.61	3.46	-	70	0.00815	0.0023	0.00192
18	1290	0.67	3.80	-	372	0.00762	0.00203	0.00171
19	1275	0.68	3.90	-	109	0.00941	0.00244	0.00204
20	1239	0.70	4.14	-	309	0.00664	0.00202	0.00167
21	1232	0.66	3.94	-	250	0.00718	0.00203	0.00171
22	1275	0.69	3.96	-	104	0.00602	0.00173	0.00151
23	1275	0.67	3.85	-	243	0.0112	0.00295	0.00242
24	1321	0.60	3.32	-	92	0.0142	0.00355	0.00287

* In the Table, τ_a is a delay time for autoignition, τ_d is a delay time in the case of ignition by the discharge.

4.2 Numerical simulation and discussion

4.2.1 Description of discharge and nearest afterglow

Under the conditions considered the discharge processes occurred on a nanosecond scale, whereas the ignition processes occurred on a microsecond scale. Therefore, we simulated the temporal evolution of densities of particles important for plasma-assisted ignition separately in the discharge phase and in the ignition one. It was assumed that the effect of discharge non-equilibrium plasma is reduced to the accumulation of active particles in the discharge phase that influence the ignition processes.

In the discharge phase, we simulated numerically the production of active particles in a CH₄:O₂:Ar=1:2:27 mixture in a high electric field during the discharge and conversion of the particles during plasma decay in the near afterglow. Active particles under consideration were electronically excited O₂ molecules and Ar atoms, O atoms, H atoms, radicals of hydrocarbon molecules, electrons and simple positive ions. The focus was on the mechanisms that could lead to dissociation of the molecules. Therefore, we neglected vibrationally and electronically excited states of O₂, which have energy insufficient to dissociate the molecules and simulated the excitation of metastable Herzberg O₂(c¹Σ_u⁻), O₂(C³Δ_u) and O₂(A³Σ_u⁺) states by the excitation of one effective metastable state with an excitation energy of 4.5 eV (referred to as O₂), by analogy with [16, 17, 18]. The excitation of the electronical states of O₂ with higher excitation energy lead to the dissociation and these precesses were referred to as electron impact dissociation of O₂. Excitation of electronical Ar states was also simulated by the excitation of one effective state (referred to as Ar) with the excitation rate being equal to the total rate of excitation of all excited Ar states. Here, there is no reason to consider excited Ar states in more detail

because little is known about the rates of their quenching in collision with O_2 and CH_4 to dissociate these molecules. Formation of negative ions and complex positive ions (Ar_2^+ , O_4^+ , etc.) was neglected because the energy of electron attachment to negative ions and dissociation energy of complex ions are too low to prevent the efficient decomposition of these particles at high (> 1000 K) gas temperatures. At the end of plasma decay, only atoms and radicals were assumed to dominate the composition of active particles, whereas the effect of long-lived excited particles on the ignition of the mixture was neglected.

The temporal evolution of densities of active particles in the discharge phase was calculated based on a numerical solution of the corresponding balance equations. Table 4.2 shows reactions considered in our kinetic model and their rate coefficients. We considered electron impact dissociation, excitation and ionization of neutral particles, quenching of electronically excited particles, charge exchange in collisions between ions and neutral particles and dissociative electron-ion recombination, the dominant mechanism of electron loss in the discharge afterglow under the conditions considered.

The rate coefficients for reactions between heavy particles were taken from previous measurements. The only exception are reactions (R13) and (R14) for which we have failed to find rate coefficient. Therefore, they were estimated. In addition, products of reaction (R13) are unknown. In any case it is expected that the rate of this reaction is high because it is energetically allowable and the energy of O_2^* excitation, 4.5 eV, is close to the dissociation energy of CH_4 . Such quenching processes have generally high rates [19]. We assumed that products of reaction (R13) are CH_3 and H , although they could be also CH_3O and OH . Our additional calculations showed that variation in the rate of this reaction and in its products does not affect strongly the total density of active particles produced by the discharge and calculated values of ignition delay time. It should be noted that the magnitude of the rate of reaction (R14) could affect the composition of positive ions and does not affect the density and composition of neutral active particles after plasma decay. The scheme of ion-molecule reactions given in Table 4.2) is somewhat oversimplified. Indeed, additional calculations taking into account a more detailed scheme showed that the dominant positive ion in the discharge afterglow could be HCO^+ rather than O_2^+ . However, the calculated density of neutral active particles are not sensitive to ion composition and most of calculations were carried out based on the scheme given in Table 4.2).

Rate coefficients for electron impact dissociation (reactions (R1) and (R2) in Table 4.2), for electron impact excitation (reactions (R3) and (R4)) and for electron impact ionization (reactions (R5) — (R7)) were calculated by solving numerically the electron Boltzmann equation in the classical two-term approximation to determine the non-equilibrium electron energy distribution [20]. When solving the Boltzmann equation, the input parameters were the reduced electric field E/n (n is the gas number density) and gas composition. The electron distribution was not sensitive to gas temperature. We considered only electron collisions with atoms and molecules of the dominant species in the gas mixture. The effect of electron-electron collisions and collisions between electrons and new particles produced in the discharge was neglected because of small densities of these particles. For electron collisions with Ar , O_2 and CH_4 , we used the available in literature, self-consistent sets of cross sections, which allow a good agreement between calculations and measurements of transport and rate coefficients in the pure gases. Fig. 4.8 shows the cross sections used in our simulation. We took into account elastic scattering of elec-

trons, vibrational excitation and dissociation of O₂ and CH₄ and electronic excitation and ionization of Ar, O₂ and CH₄. To estimate the effect of the uncertainty in electron cross sections on the calculated results, we made calculations with various sets of cross sections; in some cases, for Ar, the cross sections taken from [21] were replaced by those taken from [22] and, for O₂, the cross sections taken from [18] were replaced by those taken from [16]. It turned out that the calculated ignition delay time is not sensitive to such replacements.

Table 4.2: The kinetic scheme of the processes taken into account to simulate the production of atoms and radicals by gas discharge in the Ar:O₂:CH₄ mixture

Number	Reaction	Rate constant, cm ³ /s	Reference
Electron impact dissociation			
R1	$e + \text{O}_2 \rightarrow e + \text{O} + \text{O}$	$f(E/n)$	see text
R2	$e + \text{CH}_4 \rightarrow e + \text{CH}_3 + \text{H}$	$f(E/n)$	see text
Electron impact excitation			
R3	$e + \text{O}_2 \rightarrow e + \text{O}_2^*$	$f(E/n)$	see text
R4	$e + \text{Ar} \rightarrow e + \text{Ar}^*$	$f(E/n)$	see text
Electron impact ionization			
R5	$e + \text{Ar} \rightarrow 2e + \text{Ar}^+$	$f(E/n)$	see text
R6	$e + \text{O}_2 \rightarrow 2e + \text{O}_2^+$	$f(E/n)$	see text
R7	$e + \text{CH}_4 \rightarrow 2e + \text{CH}_4^+$	$f(E/n)$	see text
Quenching of excited Ar and O₂			
R8	$\text{Ar}^* + \text{O}_2 \rightarrow \text{Ar} + 2\text{O}$	$2 \cdot 10^{-10}$	[19]
R9	$\text{Ar}^* + \text{CH}_4 \rightarrow \text{Ar} + \text{CH}_2 + 2\text{H}$	$3.3 \cdot 10^{-10}$	[23, 24, 25]
R10	$\text{Ar}^* + \text{CH}_4 \rightarrow \text{Ar} + \text{CH} + \text{H} + \text{H}_2$	$5.8 \cdot 10^{-11}$	[23, 24, 25]
R11	$\text{Ar}^* + \text{CH}_4 \rightarrow \text{Ar} + \text{CH}_3 + \text{H}$	$5.8 \cdot 10^{-11}$	[23, 24, 25]
R12	$\text{Ar}^* + \text{CH}_4 \rightarrow \text{Ar} + \text{CH}_2 + \text{H}_2$	$5.8 \cdot 10^{-11}$	[23, 24, 25]
R13	$\text{O}_2^* + \text{CH}_4 \rightarrow \text{O}_2 + \text{CH}_3 + \text{H}$	10^{-10}	estimate
Charge exchange			
R14	$\text{CH}_4^+ + \text{O}_2 \rightarrow \text{CH}_4 + \text{O}_2^+$	$5 \cdot 10^{-10}$	Estimate
R15	$\text{Ar}^+ + \text{O}_2 \rightarrow \text{Ar} + \text{O}_2^+$	$1 \cdot 10^{-10}$	[26]
R16	$\text{Ar}^+ + \text{CH}_4 \rightarrow \text{Ar} + \text{CH}_3^+ + \text{H}$	$1.1 \cdot 10^{-9}$	[26]
R17	$\text{Ar}^+ + \text{CH}_4 \rightarrow \text{Ar} + \text{CH}_2^+ + \text{H}_2$	$2.3 \cdot 10^{-10}$	[26]
Electron-ion recombination			
R18	$e + \text{O}_2^+ \rightarrow \text{O} + \text{O}$	$2 \cdot 10^{-7} \cdot (300/T_e)$	[27]
R19	$e + \text{CH}_4^+ \rightarrow \text{CH}_3 + \text{H}$	$1.7 \cdot 10^{-7} \cdot (300/T_e)^{0.5}$	[28, 29]
R20	$e + \text{CH}_4^+ \rightarrow \text{CH}_2 + 2\text{H}$	$1.7 \cdot 10^{-7} \cdot (300/T_e)^{0.5}$	[28, 29]
R21	$e + \text{CH}_3^+ \rightarrow \text{CH}_2 + \text{H}$	$3.5 \cdot 10^{-7} \cdot (300/T_e)^{0.5}$	[28, 29]
R22	$e + \text{CH}_2^+ \rightarrow \text{CH} + \text{H}$	$2.5 \cdot 10^{-7} \cdot (300/T_e)^{0.6}$	[28, 29]

Gas discharges can be initiated and maintained at various values of electric field. In discharges, the energy gained by electrons from external electric field is lost in electron collisions with neutral particles. Electron heating in discharges and the efficiency of electron impact excitation of various states is controlled by the reduced electric field and composition of gaseous mixtures [30]. To demonstrate the efficiency of production of active

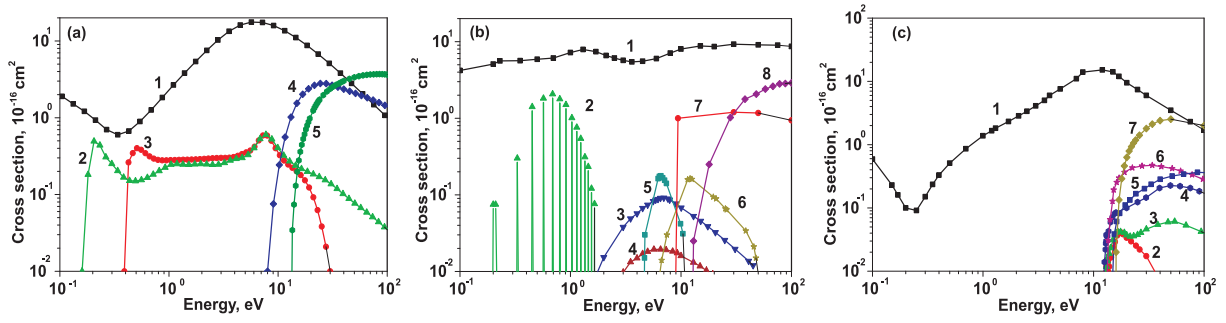


Figure 4.8: Electron collision cross-sections for (a) CH₄, (b) O₂, and (c) Ar. CH₄: (1) momentum transfer, (2)–(3) vibrational excitation, (4) electronic dissociation, and (5) ionization. O₂: (1) momentum transfer, (2) vibrational excitation, (3) excitation of a¹Δ_g electronic state, (4) excitation of b¹Σ_g electronic state, (5) excitation of electronic state with ΔE = 4.5 eV, (6) excitation of electronic state with ΔE = 6 eV, (7) excitation of electronic state with ΔE = 8.4 eV, and (8) ionization. Ar: (1) momentum transfer, (2) excitation of 1s₅ electronic state, (3) excitation of 1s₄ electronic state, (4) excitation of 1s₂ electronic state, (5) excitation of other allowed electronic states, (6) excitation of other forbidden electronic states, and (7) ionization.

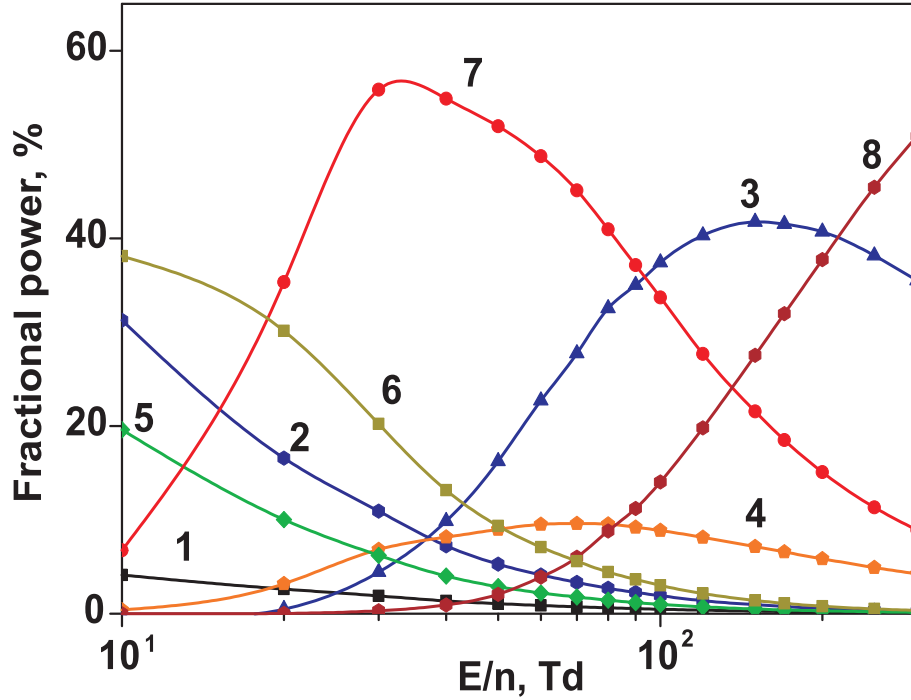


Figure 4.9: Fractional power transferred by the electrons to the neutral particles in (1) elastic collisions, (2) vibrational excitation of CH₄ and O₂, (3) excitation of Ar*, (4) dissociation of CH₄, (5) excitation of O₂ (a¹Δ_g) and O₂ (b¹Σ_g⁺), (6) excitation of O₂^{*} (ΔE = 4.5 eV state), (7) dissociation of O₂ and (8) ionization as a function of E/n for CH₄:O₂:Ar=1:2:27 mixture.

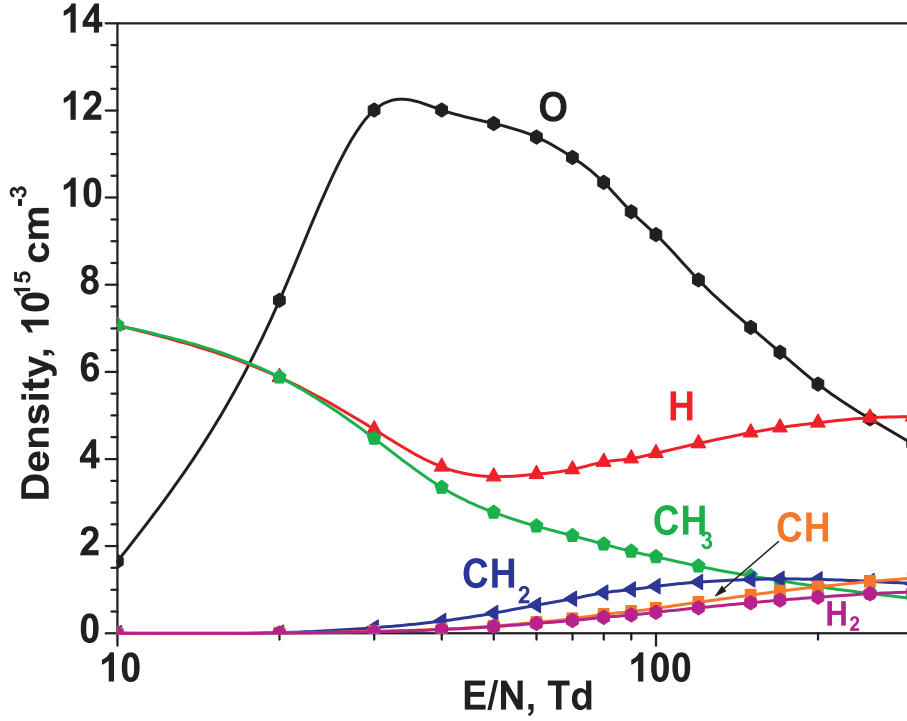


Figure 4.10: Densities of active particles produced in a $\text{CH}_4:\text{O}_2:\text{Ar}=1:2:27$ mixture for $P_5 = 1.1$ bar, $T_5 = 1500$ K as a function of E/n .

particles for the mixture under consideration, we calculated the fractional power transferred by electrons to neutral particles through various collisional mechanisms. Fig. 4.9 shows the calculated fractional power as a function of the reduced electric field, E/n , that governs the average electron energy. The amount of generated particles depends not only on the fraction power, but on the energy required to generate the particles as well. Fig. 4.10 shows the calculated density of various active particles as a function of E/n .

Typical values of the reduced electric field under the conditions considered are given in Fig. 4.4. To estimate these values, it is more appropriate to use E/n at the instant at which the current peaks. Indeed, this instant corresponds also to peak values of the deposited power $W(t)$ (see Fig. 4.11) and consequently to the most efficient production of active particles. It follows from Fig. 4.4 that active particles are most efficiently generated in our case for the reduced electric field in the range 20–120 Td. Here, according to Fig. 4.9 and Fig. 4.10, the composition of active particles should be dominated by O atoms and to some extent by products of the quenching of O_2^* (4.5 eV) molecules in collisions with CH_4 .

To simulate the evolution in time of the densities of active particles in a high electric field during the discharge, we solved numerically the balance equations using the rate coefficients calculated from the Boltzmann equation. Temporal evolution of electric field was taken from measurements. At the beginning of pulses of applied voltage (in the discharge front), there is generally a very short and high overshoot of the applied voltage that cannot be experimentally resolved. During the corresponding peak of the electric field in the discharge gap, according to approximate calculations, a noticeable density of charged particles is produced, whereas the production of neutral active particles is

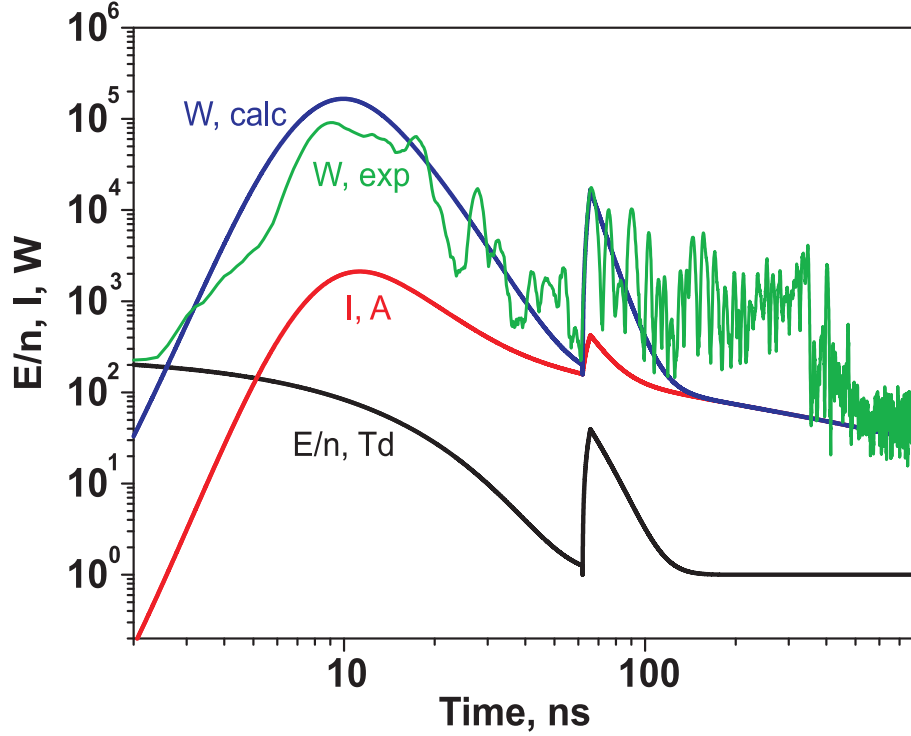


Figure 4.11: The evolution in time of the measured and calculated deposited power (in arb. units). The curves correspond to the same conditions as those in Fig. 4.3. For comparison, the temporal evolution of E/n (blue curve in Fig. 4.3(a)) and of I (dash curve in Fig. 4.3) are also given.

negligible. To take into account the production of electrons and ions in this, poorly known, phase, we considered the initial electron density at the beginning of the main pulses of applied voltage to be an adjusted parameter. This parameter was determined when calculating the evolution in time of the discharge current and adjusting it to corresponding measured data. As an example, Fig. 4.3 compares the temporal evolution of the calculated discharge current and that of the measured current under the same conditions. The calculations were based on the temporal evolution of electric field approximated by the curve in Figure 4.3. The discharge current was determined using the calculated values of electron density and electron drift velocity calculated from the Boltzmann equation as a function of the ratio E/n . The method used allowed a good agreement between measured and calculated currents to be obtained. A similar agreement was also obtained between calculated and measured values of deposited power (see Fig. 4.5) and specific deposited energy (see Fig. 4.11).

In the experiments under consideration, the main pulse of applied voltage was generally followed by several smaller pulses. The second peak in the electric field and current shown in Fig. 4.5 corresponds to the second voltage pulse. Production of active particles was simulated also in these additional discharge phases. As a rule, in this case production of atoms, radicals and excited neutral particles was noticeable, whereas production of electrons and ions was not important.

Fig. 4.12 shows the evolution in time of the mole fractions of dominant active species in the discharge and in its afterglow in the mixture under consideration. The curves cor-

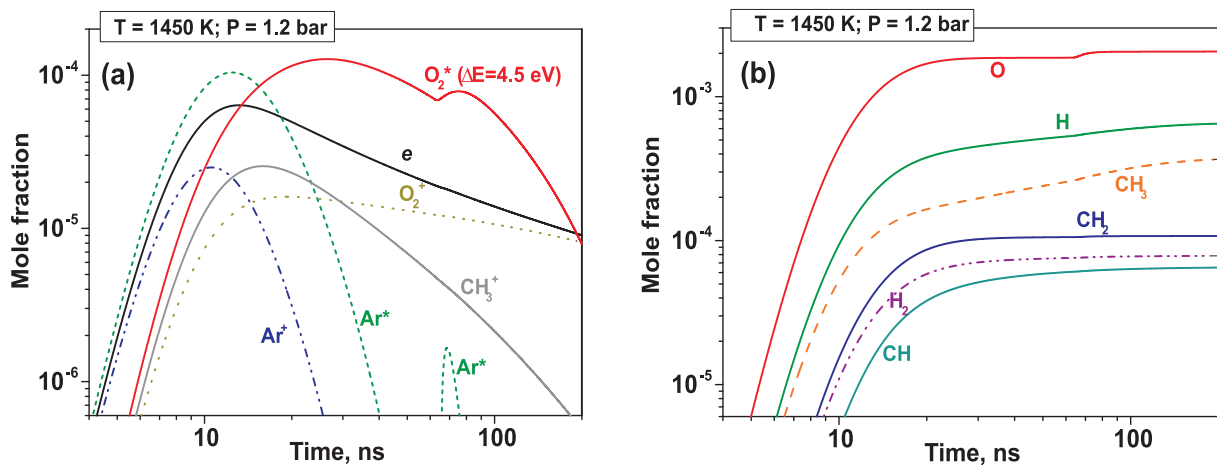


Figure 4.12: The evolution in time of mole fractions for (a) charged end excited particles and (b) atoms and radicals generated in the discharge. The curves correspond to the same conditions as those in Fig. 4.3.

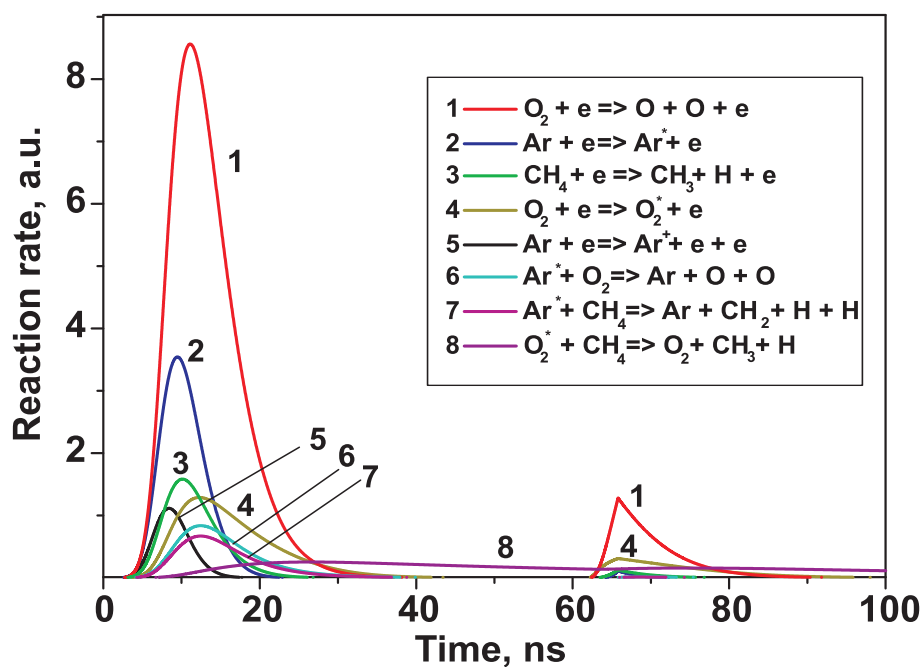


Figure 4.13: The evolution in time of the rates for production of various active species during the discharge. The curves correspond to the same conditions as those in Fig. 4.3.

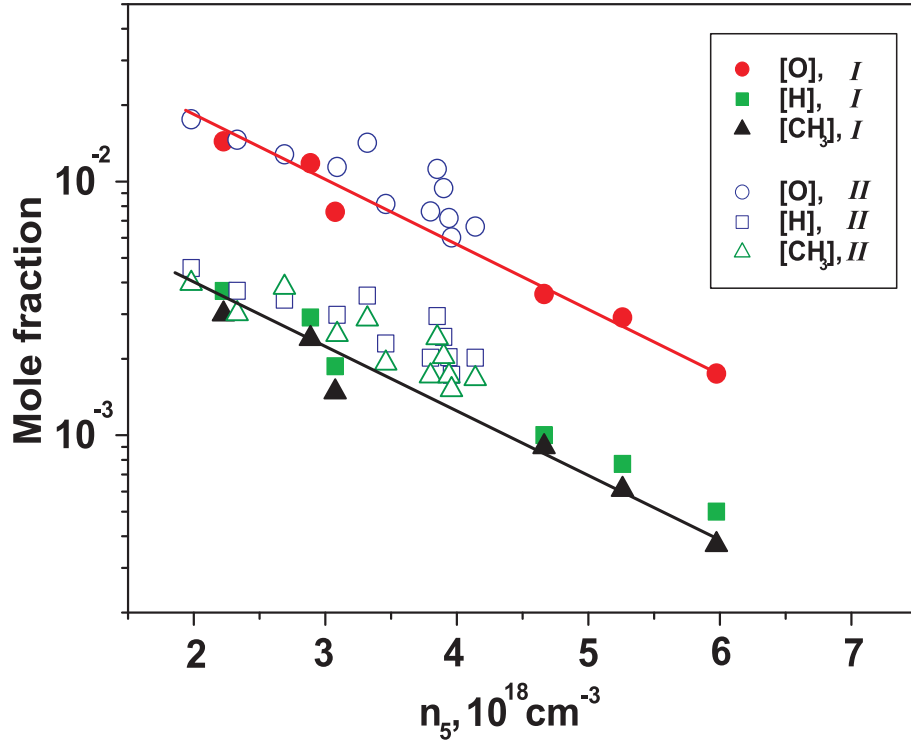


Figure 4.14: Initial data for high-temperature chemistry: densities of atoms and radicals produced by nanosecond discharge. Series *I* and *II* correspond to measurements at different values of T_5 , the values of n_5 being the same.

respond to the same conditions as those in Fig. 4.3. The temporal evolution of the rates for production of various active particles in this case is shown in Fig. 4.13. Calculations show that most of active particles was produced in the first voltage pulse due to electron impact dissociation, excitation and ionization. In the second pulse, only some additional amount of O atoms and excited O_2 molecules were formed. Between the pulses, in a zero electric field, charged particles were removed due to dissociative electron-ion recombination (reactions (R18) - (R21) in Table 4.2) producing an additional amount of atoms and radicals. The last particles were also produced due to charge exchange of Ar^+ ions on CH_4 (reactions (R16) and (R17)) and due to quenching of excited Ar atoms by oxygen and hydrocarbon molecules (reactions (R8) — (R13)). In our kinetic model, in the end charged and excited particles were excluded from the consideration and the gas mixture consisted of initial neutral species and atoms and radicals produced during the discharge and in its afterglow. The densities of atoms and radicals were used further as input parameters for a computer program to simulate ignition in the mixtures under consideration.

Density of atoms and radicals depends strongly upon the discharge development, or, more precisely, upon the gas number density. Dependence of atoms density *vs* gas number density is given in Fig. 4.14. Let us note, that the development of the discharge depends upon gas density (series *I* and *II*) and practically does not depend upon gas temperature.

4.3 Description of plasma assisted ignition

To model the autoignition we used standard RAMEC mechanism [31] with 35 components (H_2 , H , O , O_2 , OH , H_2O , HO_2 , H_2O_2 , C , CH , CH_2 , CH_3 , CH_4 , CO , CO_2 , HCO , CH_2O , CH_2OH , CH_3O , CH_3OH , C_2H , C_2H_2 , C_2H_3 , C_2H_4 , C_2H_5 , C_2H_6 , HCCO , CH_2CO , HCCOH , AR , CH_3O_2 , $\text{CH}_3\text{O}_2\text{H}$, $\text{C}_2\text{H}_5\text{O}$, $\text{C}_2\text{H}_5\text{O}_2$, $\text{C}_2\text{H}_5\text{O}_2\text{H}$) and 190 reactions. RAMEC mechanism is an extended version of GRI-Mech 1.2 mechanism [32] for the description of the ignition at relatively low temperatures. Calculations were performed in 0D approximation using CHEMKIN code [33].

The delay time was determined as the time between the schlieren signal, which corresponds to the arrival of the reflected shock wave at the diagnostic cross section, and the onset of the leading front of $\text{CH}(t)$ curve. The later was defined as the tangent to the kinetic curve at its maximum slope. Let us note here, that we performed special additional calculations where 22 reactions with electronically excited OH^* and CH^* were taken into account. The reaction rate constants were taken from [34]. It was demonstrated that we obtain the same induction delay time from dependencies $\text{CH}(t)$, $\text{OH}(t)$, $\text{CH}^*(t)$, $\text{OH}^*(t)$, or $T(t)$, where T is the gas temperature. Further, we used in the calculations $\text{CH}(t)$ curves to determine the ignition delay time.

Modelling the autoignition, we considered pressures higher than the pressures in the modelling of the discharge. This was connected with the fact that we were not able to obtain the autoignition at low experimentally: the autoignition time exceeded the work time of the shock tube. Coincidence (see Fig. 4.7) of the experimental results and calculations for the autoignition gave us the ground to use chosen kinetic mechanism to model the autoignition. We used the same kinetic scheme, but with other initial conditions. By analogy with the calculations of the discharge, we assumed 0D approximation is valid. This is confirmed by ICCD imaging of the nanosecond discharge at our conditions [35].

One of the most important questions is a question about the sensitivity of the results to the changes in $[\text{O}]$ -atoms density. Fig. 4.15 demonstrates the difference between calculations with different amounts of atomic oxygen. In spite of the fact that the difference is significant, it is still far from the difference between the autoignition and ignition by the discharge. One of the most important inaccuracy in our case is connected with the measurement of the electric field. Additional calculations show that the decrease of the electric field by 30 % leads to a decrease of radicals density by 20–30 %, and that the increase of the E/N by the same value leads to an increase in radical density by 10–20 %.

Fig. 4.16 illustrates the behavior of the reaction rates under the conditions of autoignition (Fig. 4.16(a)) and ignition by the discharge (Fig. 4.16(b)). Both regimes were calculated for the experimental point $T_5 = 1533 \text{ K}$, $P_5 = 1.1 \text{ bar}$, corresponding to plasma assisted ignition. The difference in behavior is clearly seen. Here, the additional production of active species in the discharge leads to the acceleration of the reactions.

We made the sensitivity analysis of the high-temperature kinetic scheme. The analysis was made as follows: the rate constant of each reaction was in turn increased by 50 % and the induction delay time was calculated separately for each case. The sensitivity coefficients were calculated as $(\tau_i - \tau_0)/\tau_0$, where τ_0 is the induction delay time calculated with unchanged rate constants and τ_i is the induction delay time calculated with the increased rate constant of the i -th reaction. Results of the calculations are given in Fig. 4.17. Under the ignition by the discharge the sensitivity to the reactions of chain

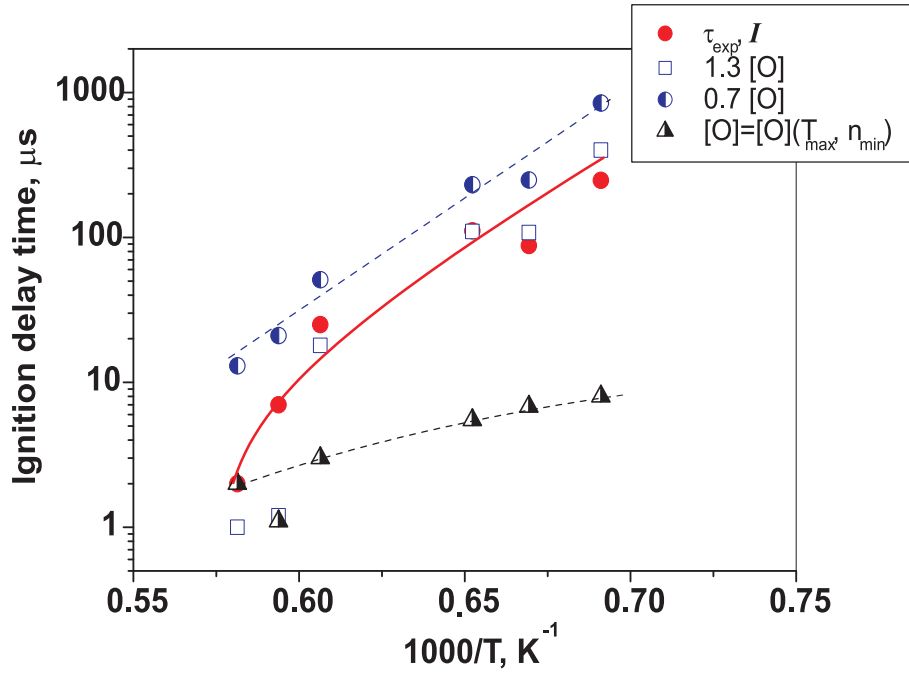


Figure 4.15: Sensitivity of the ignition delay time to the changes in density of atomic oxygen: (1) $[O]$ is 30 % higher than initial one; (2) $[O]$ is 30 % lower than initial one; (3) $[O]$ at every point is equal to the $[O]$ in the point with the highest temperature.

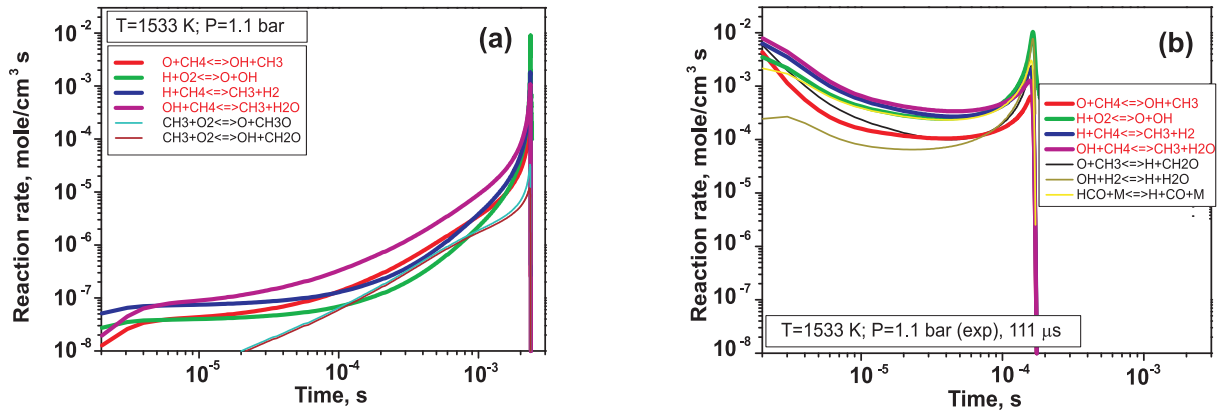


Figure 4.16: The evolution in time of the rates for the chemical reactions for (a) autoignition, and (b) ignition by pulsed discharge.

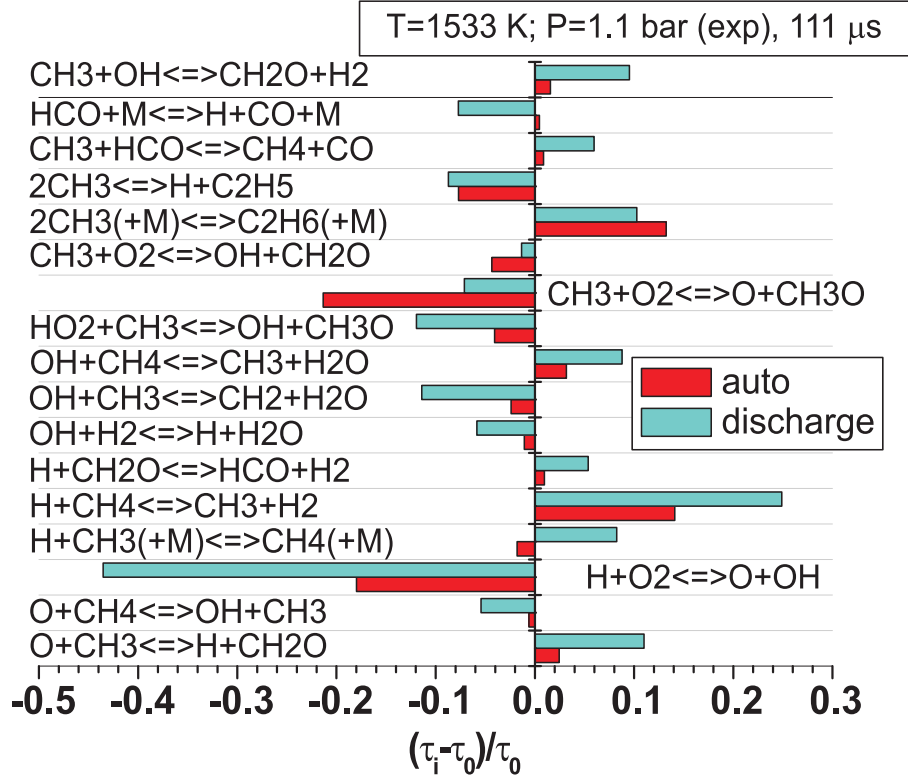


Figure 4.17: Results of sensitivity analysis for the autoignition and ignition by the discharge.

initiation decreases, and the sensitivity to the reactions of chain prolongation increases.

To demonstrate the value of the effect of plasma assisted ignition *vs* the reduced electric field we performed calculations at artificial behavior of the electric field. It was assumed that the electric field has a rectangular shape; the duration of the pulse of E/N was determined from the condition that the energy input has to be constant and equal to 14 mJ/cm³ ($T_5 = 1533$ K, $P_5 = 1.1$ bar). Initial electron density was taken to be 10¹² cm⁻³. Results of the calculations are given in Fig. 4.18. It is evident that the change in electric field from 10 to 300 Td does not lead to dramatical changes in the ignition delay time. At the same time, it is necessary to take into account that the duration of the pulse at low electric field is unreasonably long. In the range of the electric fields close to experimental ones we obtain reasonable values of the pulse duration (10⁻⁶ – 10⁻⁸ s). We have calculated the ignition delay time at lower and higher temperatures, taking them so that the gas number density (and, consequently, the production of radicals) were kept constant. It is clearly seen that in this case the values of the ignition delay time differ significantly, like it was in experiments of series *I* and *II* (see Fig. 4.7).

Thus, the calculations of the autoignition and plasma assisted ignition demonstrate that at high temperatures the discharge action leads to the development of chemical chain reactions. It is necessary to underline that at low temperatures the recombination of radicals has to be one of the most important mechanisms; this recombination is rather fast. And, when the temperature is enough for the development of the chains, the ignition is accelerated.

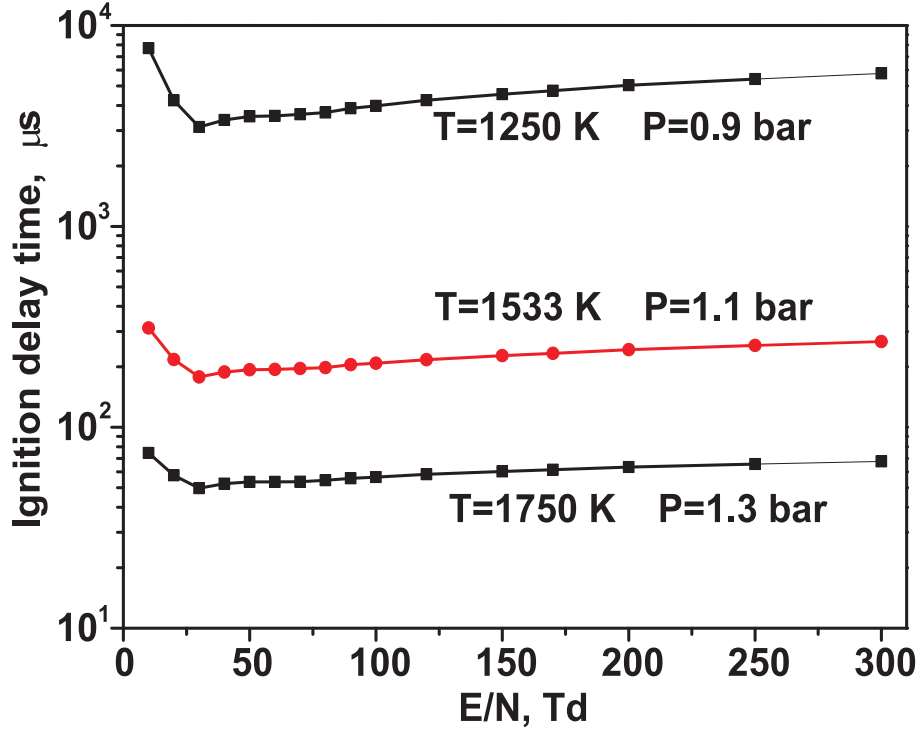


Figure 4.18: Induction delay time for the specific deposited energy 14 mJ/cm^3 as a function of reduced electric field.

4.4 Conclusions

We have made an experimental and numerical study of the ignition of methane-containing mixtures under the action of a high-voltage nanosecond discharge and showed that its initiation leads to a noticeable decrease in gas temperatures at which the mixtures are ignited and to an order of magnitude decrease in ignition delay time. The measurements agree well with ignition delay times calculated on the basis of an one-temperature, Arrhenius, chemical kinetics. To explain our observations, there is no need to use any additional mechanism suggested to favour the ignition processes, such as chemical reactions with excited or charged particles. It follows from the analysis of the calculated results that, at temperatures near the ignition threshold and at electric fields such that most of the electron energy is spent in the discharge to excite electronic levels of neutral particles and to ionize them, the main mechanism of the effect of gas discharge on the ignition of stoichiometric methane:oxygen mixtures is the electron impact dissociation of O_2 molecules in the discharge phase; this leads to an essential increase in the density of O atoms at the beginning of ignition.

Chapter 5

Kinetics of Plasma-Assisted Ignition of Hydrocarbon.

Ethane-to-Pentane: Oxygen Mixtures Diluted with Argon

5.1 Introduction

Ignition of combustible mixtures under the action of a non-equilibrium gas discharge is a complicated phenomenon in which heat transfer and chemical and hydrodynamic processes occur simultaneously with discharge processes. To gain greater insight into the mechanism of plasma assisted ignition (PAI) and combustion (PAC), sophisticated experiments should be made under controlled conditions. A promising way to study PAI and PAC is to separate in time [36] or in space [37] discharge processes and chemical reactions leading to ignition and combustion of gaseous mixtures. Based on this idea, much success was achieved in the understanding of the mechanisms of PAI/PAC in H_2 – and CH_4 – containing mixtures excited by a high-voltage nanosecond discharge [36], [38]. In this case, the separation of discharge and ignition processes allowed the development of computer models and numerical simulation of the effect of plasma on ignition. It was shown that the effect under consideration is primarily associated with faster development of chain reactions due to O and H atoms produced by electron impact dissociation of molecules in the discharge phase. This conclusion was corroborated by a good agreement between calculated ignition delay time and experimental data.

For practical purposes it is important to consider PAI/PAC for complicated fuels. For instance, kerosene contains 20–60 percent of alifatic hydrocarbons, 20–50 percent of naftenes and 5–25 percent of bi-cyclic organic compounds. Study of combustion of alkanes is important because of their wide use in car engines, gas turbine engines and heaters. Although combustion of hydrocarbons was studied for a long period of time, no universally accepted kinetic model has been developed for this process. Even the combustion of relatively simple hydrocarbons may involve hundreds and thousands of elementary steps. The most accepted models for combustion of simple hydrocarbons (CH_4 , C_2H_6 , C_3H_8 , etc.) are GRI [32] and RAMEC [31]. The mechanism of Westbrook [39] is of frequent use for describing the combustion of more complicated hydrocarbons.

To simulate PAI/PAC in hydrocarbon-containing mixtures, information is also required about the rates of electron impact production of active particles in the plasma. These rates are generally calculated based on a numerical simulation of the Boltzmann equation for electrons and using the sets of electron collision cross sections for the main components of the mixture [40]. Such cross-section sets are available only for the simplest hydrocarbons (CH_4 and C_2H_6) [40], whereas data for more complicated hydrocarbon molecules and radicals are meagre and much less reliable (see, for instance, [41], [42] and [43]).

To study the mechanism of PAI/PAC of hydrocarbons, it is reasonable to make experiments under controlled conditions and to analyze observations using computer simulation. This approach has been followed for CH_4 in [38]. In this work, the approach used in [38] has been extended to study PAI in $\text{C}_n\text{H}_{2n+2}$ -containing mixtures for $n = 2$ to 5. The ignition of stoichiometric hydrocarbon-oxygen mixtures diluted with Ar was studied experimentally and numerically under the action of a high-voltage nanosecond discharge. Ignition delay time was measured in these mixtures as a function of gas temperature and pressure with simultaneous control of the discharge current and electric field. The densities of active particles produced in the discharge were calculated and used as input parameters for the simulation of ignition process. A kinetic mechanism of PAI was determined by simulating the ignition process and comparing calculated ignition delay time and measured one.

5.2 Experiment

5.2.1 Experimental setup and methods

We studied stoichiometric $\text{C}_n\text{H}_{2n+2}:\text{O}_2$ mixtures (10 %) diluted with Ar (90 %) for $n = 2$ to 5. The experimental setup and technique of measurements have been given in the previous chapter of the Report. Ignition delay time, like in the experiments with CH_4 -containing mixture, was obtained using the CH emission ($\lambda = 431 \text{ nm}$, the $B^2\Sigma^-(v' = 0) \rightarrow X^2\Pi(v'' = 0)$ transition). The delay time was determined as the time between the schlieren signal, which corresponds to the arrival of the reflected shock wave at the diagnostic cross section, and the onset of the leading front of the emission. The onset was defined as the tangent to the emission intensity–time curve at its maximum slope.

5.2.2 Measurement of discharge characteristics

Fig. 5.1 shows typical signals from electric gauges on a nanosecond scale for ethane-containing mixture. The signals are rather similar to those obtained for methane-containing mixture. This is reasonable, because the main features of the discharge development under our experimental conditions were determined by Ar (90 %) and oxygen. Conditions of the experiments and electrical parameters for each mixture are given by Figs. 5.2–5.5. It is clearly seen (Figs. 5.2a–5.5a) that for each mixture there is an intersection in (T_5, n_5) field between the experiments on autoignition and on the ignition by nanosecond discharge. This gives an opportunity to provide a direct estimate of the efficiency of nonequilibrium plasma. The amplitude of the high-voltage pulse did not varied significantly, being within the range $110 \pm 10 \text{ kV}$ (Figs. 5.2d–5.5d). The amplitude of electric current is 2–3 kA for

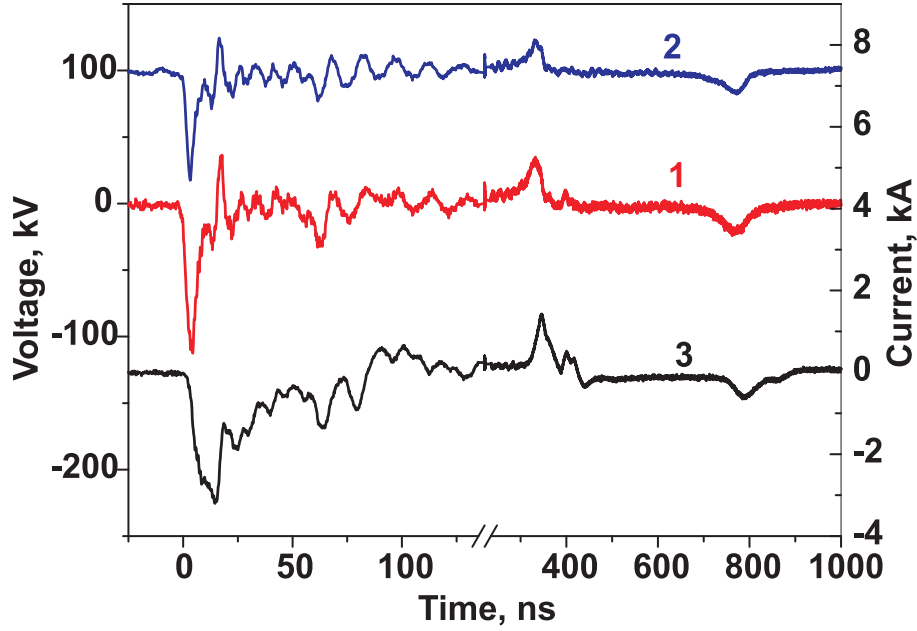


Figure 5.1: Typical signals on a nanosecond scale from (1) the capacitive gauge No 1 (see Figure 4.1), (2) capacitive gauge No 2 and (3) magnetic current gauge in the C_2H_6 -containing mixture. The gas parameters are $T_5=1318$ K and $P_5 = 0.6$ bar. The voltage amplitude is 110 kV on the high-voltage electrode.

all the experimental points (Figs. 5.2c–5.5c). The total energy input depends upon the gas density (Figs. 5.2b–5.5b). It is clearly seen that, depending upon gas density, the role of the first electric pulse and re-reflections may be different. The lower the gas density, the higher the energy input from the re-reflections.

In the discharge phase, the electric field rose fast, peaked and then decreased slowly. The discharge current evolved in time in a similar way; however, it peaked with some delay relative to the electric field. Mean electron energy and the rates of electron impact processes in the discharge phase are controlled by the reduced electric field, E/n_5 . Fig. 5.6 shows the values of reduced electric field for mixtures with different hydrocarbons at the instant at which the discharge current and specific deposited energy peaked as a function of n_5 . The values of E/n_5 decreased from 100 ± 20 Td ($1 \text{ Td} = 10^{-17} \text{ V}\cdot\text{cm}^2$) at $n_5 = 2 \times 10^{18} \text{ cm}^{-3}$ to 40 ± 10 Td at $n_5 = 5 \times 10^{18} \text{ cm}^{-3}$. The variation of E/n_5 with gas mixtures, n_5 being the same, was much smaller. This effect seems to be associated with different discharge conditions (variation in the amplitude of high-voltage pulse, etc.) and experimental error, rather than with variation in mixture percentage. Indeed, in the mixtures under consideration the fraction of the dominant species, Ar and O_2 , are almost the same, whereas the percentage of hydrocarbons is small (see Table 5.1). Therefore, the real effect of gas composition on discharge characteristics in our case must be negligible.

The discharge behaviour depended strongly on the gas number density behind a reflected shock wave, n_5 , and was not sensitive to mixture composition and gas temperature under the conditions considered. Fig. 5.7 shows the temporal evolution of the specific energy deposited in the discharge for various gas densities. The deposited power w was calculated in the same way as in paragraph 4.1.2.

Fig. 5.8 shows the specific deposited energy, w , over all high-voltage pulses as a function

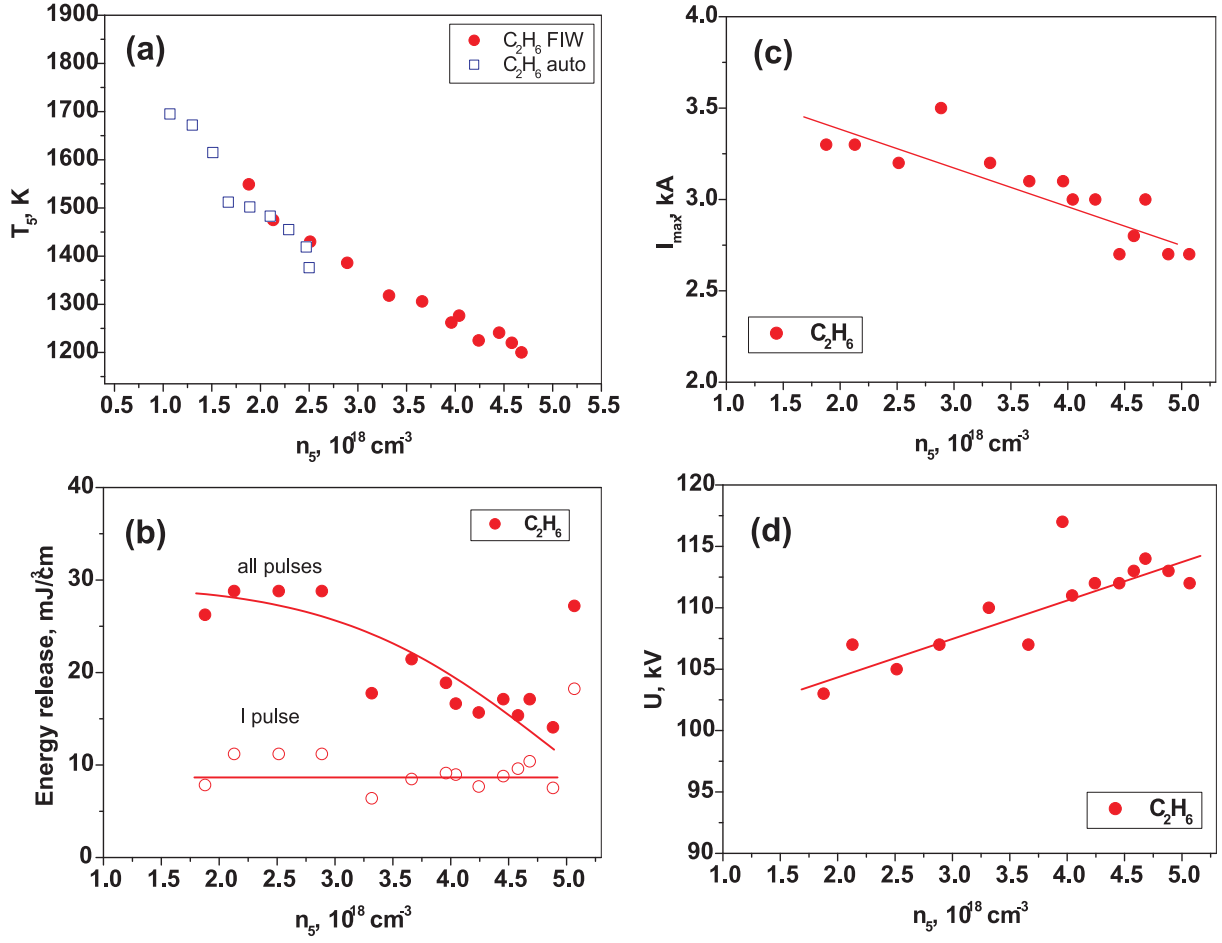


Figure 5.2: Parameters of the experiments for C_2H_6 -containing mixture: (a): dependence of gas temperature behind the reflected shock wave (T_5) upon the gas density (n_5); (b) dependence of volumetric energy input upon gas density, role of the first pulse and re-reflections is indicated; (c) maximal value of electrical current for different gas densities; (d) amplitude of high-voltage pulse on the high-voltage electrode at different gas densities

of gas number density. The values of w were in the range $10 - 30 \text{ mJ/cm}^3$. It should be noted that this energy is certainly not enough to shift the autoignition curve to the data we obtain in the experiments with the discharge. For example, in the C_2H_6 -containing mixture autoignition delay time at initial gas temperature 1700 K is equal to $55 \mu\text{s}$. Under the action of the discharge we obtain the same ignition delay time at gas temperature 1300 K . Let's assume that all the energy deposited into plasma is consumed to the heating of the gas, what is a rough upper estimate. This estimation will not give us values $50-70 \text{ K}$, and this proves that at the conditions of our experiments we definitely have non-thermal character of ignition.

5.2.3 Measurement of ignition characteristics

The behaviour of signals from schlieren gauges during the autoignition and plasma assisted ignition of CH_4 -containing mixture was discussed in [38]. In our study of the ignition of $\text{C}_n\text{H}_{2n+2}$ -containing mixtures at $n > 1$, these signals behave in a similar way and we do

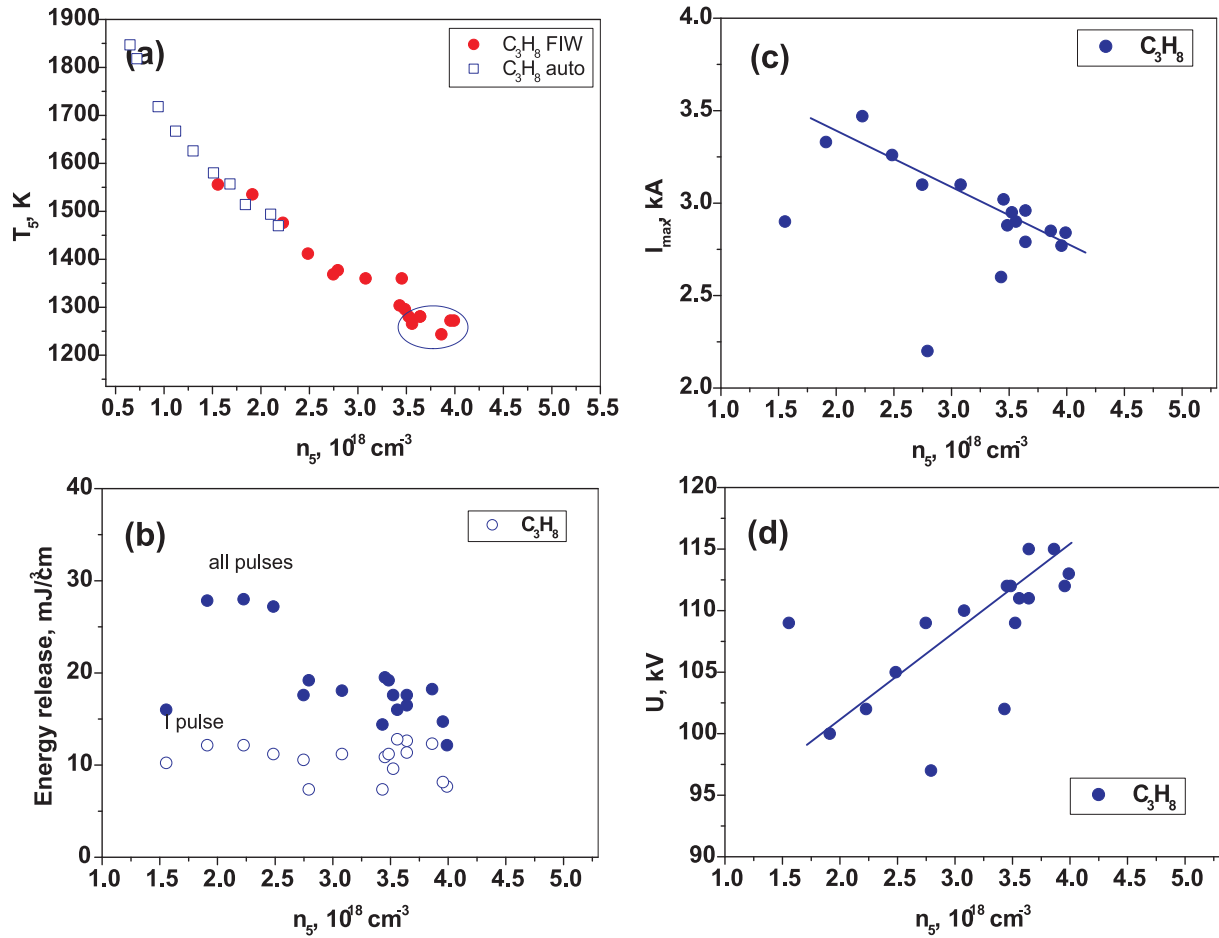


Figure 5.3: Parameters of the experiments for C_3H_8 -containing mixture: (a): dependence of gas temperature behind the reflected shock wave (T_5) upon the gas density (n_5); (b) dependence of volumetric energy input upon gas density, role of the first pulse and re-reflections is indicated; (c) maximal value of electrical current for different gas densities; (d) amplitude of high-voltage pulse on the high-voltage electrode at different gas densities

not present their records in this part of the Report.

Tables 5.2–5.5 present initial parameters measured behind the reflected shock wave and calculated mole fractions of the dominant species of active particles produced in the discharge phase, for each experiment.

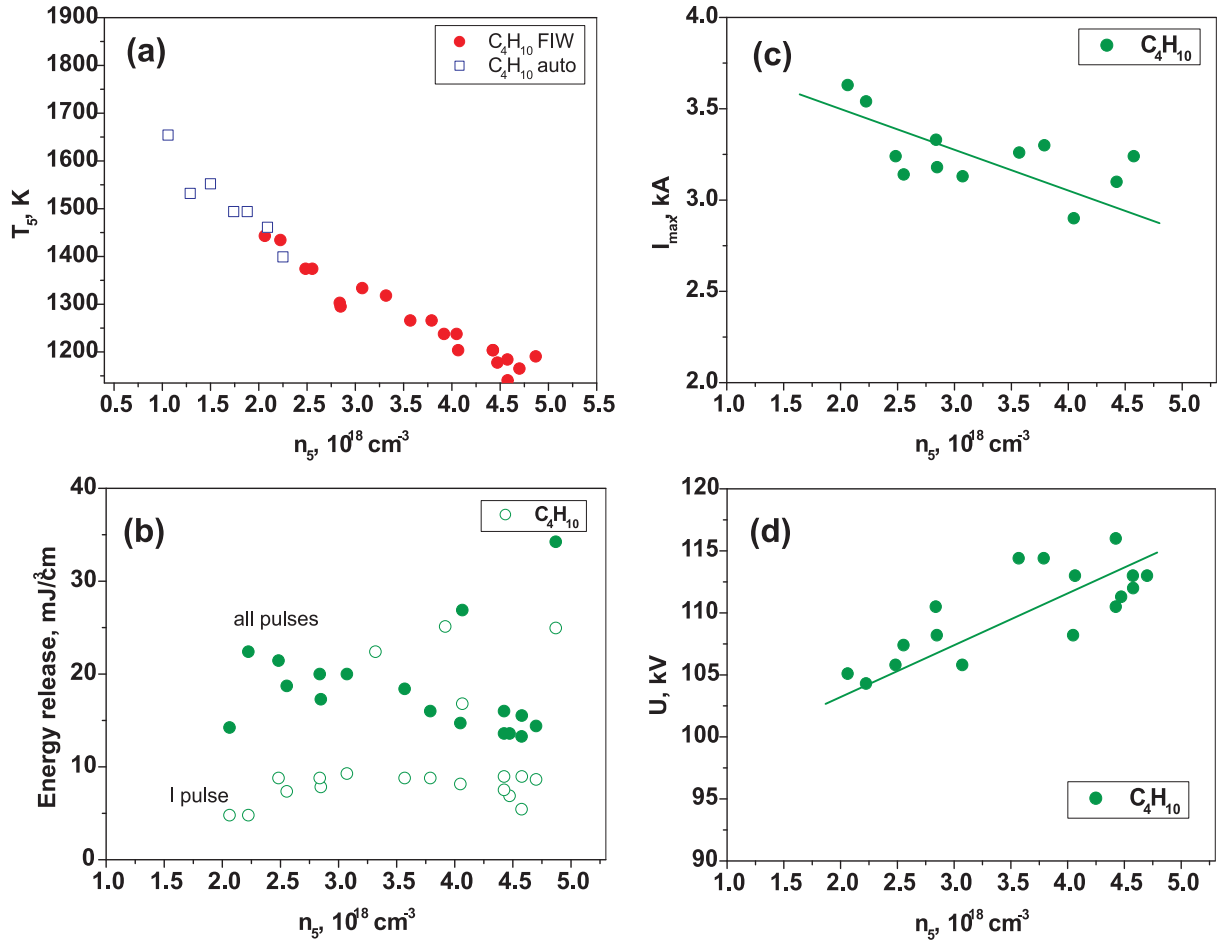


Figure 5.4: Parameters of the experiments for C_4H_{10} -containing mixture: (a): dependence of gas temperature behind the reflected shock wave (T_5) upon the gas density (n_5); (b) dependence of volumetric energy input upon gas density, role of the first pulse and re-reflections is indicated; (c) maximal value of electrical current for different gas densities; (d) amplitude of high-voltage pulse on the high-voltage electrode at different gas densities

Table 5.2: Initial gas parameters of a $C_2H_6:O_2:Ar=2:7:81$ mixture behind the reflected shock wave, measured delay times for autoignition and ignition by the discharge and calculated mole fractions of O, H and C_2H_5 .

No	T_5 , K	P_5 , bar	n_5 , 10^{18} cm^{-3}	$^*\tau_a$, μs	τ_d , μs	$[O]/n_5$	$[H]/n_5$	$[C_2H_5]/n_5$
1	1376	0.47	2.50	292	-	-	-	-
2	1419	0.48	2.47	242	-	-	-	-
3	1455	0.45	2.29	205	-	-	-	-
4	1483	0.42	2.10	168	-	-	-	-
5	1502	0.39	1.89	142	-	-	-	-
6	1512	0.34	1.67	144	-	-	-	-
7	1615	0.33	1.51	85	-	-	-	-
8	1672	0.30	1.30	77	-	-	-	-
9	1695	0.25	1.07	55	-	-	-	-
10	1276	0.70	4.04	-	147	0.00345	0.00209	0.00173
11	1200	0.76	4.68	-	238	0.00259	0.00163	0.00134
12	1220	0.76	4.58	-	209	0.00283	0.00164	0.00136
13	1241	0.75	4.45	-	245	0.0028	0.00138	0.00112
14	1225	0.70	4.24	-	156	0.00317	0.00186	0.00161
15	1262	0.68	3.96	-	119	0.00481	0.00268	0.00229
16	1306	0.65	3.66	-	68	0.0054	0.00266	0.00215
17	1318	0.60	3.32	-	53	0.00517	0.00328	0.00286

Table 5.2: Initial gas parameters of a $\text{C}_2\text{H}_6:\text{O}_2:\text{Ar}=2:7:81$ mixture behind the reflected shock wave, measured delay times for autoignition and ignition by the discharge and calculated mole fractions of O, H and C_2H_5 .

No	T_5 , K	P_5 , bar	n_5 , 10^{18} cm^{-3}	$^*\tau_a$, μs	τ_d , μs	$[\text{O}]/n_5$	$[\text{H}]/n_5$	$[\text{C}_2\text{H}_5]/n_5$
18	1549	0.40	1.88	-	4	0.0143	0.0063	0.00516
19	1386	0.55	2.89	-	25	0.00925	0.00507	0.00437
20	1430	0.49	2.51	-	12	0.0121	0.00553	0.00466
21	1475	0.43	2.13	-	7	0.0135	0.00554	0.00438

* In the Table, τ_a is the autoignition delay time and τ_d is the delay time in the case of ignition by the discharge.

Table 5.3: Initial parameters of a $\text{C}_3\text{H}_8:\text{O}_2:\text{Ar}=1:5:54$ mixture behind the reflected shock wave, measured delay time for autoignition and ignition by the discharge and calculated mole fractions of O, C_3H_7 and H.

No	T_5 , K	P_5 , bar	n_5 , 10^{18} cm^{-3}	$^*\tau_a$, μs	τ_d , μs	$[\text{O}]/n_5$	$[\text{H}]/n_5$	$[\text{C}_3\text{H}_7]/n_5$
1	1818	0.18	0.72	76	-	-	-	-
2	1718	0.22	0.94	111	-	-	-	-
3	1667	0.26	1.12	143	-	-	-	-
4	1626	0.29	1.30	154	-	-	-	-
5	1580	0.33	1.51	196	-	-	-	-
6	1557	0.36	1.68	245	-	-	-	-
7	1514	0.39	1.84	350	-	-	-	-
8	1494	0.42	2.01	374	-	-	-	-
9	1470	0.45	2.18	408	-	-	-	-
10	1847	0.17	0.65	69	-	-	-	-
11	1377	0.53	2.79	-	119	0.00705	0.00281	0.00234
12	1412	0.49	2.48	-	101	0.012	0.00437	0.00354
13	1476	0.46	2.23	-	26	0.0137	0.00534	0.00429
14	1535	0.41	1.91	-	20	0.016	0.00607	0.00477
15	1556	0.34	1.56	-	15	0.0105	0.00342	0.00224
16	1369	0.52	2.75	-	138	0.00659	0.00278	0.00231
17	1360	0.58	3.08	-	124	0.0065	0.0027	0.00222
18	1360	0.65	3.45	-	116	0.00494	0.00211	0.00175
19	1296	0.63	3.48	-	282	0.0055	0.00245	0.00204
20	1304	0.62	3.43	-	271	0.00426	0.00192	0.0016

* In the Table, τ_a is the autoignition delay time and τ_d is the delay time in the case of ignition by the discharge.

Table 5.4: Initial parameters of a $\text{C}_4\text{H}_{10}:\text{O}_2:\text{Ar}=2:13:135$ mixture behind the reflected shock wave, measured delay time for autoignition and ignition by the discharge and calculated mole fractions of O, C_4H_9 and H.

No	T_5 , K	P_5 , bar	n_5 , 10^{18} cm^{-3}	$^*\tau_a$, μs	τ_d , μs	$[\text{O}]/n_5$	$[\text{H}]/n_5$	$[\text{C}_4\text{H}_9]/n_5$
1	1399	0.43	2.25	274	-	-	-	-
2	1461	0.42	2.09	192	-	-	-	-
3	1494	0.36	1.88	153	-	-	-	-
4	1494	0.38	1.74	145	-	-	-	-
5	1532	0.27	1.29	133	-	-	-	-
6	1552	0.32	1.50	94	-	-	-	-
7	1654	0.24	1.06	48	-	-	-	-
8	1204	0.73	4.42	-	215	0.00454	0.00237	0.00192
9	1184	0.74	4.58	-	190	0.00341	0.00177	0.00159
10	1238	0.68	4.05	-	209	0.00444	0.00196	0.00174
11	1266	0.65	3.79	-	108	0.00506	0.00231	0.00205
12	1266	0.62	3.57	-	74	0.00745	0.00298	0.0026
13	1334	0.56	3.07	-	65	0.00901	0.0035	0.00301
14	1295	0.50	2.85	-	75	0.00965	0.00965	0.00299
15	1303	0.50	2.84	-	57	0.00869	0.00375	0.00329
16	1374	0.48	2.55	-	31	0.0108	0.00388	0.0033
17	1434	0.44	2.22	-	9	0.015	0.00502	0.00423
18	1374	0.47	2.48	-	30	0.0119	0.00451	0.00386
19	1443	0.41	2.06	-	10	0.0138	0.0048	0.00403

* In the Table, τ_a is the autoignition delay time and τ_d is the delay time in the case of ignition by the discharge.

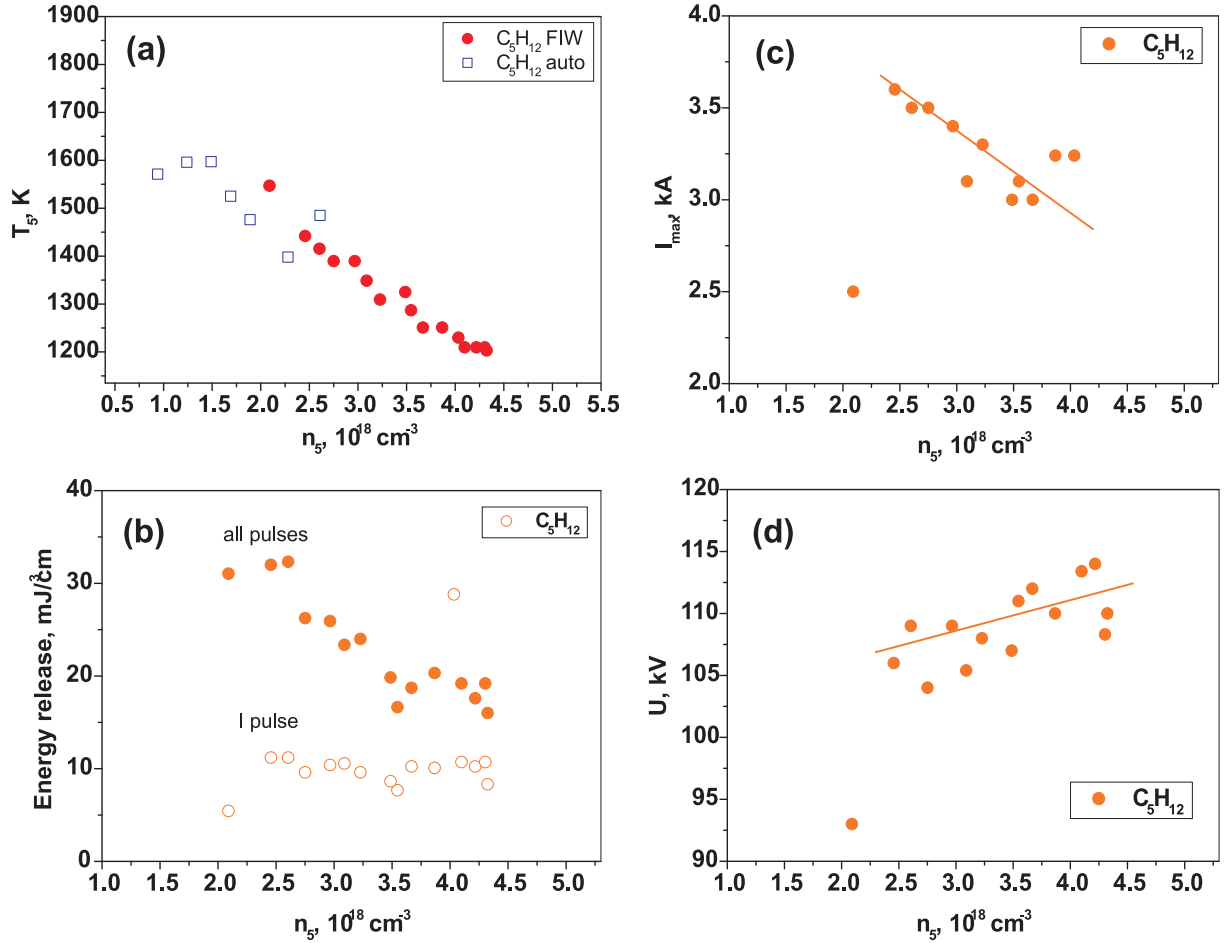


Figure 5.5: Parameters of the experiments for C_5H_{12} -containing mixture: (a): dependence of gas temperature behind the reflected shock wave (T_5) upon the gas density (n_5); (b) dependence of volumetric energy input upon gas density, role of the first pulse and re-reflections is indicated; (c) maximal value of electrical current for different gas densities; (d) amplitude of high-voltage pulse on the high-voltage electrode at different gas densities

Table 5.5: Initial parameters of a $C_5H_{12}:O_2:Ar=1:8:81$ mixture behind the reflected shock wave, measured delay time for autoignition and ignition by the discharge and calculated mole fractions of O, C_5H_{11} and H.

No	T_5 , K	P_5 , bar	n_5 , 10^{18} cm^{-3}	τ_a , μs	τ_d , μs	$[O]/n_5$	$[H]/n_5$	$[C_5H_{11}]/n_5$
1	1596	0.27	1.24	68	-	-	-	-
2	1597	0.33	1.49	90	-	-	-	-
3	1571	0.20	0.94	90	-	-	-	-
4	1525	0.35	1.69	107	-	-	-	-
5	1485	0.53	2.61	134	-	-	-	-
6	1476	0.38	1.89	150	-	-	-	-
7	1398	0.43	2.28	234	-	-	-	-
8	1230	0.68	4.03	-	154	0.00787	0.00257	0.00218
9	1251	0.66	3.87	-	75	0.00651	0.00252	0.00226
10	1251	0.63	3.67	-	109	0.00647	0.00255	0.00225
11	1287	0.62	3.55	-	120	0.00584	0.00226	0.00201
12	1325	0.63	3.49	-	65	0.00596	0.00258	0.0023
13	1309	0.58	3.23	-	60	0.00837	0.00299	0.0026
14	1349	0.57	3.09	-	41	0.00979	0.00366	0.00322
15	1390	0.56	2.97	-	32	0.00995	0.00363	0.0032
16	1390	0.52	2.75	-	25	0.0092	0.00363	0.0032
17	1415	0.50	2.60	-	12	0.0164	0.0054	0.00469

Table 5.5: Initial parameters of a $\text{C}_5\text{H}_{12}:\text{O}_2:\text{Ar}=1:8:81$ mixture behind the reflected shock wave, measured delay time for autoignition and ignition by the discharge and calculated mole fractions of O, C_5H_{11} and H.

No	T_5 , K	P_5 , bar	n_5 , 10^{18} cm^{-3}	$^*\tau_a$, μs	τ_d , μs	$[\text{O}]/n_5$	$[\text{H}]/n_5$	$[\text{C}_5\text{H}_{11}]/n_5$
18	1442	0.48	2.46	-	8	0.0167	0.00602	0.00523
19	1547	0.44	2.09	-	4	0.0156	0.00508	0.00427

These experimental data on autoignition were validated using previous data obtained by other authors. So, for C_3H_8 we compared our data with the approximation formula given by the authors of Ref. [44]. The autoignition delay is given by the expression $\tau^* = A[\text{C}_3\text{H}_8]^a[\text{O}_2]^b \exp(\theta/T)$, where the ignition delay time τ^* is in s, the concentrations $[\text{C}_3\text{H}_8]$ and $[\text{O}_2]$ are in mol cm^{-3} and the parameter θ is in K. An agreement within 50 % was found between our data and τ^* calculated with the coefficients given in Ref. [44] ($A = 4.4 \times 10^{-14}$, $\theta = 21200$, $a = 0.57$, $b = -1.22$) for all the range of our experimental conditions. The ignition delay time versus gas temperature is shown in Figs. 5.9—5.12 for various gas mixtures.

Each figure contains the results of experiments on autoignition and ignition by the discharge. It is clearly seen that the effect of gas discharge leads to a drastic decrease in ignition delay and to ignition of the mixtures at noticeably lower temperatures and gas number densities. For all the hydrocarbons, we have obtained a reasonable agreement between the experimental data and the results of the numerical modelling.

5.3 Numerical simulation and discussion

5.3.1 Description of discharge and near afterglow

Under the conditions considered the discharge processes occurred on a nanosecond scale, whereas the ignition processes occurred on a microsecond scale. Therefore, by analogy with [38], we simulated the temporal evolution of densities of particles important for plasma-assisted ignition separately in the discharge phase and in the ignition one. The effect of discharge non-equilibrium plasma was reduced to the accumulation of active particles that influence following ignition processes.

In the discharge phase, we simulated numerically the production of active particles in $\text{C}_n\text{H}_{2n+2}:\text{O}_2:\text{Ar}$ mixtures in a high electric field during the discharge and conversion of the particles during plasma decay in the near afterglow. Our kinetic model was based on that developed in [38]. Active particles under consideration were electronically excited O_2 molecules and Ar atoms, O atoms, H atoms, radicals of hydrocarbon molecules, electrons and simple positive ions. The focus was on the mechanisms that could lead to dissociation of the molecules. We neglected vibrationally and electronically excited states of O_2 , which have energy insufficient to dissociate the molecules and simulated the excitation of metastable Herzberg $\text{O}_2(\text{c}^1\Sigma_u^-)$, $\text{O}_2(\text{C}^3\Delta_u)$ and $\text{O}_2(\text{A}^3\Sigma_u^+)$ states by the excitation of one effective metastable state with an excitation energy of 4.5 eV (referred to as O_2^*), by analogy with [16, 17, 18]. The excitation of the electronical states of O_2 with higher excitation energy lead to the dissociation and these processes were referred to as electron impact dissociation of O_2 . Excitation of electronical Ar states was also simulated by the excitation of one effective state (referred to as Ar^*) with the excitation rate being equal to the total rate of excitation of all excited Ar states. Formation of negative ions and

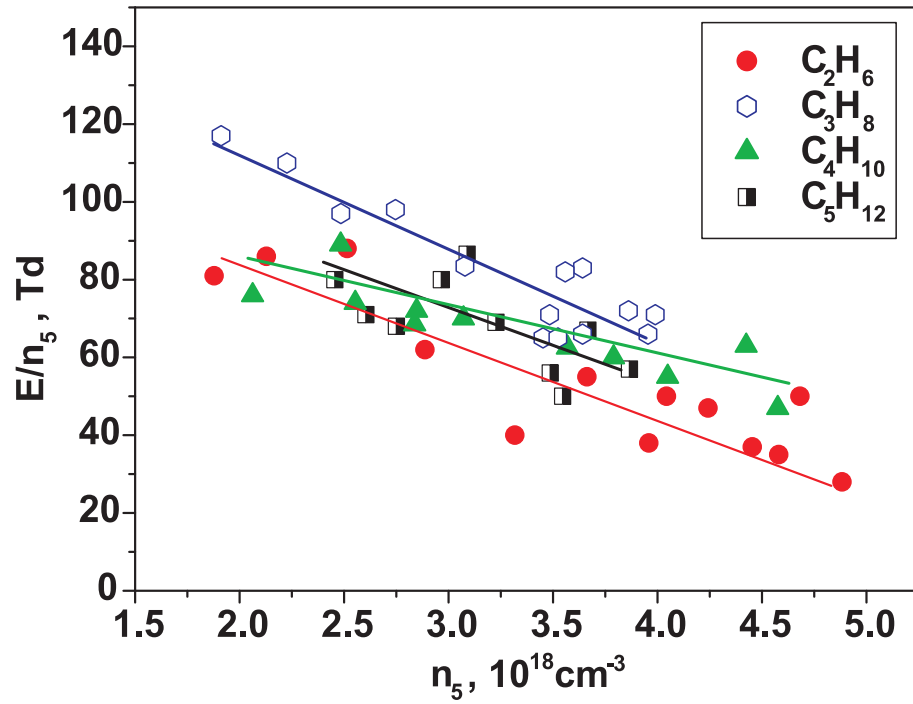


Figure 5.6: The values of the reduced electric field at the instant at which the discharge current peaks as a function of the gas number density. Solid lines are approximations of the experimental data.

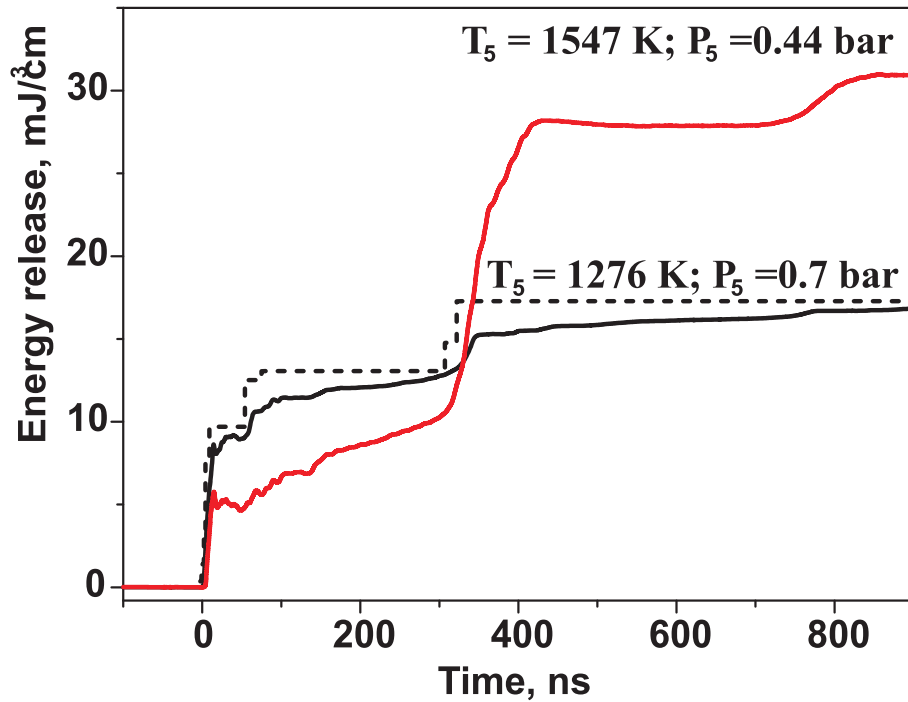


Figure 5.7: The typical temporal evolution of the specific deposited energy for various gas temperatures, pressures and gas mixture composition. Solid curves correspond to measurements and dash curves correspond to calculations.

Table 5.1: Percentage composition of mixtures under consideration

	Hydrocarbon	O ₂	Ar
C ₂ H ₆	2.22	7.78	90
C ₃ H ₈	1.67	8.33	90
C ₄ H ₁₀	1.33	8.67	90
C ₅ H ₁₂	1.11	8.89	90

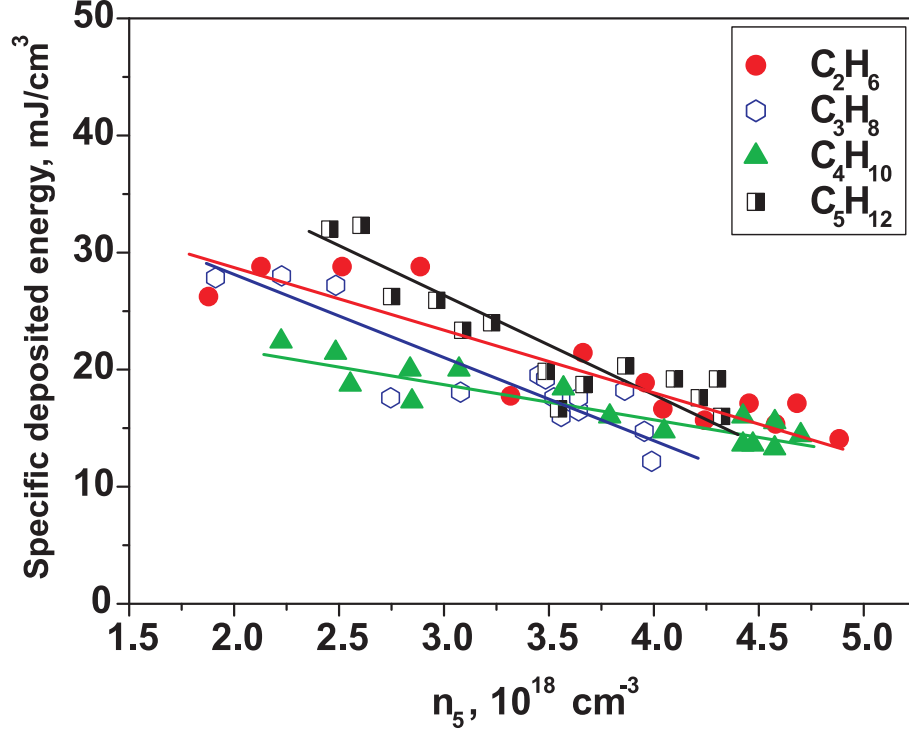


Figure 5.8: The total specific deposited energy for various gas mixtures as a function of gas density. Solid lines are approximations of the experimental data.

complex positive ions was neglected. At the end of plasma decay, only atoms and radicals were assumed to dominate the composition of active particles.

The temporal evolution of densities of active particles in the discharge phase was calculated based on a numerical solution of the corresponding balance equations. Table 5.6 shows reactions considered in our kinetic model and their rate coefficients. We considered electron impact dissociation, excitation and ionization of neutral particles, quenching of electronically excited particles, charge exchange in collisions between ions and neutral particles and dissociative electron-ion recombination, the dominant mechanism of electron loss in the discharge afterglow under the conditions considered.

The rate coefficients for reactions between heavy particles were taken from the literature. We have failed to find rate coefficients of reactions (R13) and (R14); therefore, these coefficients and products in these reactions were estimated. The products of reactions (R10), (R11) and (R12) were assumed to be similar to those of reaction (R9). The rate coefficients for reactions (R17) and (R19) were assumed to be equal to the rate

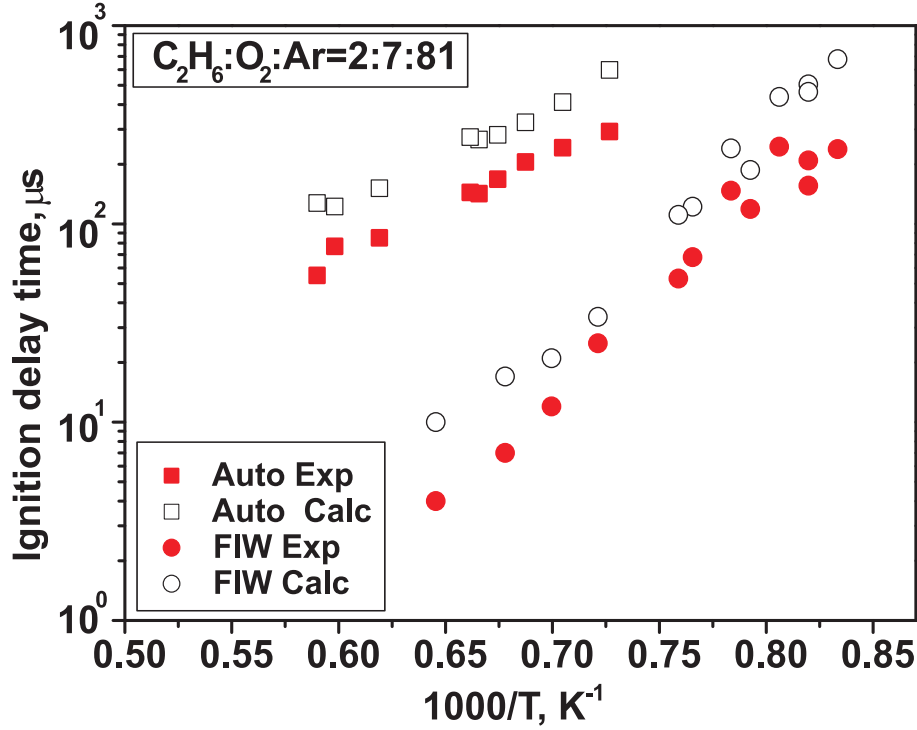


Figure 5.9: The delay time for autoignition and PAI in the $\text{C}_2\text{H}_6:\text{O}_2:\text{Ar}=2:7:81$ mixture as a function of temperature for autoignition and ignition with the discharge. Closed symbols correspond to measurements and open symbols correspond to calculations.

coefficient for reaction (R16). The products of reactions (R16) - (R19) were assumed to be similar to those for charge exchange of Ar^+ ions in collisions with CH_4 . (The products for the last reaction are given in [26].)

Little is known about rate coefficients and products for electron recombination with hydrocarbon ions. We assumed that the rate coefficients for recombination of hydrocarbon ions under consideration are equal to the rate coefficient for C_2H_5^+ ions taken from [28]. The products of electron-ion recombination were assumed to be similar to those for the channels with the highest branching ratios taken from [41].

The scheme of ion-molecule reactions given in Table 5.6 is somewhat oversimplified. Indeed, additional calculations taking into account a more detailed scheme [41, 42, 43] showed that the ion composition in the discharge and its afterglow could be different. However, the calculated density of neutral active particles are not sensitive to ion composition and most of calculations were carried out based on the scheme given in Table 5.6.

Rate coefficients for electron impact dissociation (reactions (R1) and (R2) in Table 5.6, for electron impact excitation (reactions (R3) and (R4)) and for electron impact ionization (reactions (R5) — (R7)) were calculated as a function of E/n . We used standard BOL-SIG+ software [22] to solve numerically the electron Boltzmann equation in the classical two-term approximation and to determine the non-equilibrium electron energy distribution [20]. When solving the Boltzmann equation, the input parameters were the reduced electric field E/n and gas composition. The electron distribution was not sensitive to gas temperature. We considered only electron collisions with atoms and molecules of the dominant species in the gas mixtures. The effect of electron-electron collisions and

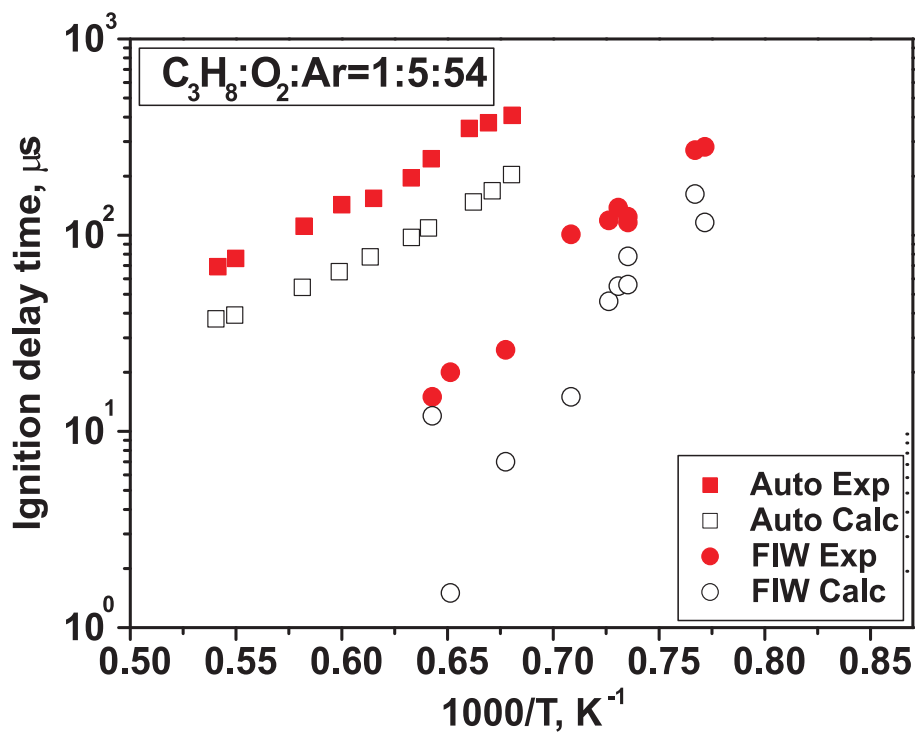


Figure 5.10: The delay time for autoignition and PAI in the $\text{C}_3\text{H}_8:\text{O}_2:\text{Ar}$ mixture as a function of temperature for autoignition and ignition with the discharge. Closed symbols correspond to measurements and open symbols correspond to calculations.

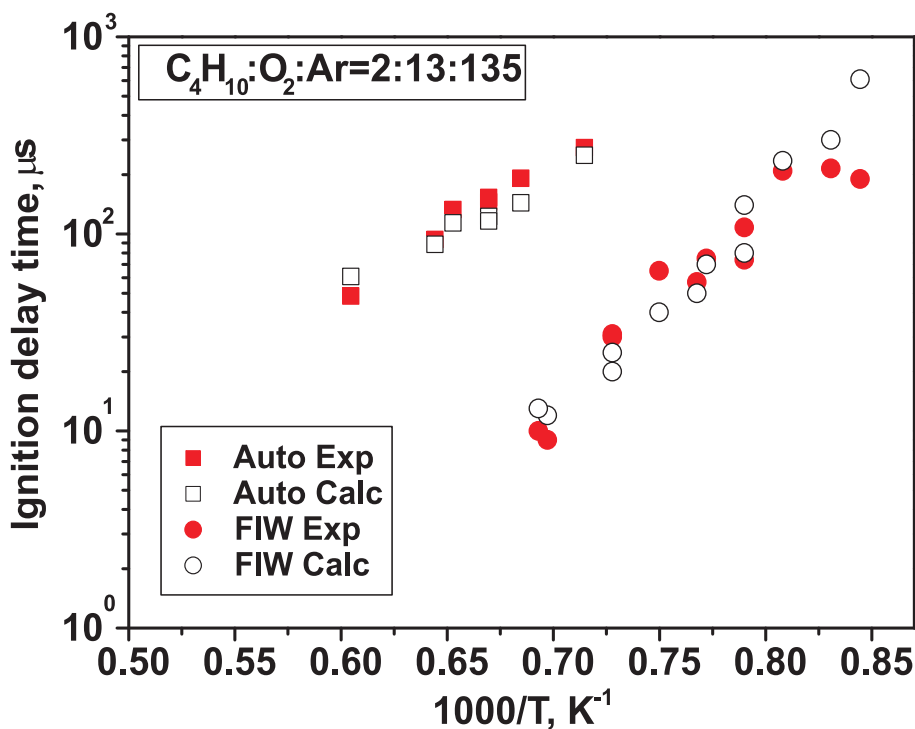


Figure 5.11: The delay time for autoignition and PAI in the $\text{C}_4\text{H}_{10}:\text{O}_2:\text{Ar}$ mixture as a function of temperature for autoignition and ignition with the discharge. Closed symbols correspond to measurements and open symbols correspond to calculations.

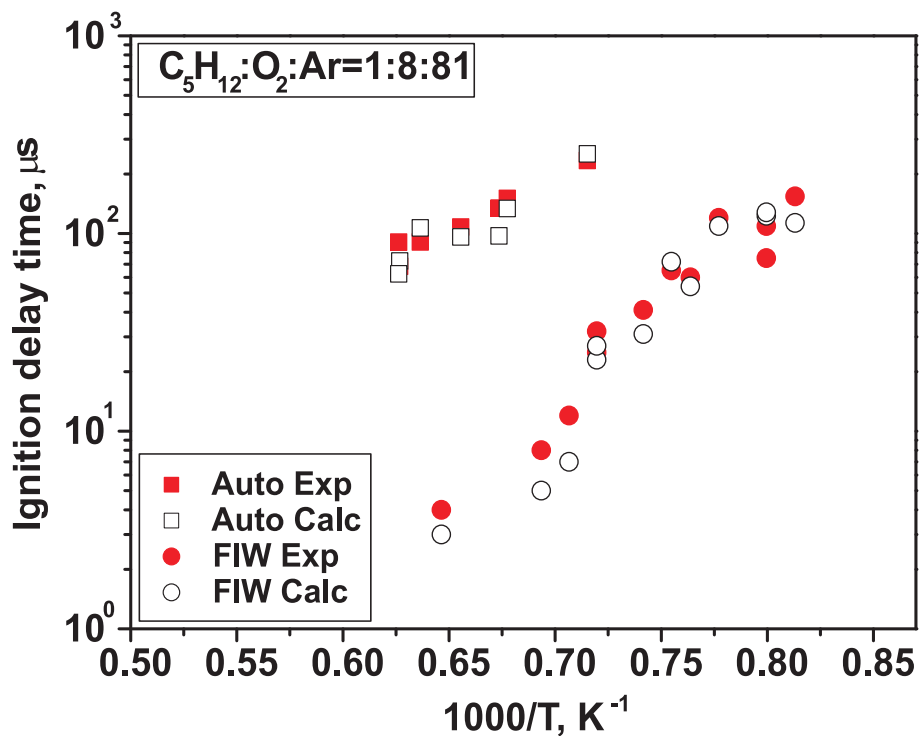


Figure 5.12: The delay time for autoignition and PAI in the $C_5H_{12}:O_2:Ar$ mixture as a function of temperature for autoignition and ignition with the discharge. Closed symbols correspond to measurements and open symbols correspond to calculations.

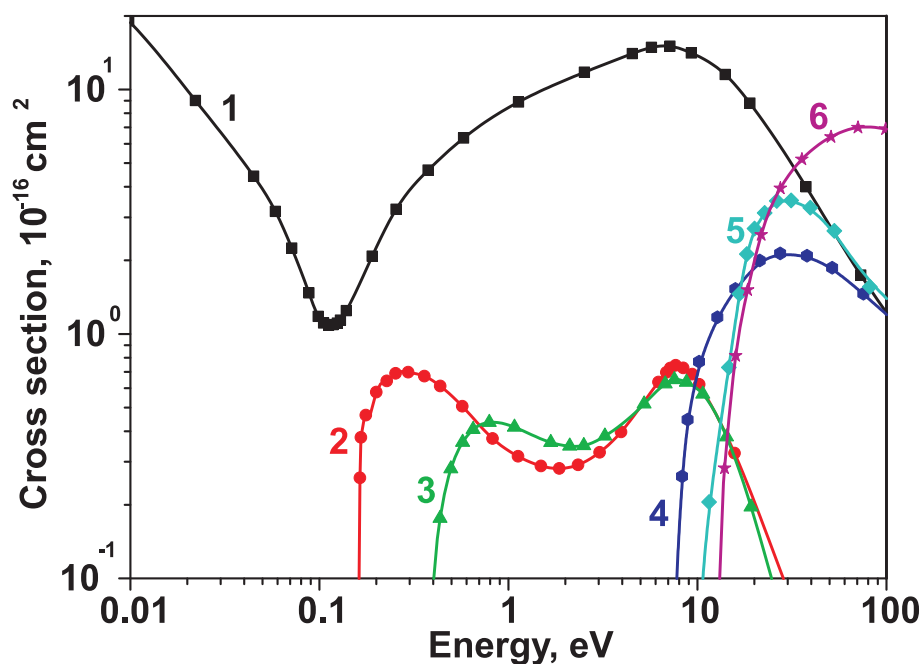


Figure 5.13: Electron collision cross-sections for C_2H_6 [45]: (1) momentum transfer, (2) vibrational excitation with a threshold of 0.168 eV, (3) vibrational excitation with a threshold of 0.371 eV, (4) electronic excitation with a threshold of 7.53 eV, (5) electronic excitation with a threshold of 10.12 eV, and (6) ionization.

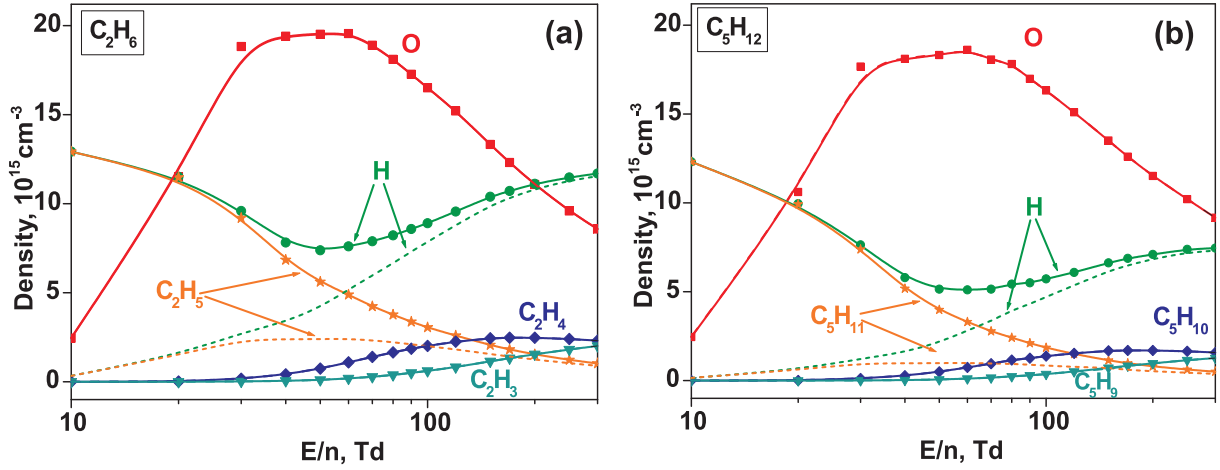


Figure 5.14: Densities of active particles produced in (a) $\text{C}_2\text{H}_6:\text{O}_2:\text{Ar}=2:7:81$ and (b) $\text{C}_5\text{H}_{12}:\text{O}_2:\text{Ar}=1:8:81$ mixtures as a function of E/n . The specific deposited energy is (a) 23 and (b) 19 mJ/cm^3 . Solid curves correspond to calculation taking into account reaction (R13) and dashed curves correspond to calculation neglecting this reaction.

collisions between electrons and new particles produced in the discharge was neglected because of their small densities. We used the available in literature, self-consistent sets of cross sections for electron collisions with Ar [21], O_2 [18] and C_2H_6 [45]; these cross sections allow a good agreement between calculations and measurements of transport and rate coefficients in the pure gases. Fig. 5.13 shows the cross sections used in our simulation for C_2H_6 . The cross sections used in our simulation for Ar and O_2 have been given elsewhere [38]. No reliable, self-consistent, sets of electron cross sections are available for C_3H_8 , C_4H_{10} and C_5H_{12} . In our simulation, these cross sections were assumed to be similar to those for C_2H_6 .

In addition, products of electron impact dissociation of $\text{C}_n\text{H}_{2n+2}$ are not known for $n > 1$. The energy of C–C bonds in these molecules is lower than that of C–H bonds and the chain initiation step in autoignition is to break the C–C bonds [46]. However, the difference between the energies of C–C and C–H bonds is much less than the average electron energy in the high-voltage discharge and products of electron impact dissociation can be quite different. To estimate production of active particles due to these processes in the discharge, we assumed that products of electron impact dissociation of $\text{C}_n\text{H}_{2n+2}$ are $\text{C}_2\text{H}_{2n+1}$ and H atoms. According to [41], it is one of the dominant channels of electron impact dissociation of C_2H_6 and C_3H_8 .

Thus, to solve the Boltzmann equation and to calculate the electron rate constants, we took into account elastic scattering of electrons, vibrational excitation and dissociation of O_2 and hydrocarbon molecules and electronic excitation and ionization of Ar, O_2 and hydrocarbon molecules.

Table 5.6: The kinetic scheme of the processes taken into account to simulate the production of atoms and radicals by the gas discharge in the $\text{C}_n:\text{H}_{2n+2}:\text{O}_2:\text{Ar}$ mixtures

Number	Reaction	Rate constant, cm^3/s	Reference
--------	----------	---------------------------------------	-----------

Electron impact dissociation			
R1	$e + \text{O}_2 \rightarrow e + \text{O} + \text{O}$	$f(E/n)$	see text
R2	$e + \text{C}_n\text{H}_{2n+2} \rightarrow e + \text{C}_n\text{H}_{2n+1} + \text{H}$	$f(E/n)$	see text
Electron impact excitation			
R3	$e + \text{O}_2 \rightarrow e + \text{O}_2^*$	$f(E/n)$	see text
R4	$e + \text{Ar} \rightarrow e + \text{Ar}^*$	$f(E/n)$	see text
Electron impact ionization			
R5	$e + \text{Ar} \rightarrow 2e + \text{Ar}^+$	$f(E/n)$	see text
R6	$e + \text{O}_2 \rightarrow 2e + \text{O}_2^+$	$f(E/n)$	see text
R7	$e + \text{C}_n\text{H}_{2n+2} \rightarrow 2e + \text{C}_n\text{H}_{2n+2}^+$	$f(E/n)$	see text
Quenching of excited Ar and O ₂			
R8	$\text{Ar}^* + \text{O}_2 \rightarrow \text{Ar} + 2\text{O}$	$2 \cdot 10^{-10}$	[19]
R9	$\text{Ar}^* + \text{C}_2\text{H}_6 \rightarrow \text{Ar} + \text{C}_2\text{H}_4 + 2\text{H}$	7×10^{-10}	[23, 24, 25]
R10	$\text{Ar}^* + \text{C}_3\text{H}_8 \rightarrow \text{Ar} + \text{C}_3\text{H}_6 + 2\text{H}$	8×10^{-10}	[23]
R11	$\text{Ar}^* + \text{C}_4\text{H}_{10} \rightarrow \text{Ar} + \text{C}_4\text{H}_8 + 2\text{H}$	9×10^{-10}	[23]
R12	$\text{Ar}^* + \text{C}_5\text{H}_{12} \rightarrow \text{Ar} + \text{C}_5\text{H}_{10} + 2\text{H}$	1×10^{-9}	[23]
R13	$\text{O}_2^* + \text{CH}_4 \rightarrow \text{O}_2 + \text{CH}_3 + \text{H}$	10^{-10}	estimate
Charge exchange			
R14	$\text{O}_2^+ + \text{C}_n\text{H}_{2n+2} \rightarrow \text{O}_2 + \text{C}_n\text{H}_{2n+2}^+$	3×10^{-10}	estimate
R15	$\text{Ar}^+ + \text{O}_2 \rightarrow \text{Ar} + \text{O}_2^+$	1×10^{-10}	[26]
R16	$\text{Ar}^+ + \text{C}_2\text{H}_6 \rightarrow \text{Ar} + \text{C}_2\text{H}_5^+ + \text{H}$	1.1×10^{-9}	[26]
R17	$\text{Ar}^+ + \text{C}_3\text{H}_8 \rightarrow \text{Ar} + \text{C}_3\text{H}_7^+ + \text{H}$	1.1×10^{-9}	see text
R18	$\text{Ar}^+ + \text{C}_4\text{H}_{10} \rightarrow \text{Ar} + \text{C}_4\text{H}_9^+ + \text{H}$	1.4×10^{-9}	[47]
R19	$\text{Ar}^+ + \text{C}_5\text{H}_{12} \rightarrow \text{Ar} + \text{C}_5\text{H}_{11}^+ + \text{H}$	1.1×10^{-9}	see text
Electron-ion recombination			
R20	$e + \text{O}_2^+ \rightarrow \text{O} + \text{O}$	$2 \times 10^{-7} \times (300/T_e)$	[27]
R21	$e + \text{C}_n\text{H}_{2n+1}^+ \rightarrow \text{C}_n\text{H}_{2n-1} + 2\text{H}$	$7.4 \times 10^{-7} \times (300/T_e)^{0.5}$	see text
R22	$e + \text{C}_n\text{H}_{2n+2}^+ \rightarrow \text{C}_k\text{H}_{2n} + 2\text{H}$	$7.4 \times 10^{-7} \times (300/T_e)^{0.5}$	see text
R23	$e + \text{C}_n\text{H}_{2n}^+ \rightarrow \text{C}_n\text{H}_{2n-2} + 2\text{H}$	$7.4 \times 10^{-7} \times (300/T_e)^{0.5}$	see text

Gas discharges can be initiated and maintained at various values of electric field. In discharges, the energy gained by electrons from external electric field is lost in collisions with neutral particles. Electron heating in discharges and the efficiency of electron impact excitation of various states is controlled by the reduced electric field and composition of gaseous mixtures [30]. To demonstrate the efficiency of production of active particles for the mixture under consideration, we calculated the amount of particles generated in the mixtures under consideration for various values of E/n . Fig. 5.14 shows the calculated density of active particles for the C_2H_6 — C_5H_{12} -containing mixtures as a function of E/n .

Typical values of the reduced electric field under the conditions considered are given in Fig. 5.7. It follows from Fig. 5.7 that active particles are most efficiently generated in our case for the reduced electric field in the range 30–120 Td. Here, according to Fig. 5.14, the composition of active particles is dominated by O atoms and to some extent by products of the quenching of O_2^* (4.5 eV) molecules in collisions with hydrocarbon molecules.

To simulate the evolution in time of the densities of active particles in a high electric field during the discharge, we solved numerically the balance equations using the rate

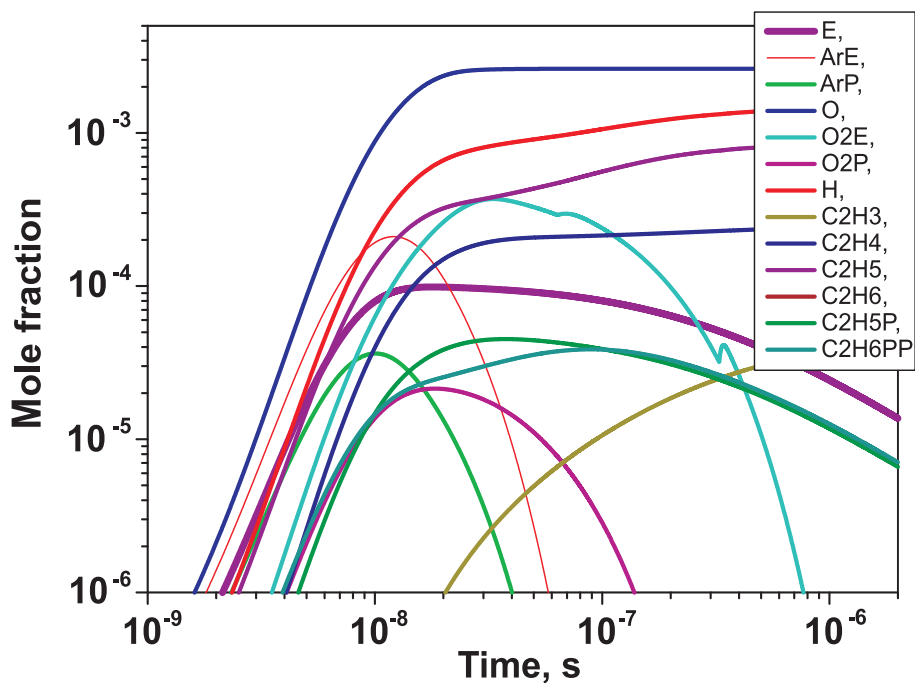


Figure 5.15: The evolution in time of mole fractions for different species generated in the discharge. for C_2H_6 -containing mixture. $T_5=1275$ K, $P_5=0.7$ bar.

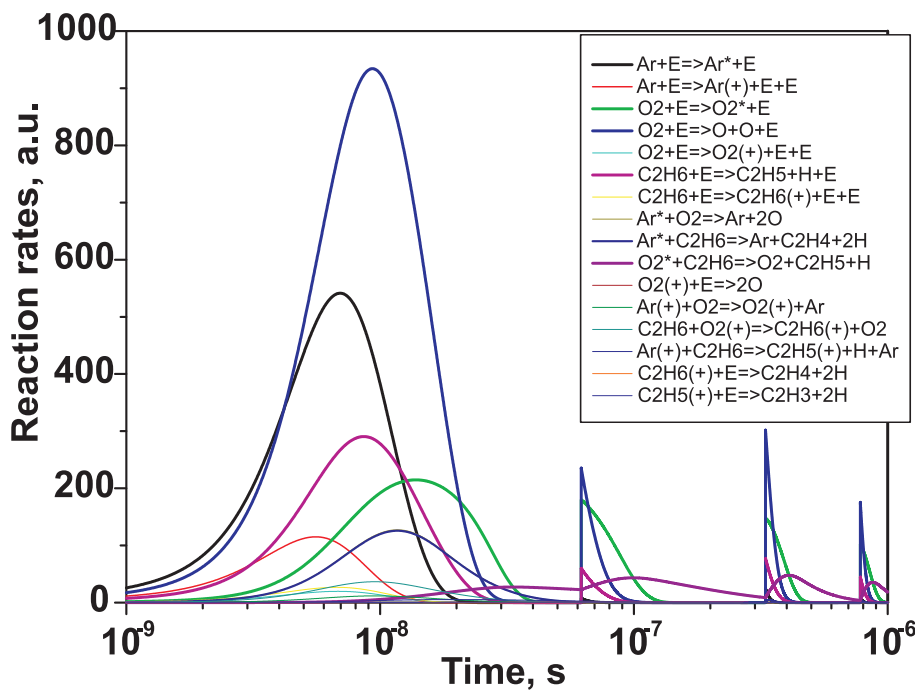


Figure 5.16: The evolution in time of the rates for production of various active species during the discharge for C_2H_6 -containing mixture. $T_5=1275$ K, $P_5=0.7$ bar.

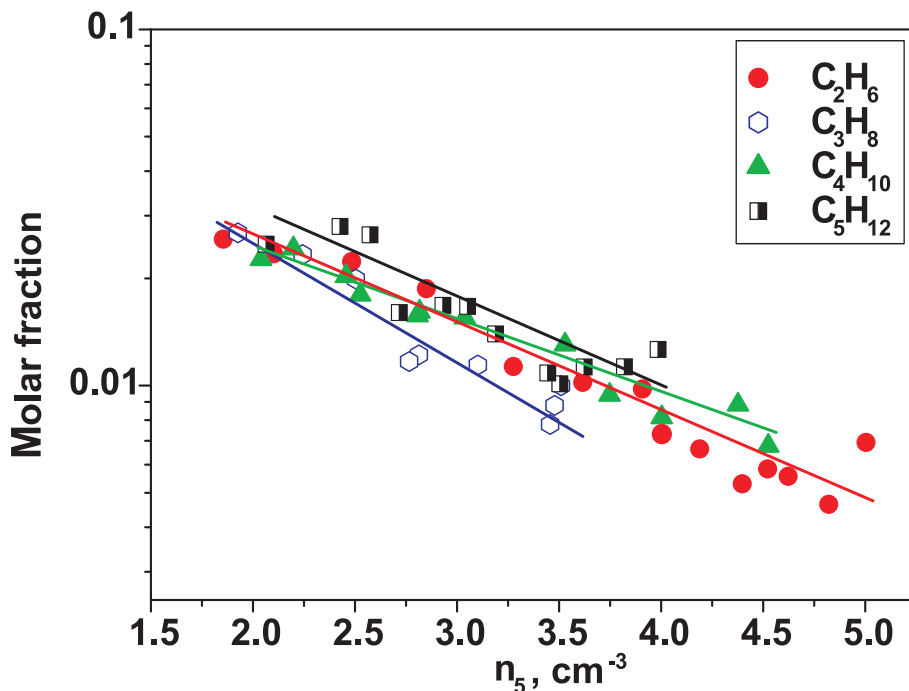


Figure 5.17: The calculated mole fractions of O, H and C_nH_{2n+1} produced by the discharge in the gas mixtures under consideration as a function of n_5 .

coefficients calculated from the Boltzmann equation. Temporal evolution of electric field was taken from measurements. At the beginning of pulses of applied voltage (in the discharge front), there is generally a very short and high overshoot of the applied voltage that cannot be experimentally resolved. During the corresponding peak of the electric field in the discharge gap a noticeable density of charged particles is produced, whereas the production of neutral active particles is negligible. To take into account the production of electrons and ions in this, poorly known, phase, we considered the initial electron density at the beginning of the main pulses of applied voltage to be an adjusted parameter. This parameter was determined when calculating the evolution in time of the discharge current and adjusting it to corresponding measured data. The method used allowed a good agreement between measured and calculated specific deposited energy (see Fig. 5.8).

In the experiments under consideration, the main pulse of applied voltage was generally followed by several smaller pulses (see Fig. 5.1, time instants 350 and 800 ns). Production of active particles was simulated also in these additional discharge phases. As a rule, in this case production of atoms, radicals and excited neutral particles was noticeable, whereas production of electrons and ions was not important.

Fig. 5.15 shows the evolution in time of the mole fractions of dominant active species in the discharge and in its afterglow in the mixture under consideration. The curves correspond to the same conditions as those in Fig. 5.6. The temporal evolution of the rates for production of various active particles in this case is shown in Fig. 5.16. Calculations show that most of active particles was produced in the first voltage pulse due to electron impact dissociation, excitation and ionization. In the second pulse, only some additional amount of O atoms and excited O_2 molecules were formed. Between the pulses, in a zero electric field, charged particles were removed due to dissociative electron-ion recombina-

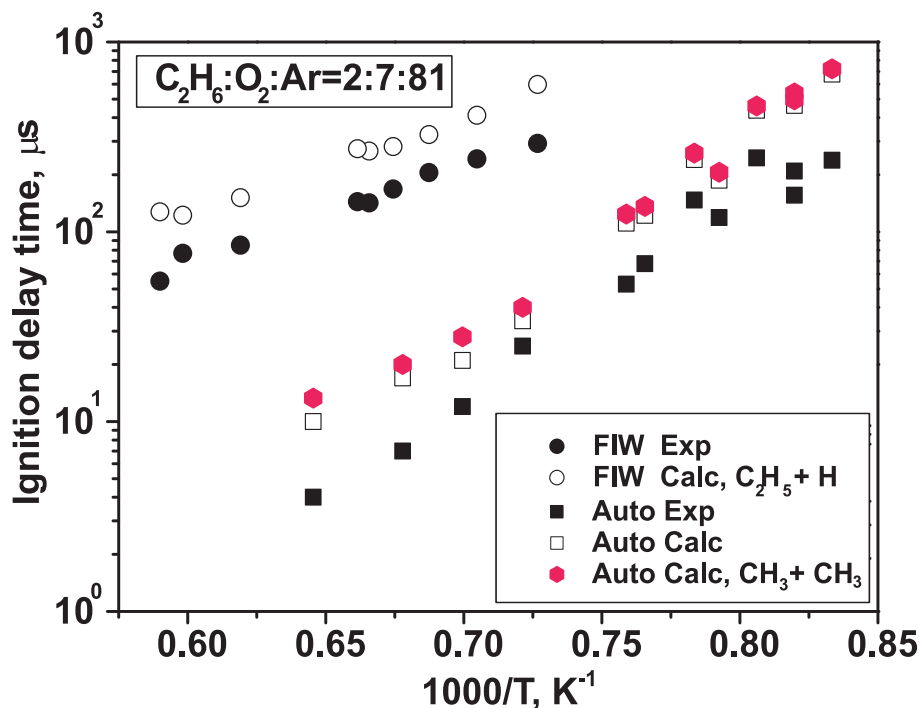


Figure 5.18: The ignition delay time in ethane containing mixtures for two different artificial ways of C_2H_6 destruction by the discharge.

tion (reactions (R18) - (R21) in Table 5.6) producing an additional amount of atoms and radicals. The last particles were also produced due to charge exchange of Ar^+ ions on CH_4 (reactions (R16) and (R17)) and due to quenching of excited Ar atoms by oxygen and hydrocarbon molecules (reactions (R8) — (R12)). In our kinetic model, in the end charged and excited particles were excluded from the consideration and the gas mixture consisted of initial neutral species and atoms and radicals produced during the discharge and in its afterglow. The densities of atoms and radicals were used further as input parameters for a computer program to simulate ignition in the mixtures under consideration.

The density of atoms and radicals produced by the discharge depends essentially on the gas number density behind the reflected shock wave, n_5 (see Fig. 5.17). Here, an increase in n_5 from 2×10^{18} to $6 \times 10^{18} \text{ cm}^{-3}$ leads to an order of magnitude decrease in the mole fraction of O atoms, from 2×10^{-2} to 2×10^{-3} . This means that the absolute density of O atoms decreases by a factor of three. The densities of H atoms and CH_3 radicals behave in a similar way. It should be noted that the discharge characteristics and production of active particles are not sensitive to gas temperature.

5.3.2 Calculated results for autoignition and plasma assisted ignition

Autoignition of hydrocarbons occurs through a number of sequential steps. They are (i) dissociation of hydrocarbon molecules to form radicals, (ii) reactions of radicals with starting molecules, (iii) reactions of chain branching, and (iv) recombination of radicals. Chemical chains develop in steps (ii) and (iii).

A general scheme of autoignition of alkanes is formulated in a hierarchical way and is

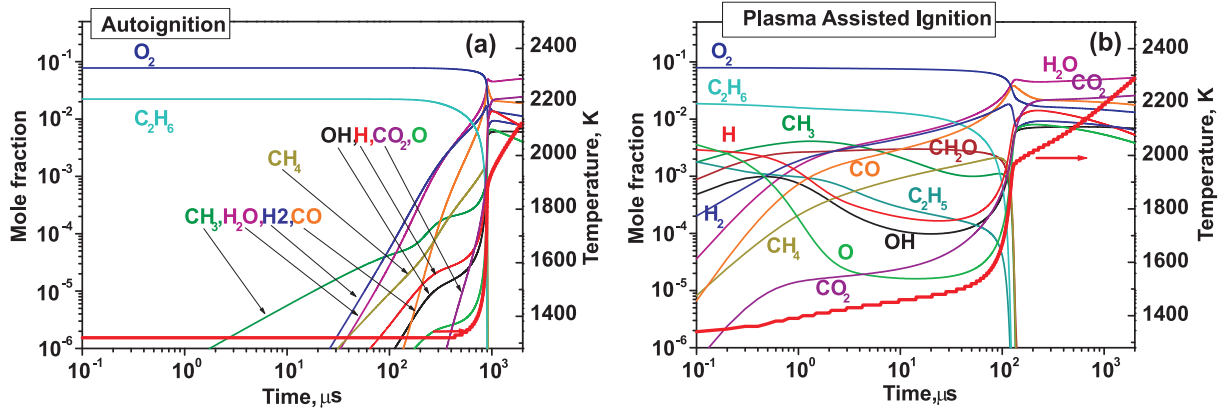
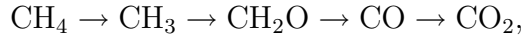


Figure 5.19: The evolution in time of the mole fractions of main components for autoignition (a) and ignition after the discharge (b) in $C_2H_6:O_2Ar$ mixture. $T_5 = 1318$ K, $P_5 = 0.60$ bar.

based on the chemistry of $H_2:O_2:CO$ systems. Ignition of methane occurs in the following way [48, 46]



at final stage mixtures being $H_2:O_2:CO$ systems. Intermediate products in ignition of C_2H_6 are not only CH_3 radicals, but ethyl radicals (C_2H_5), ethylene (C_2H_4), and acetylene (C_2H_2). It was mentioned in [49] that reactions with acetylene, like $C_2H_2 + O_2 = HCCO + OH$, affect essentially ignition delay time in this case. Indeed, in the induction phase, the density of radicals is low and reactions leading to OH formation play an important role.

For autoignition of C_nH_{2n+2} at $n > 2$, chains are initiated with the breakdown of C–C bonds to form hydrocarbon radicals, the C–C bond being weaker than the C–H bond. For instance, the energy of breakdown of the C–H bond is 435 kJ/mole in methane and 410 kJ/mole in ethane, whereas the energy of breakdown of the C–C bond in ethane is 370 kJ/mole. Nevertheless, the C–H bond is broken at high temperatures.

For ignition by the discharge, the reaction $C_2H_6 + e = C_2H_5 + H + e$ is more efficient than the reaction $C_2H_6 + e = CH_3 + CH_3 + e$. Nevertheless, the detailed information about the cross-sections of electrons interaction with hydrocarbons starting from C_3H_8 , is absent. More than that, we assumed that the process $O_2^* + C_nH_{2n+2} = O_2 + C_nH_{2n+1} + H$ is efficient without detailed discussion of the bond which is destructed in the hydrocarbon molecule due to this reaction. This was a reason to make a few additional calculations for C_2H_6 - and C_5H_{12} -containing mixtures. We replaced artificially C_nH_{2n+1} and H radicals calculated in the discharge and afterglow phase by the same total amount of CH_3 and $C_{n-1}H_{2n-1}$ radicals. The results are given by Fig. 5.18. It is clearly seen that the ignition delay time does not depend dramatically upon the way of C_2H_6 destruction: for all the range of considered experimental conditions, we obtain the shift of the ignition delay time within the size of the symbols.

Going back to the description of kinetics, it is worth mentioning that in the case of ethane ignition, CH_3 radicals are formed and the $C_2H_6 + H = C_2H_5 + H_2$ reaction takes place leading to the formation of C_2H_4 and H . Ethane is ignited much faster than

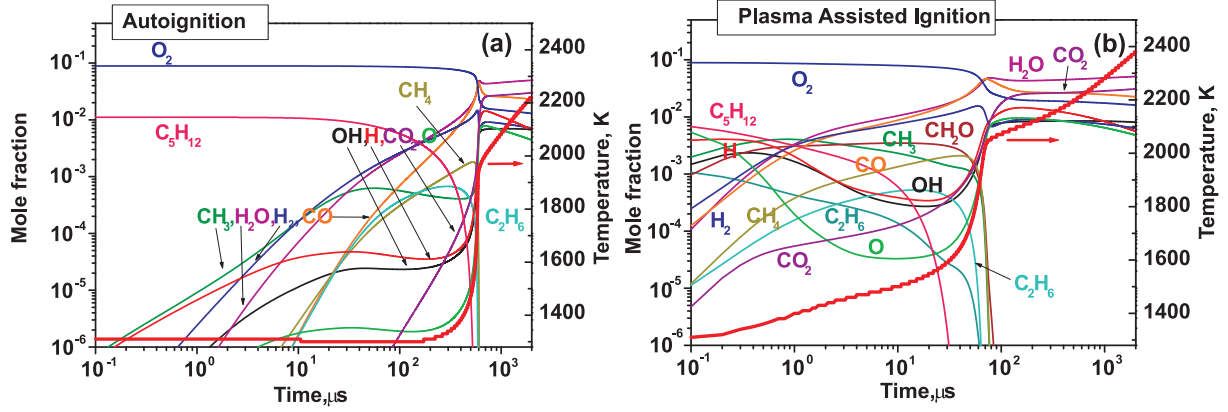


Figure 5.20: The evolution in time of the mole fractions of main components for autoignition (a) and ignition after the discharge (b) in $C_5H_{12}:O_2:Ar$ mixture. $T_5 = 1309$ K, $P_5 = 0.58$ bar.

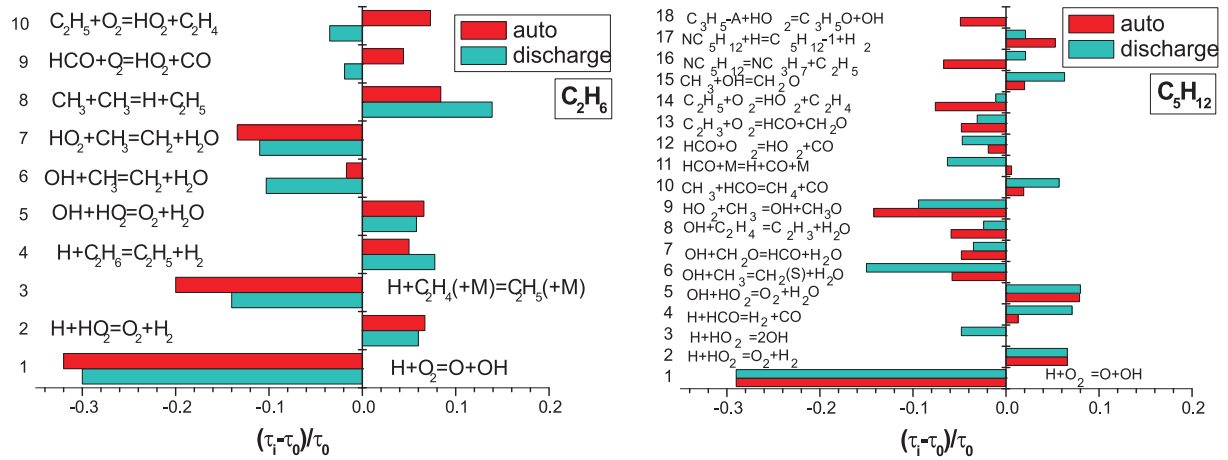


Figure 5.21: The results of the sensitivity analysis for autoignition and ignition by the discharge. (a) $C_2H_6:O_2:Ar$ mixture, and (b) $C_5H_{12}:O_2:Ar$ mixture.

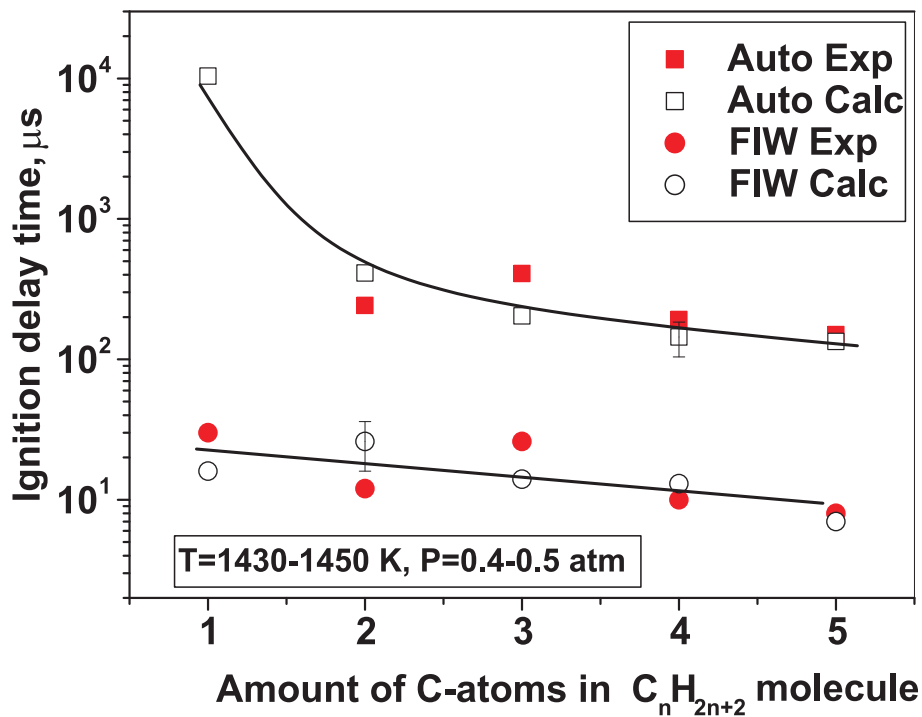


Figure 5.22: The ignition delay time for the C_nH_{2n+2} -containing mixtures versus the number of C atoms in C_nH_{2n+2} molecule. Closed points correspond to measurements, and open points correspond to calculations. The initial temperature was between 1430 and 1450 K and the pressure was between 0.4 and 0.5 atm.

does methane. Alkanes containing a large number of C are ignited through the sequence "alkane-alkyl-smaller alkyl". Reactions with H, O and OH cause the formation of alkenes as intermediate products.

This agrees with autoignition characteristics shown in Fig. 5.19a and 5.20a, for ethane and pentane, respectively. Here, in the induction stage CH_3 and C_2H_5 radicals and intermediate products, like CO, are formed. Fig. 5.19b and 5.20b demonstrate evidently the effect of non-equilibrium plasma on ignition kinetics in these gases. The "injection" of a large number of radicals at the beginning of ignition leads to a much faster decomposition of the fuel and to the formation of simpler and simpler radicals through the mechanisms typical for routine kinetic schemes of ignition; as a result, the mixtures are ignited much faster. It is seen from Fig. 5.19b and 5.20b that CH_3 , C_2H_5 , formaldehyd and CO are efficiently accumulated both in the case of C_2H_6 and in the case of C_5H_{12} . It is worth noting that efficient generation of O and H atoms in the discharge favours the conversion of alkyls into smaller alkyls and the difference in kinetic schemes for ignition of various hydrocarbons becomes smaller.

Detailed analysis of sensitivity has been made for all hydrocarbon-containing mixtures for cases of the autoignition and plasma assisted ignition. The analysis was made as follows: the rate constant of each reaction was in turn increased by 50 % and the ignition delay time was calculated separately for each case. The sensitivity coefficients were calculated as $(\tau_i - \tau_0)/\tau_0$, where τ_0 is the ignition delay time calculated with unchanged rate constants and τ_i is the ignition delay time calculated with the increased rate constant of the i -th reaction. The results of the calculations are given in Fig. 5.21. This figure

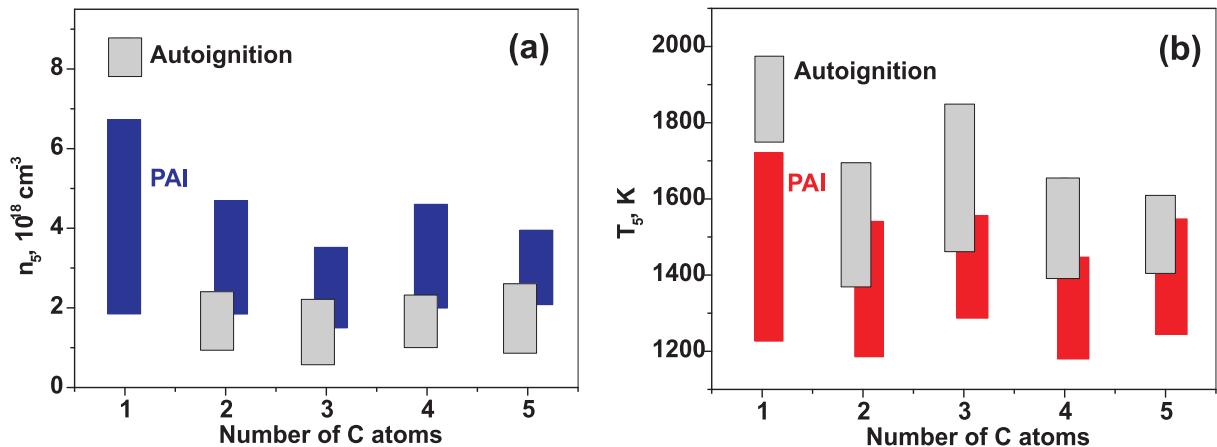


Figure 5.23: The parameters used in the experiments for the C_nH_{2n+2} -containing mixtures versus the number of C atoms in C_nH_{2n+2} molecule. (a): gas number density; (b): gas temperature.

represents only the reactions where $(\tau_i - \tau_0)/\tau_0$ are greater or equal to 0.05 at least for the autoignition or for the ignition by the discharge. It is clearly seen that we have more broad spectrum of the reactions for C_5H_{12} - containing mixture. It should be noted that we observe quite dramatic difference in the role of reaction $H+O_2=O+OH$ for methane- [38], ethane- and pentane-containing mixtures. For $CH_4:O_2:Ar$ mixture at 1500 K, the coefficient $(\tau_i - \tau_0)/\tau_0$ for this reaction changes from -0.18 for the autoignition to -0.44 for the discharge. For C_2H_6 - and C_5H_{12} - containing mixtures at 1300 K, this coefficient is approximately equal to -0.3 and does not change significantly under the action of the discharge. The role of radical-radical reactions, like $OH+CH_3=CH_2+H_2O$, increases significantly in the case of the discharge action.

If to summarize, we were able to describe the experimental data assuming that the effect of the discharge is reduced to an instantaneous injection of atoms and radicals. This led to an order of magnitude decrease in ignition delay time, in good agreement with the measurements (see Fig. 5.22). Experimental data shown in Fig. 5.22 correspond to the same conditions, namely we used 100 kV negative polarity pulses, the current peak value was 3 kA, the pulse duration was 40 ns at the half-height, and the volumetric energy input was about 30 mJ/cm^3 . We failed to ignite CH_4 -containing mixture without discharge at the same pressure (0.4–0.5 atm) because the autoignition time turned out to be beyond the range measured in this experiment. Therefore, we have performed measurements of autoignition delay times in the $CH_4:O_2:Ar$ mixture at higher pressure (2 atm) and also obtained a good correlation between experiment and calculation made at 2 atm. The analysis of the calculated results showed that the composition of active particles produced during the discharge and in its afterglow was dominated by O, H atoms and C_nH_{2n+1} radicals. The main mechanism for O-atoms production was electron impact dissociation of O_2 in the discharge phase, the main mechanism of H-atoms and C_nH_{2n+1} -radicals was quenching of electronically excited oxygen molecules $O_2(4.5 \text{ eV})$. The production of atoms and radicals due to direct electron impact dissociation of hydrocarbon molecules was less important. Additional calculations were made to determine the role of different species in the ignition by varying artificially the input composition of active particles. The efficiency of O atoms was the highest one and close to the efficiency of H atoms, while the efficiency

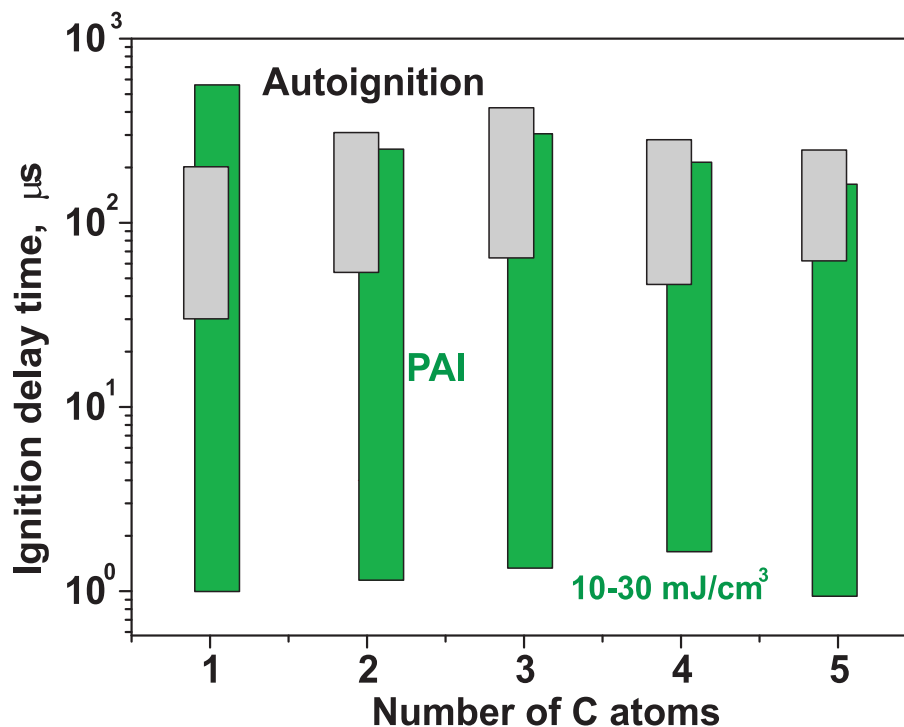


Figure 5.24: The ignition delay time for the C_nH_{2n+2} -containing mixtures versus the number of C atoms in C_nH_{2n+2} molecule. Comparison of autoignition and ignition assisted by nonequilibrium plasma of high-voltage nanosecond discharge.

of C_nH_{2n+1} radicals was much lower.

The uncertainty in the unknown cross sections for electron impact dissociation of C_3H_8 , C_4H_{10} and C_5H_{12} does not affect strongly the results of our calculations. To verify this, additional calculations were carried out with the cross sections of dissociation of these molecules increased by an order of magnitude. This led to an increase in the densities of H atoms and radicals of hydrocarbon molecules by a factor of 6–7, whereas the density of O atoms decreased by tens of percent. As a result, the total density of atoms and radicals increased only by $\sim 10\%$ in the mixtures with C_3H_8 , C_4H_{10} and C_5H_{12} and the ignition delay time did not change essentially.

Finally, Fig. 5.23 and Fig. 5.24 give an impression about the total range of parameters in shock tube–gas discharge experiments in $C_nH_{2n+2}:O_2$ stoichiometric mixtures diluted (90 %) with Ar. It is obvious that the choice of the experimental parameters allowed us direct experimental comparison of the efficiency of ignition by non-equilibrium plasma of the high-voltage nanosecond discharge.

5.4 Conclusions

So, within the framework of study of kinetics of plasma – assisted combustion we have made an experimental and numerical study of the ignition of C_2H_6 – to C_5H_{12} –containing mixtures under the action of a high-voltage nanosecond discharge at elevated temperatures and showed that its initiation leads to a noticeable decrease in gas temperatures at which the mixtures are ignited and to an order of magnitude decrease in ignition delay

time. The measurements agree well with ignition delay times calculated on the basis of an one-temperature, Arrhenius, chemical kinetics. To explain our observations, there is no need to use any additional mechanism suggested to favour the ignition processes, such as chemical reactions with excited or charged particles. It follows from the analysis of the calculated results that, at temperatures near the ignition threshold and at electric fields such that most of the electron energy is spent in the discharge to excite electronic levels of neutral particles and to ionize them, the main mechanism of the effect of gas discharge on the ignition of stoichiometric hydrocarbon–oxygen mixtures is the electron impact dissociation of O_2 molecules in the discharge phase; this leads to an essential increase in the density of atoms and radicals at the beginning of ignition. As a result, there is no need to dissociate molecules for initiation of chain chemical reactions, and the stage of the chain activation is shortened significantly.

Chapter 6

Analysis of Kinetic Behaviour of Different Components

6.1 Experimental analysis of dynamics of intermediates

Taking into account that we investigate PAI dynamics in single-shot experiments, it is desirable to obtain maximal set of experimental data during one experiment.

First of all, temporal and spectral behavior of the emission of electronically excited levels of atoms and molecules can be analysed with the help of streak camera imaging. Then, we have considered a few different techniques suitable for *in situ* control of intermediates during a delay time of plasma assisted ignition. For the experimental observation of kinetics during the ignition delay time it is desirable to have a wide dynamic ranges and high resolution of the diagnostic equipment, both in time and in amplitude. It follows from the numerical analysis of the afterglow and of the ignition stage (see, for example, Fig. 5.19(b)) that possible candidate for the analysis are electrons, hydrocarbon molecules and OH.

To measure CH₄ density, it is possible to use IR absorption at 3.39 μm . Absorption coefficient for methane in the range of interest is given by expressions [54]:

$$\varepsilon = 3.844 \times 10^4 - 18.7T \quad \text{cm}^2\text{mole}^{-1}, \quad T < 1500 \text{ K} \quad (6.1)$$

$$\varepsilon = 1.33 \times 10^4 - 2.2T \quad \text{cm}^2\text{mole}^{-1}, \quad T > 1500 \text{ K} \quad (6.2)$$

To measure IR absorption of methane, IR He-Ne laser is useful. The simplest estimations show that the absorption for our range of parameters is within the range of $I/I_0 \approx 10^{-4} - 10^{-2}$. This means that the scheme with reference beam or multi-pass cell with a number of reflections ~ 10 can be used to detect profile of CH density in time. To measure electron density under plasma assisted ignition in methane-containing mixture, we used microwave interferometry. OH density in H₂:O₂:Ar mixture was measured with the help of absorption spectroscopy.

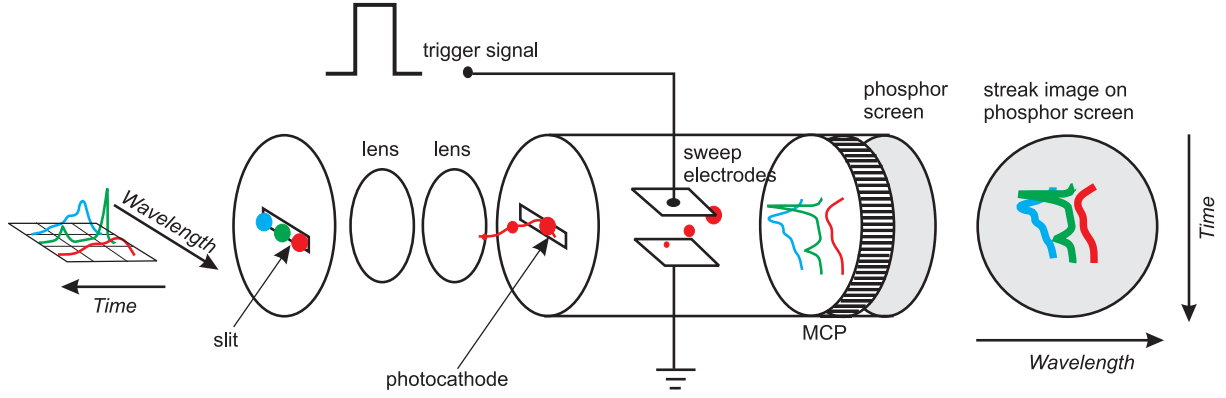


Figure 6.1: Scheme of streak-camera operation

6.1.1 Streak-camera imaging

We used sub-picosecond streak-camera C5680 Hamamatsu combined with the broad-band spectrometer (200–800 nm) to obtain temporal and spectral profiles of the emission from the discharge and the ignition. Streak-camera combined with a spectrometer is a powerful tool for spectroscopy diagnostics in pulsed discharge-shock tube experiments. It allowed us to carry out time and spectral-resolved diagnostics of processes in the discharge and in the combustion front.

The principal scheme of streak-camera is represented in Fig. 6.1. At each time instant, radiation forms an image on the photocathode of a camera. The photocathode creates electrons, they move toward the phosphor screen. Sweep electrodes deflect electrons in a vertical direction (from top to a bottom), providing time resolution. Flux of deflected electrons accelerates by MCP system and produces an optical image on a phosphor screen. This image is registered by CCD camera mounted right after the screen.

The experimental setup is schematically shown in Fig. 6.2. All the experiments have been carried out behind the reflected shock wave. Two Schlieren systems consisting of He-Ne laser, mirror and photodiode were placed along the tube. They were used to measure the shock wave velocity, and to trigger both the nanosecond discharge and streak-camera.

To obtain resolved in wavelength emission spectra, the broad-band monochromator (Troitsk, TRINITI) has been installed ahead of the streak camera. A spectral range of 600 nm (from 200 to 800 nm) was focused on the input slit of the streak-camera, and, further, onto a photocathode of a streak-camera. The length of the photocathode is equal to 6 mm. Calibration of the spectral system was made with the help of two spectral lamps, deuterium lamp DDS-30 (LOMO) and mercury lamp DRGS-12 (LOMO). The lamps were placed instead of the discharge camera, and their spectra were registered in quasi-stationary regime. The spectral range of the system was restricted by lenses and optical windows of the lamps. Streak-images, spectral profiles obtained from the images and reference spectra are given in Fig. 6.3–6.4. Wavelengths corresponding to the reference spectra of the mercury and deuterium are indicated by numbers at the streak profiles obtained with DDS-30 and DRGS-12 lamps.

The calibration plot obtained using deuterium, mercury and neon lamps, is presented in Fig. 6.6. It is clearly seen that we obtain linear dependence between the wavelength and pixel No for the wavelength range between 200 and 700 nm. The dependence is given

by formula:

$$\lambda(N) = 797.18 - 0.4675N, \quad (6.3)$$

where N is a pixels number. In the experiments, the system of two lenses L_1 and L_2 focused emission from the discharge cell on the input slit of the camera. To focus the system properly, we used miniature neon lamp (spectrum of the lamp is demonstrated by Fig. 6.5). The lamp was placed inside the discharge chamber, and the light was focused onto the entrance slit of the monochromator.

Low-speed single-sweep unit of the camera allows the following work parameters of the system: time resolution is within 50 ps, sweep time is between 5 ns and 1 ms per full screen, trigger jitter is equal to time resolution or less, trigger delay is approximately 45 ns (for the fastest range), trigger signal output is $\pm 5 \text{ V}/50 \Omega$.

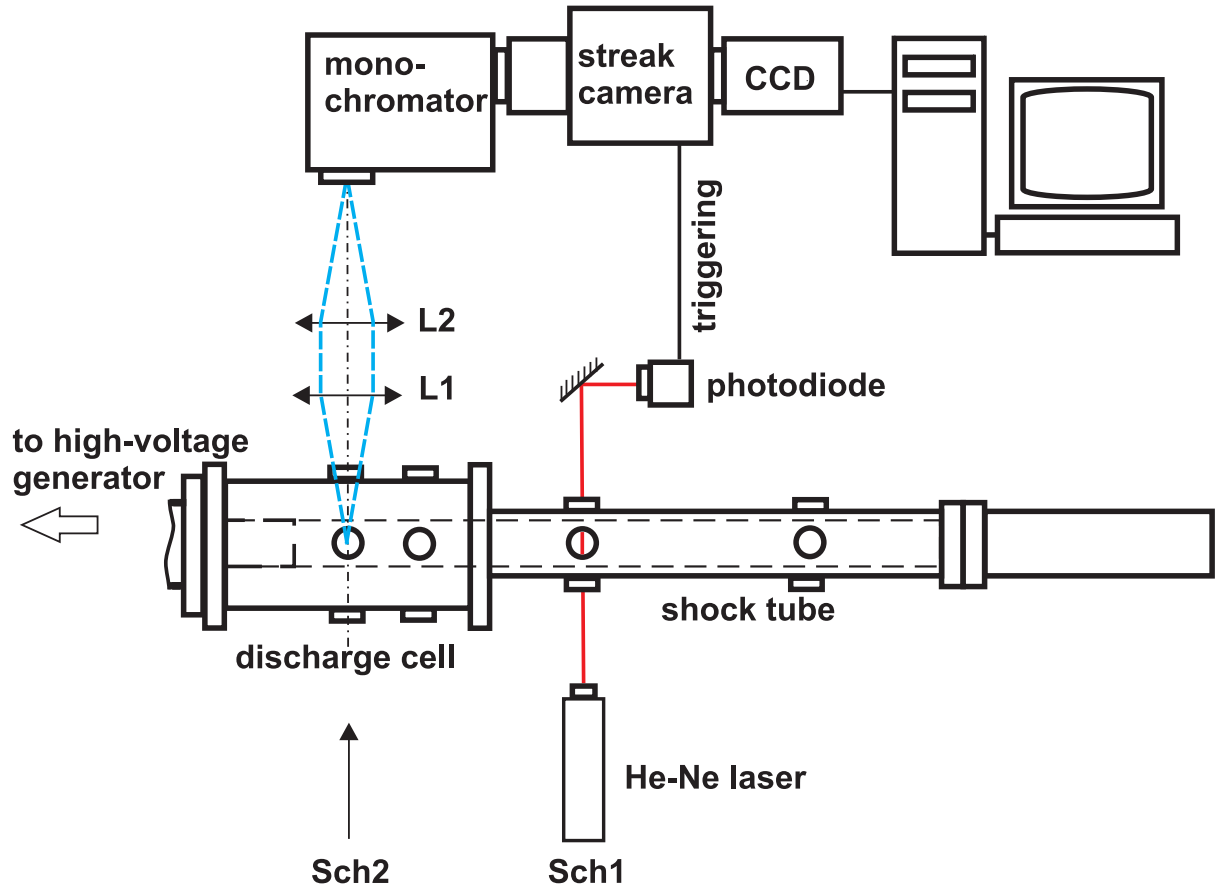


Figure 6.2: Scheme of experimental setup

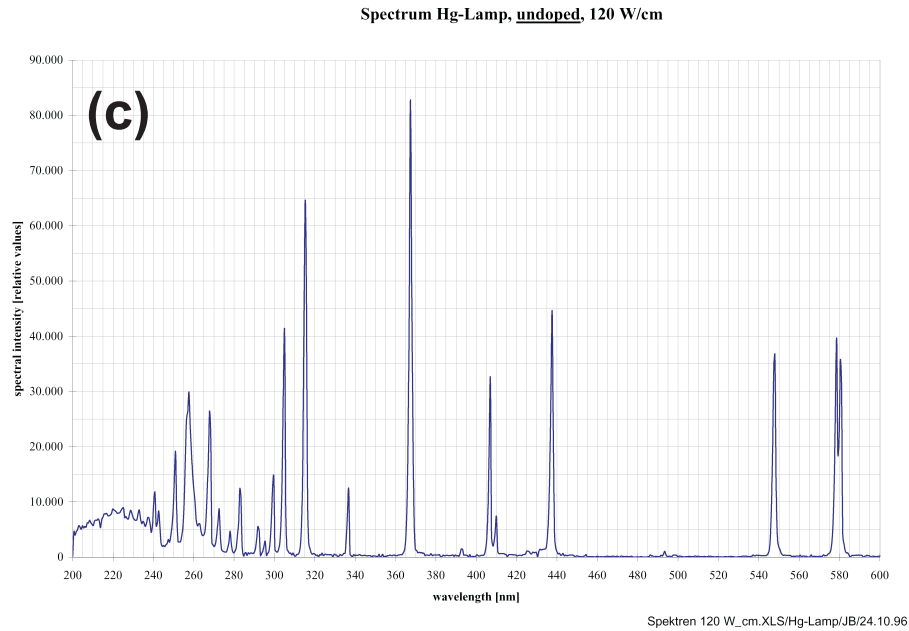
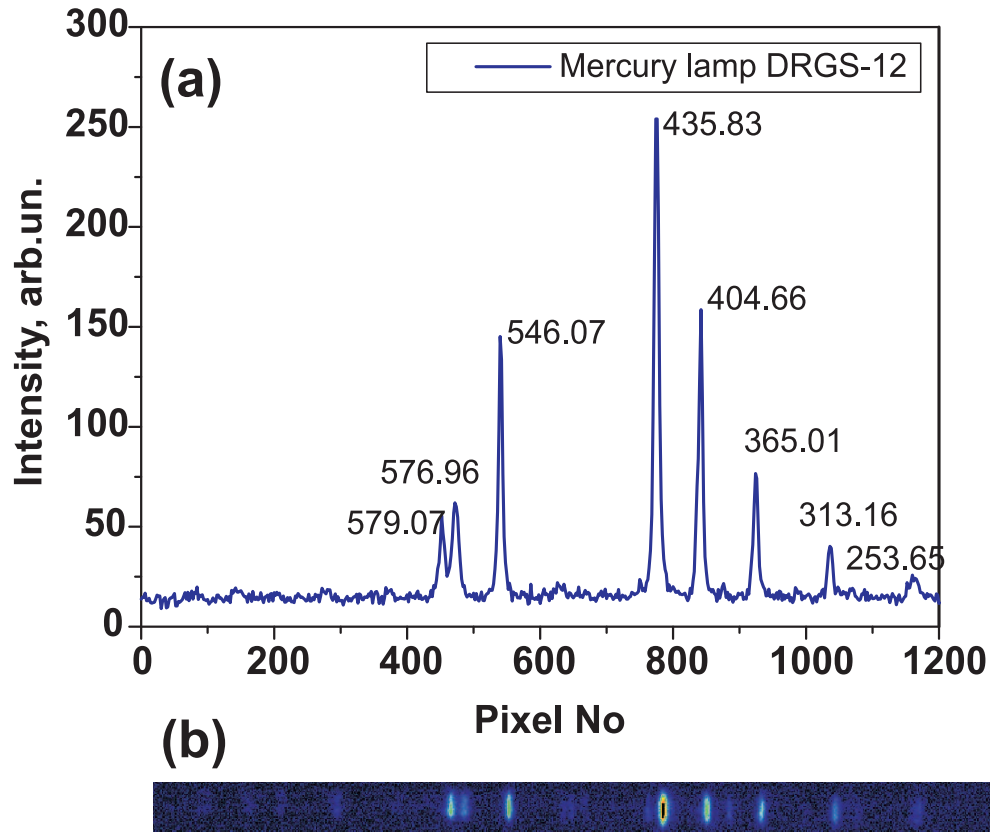


Figure 6.3: (a) spectrum, (b) streak-image of mercury lamp; (b) spectrum of mercury lamp taken from the literature [55]

6.1.2 Preliminary experimental data

Preliminary set of experiments for $C_3H_8:O_2:Ar$ mixture has been performed. Main spectral lines were identified and their behaviour in time was investigated. The typical images

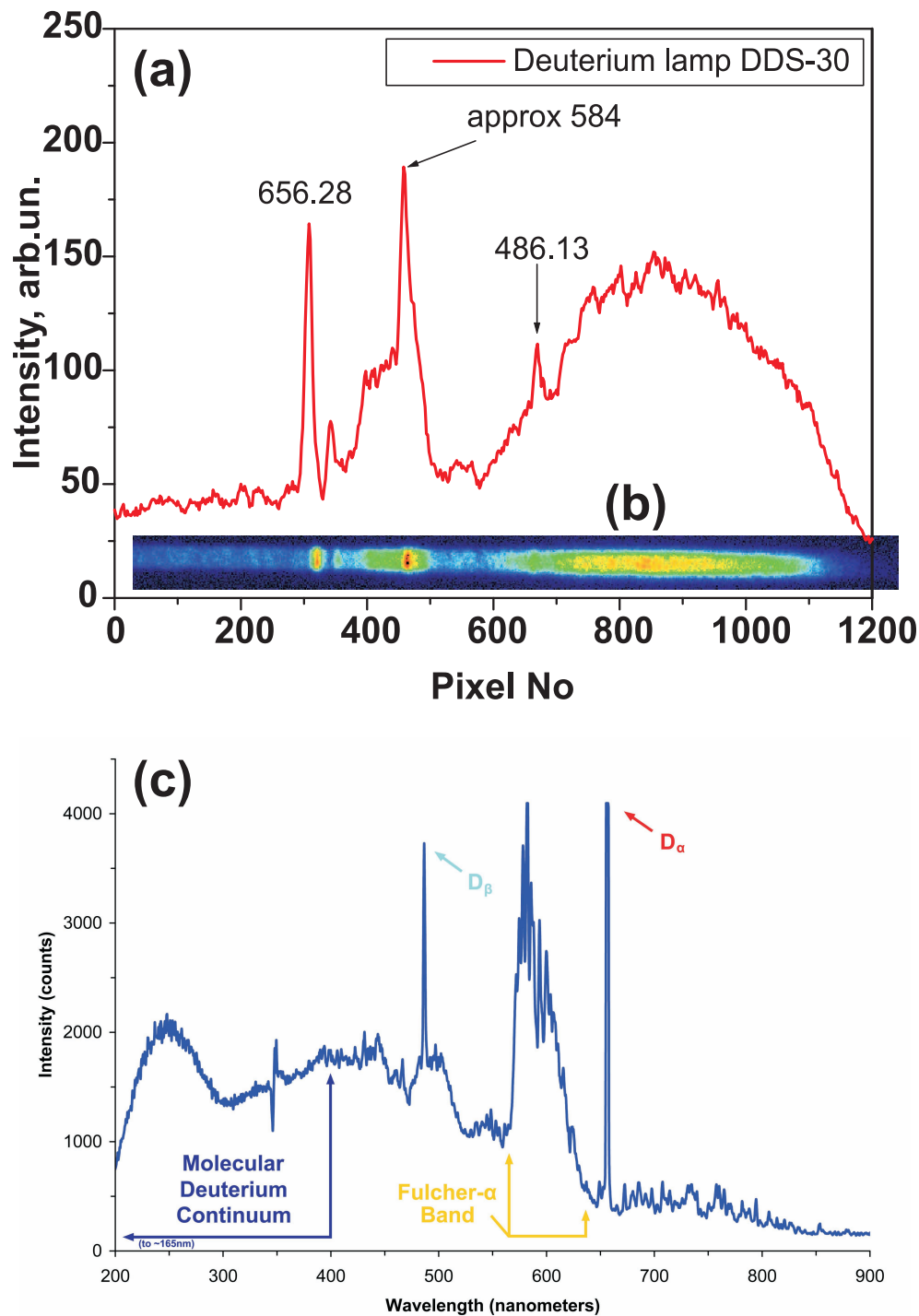


Figure 6.4: (a) spectrum, (b) streak-image of deuterium lamp, and (c) spectrum of deuterium lamp taken from the literature [56]

obtained with streak-camera are shown in Fig. 6.7.

The images are obtained in propane:oxygen stoichiometric mixture diluted with Ar (90 %), pressure and temperature are equal approximately 0.4 bar and 1500 K. Yellow lines in the left corner of every picture represent temporal behaviour of CH emission at 431 nm. It is clearly seen that application of the discharge leads to decrease of the

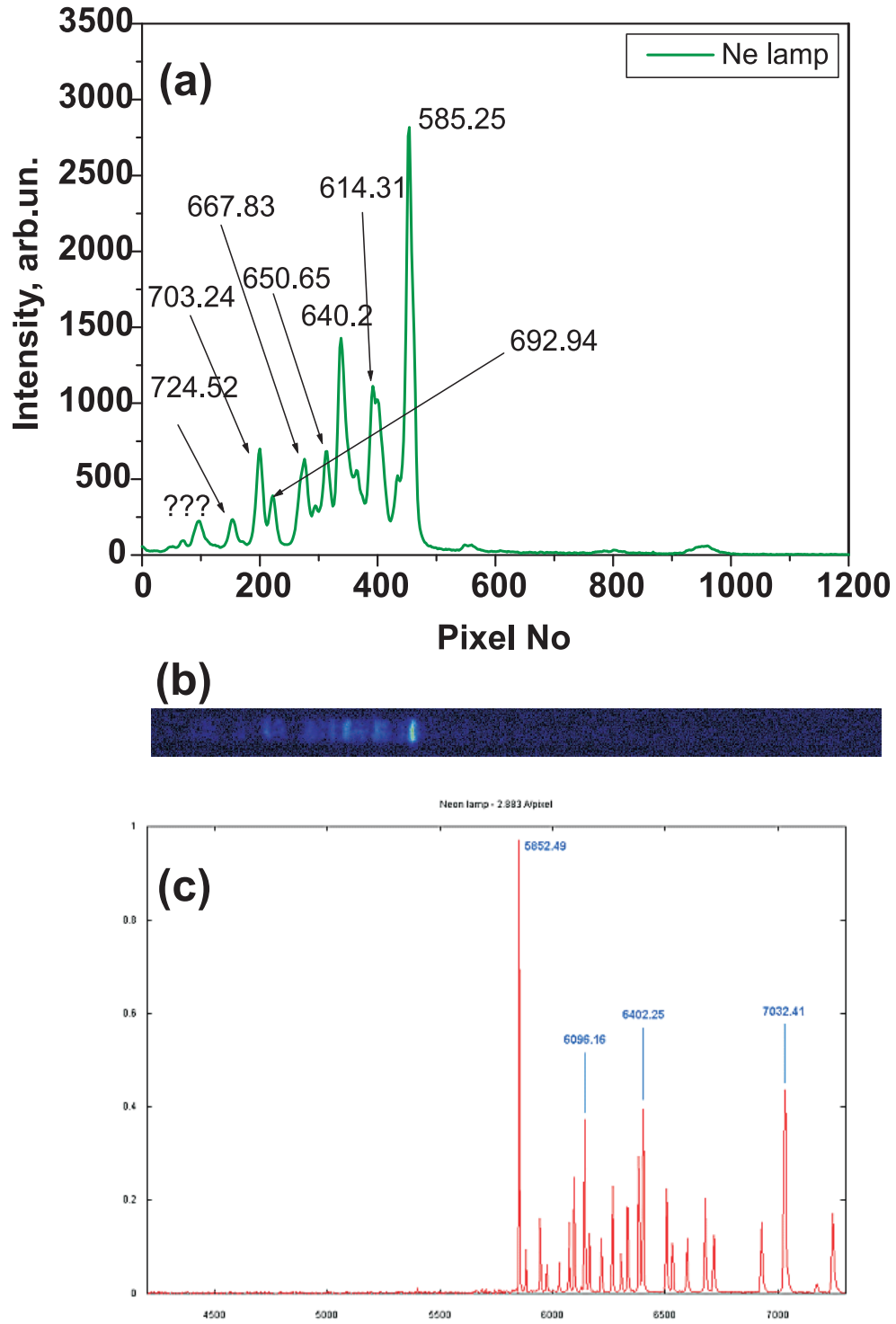


Figure 6.5: (a) spectrum, (b) streak-image of neon lamp, and (c) spectrum of neon lamp taken from the literature [57]

delay between time instant $t = 0$ (arriving of the reflected shock wave and application of the discharge) and increase of CH emission. Further, it is seen that the emission front in a case of plasma assisted ignition is smoother than in a case of autoignition. This

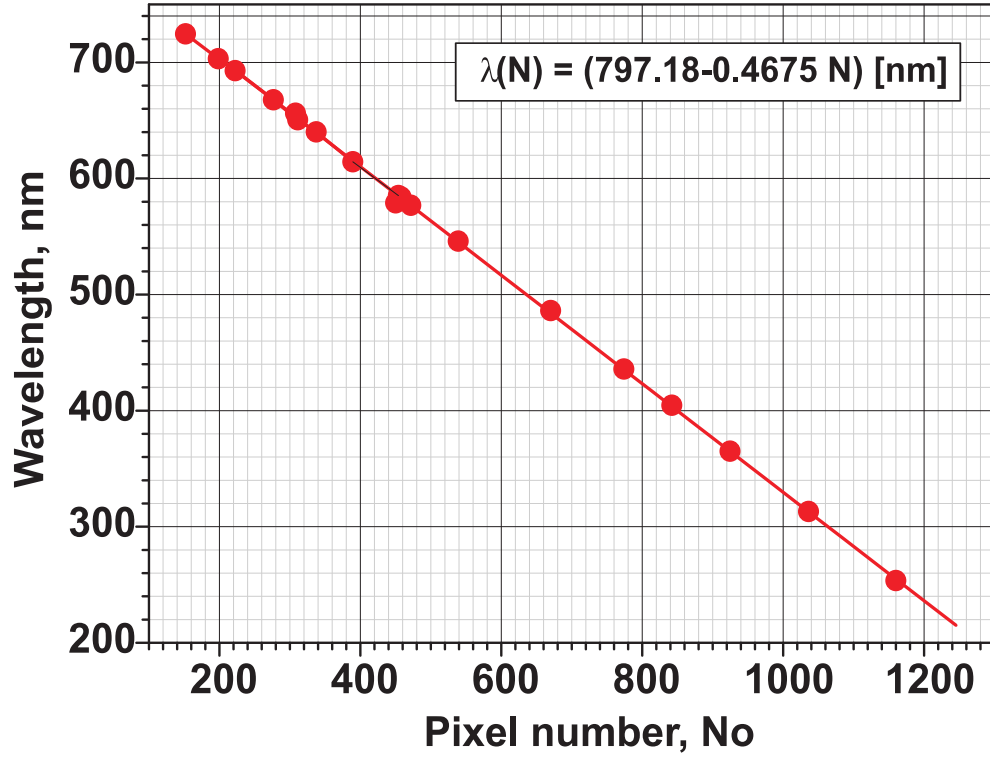


Figure 6.6: Calibration curve for the streak-camera images

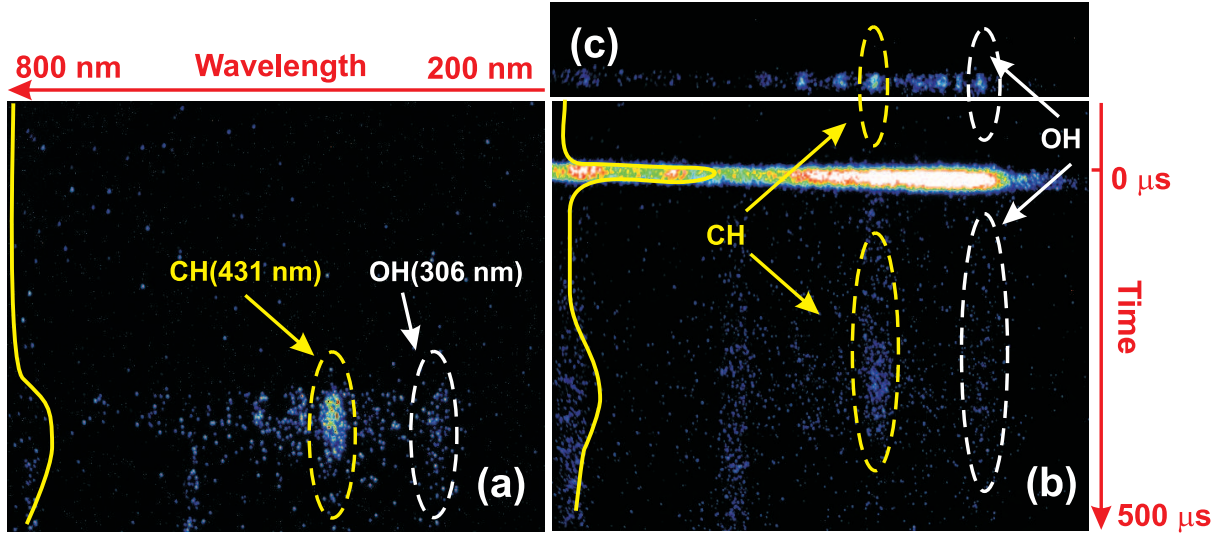


Figure 6.7: Streak images of (a) autoignition, (b) plasma assisted ignition, and (c) discharge in a cold gas, with decreased sensitivity of a streak-camera. $(C_3H_8:O_2):Ar=10:90$ stoichiometric mixture

correlates with the measurements obtained by a monochromator and photomultiplier. The discharge intensity in this regime is high, so, we give for comparison a discharge emission with decreased sensitivity of the optical system.

Let us consider the details of the images obtained. First, we have found two lines which arise from time to time on streak-images. We observed two “spectral” lines at

595 nm and 777 nm which started at the moment of camera triggering and demonstrated their presence all the sweep time with approximately constant value of amplitude (see, for example, Fig. 6.8). These lines seem to correspond to atomic oxygen transitions, and they originate in the spectra when the gas temperature is high enough. For example, we observed sharp increase of their intensity at the moment when the contact surface comes to the cross-section of measurements. To be sure that the appearance of those two lines is not an artifact we have made an additional series of experiments where we used non-combustible Ar:CO₂=99:1 mixture instead of propane-air mixture diluted with argon. He was used as a drive gas instead of air to reach higher gas temperatures. At the moment we can make a preliminary conclusion that we do observe atomic oxygen lines but this idea needs to be checked more thoroughly.

Second, we have made a series of experiments to understand the peculiarities of the behavior of the discharge and of the ignition. The discharge demonstrates the presence of the lines which are typical for nanosecond high-current discharges at ambient gas temperatures [58]. For example, emission of the second positive system of molecular nitrogen is clearly seen in the discharge in air (Fig. 6.9)). This emission is noticeable for propane-containing mixture (we did not pumped our system to the level typically used in our research for these preliminary experiments). Nevertheless, the difference between emission of the discharge in air and in propane:oxygen:argon mixture is evident: emission bands of CH (431 nm), C₂ (518 nm) and OH (307 nm) are clearly seen (Fig. 6.9)).

It should be noted that the discharge and autoignition spectra demonstrate presence of the same spectral lines (Fig. 6.10) but at the same time they demonstrate different ratio between their intensity. Indeed, the autoignition spectrum in the CH₃:O₂:Ar mixture contains dominantly CH (431 nm) emission; molecular bands of C₂ and OH emission are

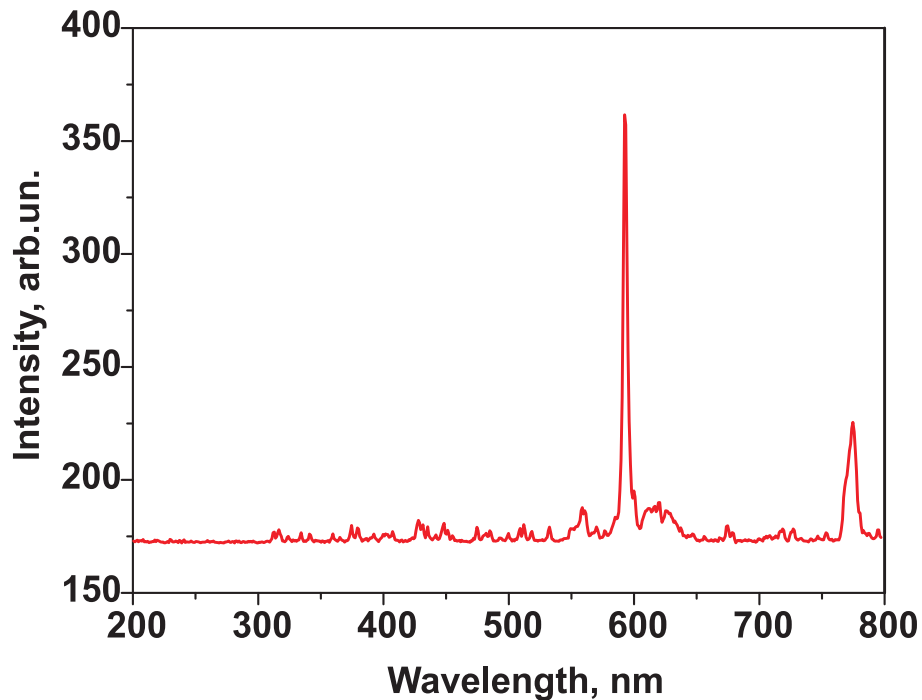


Figure 6.8: Two lines presented in streak spectra at high temperatures (see explanations in the text)

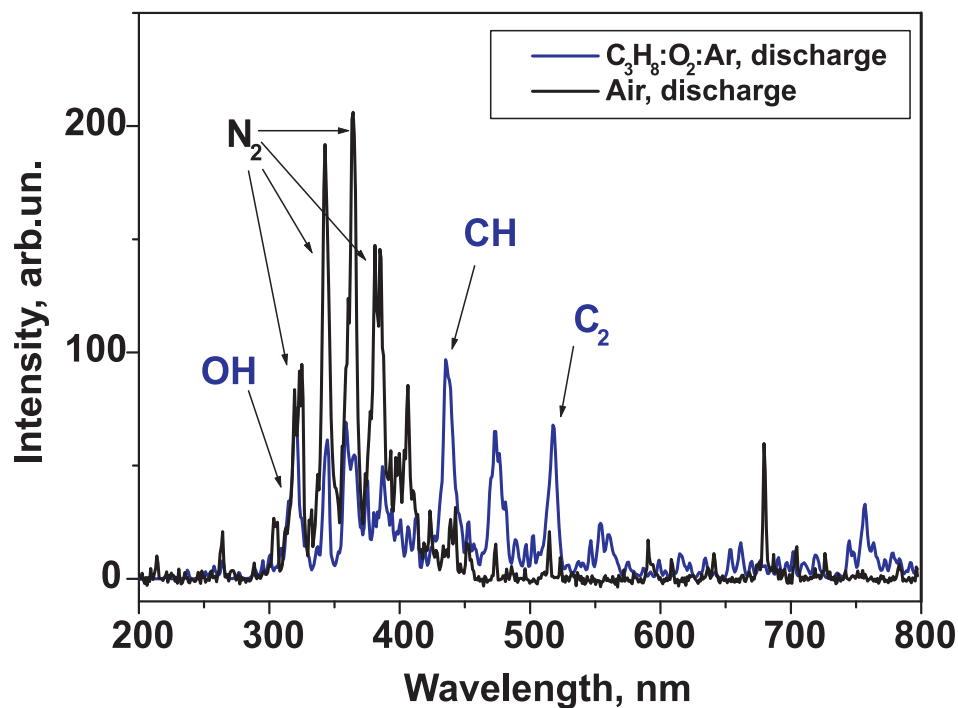


Figure 6.9: Emission spectra for the nanosecond high-voltage discharge in air and $(\text{C}_3\text{H}_8:\text{O}_2):\text{Ar}=10:90$ stoichiometric mixture

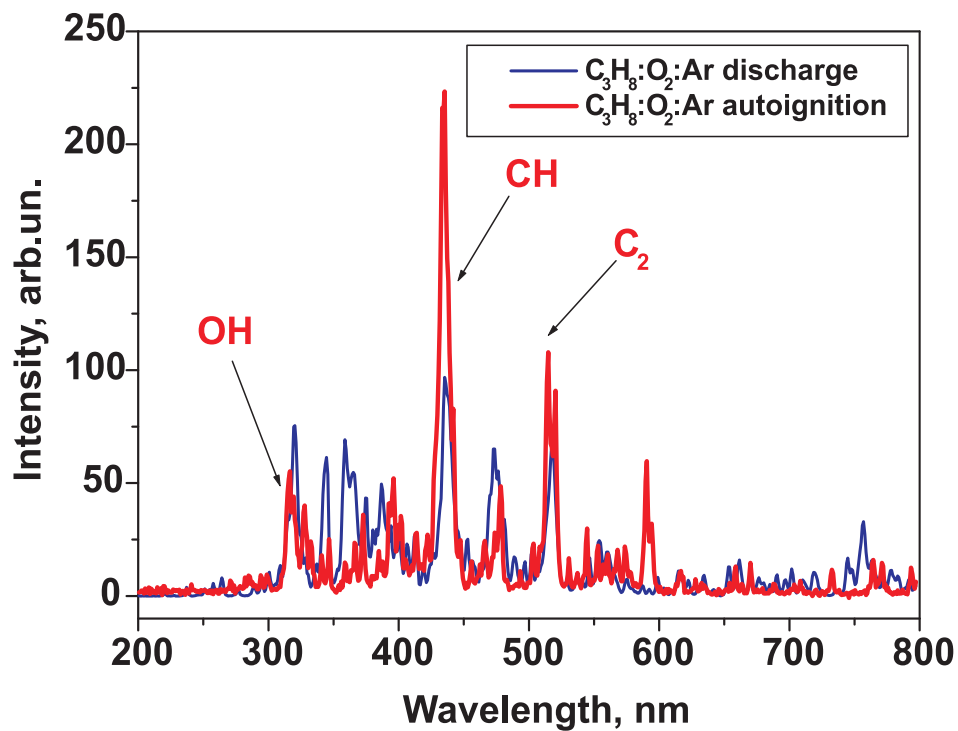


Figure 6.10: Comparison of the emission spectra of the nanosecond high-voltage discharge and of autoignition in a $(\text{C}_3\text{H}_8:\text{O}_2):\text{Ar}=10:90$ stoichiometric mixture

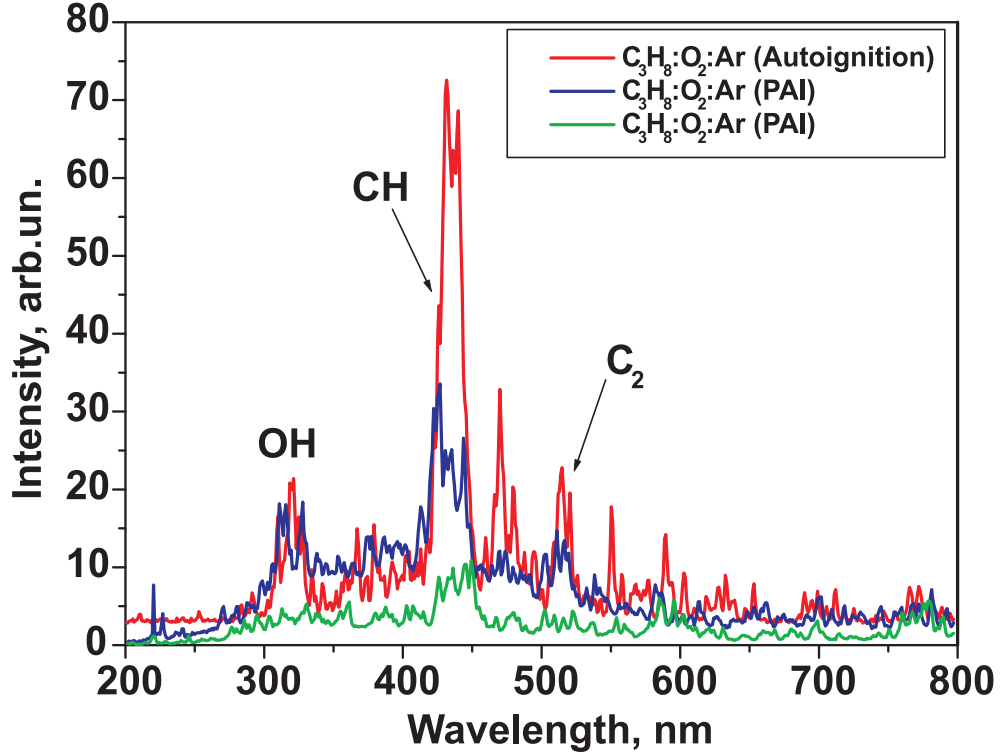


Figure 6.11: Comparison of the emission spectra of the autoignition and plasma-assisted ignition in a $(\text{C}_3\text{H}_8:\text{O}_2):\text{Ar}=10:90$ stoichiometric mixture

at least two times weaker. In the discharge, intensity of the emission of OH, CH and C_2 molecular bands is approximately equal in intensity. In both cases, we observe a line about 470 nm, which has not been identified yet.

The difference in spectra between the autoignition and plasma assisted ignition (Fig. 6.11) was not found to be significant. OH (306 nm), CH (431 nm), and C_2 (518 nm) emission bands are the most clearly pronounced. It is seen from the Figure 6.11 that the relative intensity of CH emission decreases strongly, while relative intensity of OH molecular band at 306 nm increases.

The temporal behavior of the emission of separate lines is similar to one we observed using photomultiplier and monochromator in our previous papers (see, for example, [36]). Red line in Fig. 6.12 represents CH (431 nm) emission for the autoignition of propane:oxygen stoichiometric mixture diluted with argon (90 %). The ignition takes place at 330 μs . The blue line represents the behavior of the CH emission under plasma assisted ignition. The first decay of the emission (100 – 175 μs , the time triggering is arbitrary here) is due to CH excitation in the discharge; the increase which starts immediately after the decay is connected with the start of ignition.

To summarize, the proposed optical system consisted of fast streak camera and monochromator is able to give the additional information about temporal dynamics of different molecular bands in the single-shot experiments on plasma assisted ignition.

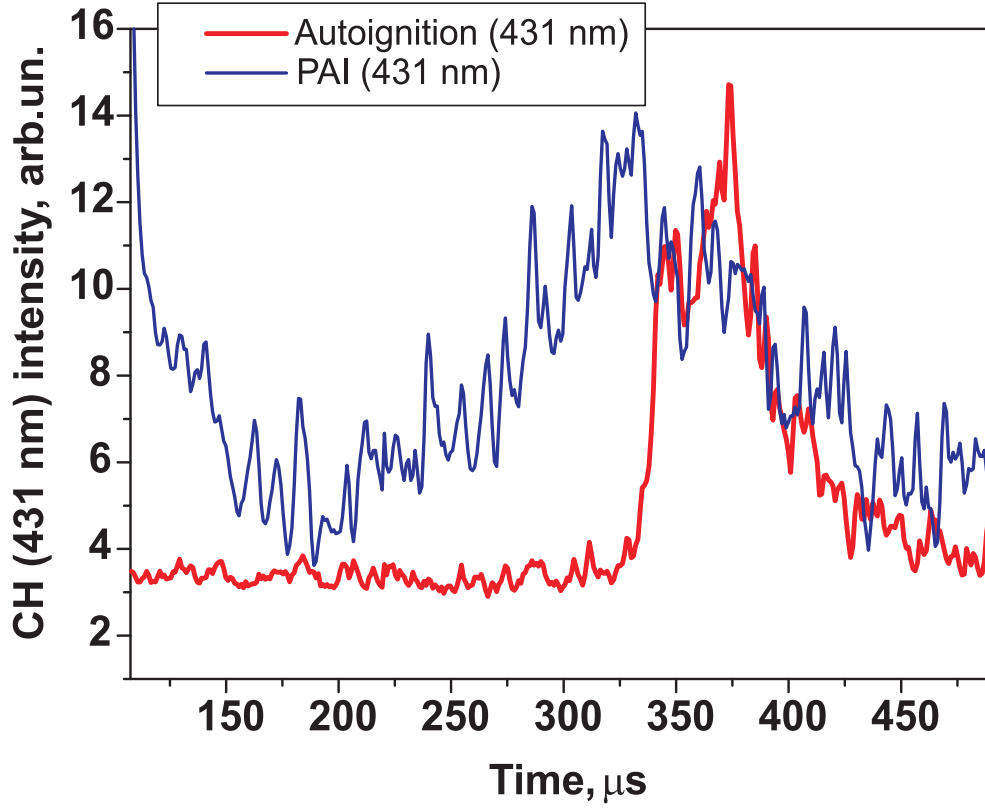


Figure 6.12: Comparison of temporal behavior of CH emission for autoignition (red line) and plasma-assisted ignition (blue line) in a $(\text{C}_3\text{H}_8:\text{O}_2):\text{Ar}=10:90$ stoichiometric mixture

6.1.3 Electron density measurements

Time-resolved electron density was measured in the afterglow of a nanosecond discharge using a two-channel microwave interferometer. The scheme of the interferometer is given by Fig. 6.13. It involved the main block, waveguide, horn antenna, and reflector. In the main block the technique of quadrature (IQ) phase sensitive detector was used, and the in-phase and $\pi/2$ -shifted-phase sensitive detectors were employed to analyze phase shifts. Output signals from the detectors were amplified and fed as inputs to the oscillograph TDS3014B, synchronously with signals from the back-current shunt and capacitive gauge.

A reference wave of frequency $\nu = 9.4 \times 10^{10}$ Hz (a wavelength of 3 mm) was produced by the generator in the main block of the interferometer. The reference wave propagated along the 1.5 m waveguide to the horn antenna with a teflon lens to form a parallel probing beam. The probing signal passed twice through the plasma and returned to the antenna and waveguide to interfere with the reference signal. Due to capacitors placed in series, signals were transferred from the detectors to the interferometer only when the shift between phases of the reference and probing waves and, consequently, wave pattern in the waveguide varied with time. Signals did not exist if plasma had not been generated in the space under consideration or if the plasma properties did not vary in time. In the simplest case of a plane uniform plasma layer, the phase shift of the probing signal, $\Delta\Phi(t)$, is related with the electron density $n_e(t)$ in a linear way [59]

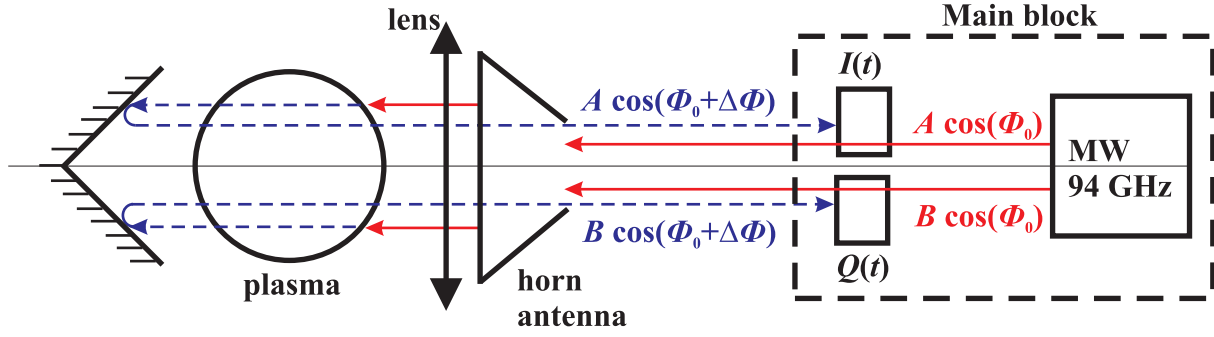


Figure 6.13: A schematic diagram of microwave interferometer

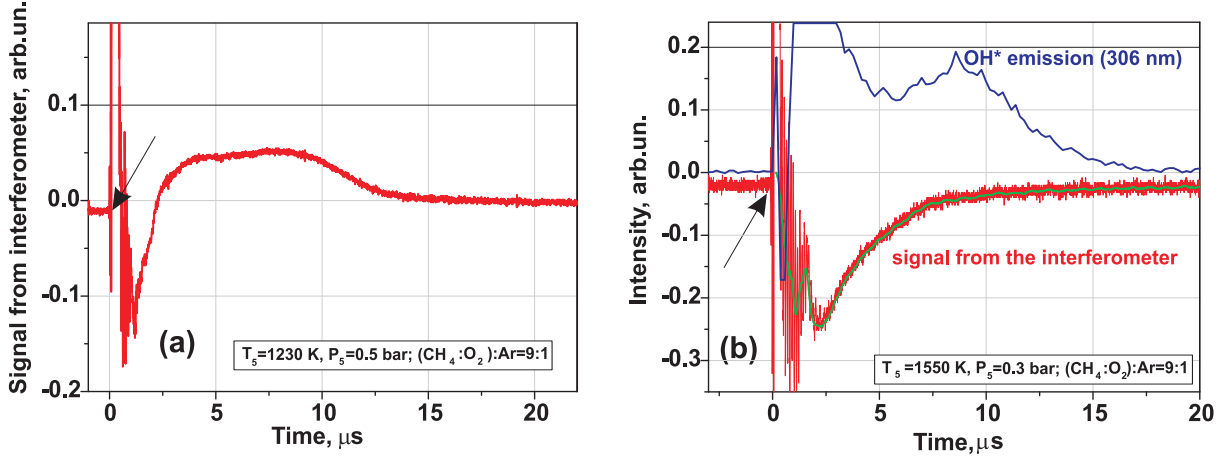


Figure 6.14: Data from (a) microwave interferometer; (b) microwave interferometer correlated with OH* emission at 306 nm at the conditions of plasma assisted ignition

$$n_e(t) = \frac{2\varepsilon_0 mc \omega \Delta\Phi(t)}{e^2 l} \quad (6.4)$$

where m is the electron mass, ε_0 is the permittivity of vacuum, c is the light speed in vacuum, e is the electronic charge, ω is the angle frequency and l is the path length of the beam through the plasma.

Equation (6.4) is correct (i) under the assumption that $\omega \gg \nu_m$, where ν_m is the collision frequency for momentum transfer between electrons and molecules, and (ii) under the assumption that electron density is uniformly distributed along the wave path in plasma. The condition $\omega \gg \nu_m$ is satisfied in the pressure range considered. Uniformity of the discharge plasma over the tube cross section was verified in [35] for similar geometry. If the phase shift exceeded $\pi/2$, the signal had at least one maximum during the plasma decay. This allowed to determine the magnitude of electron density in a given instant. At lower phase shifts signals of both of the channels decayed in time monotonously. Here, electron density had to be determined using a separate calibration for each channel.

The typical signals from one of the channels of the microwave interferometer are given by the Fig. 6.14. Arrows indicate time instant of the discharge. It is clearly seen that the relaxation of the electron density takes quite a long time, as it is demonstrated by Fig. 6.14a, where the interferometric phase shift $\pi/2$ is obtained between 3 and 10 μs .

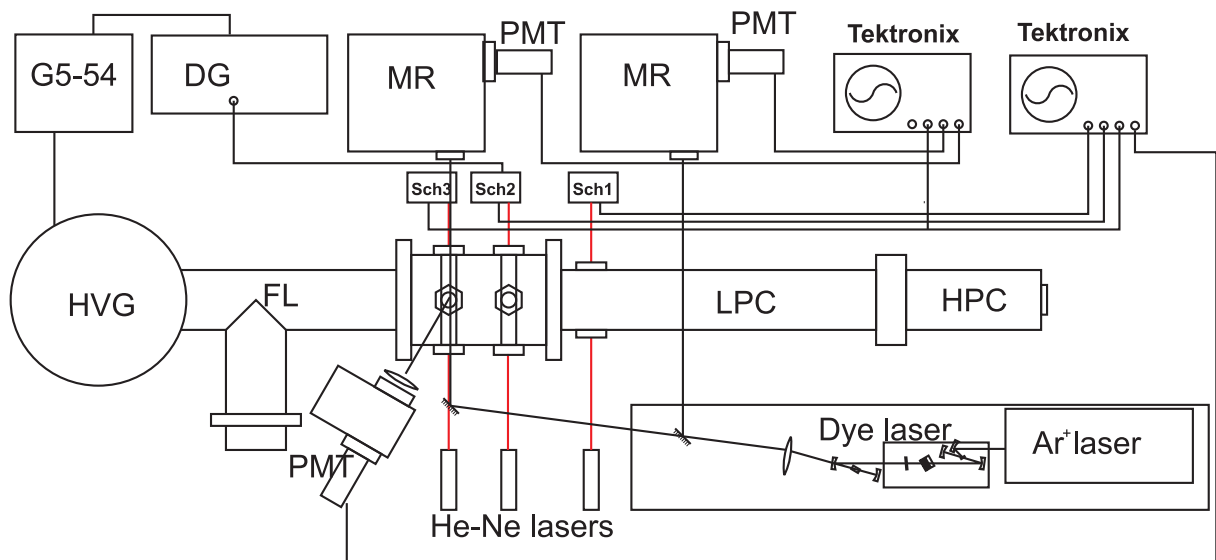


Figure 6.15: Experimental setup for OH density measurements. G5-54: synchro generator, DG: delay generator, MR: monochromator, PMT: photomultiplier, HVG: high voltage generator, FL: forming line, Sch: schlieren system detectors, LPC: low pressure chamber, HPC: high pressure chamber

The signal from the interferometer synchronized with the signal of OH emission at 306 nm is shown in Fig. 6.14b. Here, the first intensive peak of the discharge OH* emission is merged with a less intensive combustion peak.

6.1.4 Measurements of OH radicals

One of the most important intermediates in combustion is OH radical. This section describes our preliminary experiments on OH absolute density measurements in single-shot experiments on plasma assisted combustion. The main peculiarity of these experiments was that we had to synchronize up to 9 different channels of diagnostic in every experiment. The channels are listed below:

- three Schlieren-systems for the measurements of the shock wave velocity;
- microsecond emission channel for the measurements of OH emission at 306 nm due to combustion;
- nanosecond capacitive and current gauges for the measurements of electrical current, voltage, and energy input;
- nanosecond emission channel for the measurements of OH emission from the discharge;
- laser absorption system with a reference beam for the measurements of OH absorption.

OH radicals density was measured in $\text{H}_2:\text{O}_2:\text{Ar} = 6:12:82$ mixture using UV laser absorption. The laser system consisted of Ar pumping laser, and dye cw laser with

doubling system. Emission at 306.72 nm was used to measure absorption in OH ($A^2\Sigma^+ \rightarrow X^2\Pi$, $0 \rightarrow 0$), R1(4) transition. Optical detection scheme with a reference beam was used

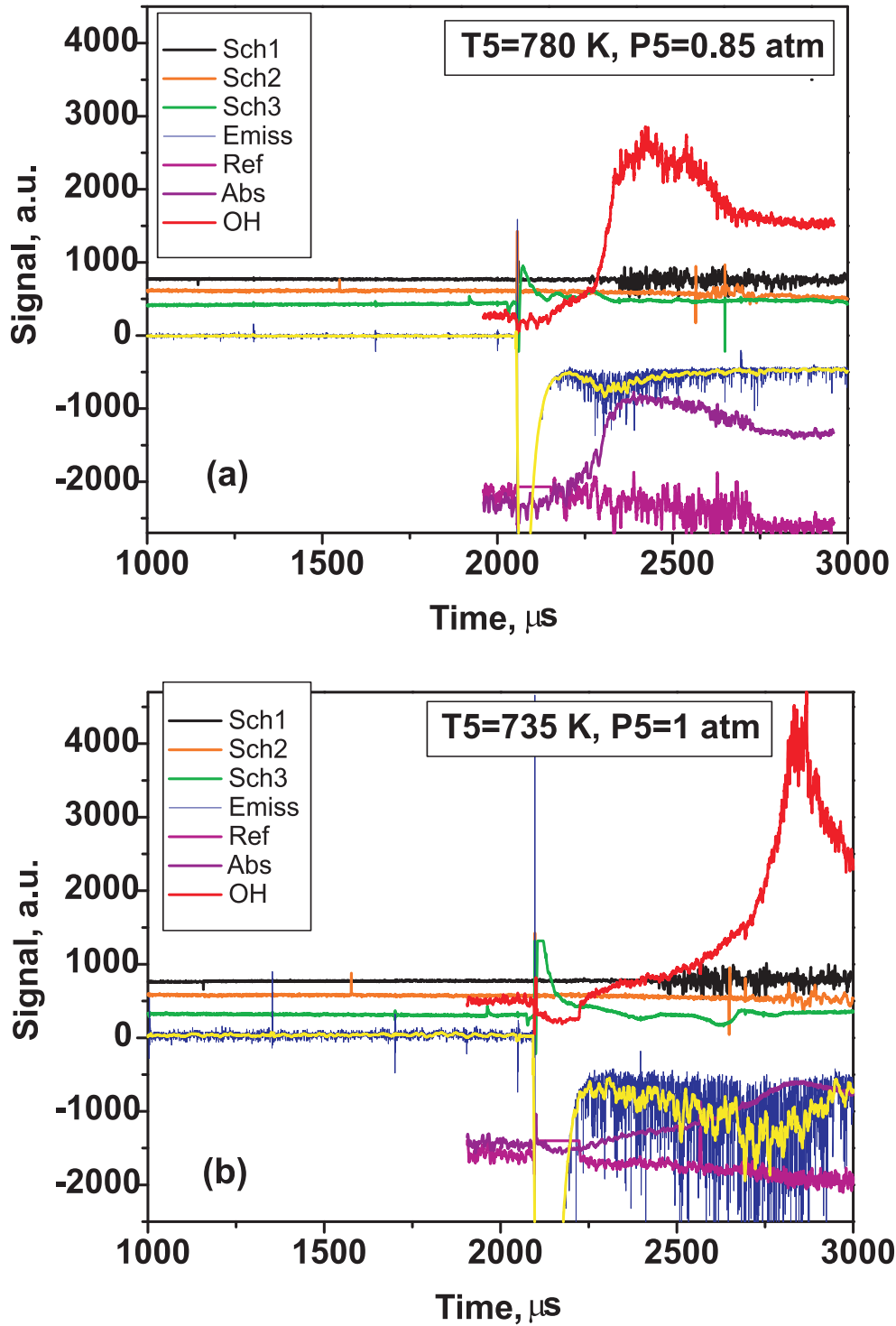


Figure 6.16: Oscillogrammes of the experiments of OH measurements. “Sch1”, “Sch2”, “Sch3” are the signals from Schlieren detectors, “Emiss” is OH emission at 306 nm, “Ref” is a laser emission, “Abs” is an absorption signal, “OH” is the preliminary data for OH density.

to measure the absorption.

Dye cw laser (Ametist SF-03, TekhnoScan, Novosibirsk, Russia) was specially designed to operate with intracavity frequency doubling system. Dye was prepared in solution with ethyl alcohol and ethylene glycol (0.95 l of ethylene glycol and 50 ml of ethyl alcohol per 1 g of Rhodamine 6G). Technical characteristics of Ametist SF-03 laser with its own resonator system are the following:

- line width is not more than 15 MGz;
- spectral range of generation at pumping by Ar laser is 575–625 nm;
- radiation output (3 W of TEM₀₀ Ar pumping) is 50 mW;
- divergence is 1 mrad;
- diameter of the output beam is 0.8 mm

In our case, the doubling BBO crystal was installed inside the laser resonator, and this changed the parameters of the laser generation. So, we investigated additionally the parameters of the laser system.

To make the absolute calibration possible, we have performed a set of autoignition experiments. These data will be compared with the calculations of the autoignition in a given gas mixture at known initial pressure and temperature. These data will be used to calculate the absorption coefficient. Knowing the absorption coefficient, the OH absolute values will be obtained for plasma assisted ignition.

The experiments were carried out for temperature range 780–1220 K and pressure range 0.5–1.2 bar in a H₂:O₂:Ar:CO₂=6:12:81:1 mixture. Two examples of the initial experimental data are given in Fig. 6.16. Velocity of the shock wave was determined from the Schlieren systems data: three He–Ne lasers were installed along the shock tube so that their beams were parallel to each other and perpendicular to the shock tube axis. Their emission was deflected on the density gradients at the instant of shock wave coming to the point where the laser beam crossed the shock tube; these instants are clearly seen in the Fig. 6.16. After the instant when the reflected shock wave came to the cross-section of measurements (negative peak on the Sch3 signal) the discharge has been initiated in the last dielectric section of the shock tube. Vertical lines at practically all oscilloscope traces correspond to the electrical noise from the discharge (time instant is about 2050–2100 μ s). After this we observed a strong OH emission from the discharge (the first peak with a fast decay, blue or yellow curve) and the second peak corresponding to the ignition. At the level of the absorption signal the laser signal was not stable enough and we had to use a scheme with two beams, when the reference signal was extracted from the absorption signal for every experiment. As a result, after the analysis of a reference signal of laser radiation (“Ref” curve) which did not go through the discharge cell and the signal passing through the discharge cell (“Abs”), we derived the OH curve in arbitrary units. It is clearly seen that the correlation between temporal behaviour of OH emission at 306 nm and OH density in the ground state is good enough.

6.2 Conclusions

Thus, detailed kinetics of different species during plasma assisted ignition at elevated pressures has been analyzed numerically for hydrogen– and hydrocarbon–oxygen mixtures diluted with 80 or 90 % of Ar. The components and techniques were selected to control the process of plasma assisted ignition during the delay time. Capabilities of absorption spectroscopy in UV and IR regions of spectra, microwave interferometry, and fast streak imaging have been analyzed. Preliminary results proving the possibility to study experimentally temporal dynamics of key species during the induction delay time have been obtained.

Chapter 7

Analysis of the Results on Plasma–Assisted Ignition in Hydrocarbon-Containing Mixtures

Thus, on the basis of experimental results and numerical modelling we conclude that, at high gas temperatures near the autoignition threshold, the main mechanism of plasma-assisted ignition is an additional production of atoms and radicals during the discharge phase. Let us consider (i) peculiarities of the discharge development; (ii) possible gas heating and its influence on the decrease of ignition delay time, that is, importance of nonequilibrium conditions in comparison to the thermal heating; (iii) energy cost for the O-atoms production by the nanosecond discharge; (iv) possible directions of further research.

7.1 Discharge development in mixtures under consideration. Influence of Ar dilution

Dilution with inert gases is typical for the shock-tube experiments: first, this leads to a decrease in the energy release in the combustion experiments; second, this causes a decrease in the role of boundary layers in the shock tube and allows 1D-description of the shock wave development and propagation. In the kinetics of ignition and combustion, Ar atoms are usually considered as a third body in collisional process.

For the discharge development, the situation is more complex and needs an additional analysis. The mean electron energy and energy losses depend strongly upon Ar dilution. Due to absence of the vibrational and rotational energy losses, in argon the same reduced electric fields lead to higher electron energies.

This fact is well-known, still, the direct experimental evidence for the nanosecond high-voltage discharge can be found in comparison of the signals from microwave interferometer for Ar, N₂ and O₂ (see Figs. 7.1–7.3). These experiments were carried out in pure gases in discharge tube 5 cm in diameter and 20 cm in length. The description of microwave interferometer is given in previous chapter (see Fig. 6.13).

It follows from the analysis of Figs. 7.1–7.3 that, under the same experimental conditions, the electron density in Ar is significantly higher than in nitrogen and oxygen.

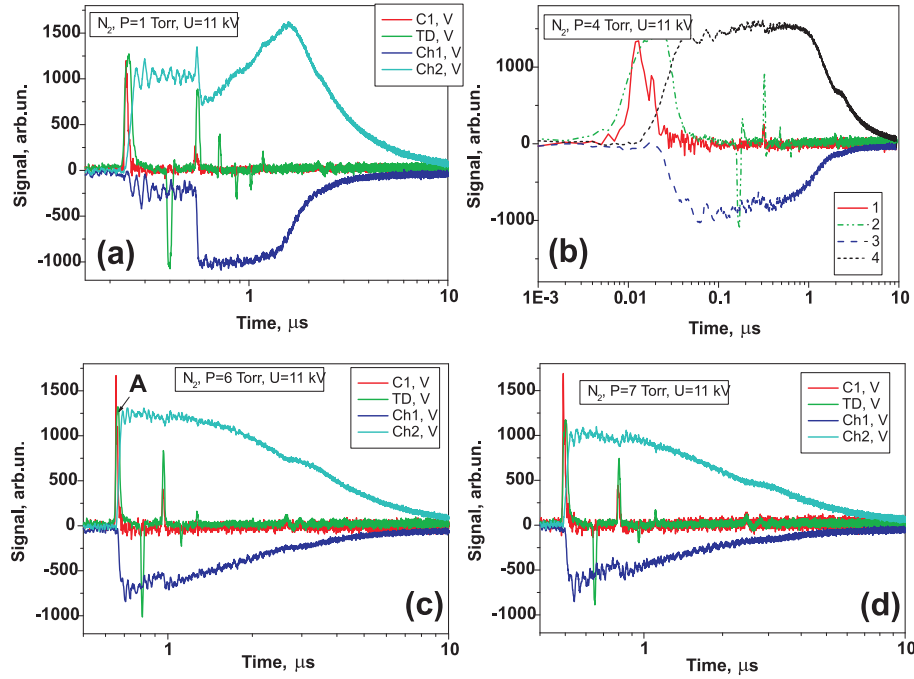


Figure 7.1: Pure nitrogen. Typical signals on a sub-microsecond scale from (C1) the capacitive gauge, (TD) back current shunt and (Ch1, Ch2) signals from two channels of microwave interferometer. The voltage amplitude is 11 kV in the cable, pulse duration is 25 ns, rise time is 5 ns, repetitive frequency is 40 Hz.

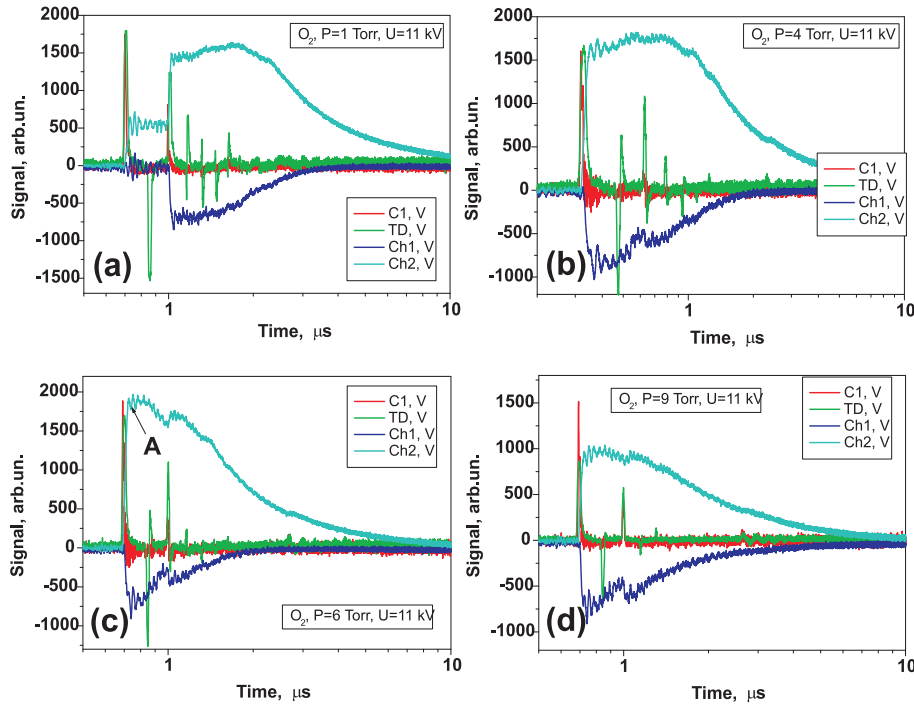


Figure 7.2: Pure oxygen. Typical signals on a sub-microsecond scale from (C1) the capacitive gauge, (TD) back current shunt and (Ch1, Ch2) signals from two channels of microwave interferometer. The voltage amplitude is 11 kV in the cable, pulse duration is 25 ns, rise time is 5 ns, repetitive frequency is 40 Hz.

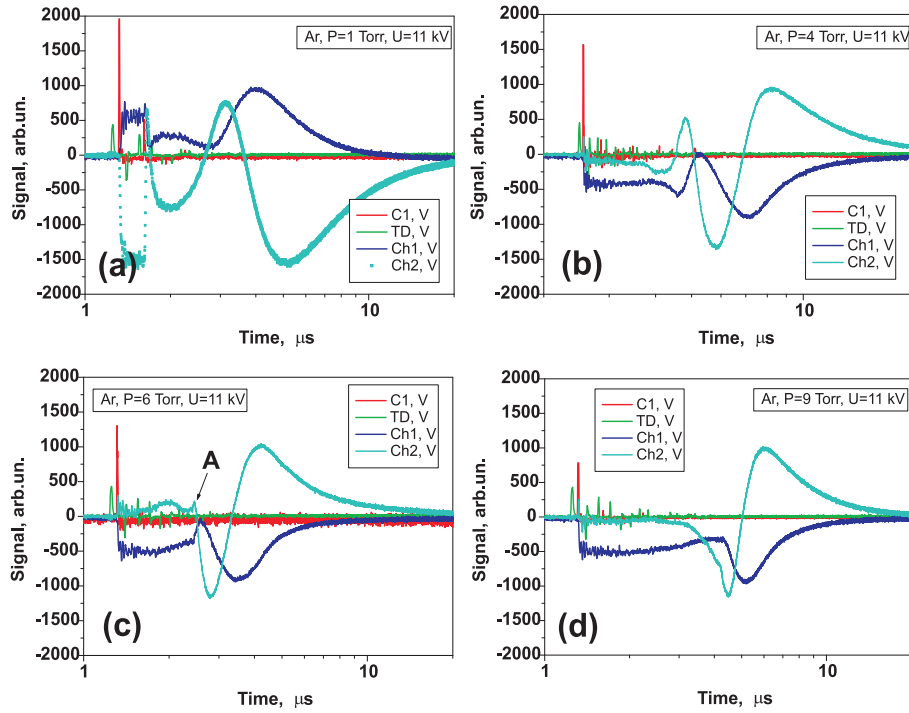


Figure 7.3: Pure argon. Typical signals on a sub-microsecond scale from (C1) the capacitive gauge, (TD) back current shunt and (Ch1, Ch2) signals from two channels of microwave interferometer. The voltage amplitude is 11 kV in the cable, pulse duration is 25 ns, rise time is 5 ns, repetitive frequency is 40 Hz.

Fig. 7.4 gives preliminary results on electron density for different gases for gas pressure 6 Torr (plots (c) in Figs. 7.1–7.3). Point A in the Figs. 7.1c–7.3c corresponds to time instant $t = 0$ in the Fig. 7.4. Dashed line in Fig. 7.4c represents the data obtained taking into account minima and maxima of the signal, solid red lines were obtained using the procedure described in previous chapter of the Report. It should be noted however that these results have to be treated with some precautions: in the case of relatively low electron density, as it is realized for N_2 or for O_2 , non-zero background due to accumulation of residual electron density between the pulses may influence the results.

Thus, Ar dilution influences strongly electron density and electron energy distribution function (EEDF) in the discharge. Consequently, the energy branching is determined strongly by Ar presence in the system. To clarify this, let us compare energy branching as a function of reduced electric field, for three cases: investigated stoichiometric $C_2H_6:O_2$ mixture with 90 % of Ar dilution (Fig. 7.5a), the same mixture without argon additions (Fig. 7.5b), and stoichiometric C_2H_6 :air mixture (Fig. 7.5c). It is clearly seen that, for a case of 90 % dilution with Ar, energy losses for molecular oxygen dissociation by an electron impact reach its maximal value at reduced fields significantly lower than in the case of mixtures without Ar, in agreement with the analysis above. Without Ar, significant part of energy is stent on excitation of internal degrees of freedom, and mean electron energy is lower at the same E/n values. It should be noted that in case of ethane–air mixture, efficient excitation of vibrational states of molecular nitrogen is significant. It may lead to additional dissociation through excitation of electronic triplet states of molecular nitrogen.

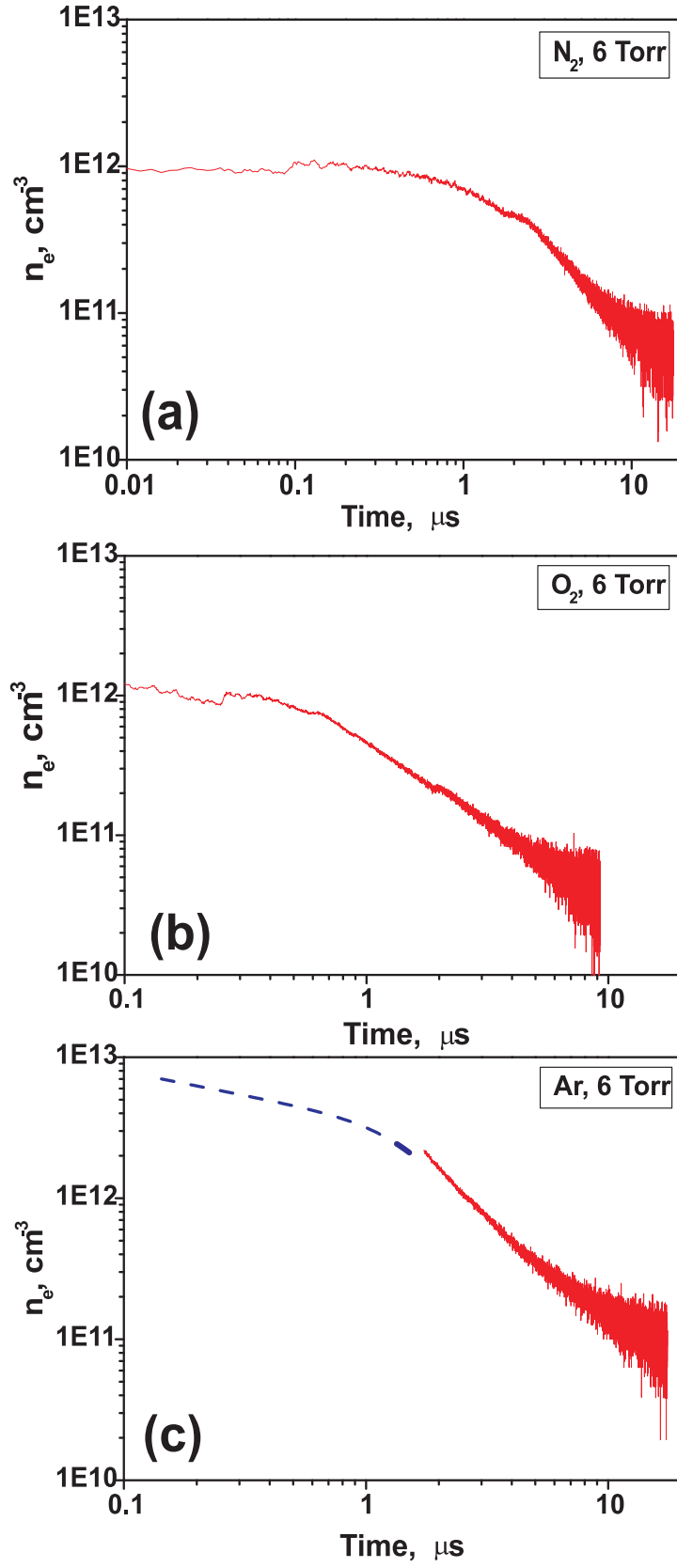


Figure 7.4: Electron density obtained from data of the Figures 7.1–7.3. (a): Nitrogen, P=6 Torr; (b) Oxygen, P=6 Torr; (c) argon, P=6 Torr. The voltage amplitude is 11 kV in the cable, pulse duration is 25 ns, rise time is 5 ns, repetitive frequency is 40 Hz.

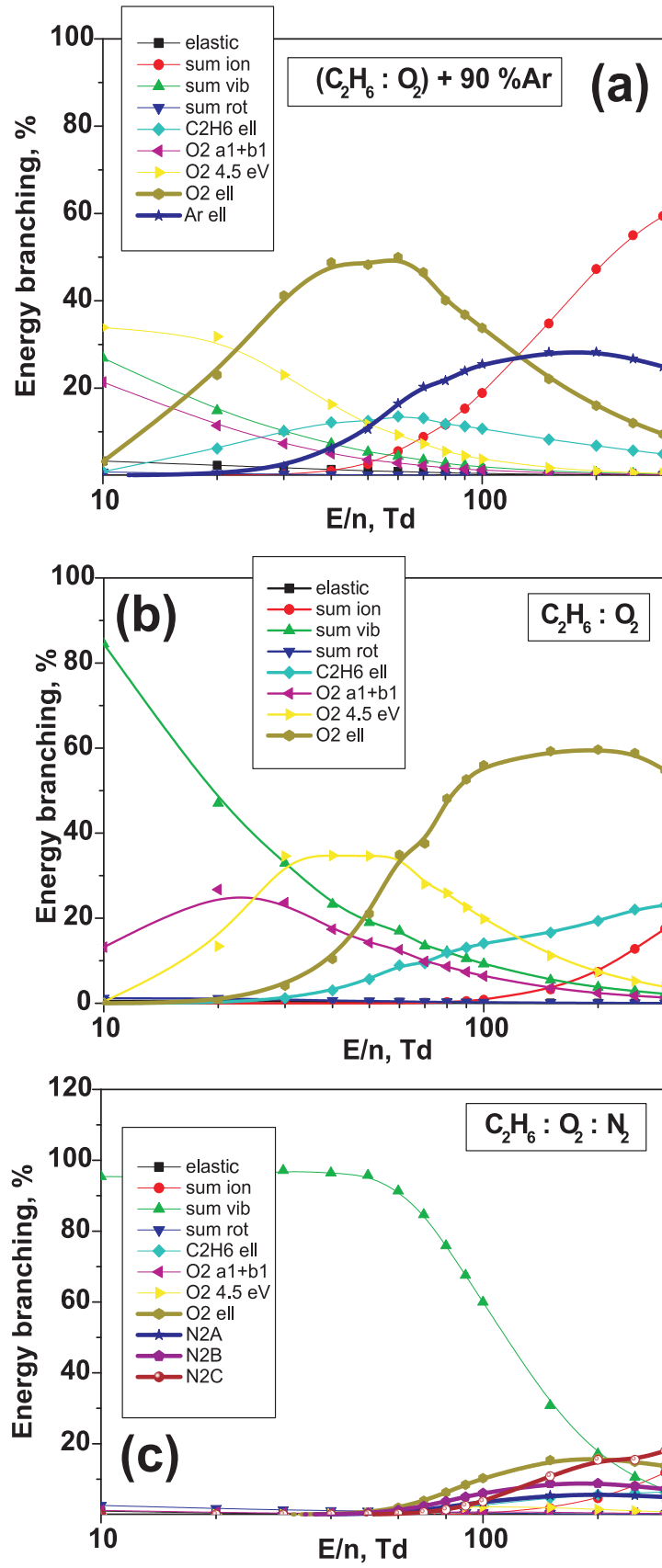


Figure 7.5: Fractional power transferred in different mixtures from electrons to neutral particles (energy branching).

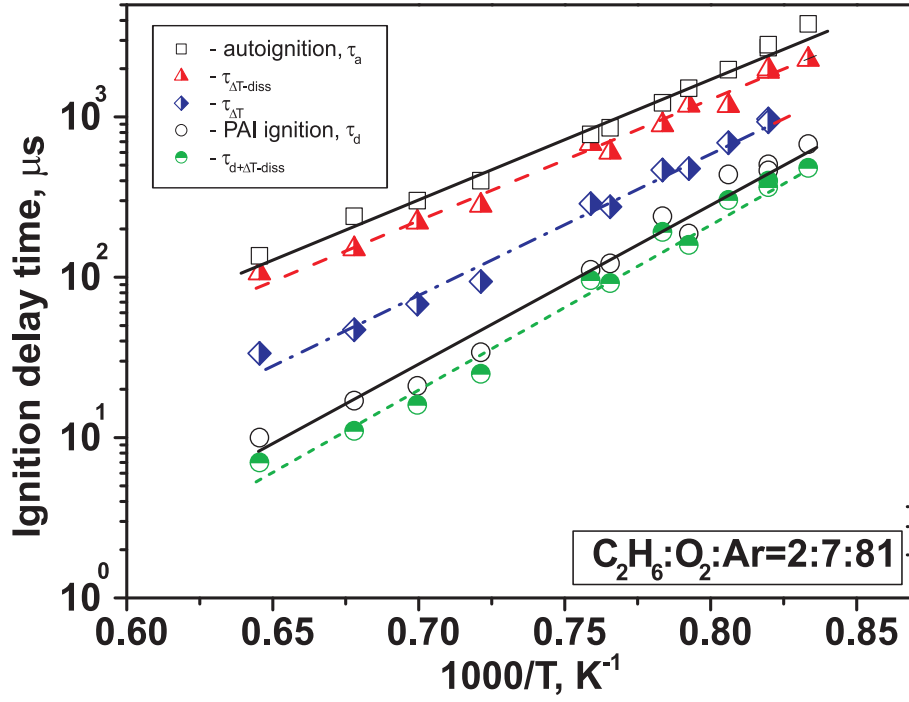


Figure 7.6: Calculated ignition delay time for different gas heating. Initial conditions (pressure P_5 and temperature T_5) correspond to those in the $C_2H_6:O_2:Ar$ mixture. See detailed explanations in the text.

To finalize, in our experimental case, Ar dilution strongly influences energy branching in the discharge. Fig. 7.5 clearly illustrates the statement that the gas mixture composition and discharge properties for any investigated mixture are determined by argon and molecular oxygen.

7.2 Analysis of gas heating. Equilibrium and nonequilibrium energy input

To make unambiguous conclusion about role of nonequilibrium plasma in decrease of the ignition delay time, it is necessary to measure or, at least, to estimate maximal possible gas heating and to analyze how high the shift of the ignition delay time can be due to this additional heating.

The analysis has been made in the following way. Total energy input to the gas was measured for each experiment by controlling discharge current and electric field. To obtain the specific deposited energy, we divided the energy input by discharge volume assuming that discharge develops uniformly between capacitive detectors C1 and C2.

To analyze gas temperature in the experiments, we calculated the gas heating assuming that all energy deposited in the discharge is spent only on heating and neglecting the effect of radical production. The most evident situation was obtained for methane-containing mixture. In spite of the fact that the assumption significantly overestimates possible heating by the discharge, the calculated increase in gas temperature in the discharge, ΔT , is not enough to explain our experimental data by the autoignition due to gas heating.

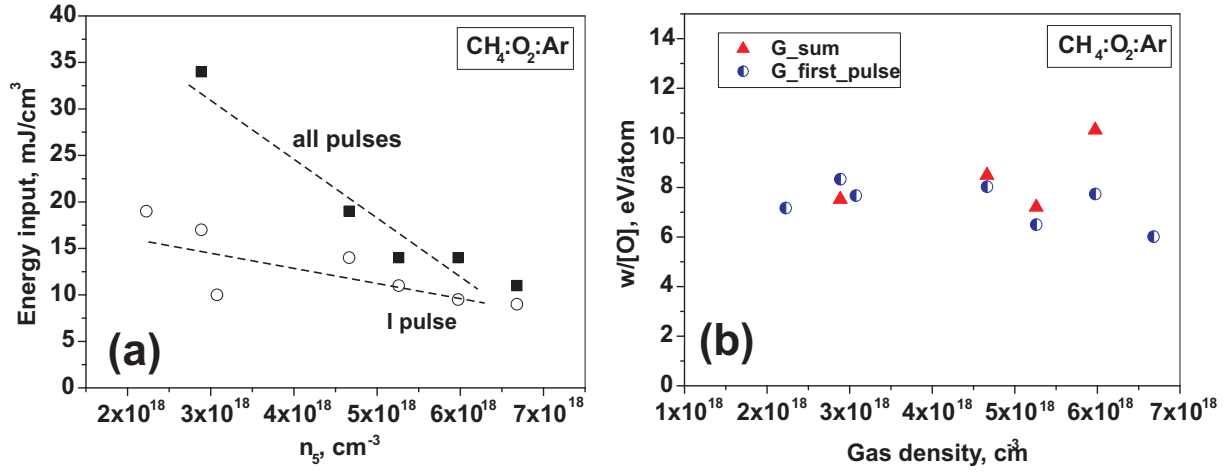


Figure 7.7: $\text{CH}_4:\text{O}_2:\text{Ar}$ mixture. (a): specific deposited energy during the first pulse of nanosecond generator (hollow symbols) and total specific deposited energy (filled symbols); (b): energy efficiency of O-atoms production in the first pulse and in total during all the reflections of high-voltage pulse.

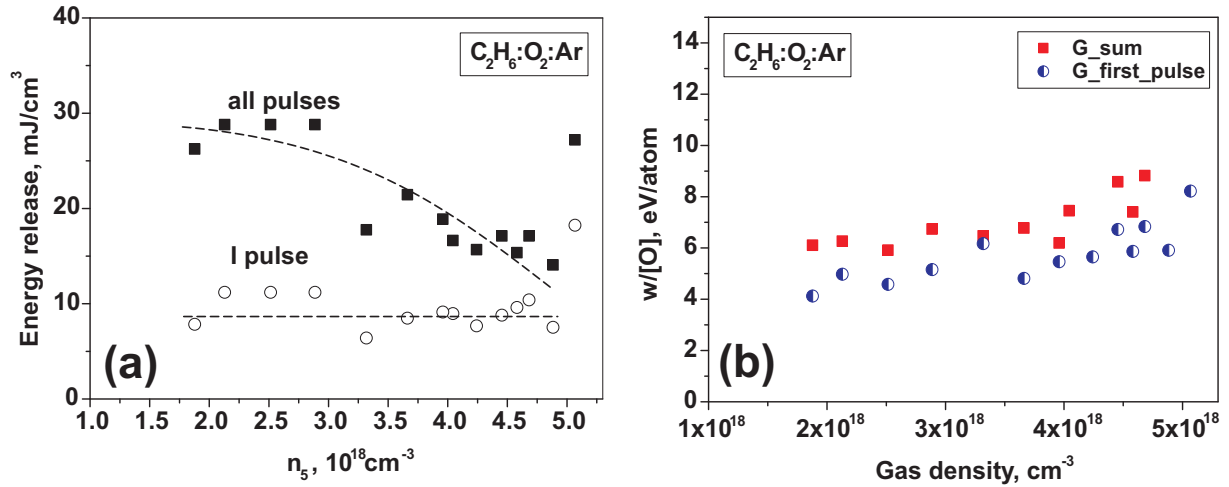


Figure 7.8: $\text{C}_2\text{H}_6:\text{O}_2:\text{Ar}$ mixture. (a): specific deposited energy during the first pulse of nanosecond generator (hollow symbols) and total specific deposited energy (filled symbols); (b): energy efficiency of O-atoms production in the first pulse and in total during all the reflections of high-voltage pulse.

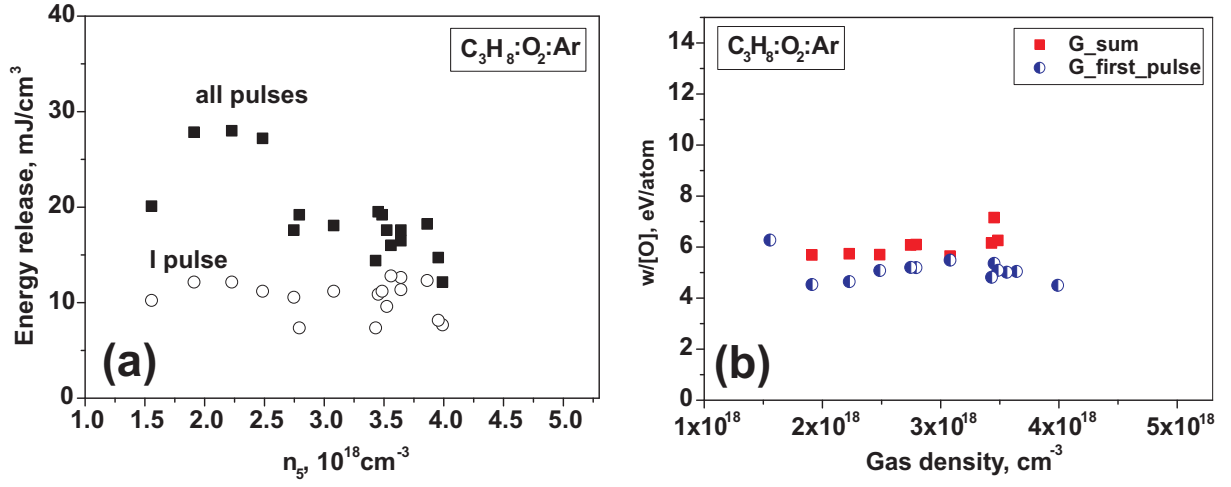


Figure 7.9: $C_3H_8:O_2:Ar$ mixture. (a): specific deposited energy during the first pulse of nanosecond generator (hollow symbols) and total specific deposited energy (filled symbols); (b): energy efficiency of O-atoms production in the first pulse and in total during all the reflections of high-voltage pulse.

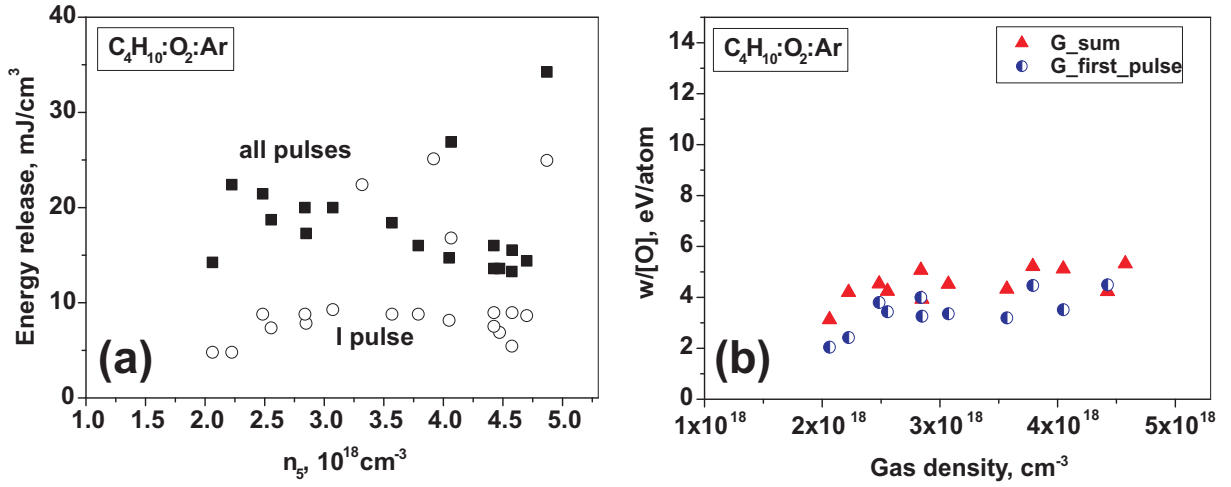


Figure 7.10: $C_4H_{10}:O_2:Ar$ mixture. (a): specific deposited energy during the first pulse of nanosecond generator (hollow symbols) and total specific deposited energy (filled symbols); (b): energy efficiency of O-atoms production in the first pulse and in total during all the reflections of high-voltage pulse.

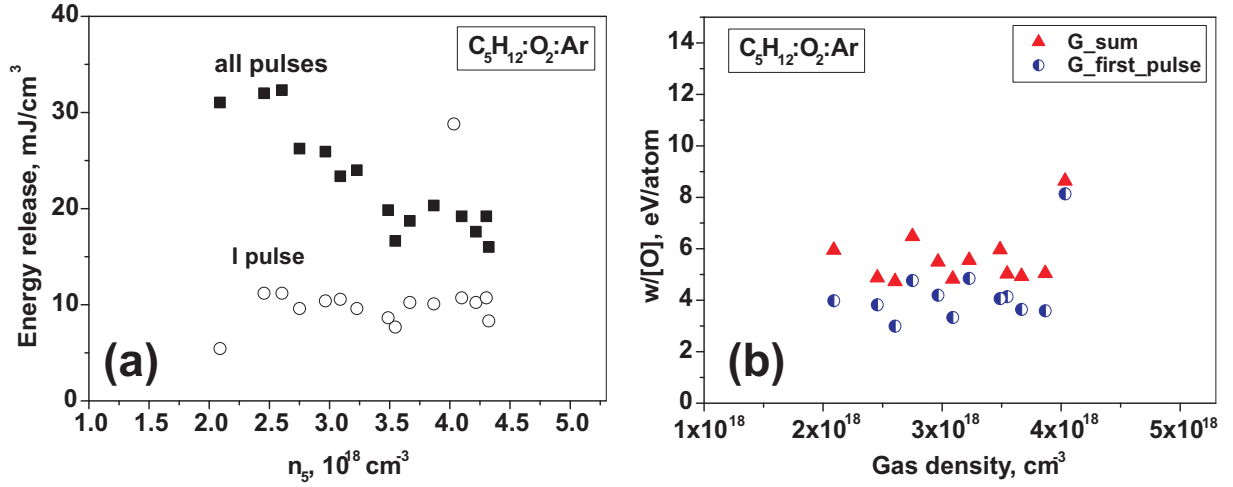


Figure 7.11: $C_5H_{12}:O_2:Ar$ mixture. (a): specific deposited energy during the first pulse of nanosecond generator (hollow symbols) and total specific deposited energy (filled symbols); (b): energy efficiency of O-atoms production in the first pulse and in total during all the reflections of high-voltage pulse.

For example, for $T_5 = 1530$ K and $P_5 = 1.1$ bar, we obtain $\Delta T \approx 70$ K. This shifts autoignition delay time from 2200 to 900 μs , whereas the measured value is 100 μs . To obtain the required value due to gas heating, it is necessary to have $\Delta T \approx 350$ K, much higher than that corresponding to gas heating during the discharge. Thus, the observed decrease of ignition delay time is of non-thermal nature.

The estimates for C_nH_{2n+2} -containing mixtures are not so evident, still they give unambiguous results. Additional calculations were made for the C_2H_6 -containing mixture to prove that the effect of plasma is primarily associated with non-equilibrium energy input. The results are given by Fig. 7.6. Under the same conditions, we calculated (i) autoignition delay time, τ_a , (ii) ignition delay time, $\tau_{\Delta T-diss}$, under assumption that the deposited energy minus the energy spent to produce radicals is fast transformed into gas heating and neglecting the effect of radicals, (iii) delay time, $\tau_{\Delta T}$, assuming that all energy deposited in the discharge is spent only to heating and neglecting the effect of radicals, (iv) delay time, τ_d , neglecting gas heating by the discharge and taking into account the effect of radicals (the assumption used above in this paper), and (v) delay time, $\tau_{(d+\Delta T-diss)}$, taking into account gas heating in the discharge by analogy with (ii) and the non-equilibrium effect of radicals. As a result, we obtained their ratio $\tau_a : \tau_{(\Delta T-diss)} : \tau_{\Delta T} : \tau_d : \tau_{(d+\Delta T-diss)} = 100 : 75 : 20 : 7 : 5$. The assumption (iii) significantly overestimates possible heating by the discharge, whereas the assumption (ii) gives more real upper bound of the heating.

It follows from these calculations that the experimentally observed difference between autoignition delay time and ignition delay time with the discharge can be explained only by the effect of radicals produced in the discharge, the role of heating in this phase being much smaller. Consequently, a decrease in ignition delay time under the discharge is related with the non-thermal plasma processes.

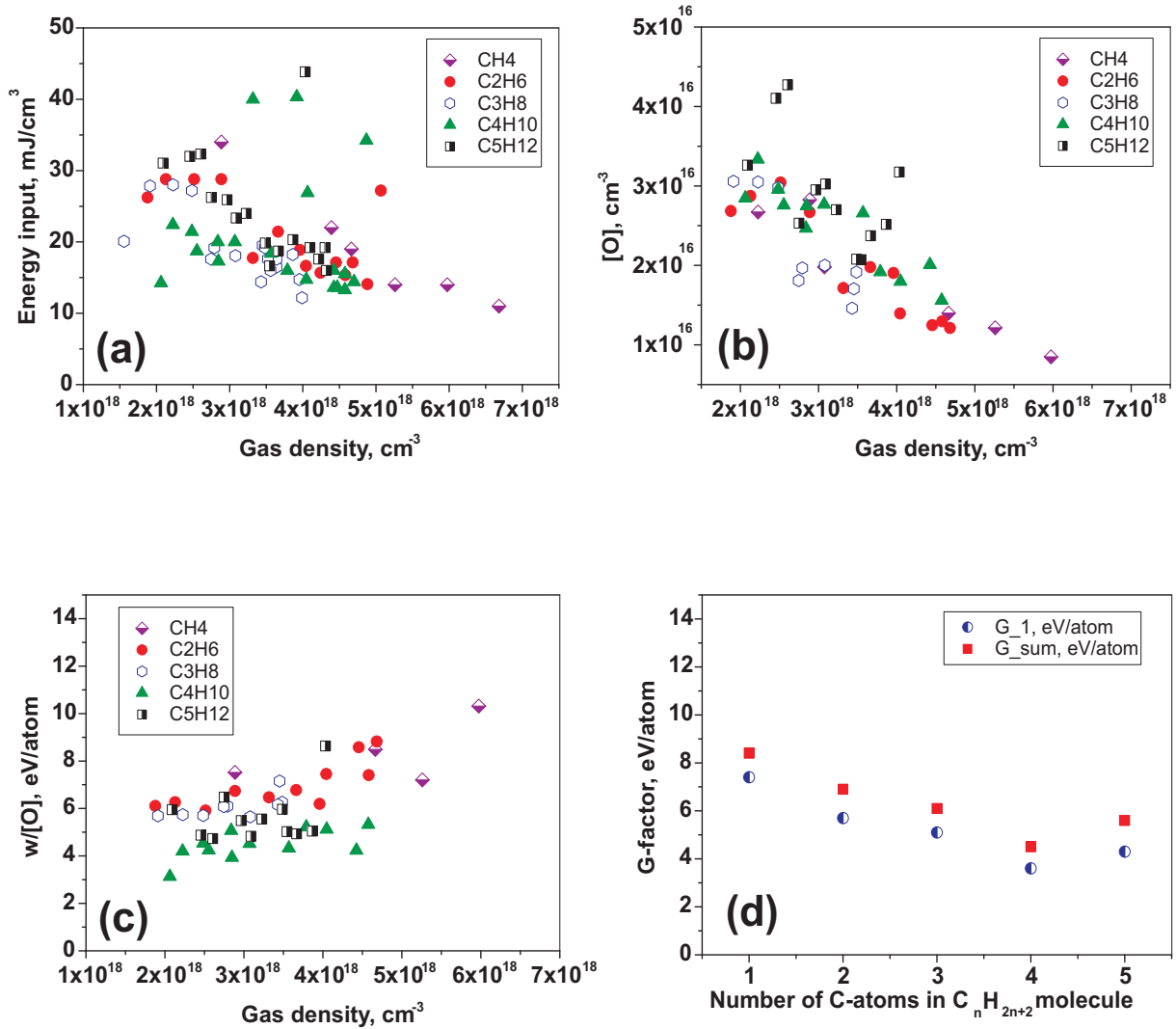


Figure 7.12: Analysis of energy consumption, (a): total specific deposited energy for different hydrocarbon-containing mixtures; (b): total O-atoms density; (c) Energy consumption for one O-atom formation for different hydrocarbons; (d) average values of O-atom formation energy cost for different hydrocarbon-containing mixtures.

7.3 Energy efficiency of O-atoms production by nanosecond discharge

Taking into account that under our experimental conditions molecular oxygen dissociation is a dominating process in a wide range of reduced electric fields, there is a reason to analyze the energy efficiency of O atoms as a total energy deposited in plasma divided by O-atoms density.

The data of the energy efficiency for all investigated mixtures (methane-to pentane stoichiometric mixtures with oxygen diluted with 90 % of Ar) are summarized below. Figs. 7.7–7.11 illustrated behavior of energy input and O-atom formation energy cost for different mixtures. The non-matched load allows analysis of discharge peculiarities at different electric fields because, as it was described earlier, the electron density in

secondary (reflected) pulses is higher, and the electric field is lower than in the first (incident) pulse of the high voltage. The O atoms production “follows” the electric field, and, finally, O-atom formation energy cost in the first pulse and “summary” O-atom formation energy cost do not differ significantly. In spite of the fact that the energy input in the first pulse is approximately half of the total energy input, the dissociation in the first pulse is the most efficient, and, finally, the O-atom formation energy cost in the first pulse of high voltage is about 1 eV/atom lower than the “summary” O-atom formation energy cost.

It is important that, under our experimental conditions, we obtain similar values of energetic efficiency of O-atoms production for all considered mixtures. This is illustrated by Fig. 7.12, where plots (a) and (b) give values of deposited energy and O-atoms density *vs* gas number density, respectively, and plots (c) and (d) represent O-atom formation energy cost *vs* gas number density and average values of O-atom formation energy cost upon number of C-atoms in the hydrocarbon molecule of fuel we used.

Chapter 8

Diagnostic of Unexcited OH During Plasma Assisted Ignition

8.1 Introduction

It has been discussed in the previous chapters that diagnostics of intermediates in the period of induction delay time between the nanosecond discharge and initiation of combustion may have a significant influence on understanding of the total picture of ignition by nonequilibrium plasma. The idea to measure *in situ* combustion intermediates and to combine these measurement with detailed kinetic modelling is developed by different authors [60, 61].

Team from Ohio State University discuss [60] recent results of plasma assisted combustion experiments using high-voltage, nanosecond pulse duration, high pulse repetition rate discharge and kinetic modelling calculations. Kinetic model used to analyze these experiments has been validated using time-resolved Two Photon Absorption Laser Induced Fluorescence (TALIF) measurements of O atom concentration generated by the pulsed discharge. In these experiments, absolute O oxygen concentrations have been measured in air, methane-air, and ethylene-air plasmas, as a function of time after initiation of a single 25 ns discharge pulse, and in burst mode, in which a sequence of 2-100 discharge pulses is initiated at 100 kHz. Comparing their calculation with the results on experiments on plasma assisted ignition the authors conclude that the model correctly predicts oxidized fuel fractions and resultant temperature rise in the plasma in the oxidation regime but significantly overpredicts burned fuel fractions in the ignition regime. Transition from the oxidation to the ignition regime predicted by the model is consistent with the experiment. The model poorly predicts some product species concentrations (CO_2 , CH_2O , and C_2H_2). Comparison of product species concentrations predicted utilizing two widely used hydrocarbon reaction mechanisms showed significant differences. Since these mechanisms have not been validated at near-room temperatures, the authors suggest that they may be inapplicable at the conditions of their experiments. They report the need for development of an accurate low-temperature plasma chemical fuel oxidation reaction mechanism.

Scientists from Ecole Centrale, Paris [61] investigated nanosecond repetitively pulsed discharge in preheated atmospheric pressure air or nitrogen 300–100 K (flow rates 1–17 m/s) using advanced laser technique. According to a chemical kinetic model the formation of atomic oxygen in the discharge is a two-step mechanism. Excited molecular

nitrogen formed via electron–impact excitation reacts with molecular oxygen to produce atomic oxygen. To validate the kinetic model, the densities of ground state atomic oxygen as well as the excited electronic state $N_2(A)$ have been measured. The small plasma volume ($1\text{--}5\text{ mm}^3$) and the short lifetimes of plasma species (tens of nanoseconds) required advanced diagnostic techniques. Two photon Absorption Laser Induced Fluorescence (TALIF)) and Cavity Ring Down Spectroscopy (CRDS) have been employed to measure atomic oxygen and $N_2(A)$, respectively. The decay time for O–atoms in the discharge afterglow was found to be $25\text{ }\mu\text{s}$, decay time for $N_2(A)$ molecules was found to be 900 ns . The obtained results are valuable for the understanding of discharge behaviour, the induced plasma chemistry, and also for the validation of the kinetic model.

Coming back to our previous numerical results, let us consider details of plasma-induced kinetics under plasma assisted ignition. Fig. 8.1 demonstrates the effect of non-equilibrium plasma on ignition kinetics. The “injection” of radicals at the beginning of ignition leads to a much faster decomposition of the fuel and to the formation of simpler radicals through the mechanisms typical for routine kinetic schemes of ignition; as a result, the mixtures are ignited much faster. Indeed, the autoignition delay time at these conditions is equal $570\text{ }\mu\text{s}$ for propane–containing mixture and $400\text{ }\mu\text{s}$ for butane–containing mixture.

It is seen from Fig. 8.1 that CH_3 , C_2H_5 , formaldehyde and CO are efficiently accumulated both in the case of C_3H_8 and in the case of C_4H_{10} . It is worth noting that the efficient generation of atoms and radicals in the discharge favours the conversion of alkyls into smaller alkyls and the difference in kinetic schemes for ignition of various hydrocarbons including methane becomes smaller.

It is clearly seen also, that kinetic curve of OH radical has a specific shape with minimum during the ignition delay time. First, we observe decay of OH mole fraction because of recombination processes. Starting from a certain time instant (approximately $20\text{ }\mu\text{s}$), the OH density increases due to starting reactions which correspond to a common combustion chemistry. Typical densities of OH radical during the ignition delay period are about $10^{14} - 10^{15}\text{ cm}^{-3}$.

So, it would be desirable to develop experimental technique and to measure kinetic curve for absolute OH–density during plasma assisted ignition, and especially during the induction delay period.

8.2 Experimental setup

We used the idea to measure OH–density in the ground state *in situ* during the shock tube experiment. This approach has its own drawbacks and advantages. Unfortunately, the single–shot regime does not allow accumulation and averaging of the signal, so, all the experiments were made in single–pulse mode. On the other hand, we used cw laser system for laser absorption measurements, and this gave the kinetic curve of OH in real time.

8.2.1 Shock tube – nanosecond discharge setup

The experimental setup and measurement technique have been given in detail elsewhere [38]. Measurements were performed behind a reflected shock wave. The shock tube (a

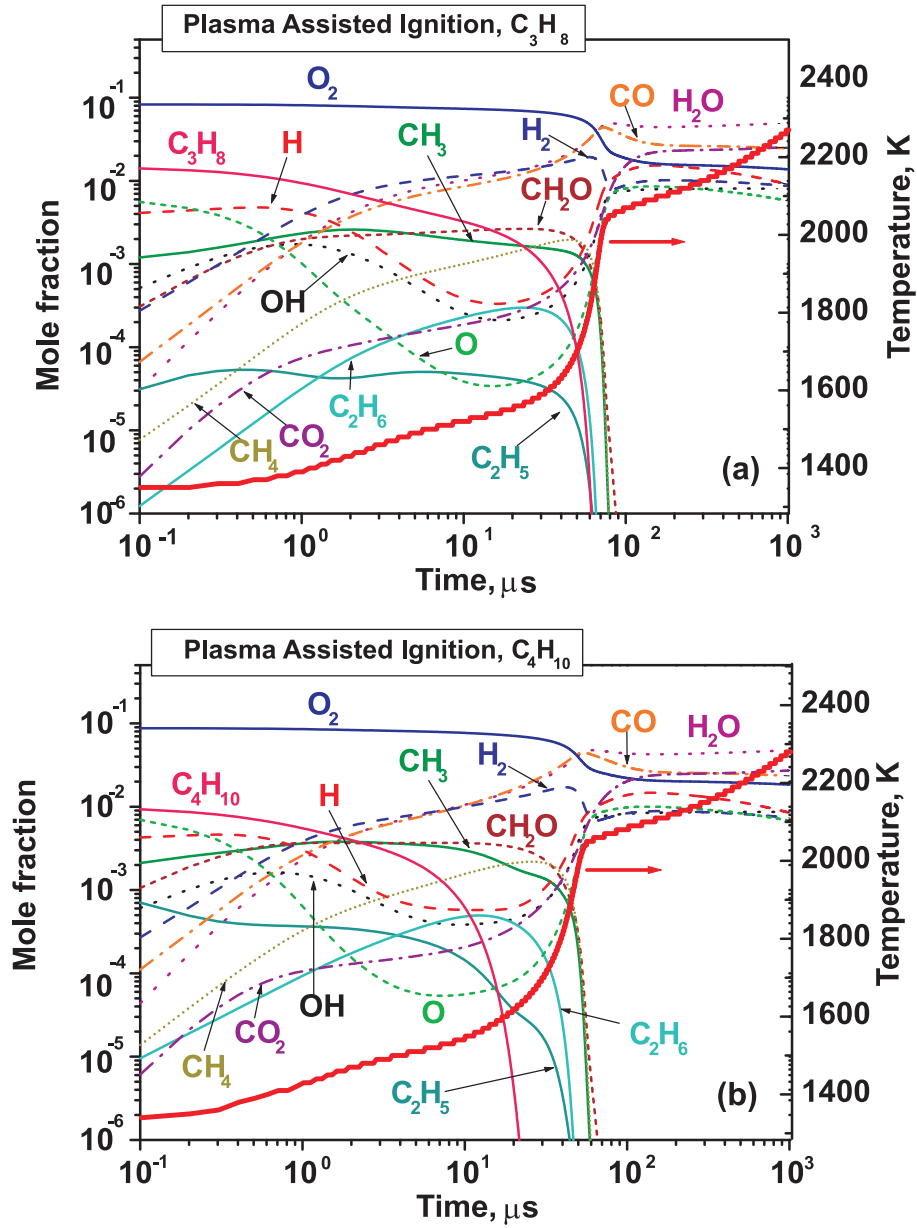


Figure 8.1: The evolution in time of the mole fractions of main components for plasma assisted ignition (a) in the $\text{C}_3\text{H}_8:\text{O}_2:\text{Ar}$ mixture at $T_5 = 1350$ K and $P_5 = 0.6$ bar; (b) in the $\text{C}_4\text{H}_{10}:\text{O}_2:\text{Ar}$ mixture at $T_5 = 1350$ K and $P_5 = 0.6$ bar. The gas temperature evolution is represented by the thick red line.

25×25-mm² square cross section) had a 1.6-m-long working channel. The last 20-cm section of the shock tube was made from plexiglas. There were two pairs of windows for optical diagnostics along the stainless steel working channel and eight quartz or MgF₂ optical windows, each 20 mm in diameter, in the dielectric section. The metal end plate of the tube served as a high-voltage electrode. The grounded steel section of the shock tube comprised as a second electrode.

A nanosecond discharge was initiated at the instant at which the reflected shock wave arrived at the observation point. It is important to our measurements that the gas temperature and the composition of the mixture did not vary in the diagnostic cross section from the instant of shock wave arrival to the instant of plasma production. Therefore, the discharge was initiated shortly after the passage of the shock wave through the diagnostic cross section. The high-voltage generator provided a starting voltage in the range 100–160 kV with a rate of voltage rise of tens of kilovolts per nanosecond. The discharge front propagated from the high-voltage electrode with a high velocity (10^9 – 10^{10} cm/s). The discharge closed to the stainless steel section of the shock tube, the interelectrode distance was about 20 cm.

The shock wave velocity was measured by the Schlieren systems, which consisted of He–Ne lasers mounted at different points along the shock tube and photodiodes. The gas number density (n_5), pressure (P_5), and temperature (T_5) behind the reflected shock wave were determined using the initial gas mixture composition, initial pressure, and velocity of the incident shock wave.

The emission generated during combustion was monitored in the direction perpendicular to the shock tube axis at a distance of 55 mm from the end plate with the help of an MDR-23 monochromator (1.2 nm/mm, 1.2-m focal length, 1200 groove/mm, manufactured by LOMO), an FEU-100 photomultiplier (PMT) manufactured by MELZ, and a Tektronix TDS 3054 oscilloscope. A vertical 2×20-mm² slit was installed on the optical window. The ignition delay time was obtained using the OH emission at 306 nm or CH emission at 431 nm. The delay time was determined as the time between the Schlieren signal, which corresponds to the arrival of the reflected shock wave at the diagnostic cross section, and the onset of the leading front of the emission. The onset was defined as the tangent to the emission intensity–time curve at its maximum slope.

The system for monitoring electric parameters of the nanosecond discharge included a magnetic current gauge measuring the discharge current and capacitance gauges located at two different points along the discharge section and measuring the shape and amplitude of the high-voltage pulse. The gauges were calibrated with a high-voltage signal of known amplitude and duration. The signals from the gauges were displayed using a Tektronix TDS 3054 oscilloscope. All cables were extra shielded and the oscilloscopes were placed in a Faraday cage to reduce high-frequency electric noise.

In addition to standard scheme, the laser absorption diagnostics has been arranged. Fig. 8.2 represents typical experimental scheme without details of synchronization. Scheme with a reference beam has been used for OH absorption measurements.

8.2.2 Laser system: general description

CW dye jet laser “AMETIST-03” (Novosibirsk, Russia) was used as a radiation source for absorption measurements. The resonator of a laser has been modified, intra-cavity

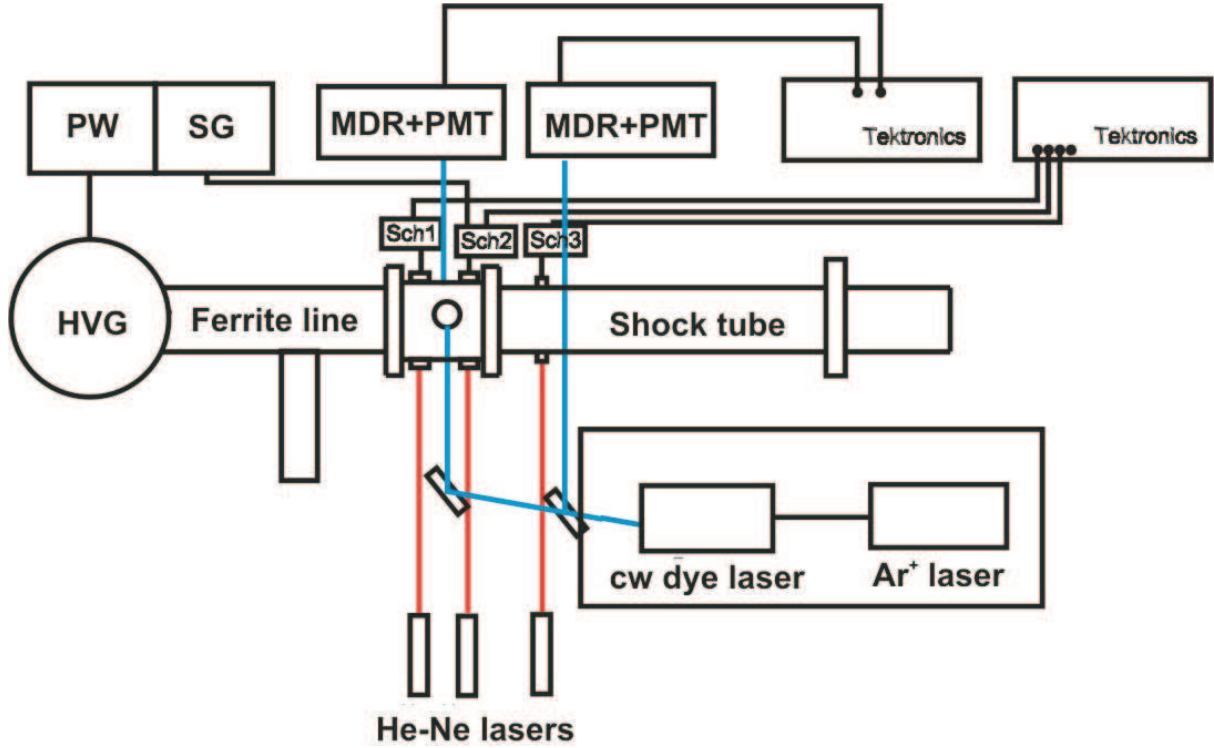


Figure 8.2: Experimental setup and absorption diagnostic scheme. HVG: high-voltage generator, MDR+PMT: monochromator and photomultiplier, SG: synchrogenerator, PW: power supply, Sch1, Sch2, Sch3: Schlieren-systems.

frequency doubling has been used to get a wavelength of ~ 300 nm. Ar^+ laser LGN-402 (L'viv, Ukraine) has been used as a pumping laser. The generation wavelength for Ar^+ laser was 457.9–514.5 nm, peak power output was about 4 W.

The AMETIST dye cw laser is based upon the simple linear cavity, which is characterized by the low threshold generation, and relatively easy cavity alignment. Quartz nozzle of the laser provides high dye jet quality (with respect to stability, flatness and homogeneity). The nozzle mount has an additional channel for spilled dye, preventing dye spilling at the moment of start or shut-down. Dye flow system is made of stainless steel and synthetic materials not interacting with the laser dyes and the solvents. The filter, the heat exchanger (jacket cooling) and the smoother (air buffer) are combined in one device. The dye flow system provides a high dye jet velocity, up to 15 m/s and higher to the turbulence threshold. The scheme of the dye flow system is given by Fig. 8.3.

The dye laser is based on 3-mirror cavity with a flat out-coupling mirror. One 3-plate birefringent filter (Lyot Tailor's filter) and two quartz thin etalons are used for frequency selection in the wavelength range 520–780 nm (see Fig. 8.4). The generation threshold for dye laser is about $P_0 = 2$ W of pumping radiation, steady frequency selection with all the selectors was possible at $P_0 = 3$ W and higher.

We used Rhodamine 6G solution in ethylene glycol, the solution (maximum volume of the solution is up to 1.2 l, and the total volume of the dye flow system reservoir is 2 l) was prepared in the following way: (i) 1.0 g of Rhodamine 6G was solved in 50 ml of ethyl alcohol; (ii) the solution was mixed with 0.95 l of ethylene glycol.

To adjust the frequency doubling system, we first obtained typical power dependencies

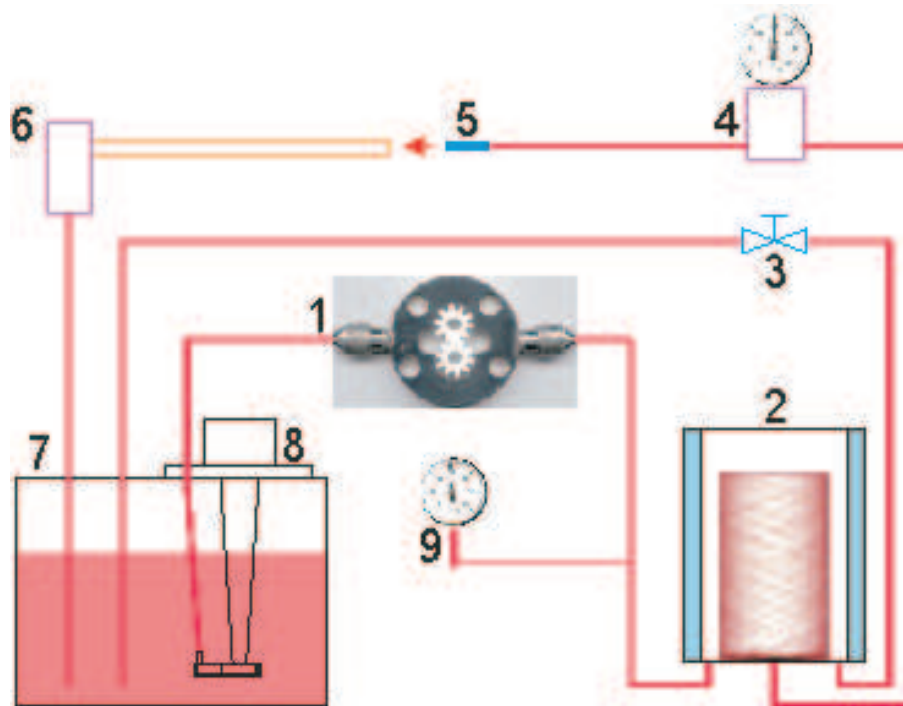


Figure 8.3: Scheme of the dye flow system of cw laser. 1: gear-type pump, 2: dampener-filter-heat exchanger, 3: by-pass valve for the actuating pressure adjustment, 4: auxiliary dampener, 5: quartz nozzle, 6: downcomer, 7: reservoir, 8: rotary mini-pump (hydro-starter), 9: pressure gauge. The dye flow system is powered by 380 VAC, 50 Hz, 3-phases.

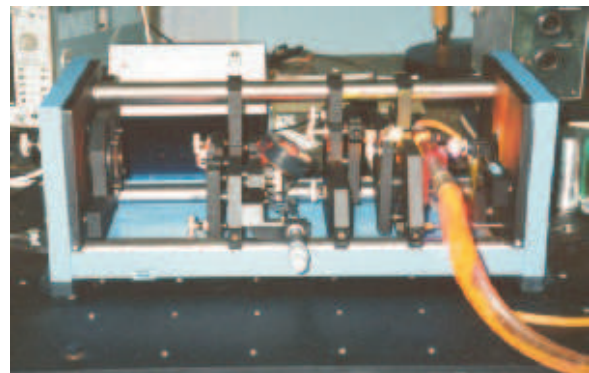
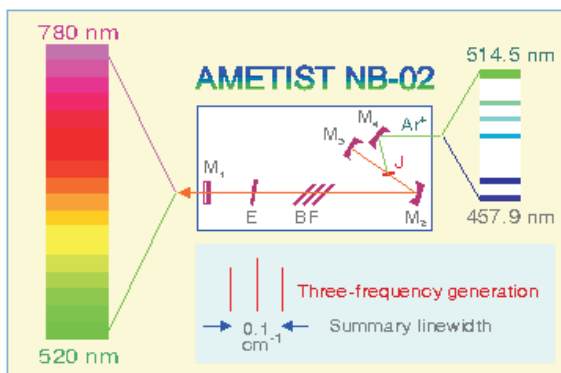


Figure 8.4: Scheme of the AMETIST dye cw laser (Tekhnoscan, Novosibirsk, Russia) and photo of the laser.

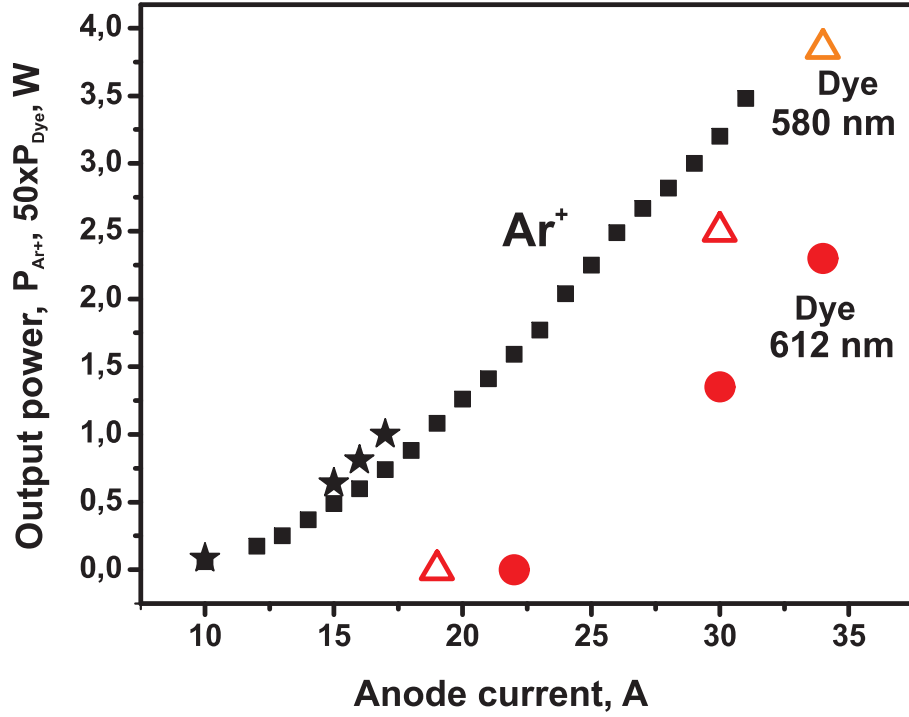


Figure 8.5: Output laser power *vs* anode Ar⁺ laser current.

for dye laser in visible range of spectrum (575–625 nm). Output Ar⁺ laser power and output dye cw laser power *vs* Ar⁺ laser current are given in Fig. 8.5. The data were obtained using IMO–2 power meter. The data are given for two wavelengths of the dye laser: 600 nm and 614 nm in 3–mirror configuration of the cavity. At Ar⁺ laser power 4 W (corresponds to anode current of 34 A) we obtained 77 mW for yellow region of spectrum ($\lambda = 580$ nm) and 46 mW for red one ($\lambda = 612$ nm). It should be noted that at second harmonic frequency (UV range of spectrum) without additional selectors we obtained about 3 mW.

To generate UV-light, the cavity has been supplied with two additional mirrors and nonlinear BBO crystal. Photo of external part of the cavity is given in Fig. 8.6. For the convenience of adjustment, all the mirrors and crystal are mounted on separate 3D-holders. This allows easy re-adjusting of the laser with UV-doubling system to standard 3–mirror dye configuration. In spite of decrease of the total transmission coefficient for the first harmonics from 4.5 % to 0.5 %, the re-adjustment of the cavity resulted in somewhat decrease of Q-quality. As a result, the threshold of generation increased by 10–20 %. In our opinion, this fact is mainly connected with the losses because of the reflection from the BBO crystal edges.

Beta Barium Borate (BBO) was used as a doubling crystal. The crystal had dimensions of $5 \times 5 \times 10$ mm, and it was optimized for 300 nm. To use this crystal for generation of UV-light corresponding to OH absorption (~ 300 nm), we had to rotate the crystal at an angle $\sim 10^\circ$.

Photomultipliers FEY–100 (MELZ, Moscow, spectral sensitivity region is 200–800 nm, response time is 2 ns) were used as detectors of UV-light. The photomultipliers were connected to exit slits of monochromators MDR–23 (LOMO, St. Petersburg, 1.2 nm/mm,

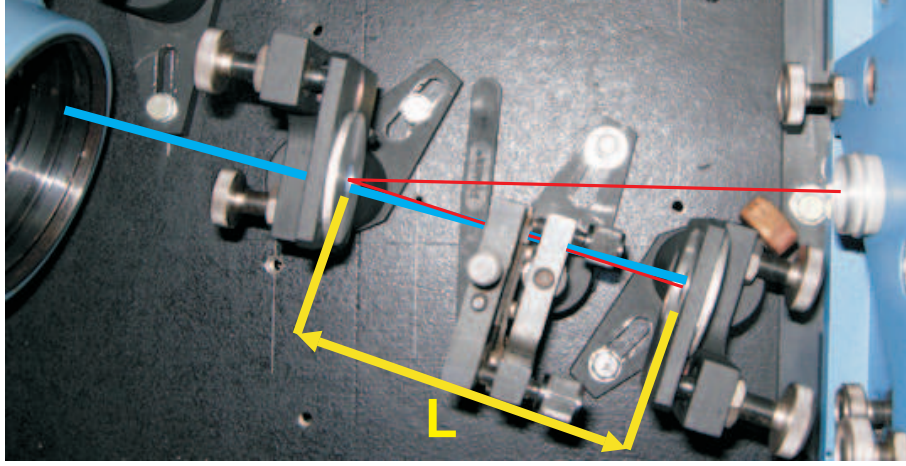


Figure 8.6: Photo of the external part of dye laser cavity (doubling system)

grid 1200 s/mm). Laser beam was split into two beams by means of the beam splitter, and the scheme with a reference beam was used. During the adjustment procedure reference beam was directed to CCD high resolution spectrometer (see description below), and during the experiments the beam was directed to the entrance slit of the the MDR-23 monochromator and used as a reference signal.

8.2.3 Analysis of available diagnostic techniques

The peculiarities of experimental setup allow using different techniques for measurements of OH radicals density. Two of them, namely laser induced fluorescence (LIF) and laser absorption, have been analyzed. To obtain OH radicals density *vs* time under conditions of a single-shot shock tube experiment, we have to use cw laser radiation. The output of used laser system in UV-range does not exceed $W_{las} = 3$ mW.

For laser induced fluorescence, the efficiency of conversion of the pumping UV laser radiation into fluorescence has to be taken into account. Let us assume that this value does not exceed $\alpha = 0.1$ %. Further, the gas density behind the reflected shock wave in considered experiments is equal to $(2 - 8) \times 10^{18} \text{ cm}^{-3}$. This means that quenching of OH* radicals should to be considered. The radiative lifetime of OH radical (OH($A^2\Sigma^+ \rightarrow X^2\Pi$ 0-0 R1(4)) transition) is is $0.77 \mu\text{s}$ [62]. Typical quenching coefficients depend strongly upon the quencher: for example, it equals to $0.92 \times 10^{-10} \text{ cm}^3/\text{s}$ for H_2 molecule, and $5 \times 10^{-10} \text{ cm}^3/\text{s}$ for H_2O molecule [63]. In any case, the quenching will result in significant decrease of fluorescence emission: $\beta \sim 0.1 - 0.01$.

It is the most important in our case, that the aperture of the optical window restricts significantly the fluorescent light collection (see Fig. 8.7 for more detailed explanation). The following part of fluorescence can be collected: $\phi = (\pi \cdot (1.2 \text{ cm})^2) / (4\pi \cdot (9 \text{ cm})^2) = 6 \cdot 10^{-3}$.

Finally, the output of fluorescence signal can be estimated as

$$W_{fl} = \alpha\beta\phi W_{las} = 0.1 \times 0.01 \times 6 \cdot 10^{-3} \times 3 \cdot 10^{-3} = 1.8 \times 10^{-8} \text{ W}$$

For FEY-100 photomultiplier, the spectral sensitivity of the photocathode is $K = 2 \cdot 10^{-2} \text{ A/W}$. Thus, the cathode current does not exceed $I_c = KW_{fl} = 4 \times 10^{-12} - 4 \times 10^{-11} \text{ A}$,

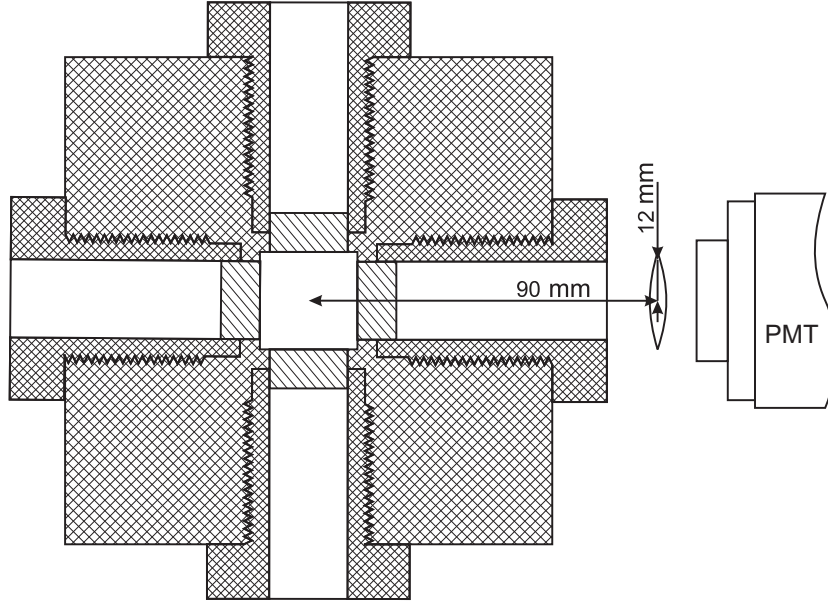


Figure 8.7: Schematic view of the cross-section of the discharge cell (the last section of the shock tube).

and, taking into account that the gain of FEY-100 photomultiplier is $G \sim 10^6$, we obtain finally for anode current $I_A = GI_c = 4 - 40 \mu\text{A}$. Taking into account that the signal-to-noise ratio would be too high under the measurements, we decided not to use LIF technique and to concentrate on absorption measurements.

It should be noted here that the stability of UV radiation was moderate: the deviations in the millisecond time scale were up to 20 %, and in the microsecond scale up to 10 %, respectively. Maximum estimated absorbance was about 20 %. As a result, we decide to use absorption diagnostic scheme with a reference beam.

8.2.4 Laser system: description of doubling system

The detailed scheme of the dye with doubling system is given in Fig. 8.8. Pumping Ar^+ laser radiation was focused by a 50 mm curvature spherical mirror on the dye jet.

In standard configuration of AMETIST-03 dye laser, the cavity consists of three mirrors, M1, M2, and M3. Inside the resonator, radiation is selected by Lyot Tailor's filter (rough selection) and thin quartz etalon (fine selection) of 0.5 mm in width. Minimal linewidth reported by customer in the configuration with two thin etalons is 15 MHz.

Modification of the cavity of dye laser to obtain UV radiation was made with the help of two additional mirrors M4 and M5, which were mounted instead of flat output mirror M3. Between M4 and M5 mirrors, in the focal point between them, the BBO crystal was installed. So, finally, the 3-mirror optical cavity was replaced with 4-mirror one with nonlinear optical element (BBO crystal). This allowed generation of UV radiation at wavelength $\lambda \sim 307 \text{ nm}$, corresponding to OH radical transition ($X^2\Pi \rightarrow A^2\Sigma^+, 0-0$). On the other hand, this changes laser radiation parameters, in particular the line width. For our task, it was critical to know the laser line width, so, the additional analysis has been made to compare line widths of laser radiation and width of absorption coefficient

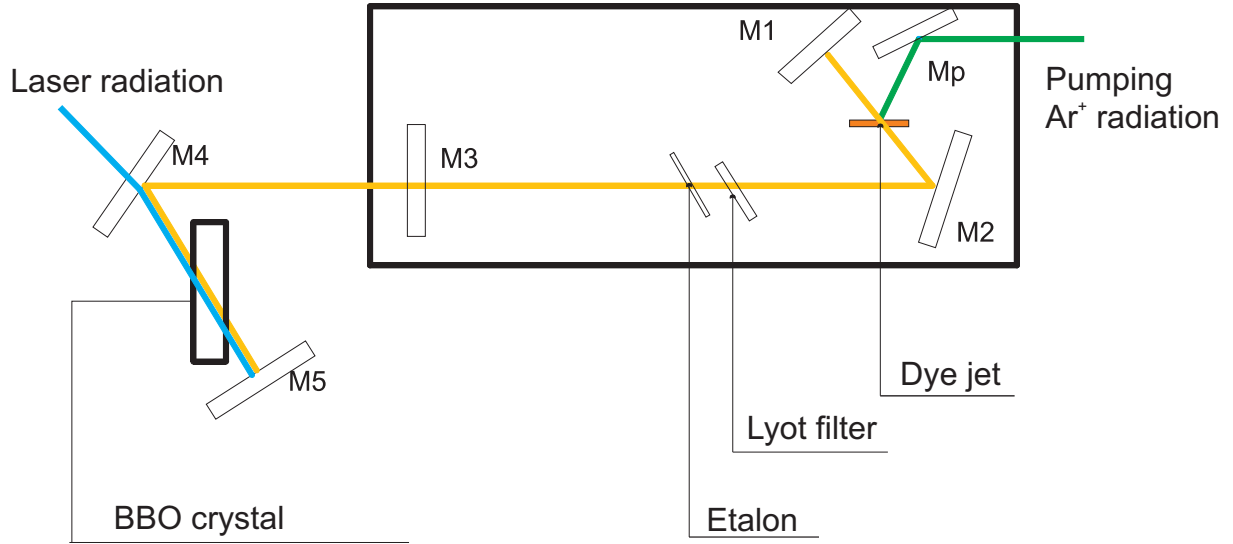


Figure 8.8: Scheme of optical part of AMETIST-03 dye laser.

profile.

Alignment of doubling system

It was necessary to propose relatively simple and stable scheme of alignment of the external laser cavity. It is known from the theory of optical cavities that any optical cavity with non-distributed parameters can be replaced with two-mirror cavity with the same optical properties [64]. The typical stability diagram for two-mirror cavity is given in Fig. 8.9. It is possible to select two regions of stability in coordinates $(1 - L/R_i)$ (here L is a distance between mirrors and R_i is a curvature radius of the i -th mirror) with the single common point. At the negative values of $(1 - L/R_i)$ the cavity properties correspond to concentric cavity ones, and at the positive values of $(1 - L/R_i)$ they correspond to a flat resonator. Taking into account that concentric cavities are more steady at small mechanical displacements, the distances between the mirrors in 4-mirror scheme were taken from the “negative” stability region (marked with a pink circle on the scheme).

Disposition of the mirrors was arranged so that both 3-mirror cavity with a flat output mirror (visible emission generation) and 4-mirror modified laser cavity (visible emission generation) were in the region of a stable generation. This allowed easy replacement of the mirrors during the alignment procedure. After obtaining a stable generation in yellow light in 3-mirror configuration, the output flat mirror is removed. As a result, we obtain the generation in visible range and UV-range of spectrum in modified 4-mirror cavity.

Alignment of laser frequency

As it was mentioned, we use different optical elements for selection of laser radiation in jet dye laser cavity. Rough adjustment is provided with Leot filter. This filter allows selection of a laser line in all the spectral range of dye generation, and the width of the line is 30 GHz. Two Fabry–Perot etalons serve for a fine wavelength selection, their widths are 0.5 and 8 mm, respectively. In our experiments, we used a thin Fabry–Pero etalon only because of unacceptably low output of the UV emission with two etalons. Thin

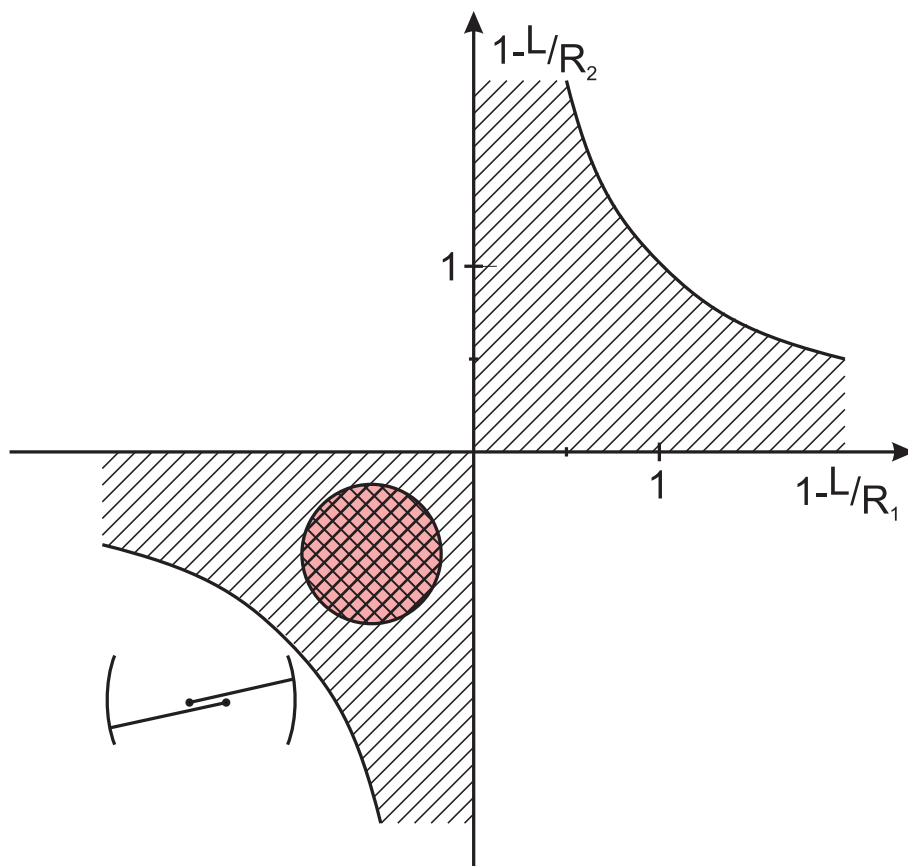


Figure 8.9: Scheme of stability regions of a laser cavity.

etalon provides 3–5 GHz line (in yellow) and allows wavelength turning within a range of 0.2 nm.

When working in 4-mirror scheme, we adjusted second harmonic frequency in two steps. First, we looked for the crystal angle, at which the emission at $\lambda = 300$ nm is maximal (the available crystal was optimized on 300 nm doubling). After this, we aligned roughly the resonator to obtain emission at $\lambda = 614$ nm without losing doubled frequency emission at $\lambda = 307$ nm. To reach the maximal efficiency of the frequency doubling, it is necessary to satisfy wave synchronism condition. That is why, during the alignment, we rotate the crystal smoothly, compensating the changes in alignment by rotating of the external mirror. The wavelength $\lambda = 307$ nm corresponds roughly to rotational lines of $\text{OH}(\text{A}^2\Sigma^+ \rightarrow \text{X}^2\Pi \ 0-0)$ transition. At this step, we measure the emission wavelength in UV with the help of CCD spectrometer. Spontaneous emission from a test propane–butane flame of a commercial burner is focused onto the entrance slit of the same spectrometer. Doing this, we compare rotational OH spectrum with a position of a laser line with an accuracy of about 0.5 Å, and this accuracy is not enough to adjust the coincidence of laser light and absorption profile.

The second step is a fine alignment to get the coincidence of the laser line and absorption profile. At this stage, we mount the thin etalon into the cavity, and use only this etalon for the adjustment. To guarantee the single-mode operation of the thin etalon we use qualitative control of the interferometry pattern obtained from an additional Fabry–

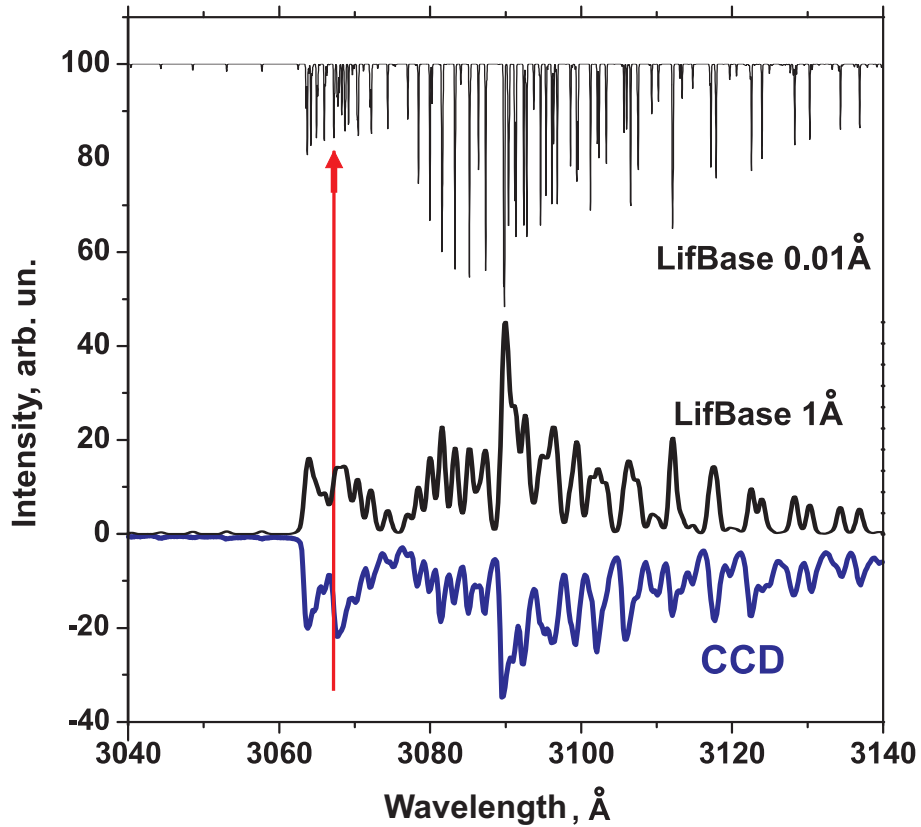


Figure 8.10: Experimentally measured OH emission spectrum (blue curve) and numerically simulated OH emission spectra (black curves) with different spectral resolution.

Perot interferometer placed into the main harmonic laser beam reflected from the dye jet (parasitic laser light). The intermode distance of this additional interferometer is equal to 1 cm^{-1} , this allows resolution of adjacent modes of the thin etalon in the laser cavity and fine adjustment of the wavelength of UV laser radiation.

Finally, we prove the coincidence of laser wavelength and absorption profile of rotational line of OH spectrum detecting a sharp decrease of the laser beam which cross the flame of the test burner. The decrease is registered by photomultiplier with monochromator, that is by the same diagnostic system which is used in real experiments for OH density measurements. To illustrate the position of the laser radiation against OH rovibrational spectra, we plot (see Fig. 8.10) the OH emission obtained experimentally with superposed laser emission, and results of the numerical modelling of the emission using LIFBASE code [65] with the resolution close to Doppler broadening at the temperature 1500 K. The transition $\text{OH}(\text{A}^2\Sigma^+ \rightarrow \text{X}^2\Pi \text{ } 0-0 \text{ } \text{R1}(4))$ is marked with an arrow.

8.3 Analysis of the overlap of absorption and emission profiles

8.3.1 Analysis of absorption profile of OH radical

Two broadenings are the most important for OH absorption spectrum: Doppler broadening and pressure collisional broadening. Doppler broadening leads to Gaussian line shape, the width on the half-height being equal to

$$\Delta\omega = \sqrt{\frac{8RT}{\pi\mu}} \cdot \frac{1}{c\lambda}, \quad (8.1)$$

where μ is an OH molecular weight, being equal to 17 g/mole. At the wavelength $\lambda = 300 \text{ nm}$, and temperature $T = 1500$, that is at the conditions typical for our experiments, the Doppler broadening is equal to 0.15 cm^{-1} ($1.36 \cdot 10^{-3} \text{ nm}$).

Being broadened by collisions, the spectral line has Lorentz shape. Papers [66, 67] report experimentally measured collisional broadening for the OH line under study for different pressures. Experimentally obtained plot gives a linear dependence, collisional broadening at a pressure of 0.5 atm (typical for our gas densities under the recalculation taking into account the difference in gas temperatures) is equal to 0.18 cm^{-1} ($1.62 \cdot 10^{-3} \text{ nm}$).

Thus, the finally obtained line shape is a result of Doppler broadening and pressure broadening, the width of the resulting Voigt lineshape is 0.23 cm^{-1} ($2.01 \cdot 10^{-3} \text{ nm}$).

8.3.2 Analysis of spectral width of UV laser light

Laser spectrum is a set of equidistant lines, which correspond to different longitudinal modes of the laser cavity. The number of lines is restricted by a shape of the generation line, which is determined by (i) width of the spectrum of generation; (ii) spectral parameters of intracavity selectors. The width of the lines is determined by a Q-quality of the resonator. For the analysis we assume that the intensity of a laser generation does not

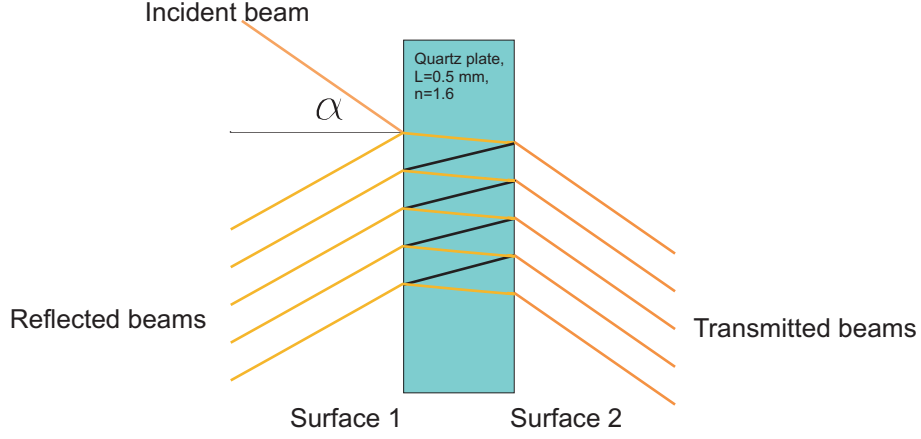


Figure 8.11: Scheme of laser beam transmission through Fabry-Perot etalon.

depend upon frequency within the range of 3×10^{15} Hz — 3.2×10^{15} Hz, and the Liot filter selects from the considered range the line with the width equal to 35 GHz.

Let us consider the amplitude envelope of the spectrum which is determined by Fabry-Perot thin etalon (thin quartz plate) with the width of $L = 0.5$ mm and refraction coefficient $n = 1.6$. Reflection coefficient for the surfaces of etalon is equal to $r = 0.25$, the degree of the etalon inclination in respect to the laser beam is equal to α . The plane polarized mode wave $E(t)$ with the spectral width of 35 GHz goes through the Fabry-Perot thin etalon:

$$E(t) = E_0 e^{i(\omega t - \frac{2\pi L n}{\lambda})}$$

We derive the intensity of the transmitted radiation upon the frequency of incident radiation. When the beam goes through the etalon, we consider partial reflection and passing through. As a result, the wave is splitting to two waves with the ratio of amplitudes determined by refraction and transmission indices (see Fig. 8.11 for illustration).

Finally, the infinite number of beams will go out from the interferometer, reflected from the surface 2 and passing through the surface 1. The amplitude of the i -th beam will depend upon the number of re-reflections:

$$E_i = (1 - r)^2 r^{2i} E_0 \exp \left(i \left(\omega t - 2(i + 1) \frac{2\pi L \cos(\frac{\alpha}{n})}{\lambda} \right) \right)$$

Total amplitude of the transmitted line is calculated as the sum of the amplitudes of all the beams:

$$\begin{aligned} E(\omega, t) &= \sum_{i=0}^{\infty} (1 - r)^2 r^{2i} E_0 \exp \left(i \left(\omega t - 2(i + 1) \frac{2\pi L \cos(\frac{\alpha}{n})}{\lambda} \right) \right) = \\ &= \frac{(1 - r)^2}{1 - r^2 \exp \left(-i \left(\omega t - \frac{4\pi L \cos(\frac{\alpha}{n})}{\lambda} \right) \right)} \times \exp \left(i \left(\omega t - \frac{4\pi L \cos(\frac{\alpha}{n})}{\lambda} \right) \right) \end{aligned}$$

The intensity of the transmitted light is equal to

$$I(\omega) = EE^* = I_0 \frac{1}{1 + \frac{4r^2}{(1-r^2)^2} \sin^2(L \cos(\frac{\alpha}{n}) \omega / c)} \quad (8.2)$$

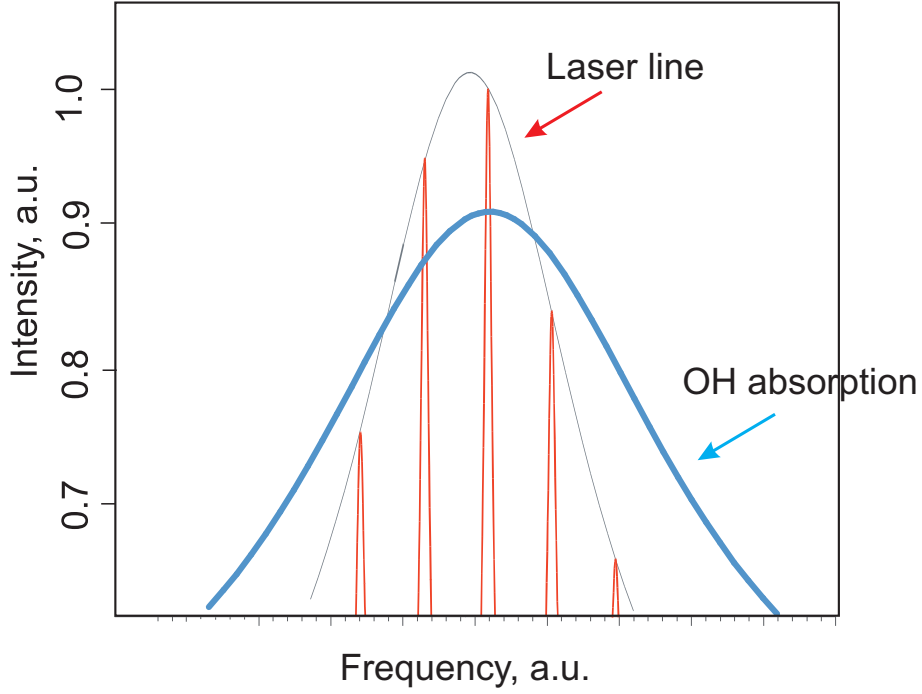


Figure 8.12: Overlapping of laser line and OH absorption.

Equation (8.2) describes the amplitude envelope of the laser emission. The width of the envelope at the half-height is equal to (in GHz):

$$\Delta\omega = 5.4\cos(\alpha n)$$

Thus, when the angle between Fabry–Perot selector and the cavity axis is equal to Brewster angle, the width of the generation line is approximately equal to 3 GHz (0.1 cm^{-1} , or $0.7\cdot 10^{-3}\text{ nm}$) in the visible range. The frequency doubling depends quadratically upon the laser light intensity, so, for UV-range of spectrum the line width will be 1.41 times more narrow.

Narrow lines are selected by the cavity inside the envelope. Intermode distance for the cavity can be estimated assuming that geometrical length (1.5 m for 4-mirror cavity) is equal to optical one. Assuming this, we neglect all the optical elements with the refraction coefficients $n > 1$. From the standing wave conditions, we obtain $\Delta\omega = 2\pi\cdot c/L \approx 1.2\cdot 10^9\text{ Hz}$. Thus, at the amplitude envelope width 5 GHz, we have 5 lines in the spectrum. They are separated by a distance of 1.2 GHz (10^{-4} nm).

Finally, we conclude that, under our experimental conditions, the spectral width of the the laser spectrum is smaller than the width of the absorption profile of OH radical, the ratio between their widths is equal to 3–4. This means that the spectral distribution of the laser light has not to be taken into account when calculating the absolute absorption coefficient, because all the emitted emission is absorbed by OH radical. Spectra of laser radiation and OH absorption are given schematically in Fig. 8.12. Taking into account that before each experiment we adjusted the spectral position of laser light so that absorption by OH in propane–butane flame was maximal, we assume that for each experiments center of laser line and of OH emission coincided.

8.4 Results and discussion

8.4.1 Experimental data

Table 8.1 summarizes initial parameters for autoignition experiments, while table 8.2 contains initial parameters for the plasma assisted ignition. The experiments were carried out in the stoichiometric $\text{H}_2:\text{O}_2$ mixture diluted with 90 % of Ar. Initial parameters for autoignition and plasma assisted ignition (designated as FIW, or ignition by fast ionization wave) are given in Fig. 8.13.

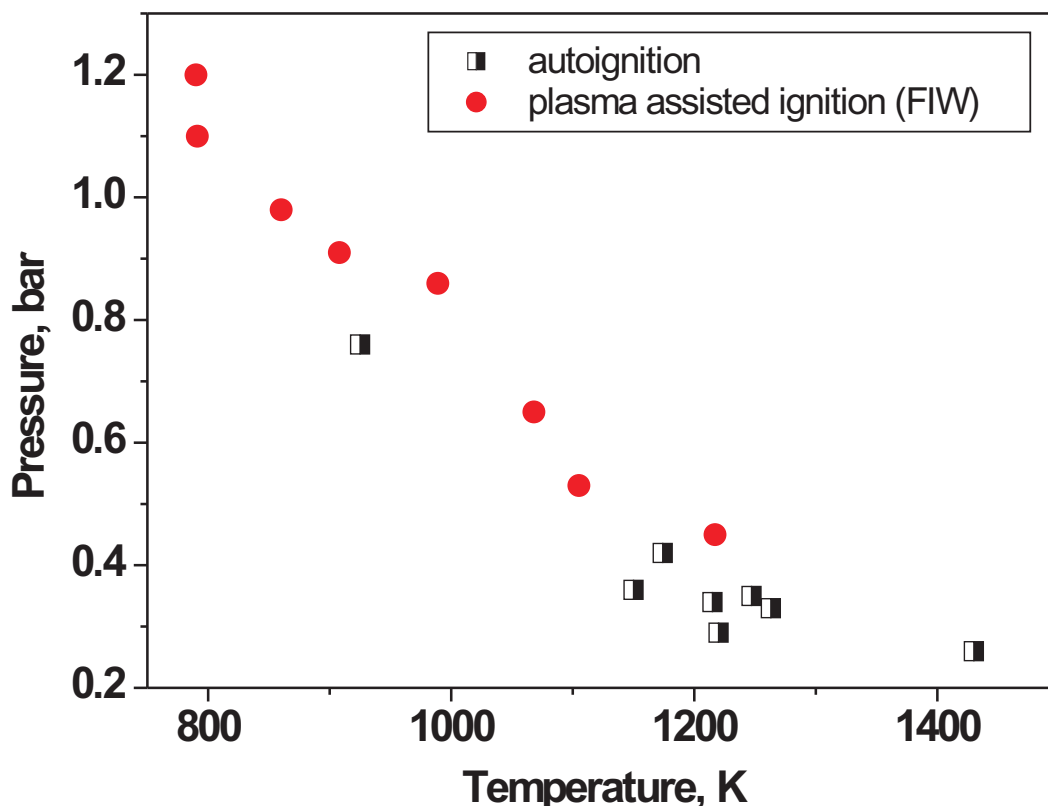


Figure 8.13: $\text{H}_2:\text{O}_2$ stoichiometric mixture diluted with Ar (90 %). Initial parameters of the experiments: pressure and temperature behind the reflected shock wave.

For each experiment, we obtained dependencies of the most important parameters upon time. We controlled (i) three Schlieren signals (they were used to calculate gas temperature T_5 and pressure P_5 behind the reflected shock wave knowing the shock wave velocity and initial gas pressure P_0); (ii) OH emission at wavelength 306 ± 2 nm (the emission was detected in direction perpendicular to a laser beam); (iii) reference UV laser signal at the wavelength $\lambda = 307$ nm; (iv) UV laser signal, passed through the discharge cell.

The experimental data obtained for autoignition are given in Figs. 8.14–8.15. Three positioned in sequence Schlieren systems give three consequent peaks from the incident shock wave. Knowing the distance between the detectors (250 mm between the first and the second He–Ne lasers, and 226 mm between the second and the third ones), it is possible to calculate the shock wave velocity. The third Schlieren system installed in the

Table 8.1: Initial conditions: autoignition experiments.

No exp	T_5 , K	P_5 , bar
1	925	0.76
2	1150	0.36
3	1220	0.29
4	1247	0.35
5	1430	0.26
6	1263	0.33
7	1215	0.34
8	1174	0.42

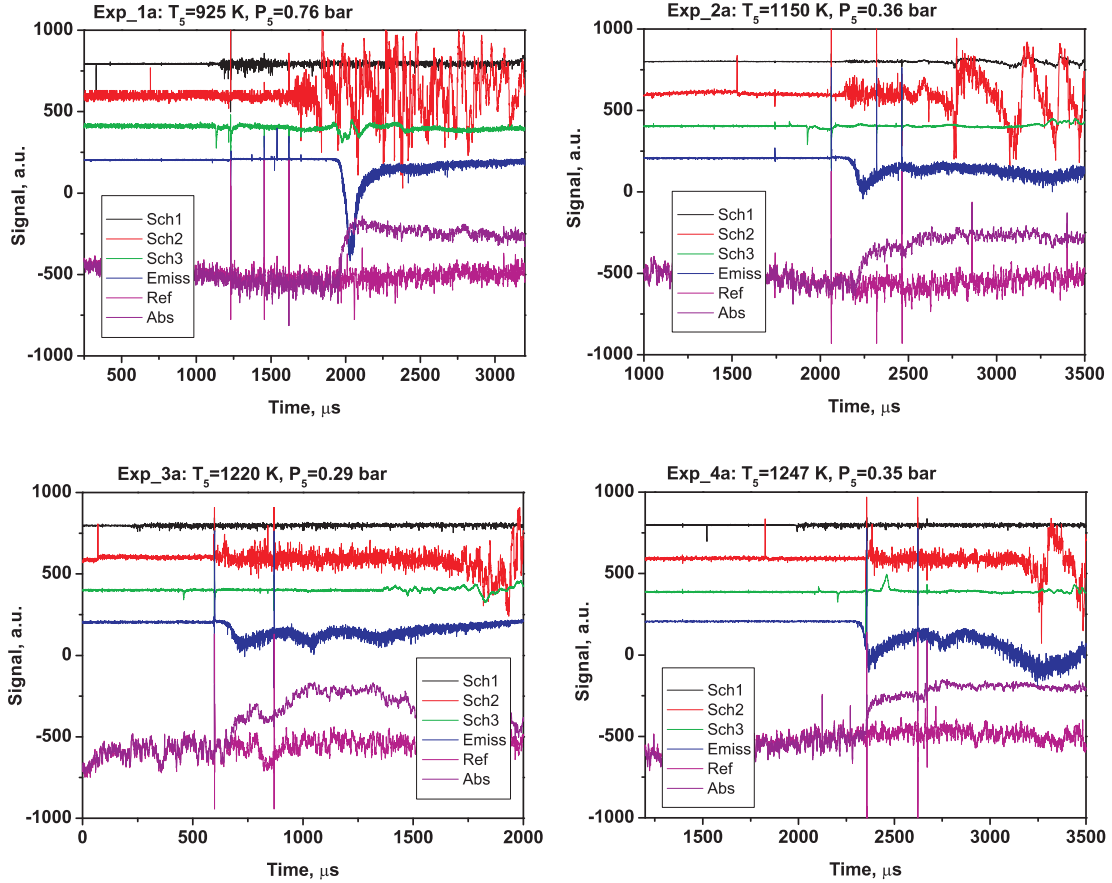


Figure 8.14: $H_2:O_2$ stoichiometric mixture diluted with Ar (90 %). Experimental oscillogramms for autoignition regimes (to be continued). Sch1, Sch2, Sch3: signals from Schlieren systems, Emiss: signal from photomultiplier, $\lambda=306$ nm, Ref: reference laser signal at 307 nm, Abs: absorption of laser radiation at 307 nm.

Table 8.2: Initial conditions: plasma assisted ignition experiments.

No exp	T_5 , K	P_5 , bar
1	1217	0.45
2	1105	0.53
3	1068	0.65
4	989	0.86
5	908	0.91
6	860	0.98
7	791	1.10
8	780	1.20

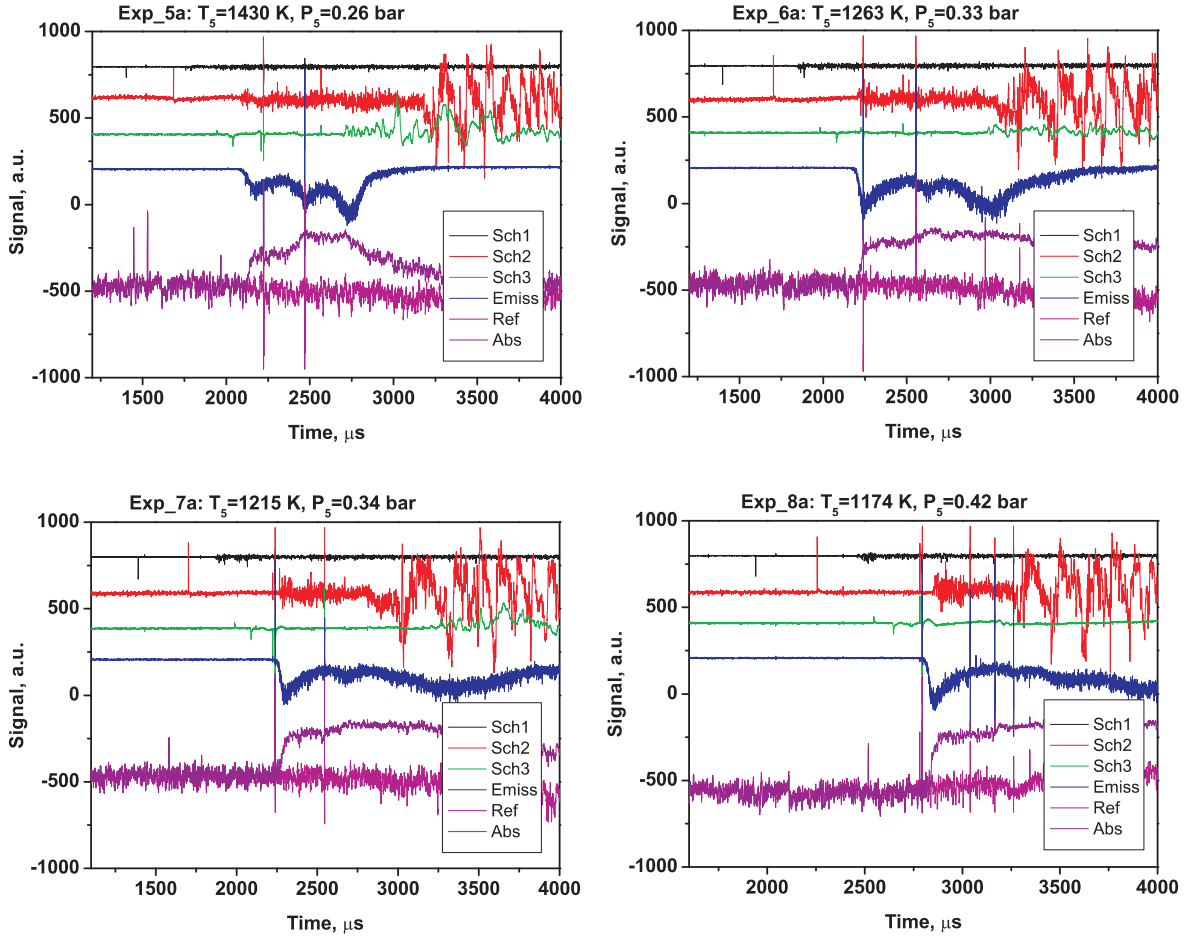


Figure 8.15: $H_2:O_2$ stoichiometric mixture diluted with Ar (90 %). Experimental oscillograms for autoignition regimes.

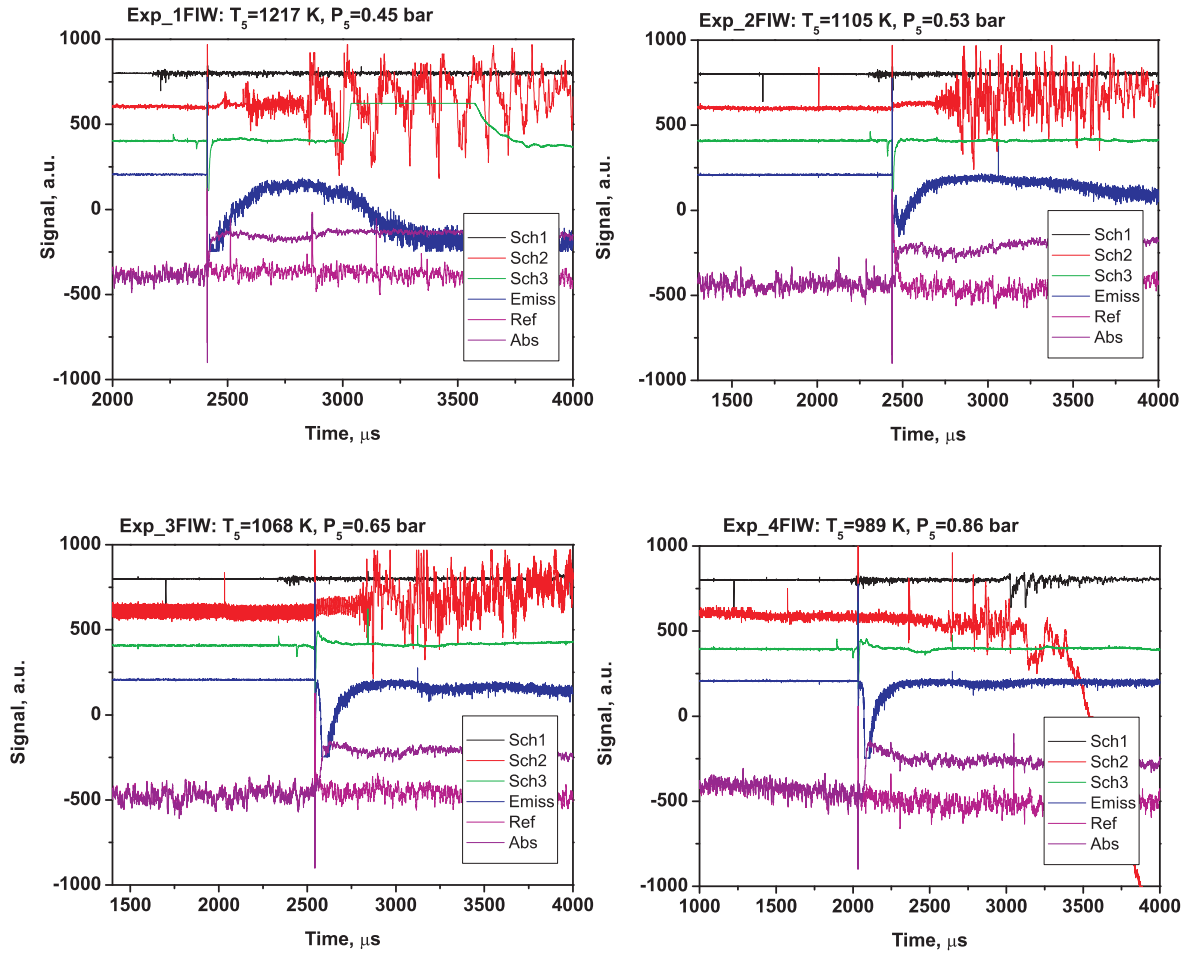


Figure 8.16: $\text{H}_2:\text{O}_2$ stoichiometric mixture diluted with Ar (90 %). Experimental oscillogramms for plasma assisted ignition (to be continued). Sch1, Sch2, Sch3: signals from Schlieren systems, Emiss: signal from photomultiplier, $\lambda = 306 \text{ nm}$, Ref: reference laser signal at 307 nm, Abs: absorption of laser radiation at 307 nm.

cross-section of observation demonstrates also the signal from the reflected shock wave. This is zero-time point for calculation of the ignition delay time for autoignition. It should be noted that shock tube experiments are restricted by the time instant when the contact surface comes to cross-section of observation. For our experimental conditions, this time is typically 400–600 μs , depending upon the initial parameters of the experiments. nevertheless, we give the oscillogramms for longer time. Finally, we provided data treatment for a few hundreds of microseconds only for each experiment. It is clearly seen that absorption by OH radicals in the ground state correlates in time with OH^* emission for all considered regimes.

The experimental data obtained for plasma assisted ignition are given in Figs. 8.16–8.17. The time instant of the discharge initiation is clearly indicated with a vertical line, corresponding to electrical noise. The line is clearly seen in all the oscillogramms. This is zero-time line for calculation of the ignition delay time for plasma assisted ignition.

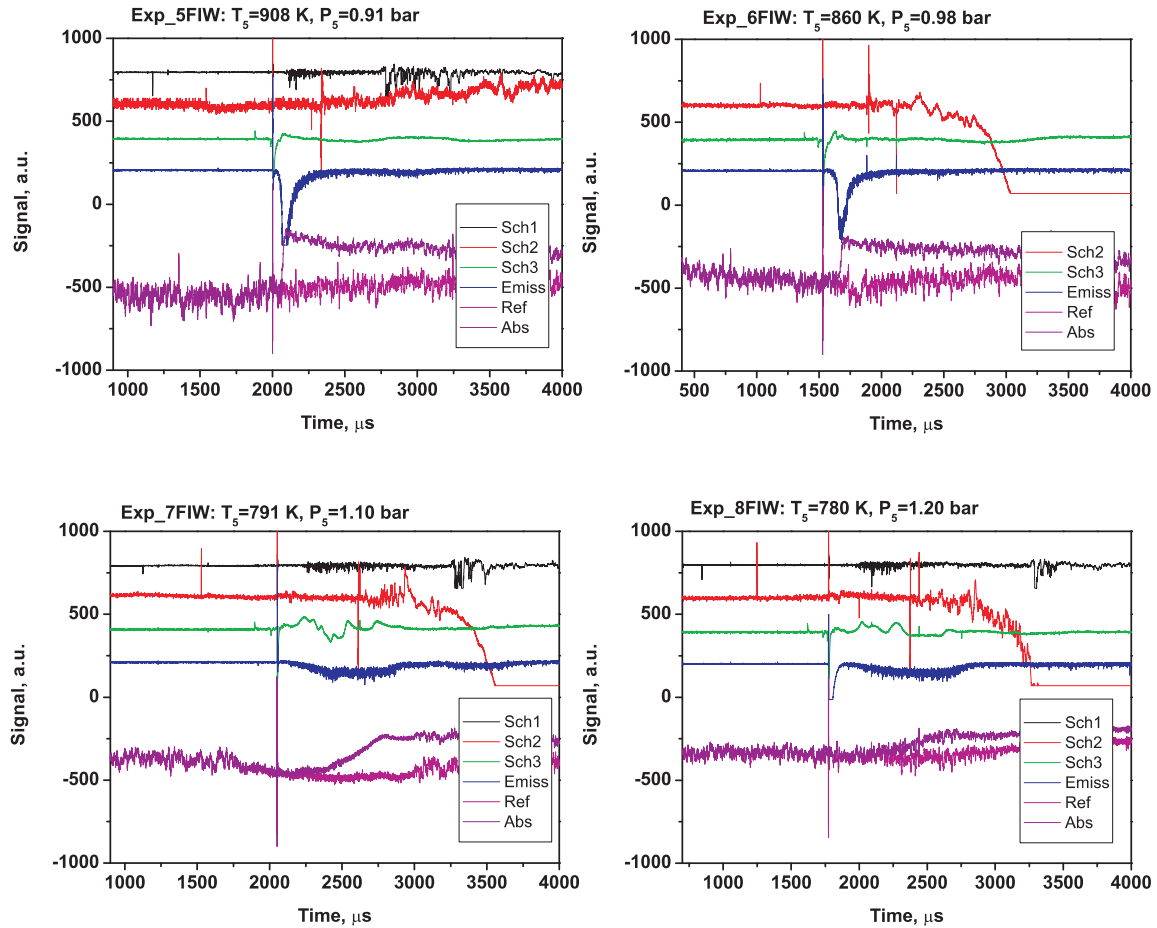


Figure 8.17: $\text{H}_2\text{:O}_2$ stoichiometric mixture diluted with Ar (90 %). Experimental oscillograms for plasma assisted ignition.

8.4.2 Absolute calibration of OH density

The advantage of a shock tube technique lies in the fact that composition of gas mixture can be calculated with a high accuracy for the process of autoignition. We used GRI 1.2 mechanism to model kinetics in the considered mixture. The coincidence between experimentally measured and calculated ignition delay time was rather good. The main idea of the calibration is the following:

- (i) The dependence of OH density as a function of time for autoignition is obtained experimentally (in arbitrary units) for different initial pressures and temperatures;
- (ii) Kinetics in these regimes is calculated, and dependencies of OH density upon time is obtained numerically (in absolute values);
- (iii) The absorption coefficient is calculated for each autoignition regime assuming that OH temporal behaviour obtained experimentally corresponds to measured OH(t) dependence;
- (iv) The dependence of OH density upon time for plasma assisted ignition is obtained experimentally (in arbitrary units) for different initial pressures and temperatures; the data are recalculated to absolute units using the absorption coefficient obtained according to (i)–(iii).

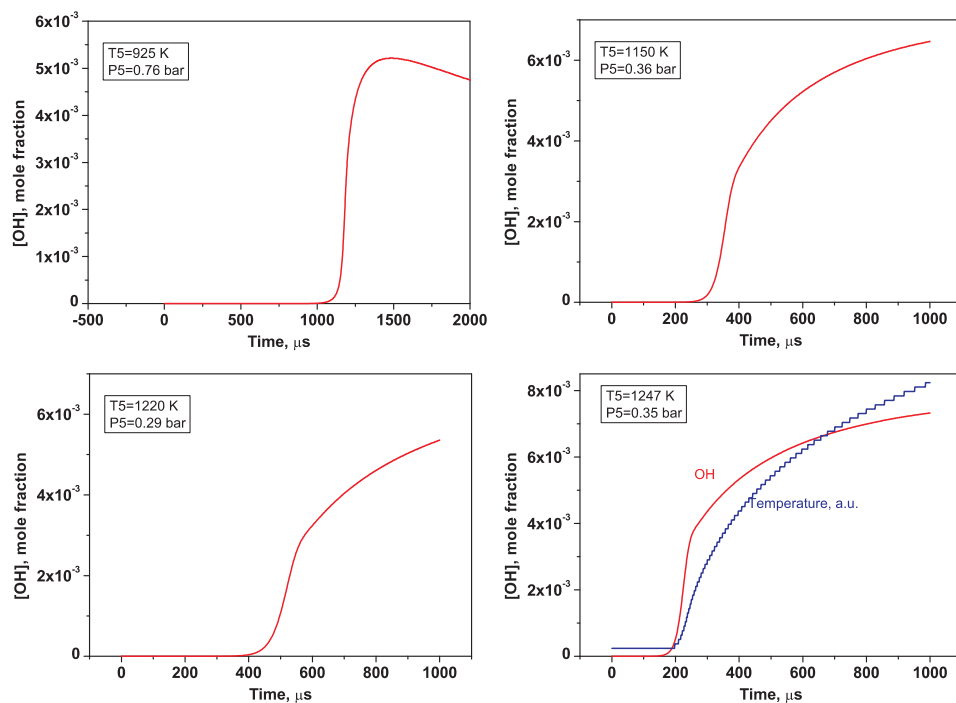


Figure 8.18: H₂:O₂ stoichiometric mixture diluted with Ar (90 %). Calculated OH density upon time for different experimental regimes (to be continued).

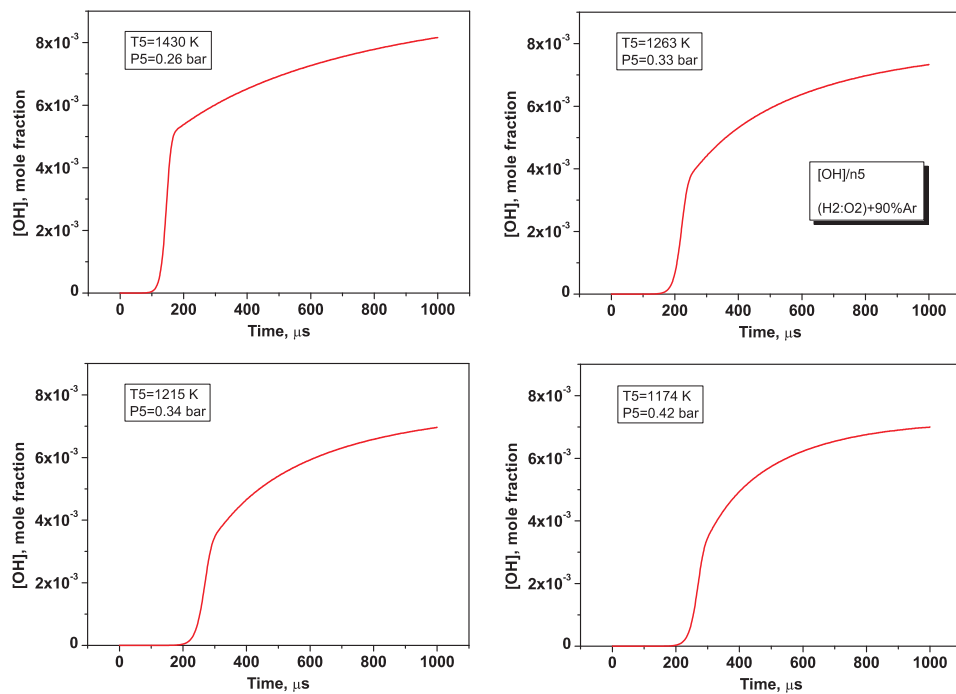


Figure 8.19: H₂:O₂ stoichiometric mixture diluted with Ar (90 %). Calculated OH density upon time for different experimental regimes.

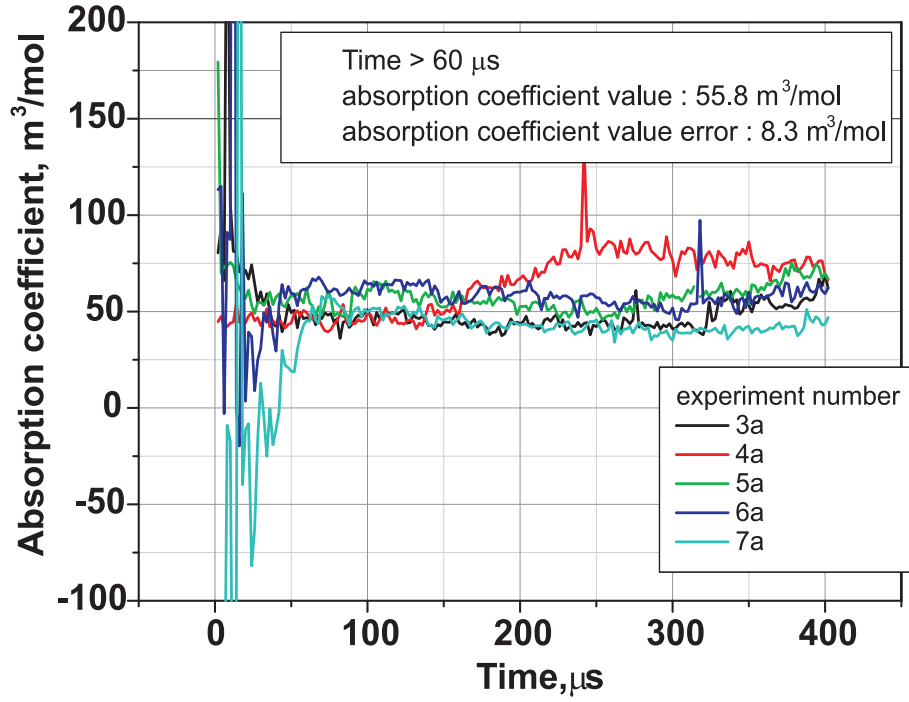


Figure 8.20: Coefficient k obtained from comparison of experimentally obtained $[\text{OH}](t)$ dependence and calculations for the same initial conditions.

To recalculate ratio of transmitted and reference laser intensities into OH density (in arbitrary units) we used Bugger–Lambert law assuming that OH density is distributed uniformly along the cross-section of measurements:

$$\ln \left(\frac{I_0(t)}{I_{\text{abs}}(t)} \right) = l \cdot [\text{OH}](t) \cdot k,$$

where k is an absorption coefficient. Figs. 8.18–8.19 represent calculated OH density upon time for different experimental regimes, and Fig. 8.20 gives the absorption coefficient k calculated for a few experimental regimes. Only the initial part of the experimentally obtained oscillogramms was treated to avoid the problems connected with coming of the contact surface to the observation point. It is clearly seen that the coefficient k is constant with a good accuracy within the investigated range of parameters. The obtained value $k = 56 \pm 8 \text{ m}^3/\text{mole}$ was used to normalize experimentally obtained OH density under plasma assisted ignition experiments.

It should be noted also that, because of relatively small difference in temperature range for autoignition (900–1400 K) and plasma assisted ignition (780–1200 K), we do not expect significant changes in Doppler broadening of OH absorption line. Consequently, all the discussion concerning comparison of absorption and laser emission profile remains valid for the conditions of experiments on plasma assisted ignition.

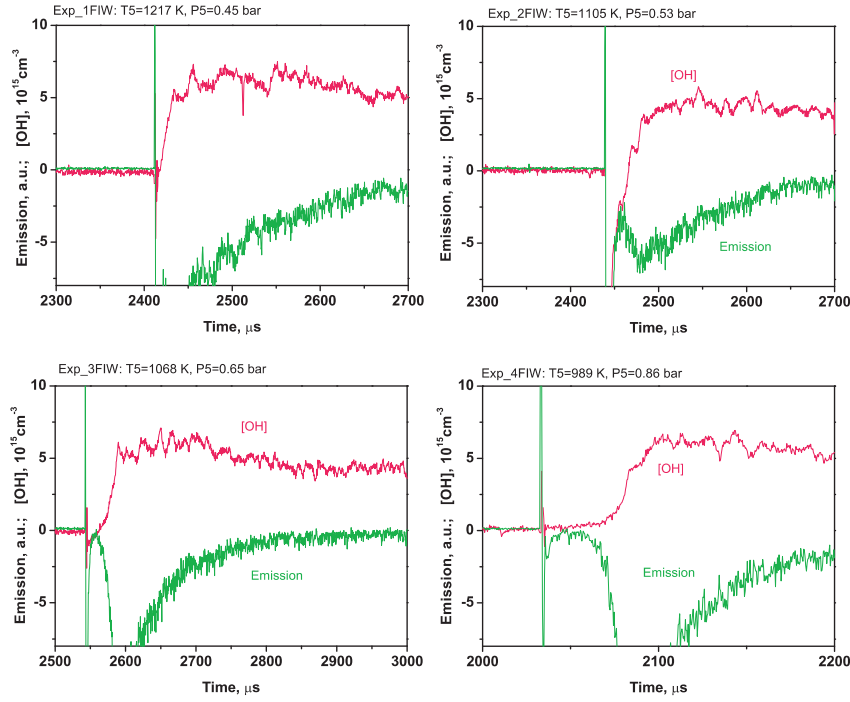


Figure 8.21: $\text{H}_2:\text{O}_2$ stoichiometric mixture diluted with Ar (90 %). Plasma assisted ignition. Measured OH density upon time for different experimental regimes (to be continued).

8.4.3 OH density measurements for plasma assisted ignition experiments

Figs. 8.21–8.22 represent finally obtained dependencies of OH density *vs* time for the conditions of plasma assisted ignition. It is possible to conclude that OH density correlates in time with OH^* emission: OH^* emission peaks at the time instant of a maximum derivative of $[\text{OH}](t)$. Further, OH^* emission decays with time, and this correlates with the well-known statement that OH^* production takes place in the front of ignition due to chemical luminescence reactions.

Let us note that at the moment we measure the behaviour of OH density in the process of the plasma assisted ignition but the sensitivity of the system is not enough to detect $[\text{OH}](t)$ during the ignition delay time. To do this, it is necessary to increase stability of the pumping Ar^+ laser, and to decrease signal-to-noise ratio.

Fig. 8.23 represents the ignition delay times determined on the basis of OH^* emission and OH absorption profiles. The difference which is evident in the case of plasma assisted ignition is explained by a relatively smooth increase of OH density. This effect is especially clearly pronounced for low temperature region where typical time of $[\text{OH}]$ increase reaches hundreds of microseconds (marked with a yellow circle in the Figure).

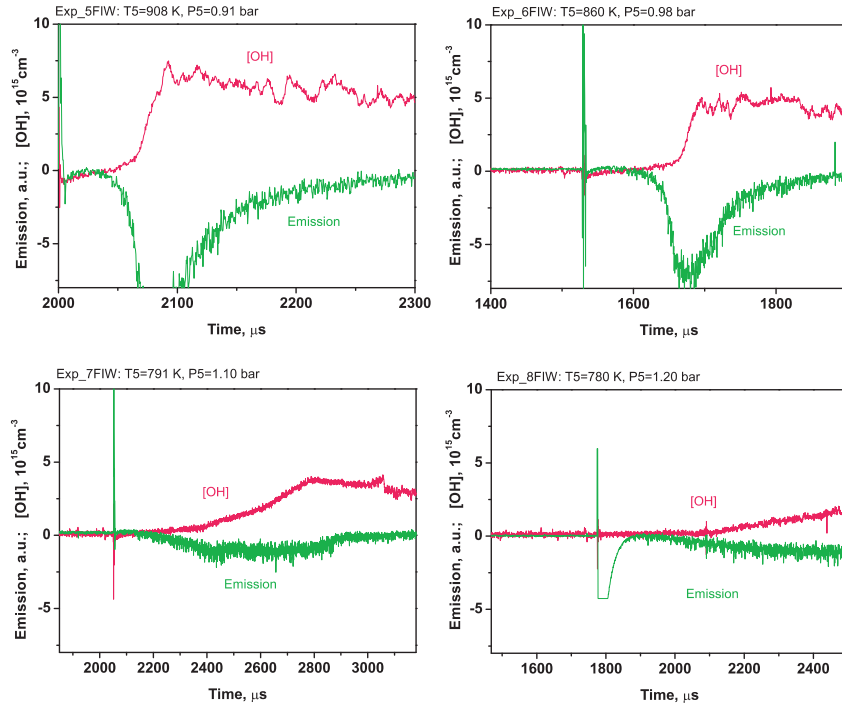


Figure 8.22: $\text{H}_2:\text{O}_2$ stoichiometric mixture diluted with Ar (90 %). Plasma assisted ignition. Measured OH density upon time for different experimental regimes.

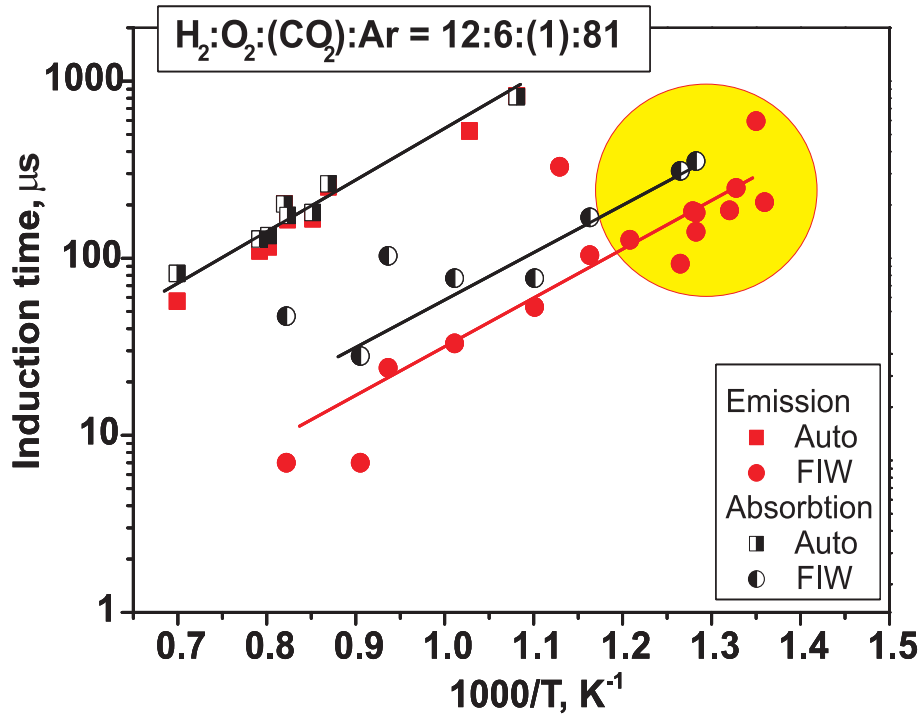


Figure 8.23: Ignition delay time for $\text{H}_2:\text{O}_2:\text{Ar}$ mixture with CO_2 additions. Comparison of ignition delay time determined using OH^* emission and OH absorption profiles.

8.5 Conclusions

Detailed kinetics of intermediates during the ignition delay time has been calculated. Species and techniques were selected to control the process of plasma assisted ignition during the delay time.

The UV laser absorption technique for OH density measurements has been adjusted for the single-shot experiments on plasma assisted ignition. The experiments were carried out in the shock tube combined with the discharge section.

The calibration procedure to obtain absolute values of OH radicals has been proposed and realized. The procedure was based on the autoignition experiments. For these experiments, the calculations of OH density dependence upon time have been made. The results of calculations were compared with the results of the experiments for the same initial pressure and temperature under assumption that OH density distribution is uniform along the axis of measurements. Finally, the absorption coefficient has been determined for the conditions of our experiments.

Behavior of OH radicals density during the process of plasma assisted ignition has been investigated. We received that the $[\text{OH}](t)$ dependencies are in a good correlation with OH^* emission behaviour. OH^* emission peaks at the time instant of a maximum derivative of $[\text{OH}](t)$. A good agreement was obtained between the ignition delay times calculated on the basis of $[\text{OH}](t)$ absorption and on the basis of $\text{OH}^*(t)$ emission.

Chapter 9

Laser Flash-Photolysis and Gas Discharge in N₂O–Containing Mixtures: Kinetic Mechanism

9.1 Introduction

Considerable recent attention has been focused on the study of ignition of combustible mixtures with nonequilibrium plasma. Experiments with high speed gas flows [68, 69], with laboratory and pilot gas-jets [70, 71], with specially designed flow reactors [72] and with shock tubes [36, 38] showed possibilities to extend the range of parameters for combustion and to shorten ignition delay time.

Ignition and combustion, which are sustained by nonequilibrium plasma, are caused by interaction of a number of physical phenomena. In order to give an adequate description of plasma assisted ignition/combustion (PAI/PAC) it is necessary to combine detailed knowledge in gas discharge physics, hydrodynamics, and chemical kinetics, both high-temperature and that taking into account excited and charged particles. Many of these phenomena are rather complicated and have not yet been clearly understood. Available kinetic models of plasma-assisted ignition [73]—[78] are difficult to compare quantitatively with experimental data because of the lack of information about plasma parameters, temporal evolution and spatial distribution of active species, responsible for ignition, etc.

Generally, thoroughly arranged experiments are necessary to gain a profound understanding of the physics of ignition by nonequilibrium plasma. It is very important to divide the discharge impact and combustion process in time or in space; this means that the total duration of the discharge has to be at least one order of magnitude less than the typical ignition delay time; in situ measurements are to be conducted with high spatial and temporal resolution; the results should be provided with unambiguous treatment.

In our previous EOARD supported Project, we proposed to use a laser flash–photolysis [79, 80, 81, 82] as a way of experimental extraction of a single sort of active species in combustible mixture. In this case, it seems to be reasonable to obtain direct experimental comparison between autoignition, ignition by the discharge and laser flash–photolysis. The general idea of experiments is given in Fig. 9.1. The nanosecond discharge always produces a set of active species including excited, ionized and dissociated species; efficiency of their excitation depends strongly upon reduced electric field. Laser flash–photolysis

produces the only sort of active species, namely oxygen atoms in $O(^1D)$ stage. Keeping the experimental conditions so that energy input is equal for the discharge and flash-photolysis initiation we expected to obtain much pronounced decrease of ignition delay time for laser flash-photolysis experiments.

Experiments were carried out behind reflected shock wave in temperature and pressure ranges comprised 850 – 2100 K and 0.1 – 1.0 atm. We examined ignition of $N_2O:H_2:Ar = 1:1:8$ and $O_2:N_2O:H_2:Ar = 0.3:1:3:5$ mixtures. To make the shift of ignition delay more pronounced, we added small amount of molecular oxygen (a few percent) to the gas mixture. This caused significant increase of effect due to additional chemical chains with O and OH radicals. There were three types of experiments for each set of initial experimental parameters: autoignition, ignition in presence of nonequilibrium plasma of nanosecond high-voltage discharge and flash-photolysis aided ignition.

It was found that there is a well-pronounced decay of the ignition delay time both for laser-flash photolysis and plasma assisted ignition. The kinetic model to describe the autoignition of N_2O -containing mixture has been proposed and validated. At that stage we failed to obtain quantitative agreement between results of calculations and experimental data. To get coincidence between experimental and numerical data on ignition delay time, we had to multiply experimentally obtained $O(^1D)$ density by factor of 0.3. It was also unclear why ignition by the discharge is so efficient in comparison with laser flash-photolysis action. At the same energy input the discharge is more efficient in spite of the broad energy distribution over internal degrees of freedom.

So, during this stage we (i) prepared a brief review of papers of the other authors where decrease of ignition delay time was investigated by means of laser flash-photolysis; (ii) carried out additional experiments to check a spatial distribution of the laser radiation; (iii) carried out additional experiments with simplified kinetics to validate reliability of $[O(^1D)]$ calculations from experimentally obtained energy input; (iv) carried out measurements of electrical parameters of plasma assisted ignition and prepared data for calculations of plasma assisted ignition for $N_2O:H_2:O_2:Ar$ mixtures; (v) analyzed available cross-sections and set of reactions to model a nanosecond discharge and its afterglow for $N_2O:H_2:O_2:Ar$ mixtures.

9.2 Brief description of experimental results on decrease of the ignition delay time

The kinetics of N_2O -containing mixtures itself is of great interest, because nitrous oxide is a good source of atomic oxygen in both the ground ($O(^3P)$) and excited ($O(^1D)$) states. As a source of atomic oxygen, N_2O is widely used in kinetic experiments. The question of the efficiency of using nonequilibrium plasmas for initiation of combustion still remains open. The discharge produces a lot of species: electronically excited atoms and molecules, ionized particles, vibrationally excited components. The relative role of different species is under discussion now. To check the role of excited and dissociated species we carried out experiments with excitation by laser flash-photolysis with dissociation of molecules of the mixture at wavelength of 193 nm.

The ignition delay time in N_2O -containing mixtures was measured in a square shock tube with the working part 1.6 m long. The experiments were performed behind a reflected

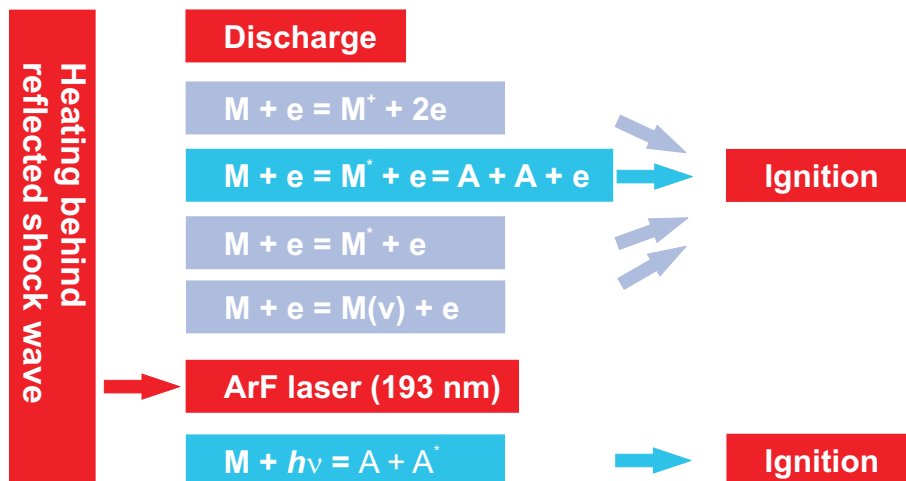


Figure 9.1: Idea of the experiments on comparison of the efficiency of laser flash-photolysis and nanosecond discharge in their efficiency to initiate combustion.

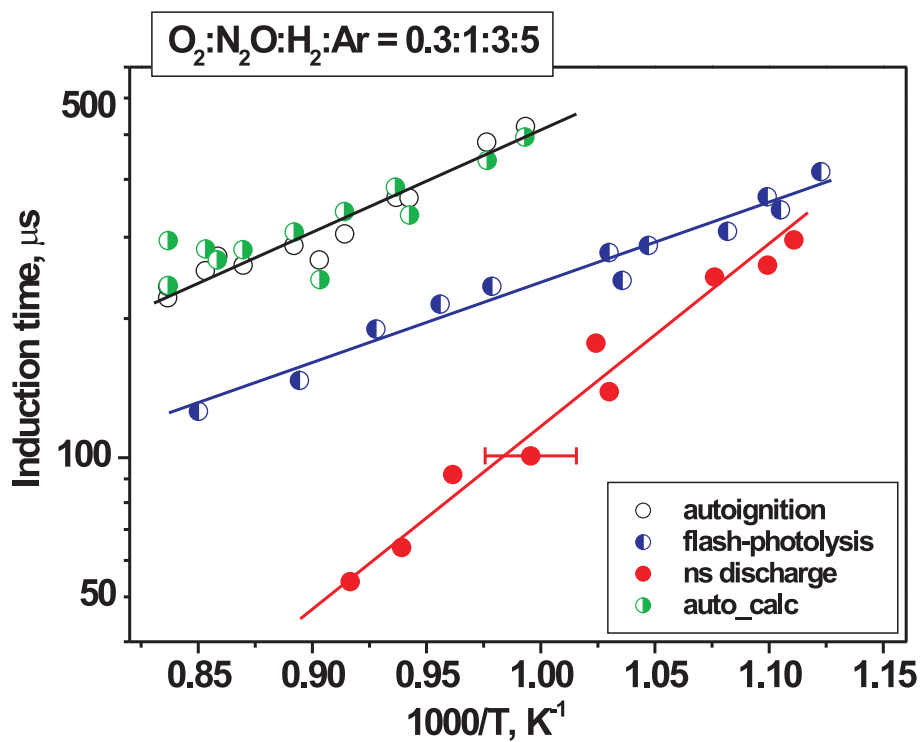


Figure 9.2: Ignition delay time vs temperature. Comparison of autoignition, ignition by flash-photolysis and by the discharge.

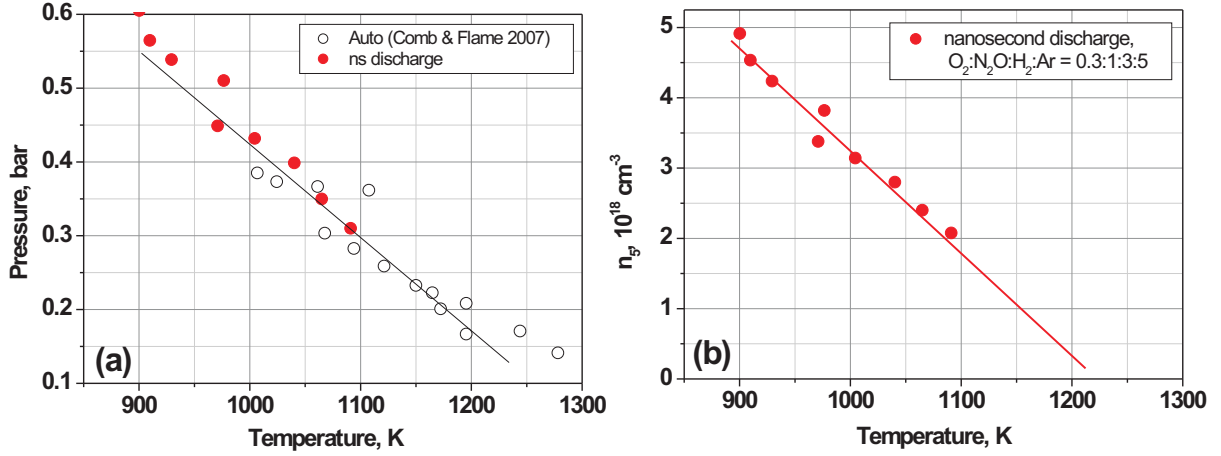


Figure 9.3: Initial parameters of oxygen-containing gas mixture: relationship between gas density, temperature, and pressure. (a) comparison of initial parameters for the discharge and for autoignition; (b) gas density *vs* temperature for experiments in the discharge.

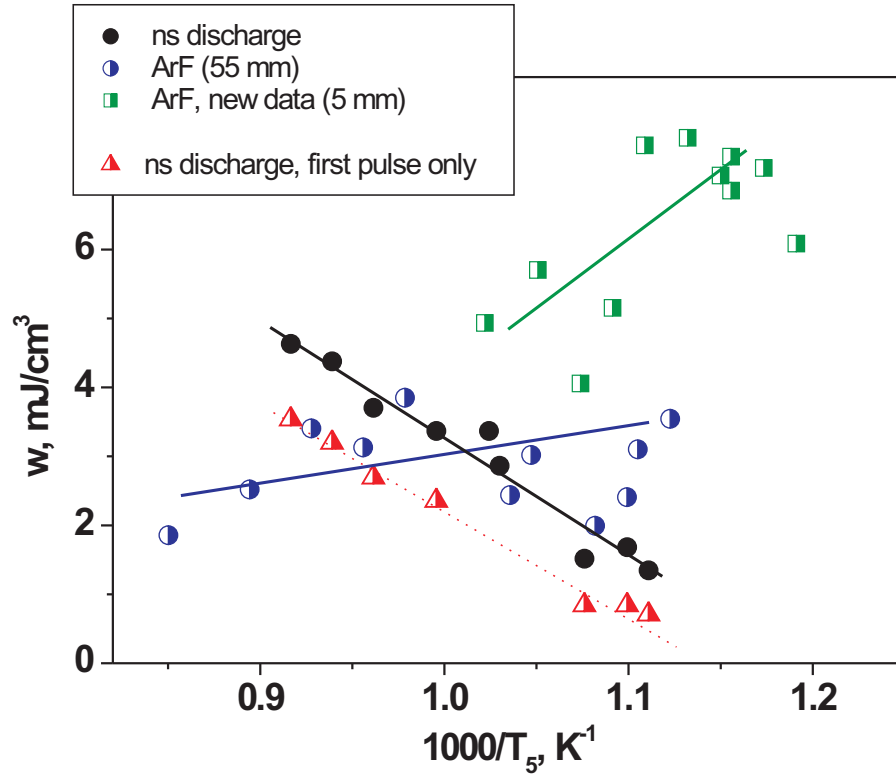


Figure 9.4: Energy input in experiments with flash-photolysis and with the discharge.

shock wave at a distance of 55 mm or 5 mm from the tube end. The thermodynamic parameters of gas under investigation behind the reflected shock wave were determined using the ideal shock tube theory. Special attention in the experiments was given to the quality of plug, which was largely defined by the quality of the shock tube channel. The maximal size of steps and clearances when mounting windows and assembling shock tube sections did not exceed 0.5 mm. Two pairs of quartz windows of diameter $d = 25$ mm and two cross sections with four windows of diameter $d = 20$ mm in the side walls of the shock tube enabled us to perform optical diagnostics of shock wave. In what follows, the cross section that is closest to the ST end will be referred to as diagnostic cross section. The incident shock wave velocity required for calculations was determined using three laser Schlieren gages located in series at three points along the shock tube. The deceleration of shock wave in the shock tube channel was taken into account in the calculations. The mixtures to be investigated were prepared using high-purity gases O₂ (99.99 %), H₂ (99.999 %), Ar (99.998 %), and medicinal-purity N₂O (98 %). The accuracy of mole fractions which made up the gas mixture being investigated was at least 0.0025 and was largely defined by the purity of N₂O and by the inleakage to a low-pressure chamber. The working chamber and the high-pressure chamber were separated by a metallized lavsan (Russian equivalent of Dacron) diaphragm 12 μ m thick bursting at a pressure difference $\Delta P \approx 3$ atm.

The experiments were repeated with the same mixture for autoignition, discharge initiation of ignition and ArF flash-photolysis. Ignition delay times were compared for all cases. The diagnostic system used for ignition by the discharge, described in details elsewhere [36] was modified to control ignition by laser flash-photolysis. A flash of UV-radiation of ArF excimer laser ("Center of Physical Devices" production, Troitsk,) was initiated behind the reflected shock wave instead of the nanosecond discharge. Laser output reached 0.2 J. The laser radiation was supplied to the dielectric section of the shock tube through the optical window perpendicularly to the shock tube axis in the same cross-section where we performed measurements in a case of the ignition by nanosecond discharge. Laser spot had approximately rectangular shape with 5x21 mm dimensions. A piezoelectric detector (PEM21) with 21 mm diameter of receiving site was used to determine energy input from laser radiation into the gas. Signal from PEM21 was controlled every time before the experiment, when the system was pumped up to 10^{-2} Torr and then during the experiment. Knowing spectral transmission of MgF₂ windows in this spectral range (were controlled by Varian Cary50 Spectrophotometer) we calculated energy input into a gas. We organized experiment so, that energy input in the discharge and energy input from a laser were within one order of magnitude. In order to measure the ignition delay time, the emission of mixture was measured in the diagnostic cross section at a wavelength of 306.4 nm; this corresponds to transition of excited OH radical to the ground state ($A^2\Sigma \rightarrow X^2\Pi$). The delay time was the length of time between the Schlieren signal which corresponds to the coming of reflected shock wave to the diagnostic cross section and the point of intersection of the time axis with the leading front of emission. The point of intersection was determined tangentially to the curve constructed at the point of maximum of signal derivative. The optical system included a condenser which focused the image of window in the measuring cross section onto the slit of MDR-23 monochromator. The emission was then detected by a FEU-100 photomultiplier connected to the monochromator. A vertical 2×20 mm slit was installed on the window. The signals

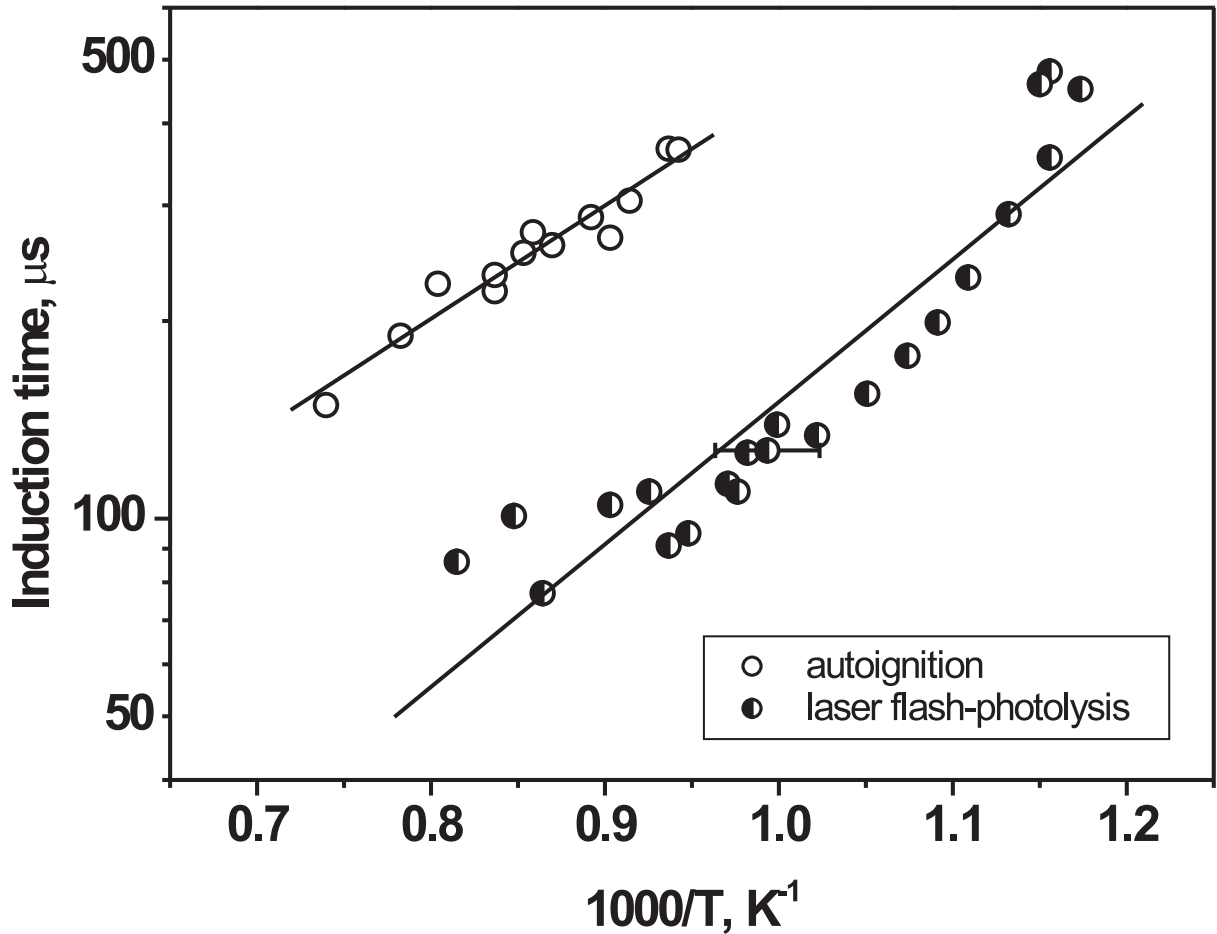


Figure 9.5: Decrease of the ignition delay time. Comparison of autoignition and laser flash-photolysis. Experiments 5 mm apart from the end plate.

from the schlieren sensors and photomultiplier were delivered to the inputs of TDS 3014 Tektronix oscillograph. To make these experiments, we chosen N_2O as a main absorbing component. Really, N_2O is known to be very efficient as an oxidant. On the other hand, it absorbs radiation at 193 nm better than molecular oxygen.

We found that both nanosecond discharge and flash-photolysis give noticeable shift of the ignition delay time. Fig. 9.2 represents ignition delay time vs gas temperature. It is clearly seen that we obtain temperature shift of 100-150 K for laser flash-photolysis and shift of 150–200 K for nanosecond discharge. Results of numerical calculations according to the scheme proposed in [83] is given in the same Figure. A good correlation between the numerical calculations and experimental data is clearly seen.

Fig. 9.3 gives an impression about initial parameters of the experiments for the $\text{O}_2:\text{N}_2\text{O}:\text{H}_2:\text{Ar} = 0.3:1:3:5$ mixture. We have a region of intersection for autoignition and plasma assisted ignition (1000 – 1100 K and 0.3 – 0.4 bar). Gas densities in the discharge are within a range of $(2 - 5) \times 10^{18} \text{ cm}^{-3}$.

Energy input in the discharge and energy input from laser flash have different tendency with a gas density (see Fig. 9.4). Energy input from the discharge decreases with gas density. This peculiarity is explained by the fact that the discharge development depends significantly upon gas density. With pressure increase at fixed gas temperature, discharge

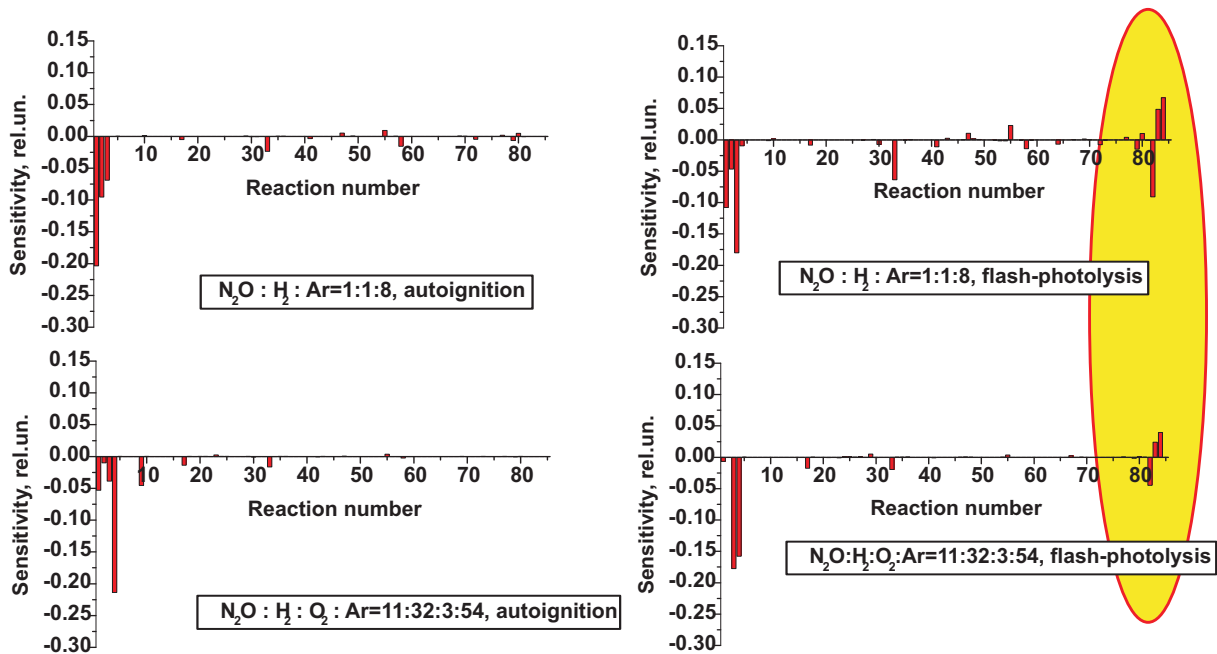


Figure 9.6: Sensitivity analysis of the numerical scheme for different mixtures. Autoignition and laser flash-photolysis.

front decelerates and, finally, at high pressures, a uniform nanosecond breakdown transforms to a nanosecond pulsed corona from high-voltage electrode. In the same Figure, we give a plot of energy input in the first pulse from the high-voltage generator (red symbols) and in all the pulses, or total energy input (black symbols). The peculiarities of the energy input in the discharge will be discussed below. Let us note that new experimental data are given with green symbols. They represent flash-photolysis measurements performed near the end plate (5 mm apart), while “old” data are obtained 55 mm apart from the end plate of the shock tube. For ignition by the discharge, 55 mm distance from the end plate does not lead to experimental error, because the ignition delay time is relatively short. For flash-photolysis, it is necessary to be careful as far as long ignition delays may be caused by contact surface arriving to the cross-section of measurements instead of achieved ignition initiation. So, Fig. 9.2 gives data for autoignition obtained 5 mm apart from the end plate and discharge and flash-photolysis data obtained 55 mm apart from the end plate.

The energy input into flash-photolysis increases with gas density, what is quite evident. Really, increase in gas density leads to an increase in density of absorbing molecules. In spite of the opposite trend, the energy input for both series of experiments is within one order of magnitude.

For the numerical modelling of the ignition by flash-photolysis, we used data on decrease of the ignition delay time by flash-photolysis obtained 5 mm apart from the end plate. The data are given in Fig. 9.5.

Zero-dimensional simulation of autoignition was performed using CHEMKIN computer code [83]. The calculations were performed at constant pressure. The GRI2.11 mechanism [3] for the combustion of methane-air mixtures was used in the scheme as the basis of hydrogen-oxygen kinetics. This mechanism was supplemented with the reactions

of formation and quenching of OH radical in the $A^2\Sigma$ state for comparison of the numerical calculation results. The scheme was validated using experimental results on ignition [4] and unimolecular decomposition of N_2O [5]. Detailed sensitivity analysis of proposed numerical scheme was performed.

The results of sensitivity analysis are given in Figure 9.6. It is clearly seen that there is a limited group of processes which influence the ignition delay time. One of the most important reactions is



(numbers of reactions here and further correspond to their numbers in numerical scheme and in Figure 9.6) This reaction leads to gas heating increasing rates of other reactions. We were able to estimate the rate constant of this reaction. Quite significant are the following reactions:



Action of laser flash-photolysis has been modelled adding a fixed amount of $O(^1D)$ at the initial time instant. As a consequence, for a case of modelling of experiments with laser flash-photolysis, reactions with $O(^1D)$ become important:



It should be noted that reactions (R83) and (R84) decrease an efficiency of laser flash-photolysis as an initiator of ignition, leading to products which are "useless" in our experimental conditions. Calculations demonstrated rather good correlation with the experimental data for autoignition and significant discrepancy for ignition by laser flash-photolysis. To get coincidence between experimental and numerical data, we had to multiply $O(^1D)$ density obtained in experiments by factor of $\gamma = 0.3$, otherwise the discrepancy between experiment and modelling is rather noticeable, but qualitatively we can see the same tendency as in experiments. Reactions (R82)—(R84) are relatively well-known and their variation within reasonable limits lead to only insignificant change in ignition delay time. So, the numerical scheme and the results of experiments needed additional analysis to obtain quantitative agreement. Two additional sets of experiments were carried out to validate obtained experimental data. Namely, (i) we measured distribution of 193 nm emission across the laser beam; (ii) we organized some special conditions of the experiment, when it was possible to validate $O(^1D)$ -atoms density measurements by ozone measurements. Two next sections describe these measurements.

9.3 Measurements of spatial distribution of laser emission

To measure spatial distribution of excimer ArF laser emission ($\lambda = 193$ nm), we used 2D matrix of pyroelectric sensors (supplied by "Center of Physical Devices" production, Troitsk), and the measurements were made with the help of engineers from "Center of Physical Devices" company. The 2D sensor was installed in the laser beam perpendicularly

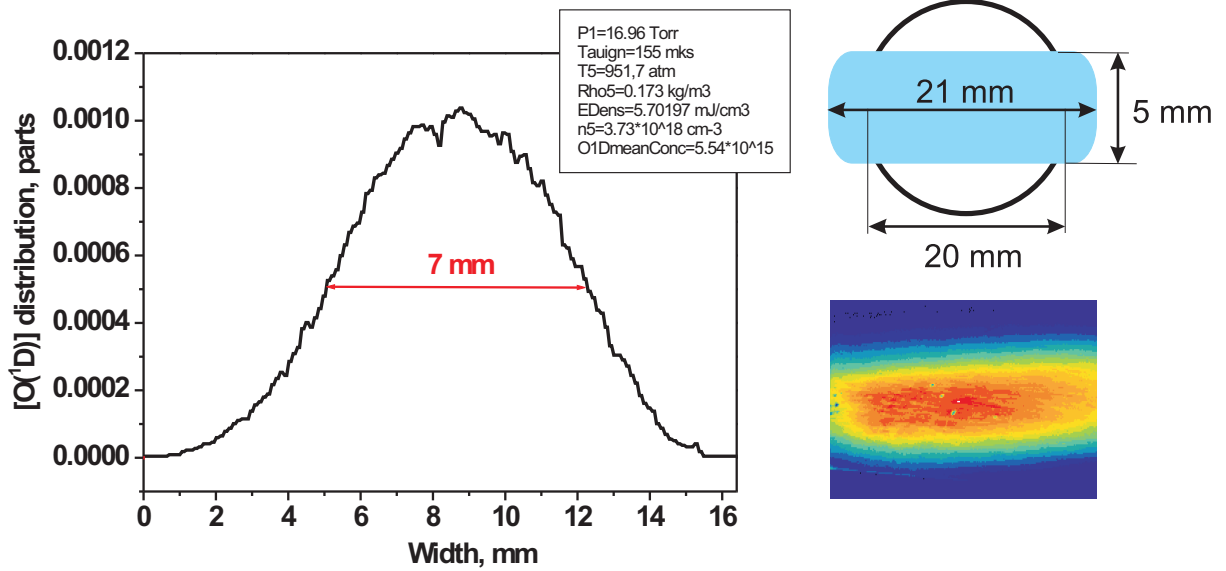


Figure 9.7: Distribution of $O(^1D)$ -atoms density due to nonuniformity of the laser beam. Schematic view of a laser spot and 2D image of emission intensity are given on the right hand side. Laser energy in the cross-section of inlet window is equal to 120 mJ.

to the direction of the beam propagation at the position which corresponds to the inlet window of the discharge section (made of MgF_2). The typical shape of the laser spot is given in Figure 9.7, right upper corner. The emission distribution is given in the same Figure, lower right corner. Red color corresponds to maximal intensity, blue color corresponds to minimum intensity of the radiation. Typical laser energy near the laser output window (before mirrors and absorption by air at the length of about 3 m, equal to distance between laser output window and inlet window of the discharge system), was equal to 170 mJ.

Relative density profile of $O(^1D)$ -atoms, calculated from the emission distribution, is given in the left part of the Figure 9.7. It is clearly seen from the Figure, that $O(^1D)$ fits Gaussian profile with a width on the half height of about 6–7 mm. This means that it is not possible to obtain as high error as factor of 0.3 in $[O(^1D)]$ value assuming that all energy release takes place uniformly throughout $5 \text{ mm} \times 21 \text{ mm}$ cross-section. Indeed, square under the Gaussian curve on the interval $[-\delta; +\delta]$ is equal to 0.7 when the curve is normalized to unity. As far as $2\delta = 6 \text{ mm}$ is close to the assumed width of the laser spot (determined from the photo-paper) $l = 5 \text{ mm}$, we obtain the difference between value of $[O(^1D)]$ calculated in the assumption of uniform energy distribution and maximal value of $[O(^1D)]$ calculated with Gaussian energy distribution within 10-20 %, and ignition always takes place in the point with maximal $O(^1D)$ density.

It should also be noted that we obtain rather good repeatability of the laser emission from pulse to pulse. To prove that, 2D images for different energy input are given in Figure 9.8, 3 cases per each energy input. It is clearly seen that the stability of laser emission is high enough.

So, we failed to explain factor $\gamma = 0.3$ necessary for coincidence between the calculations and the experimental data by a spatial distribution of laser radiation. The next step was to check the validity of procedure of $[O(^1D)]$ calculations from measured laser

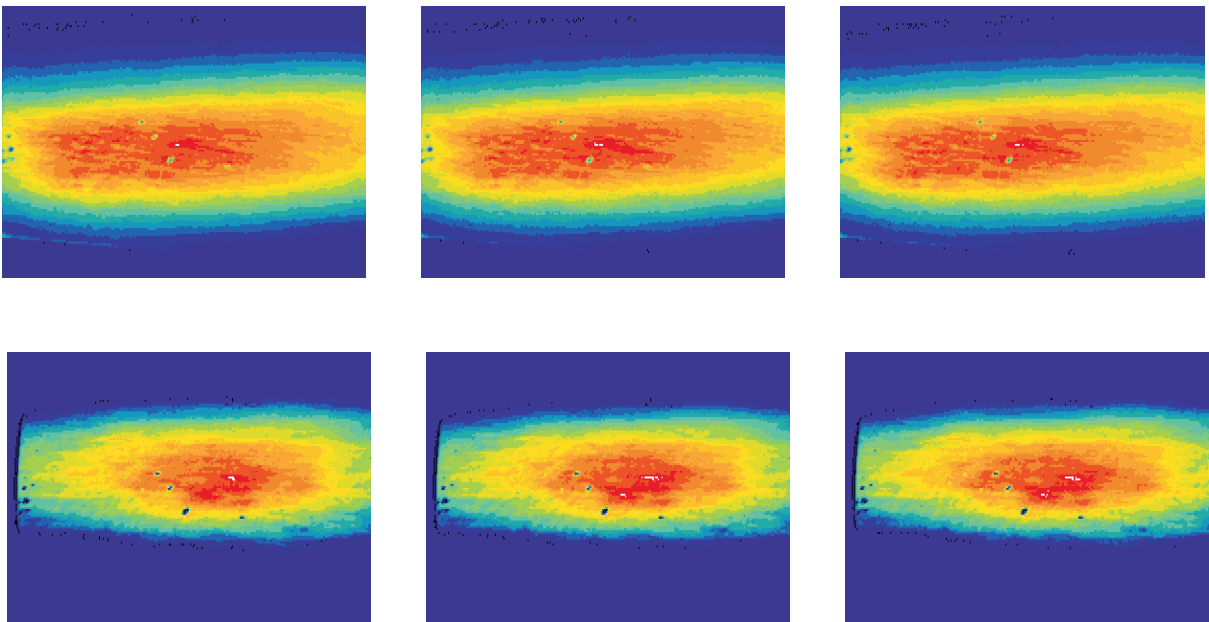


Figure 9.8: 2D images of laser emission intensity at $\lambda = 193$ nm. Laser energy in the cross-section of inlet window is equal to 120 mJ (upper row) and to 24 mJ (lower row).

energy input assuming that the quantum efficiency of the process is equal to unity.

9.4 Measurements of ozone density: validation of calculations of $[O(^1D)]$ from absorbed laser energy

The idea of the experiment was the following: (i) to organize laser flash-photolysis in a given mixture, where flash-photolysis in the mixture will lead to $O(^1D)$ -atoms production and, further, will unambiguously lead to ozone production; (ii) to measure ozone density using UV absorption technique at $\lambda = 250$ nm; (iii) to compare quantitatively obtained densities of ozone with those of O_3 calculated on the basis of initial $O(^1D)$ density. Initial $O(^1D)$ density has to be calculated on the basis of measured energy input.

The experimental setup and absorption coefficient in Hartley band are given in Figure 9.9. We used deuterium lamp DDS-30 (emission spectrum is given in Fig. 9.10, upper plot) with a narrow-band interfilter (250 ± 5 nm) to produce UV emission at 250 nm. After passing through the last section of the shock tube, the emission was collected by a low-resolution (2 nm/mm) monochromator and photomultiplier FEU-100. Ozone density was calculated using Bugger-Lambert law in assumption that O_3 distribution is uniform along the measurement line:

$$I = I_0 \exp(-[O_3]\sigma x), \quad (9.1)$$

where I_0 and I are intensities of incident emission and emission absorbed by ozone; σ is the cross-section of absorption, and x is the path of radiation through the reactor.

Gas mixture $N_2:O_2:N_2O=92:4:4$ at ambient initial temperature $T = 295$ K and initial pressure $P = 1$ atm was used for the experiments. It is important that under these

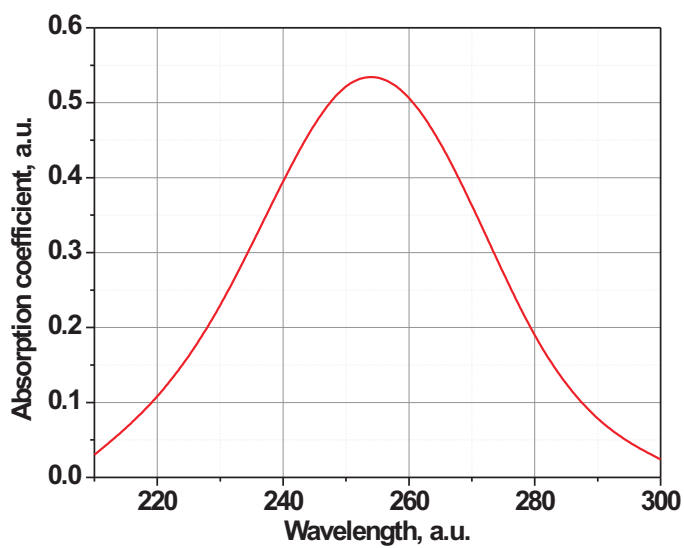
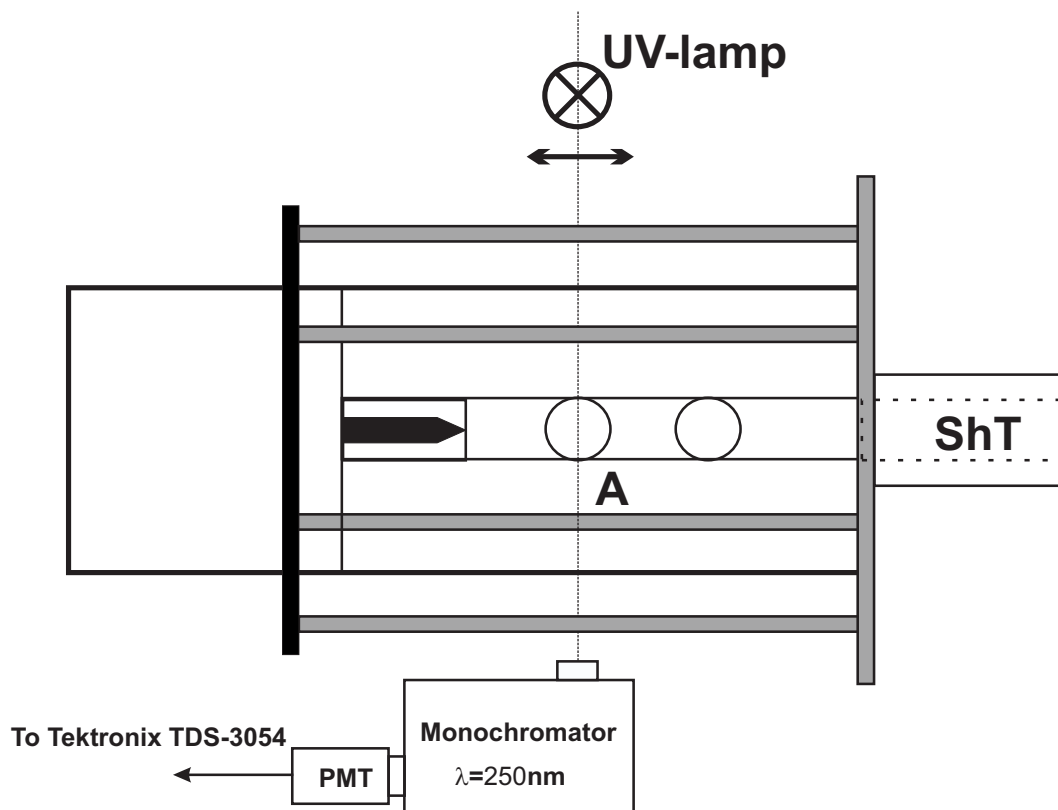


Figure 9.9: Scheme of experimental setup for O_3 density measurements by absorption of UV-emission at $\lambda = 250 \text{ nm}$ (upper part of the Figure). Shape of absorption coefficient for O_3 molecule (lower plot).

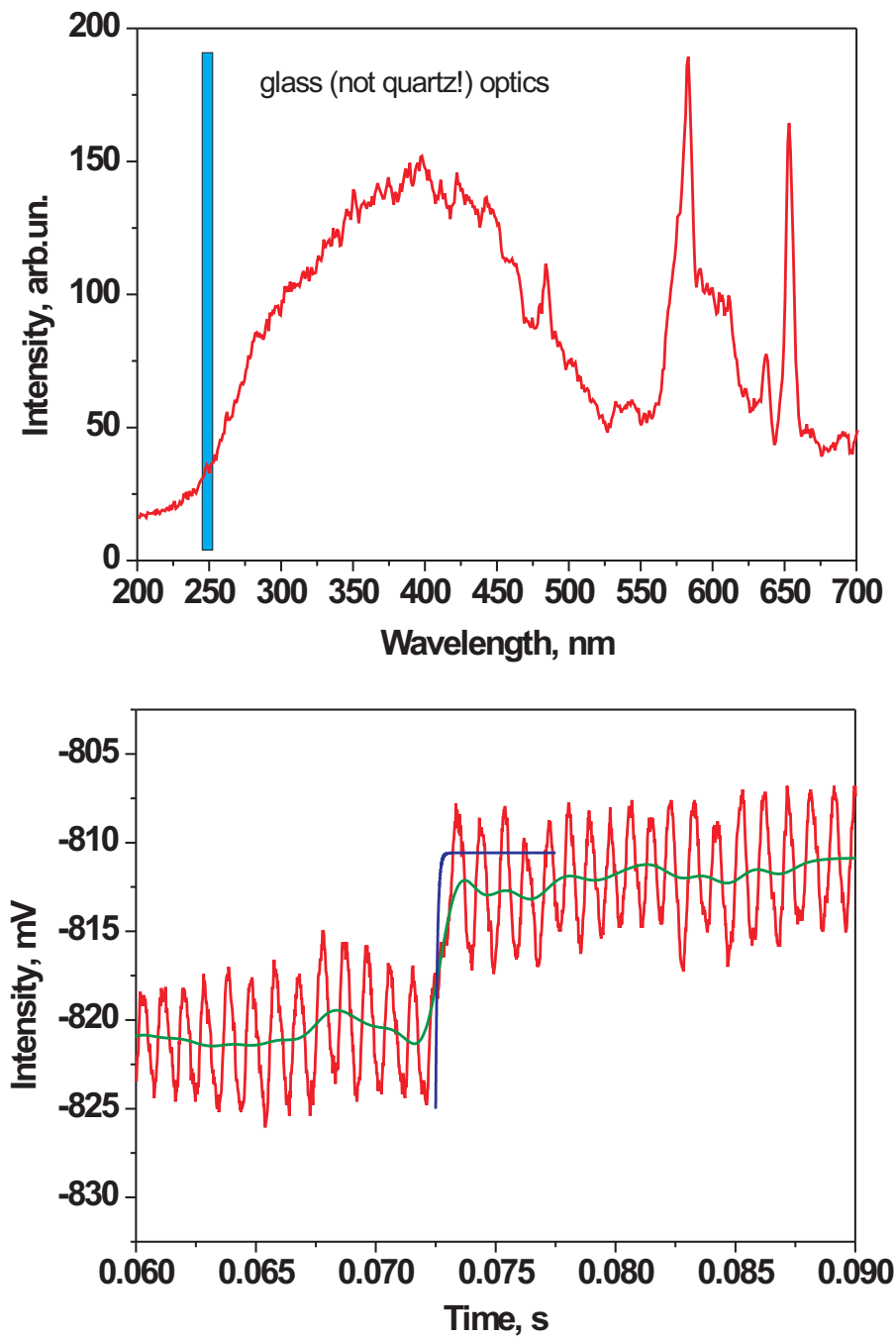


Figure 9.10: Spectrum of DDS-30 deuterium lamp (upper plot). Typical oscillogram of the emission at 250 nm. The emission trace is given by a red curve. Green curve corresponds to smoothed signal, and blue curve represents the results of calculations (lower plot).

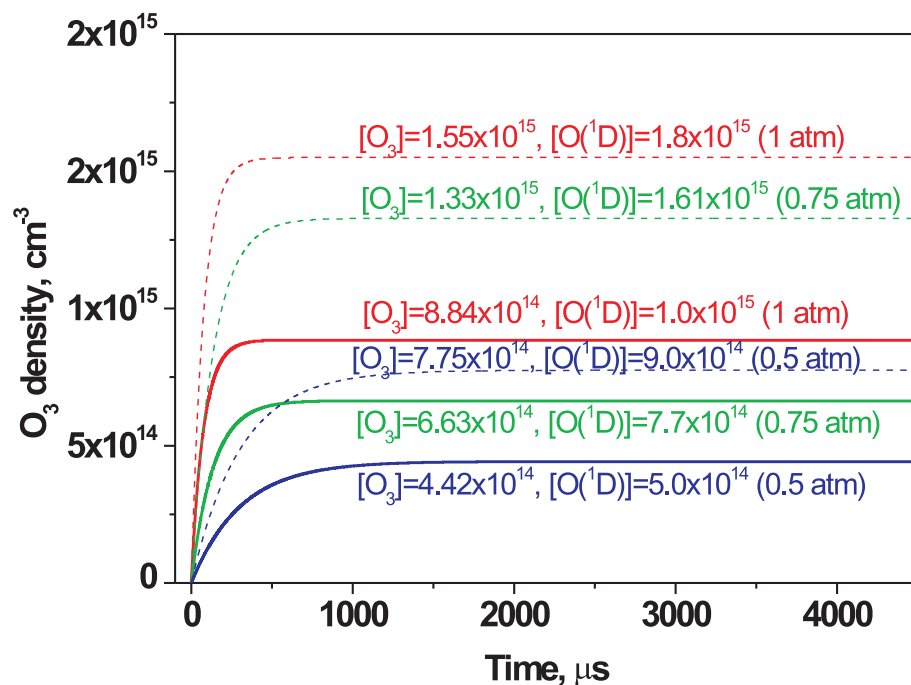


Figure 9.11: Calculated kinetic curves of ozone for $\text{N}_2:\text{O}_2:\text{N}_2\text{O}=92:4:4$ mixture. Kinetic mechanism (reactions (N1)-(N4)) is given in the Table 9.1, different initial pressures and $\text{O}(^1\text{D})$ densities are considered.

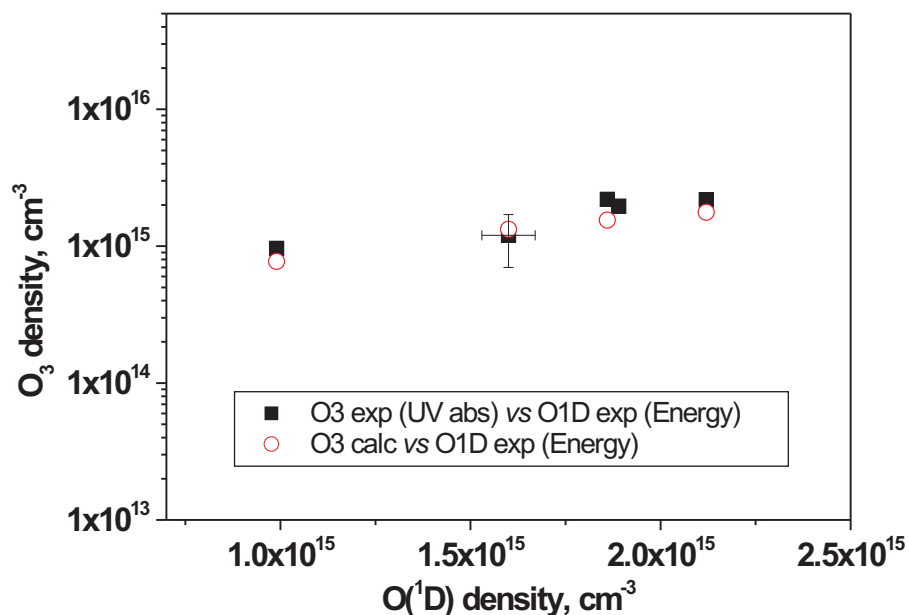
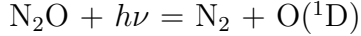


Figure 9.12: Comparison of calculated and measured values of ozone density for different initial densities of $\text{O}(^1\text{D})$. $\text{N}_2:\text{O}_2:\text{N}_2\text{O}=92:4:4$ mixture, $T = 295 \text{ K}$, $P = 1 \text{ atm}$.

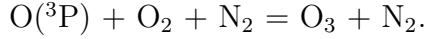
conditions we keep the N_2O density $[\text{N}_2\text{O}] = 5 \times 10^{17} \text{ cm}^{-3}$, as it was in experiments on ignition by a laser flash-photolysis. Under the action of the laser radiation, we obtain N_2O dissociation. It was postulated that quantum efficiency of N_2O dissociation by laser radiation with $\text{O}(^1\text{D})$ production is equal to unity:



Further, quenching of excited atoms on the main components of the mixture takes place:



And, finally, O-atoms in the ground state react with O_2 (nitrogen molecule is used as the third body here) producing ozone:



We calculated temporal behaviour of ozone production, considering the following reactions:

Table 9.1: The kinetic scheme of the processes taken into account to simulate the production of ozone by flash-photolysis in the $\text{N}_2:\text{O}_2:\text{N}_2\text{O}$ mixture.

Number	Reaction	Rate constant, cm^3/s , cm^6/s
N1	$\text{O}(^1\text{D}) + \text{N}_2\text{O} \rightarrow \text{NO} + \text{NO}$	1.1×10^{-10}
N2	$\text{O}(^1\text{D}) + \text{O}_2 \rightarrow \text{O} + \text{O}_2$	4.0×10^{-11}
N3	$\text{O}(^1\text{D}) + \text{N}_2 \rightarrow \text{O} + \text{N}_2$	2.6×10^{-11}
N4	$\text{O} + \text{O}_2 + \text{N}_2 \rightarrow \text{O}_3 + \text{N}_2$	6.2×10^{-34}

The results of calculations are given in Fig.9.11. Plots of $[\text{O}_3]$ dependence *vs* time for given initial $\text{O}(^1\text{D})$ densities for different initial gas pressures and $\text{O}(^1\text{D})$ densities are represented in the Figure. It is clear that O_3 density increases sharply, during 100–200 μs , and then remains constant.

Comparison of calculated and measured values of ozone density gives a rather good correlation (see Fig. 9.12). Rate constants of reactions (N1)–(N4) are well-known. So, it can be concluded that, under our experimental conditions, calculation of $\text{O}(^1\text{D})$ on the basis of experimentally measured energy input with a quantum efficiency of photodissociation equal to unity is justified.

9.5 Measurements of electrical parameters of plasma assisted ignition for $\text{N}_2\text{O}:\text{H}_2:\text{O}_2:\text{Ar}$ mixture

Table 9.2: Initial gas parameters of a $\text{N}_2\text{O}:\text{H}_2:\text{O}_2:\text{Ar}$ mixture behind the reflected shock wave, and measured delay times for ignition by the discharge

No	T_5 , K	P_5 , bar	n_5 , 10^{18} cm^{-3}	τ , μs
1	1004	0.43	3.16	101
2	1040	0.40	2.81	92
3	1065	0.35	2.41	64
4	1091	0.31	2.09	54
5	976	0.51	3.84	177
6	929	0.54	4.26	246
7	910	0.56	4.56	261
8	900	0.61	4.94	296
9	877	0.62	5.22	506
10	877	0.67	5.60	523
11	864	0.70	5.92	743
12	868	0.69	5.80	698

After analyzing the oscillograms of the experiments, we chose 7 the most reliable experiments for kinetic analysis (see Table 9.2). Experiment N 7 was excluded because of absence of current oscillogram (nevertheless, we have results on decrease of the ignition delay time). Experiments NN 9–12 (the lowest temperatures) were excluded on suspicion of influence of hydrodynamics on the results. So, we came to the conclusion that we use experiments NN 1–3 and NN 5–8 for the analysis of dynamics of energy input, current and electric field, and further analysis of kinetics in the system.

Fig. 9.13 gives temporal dependence of energy input for all selected points. First pulse makes a major contribution to the energy input (50–70 %). This is illustrated by Fig. 9.14, where energy input in the first pulse and total energy input in the discharge (taking into account all reflections of the high-voltage pulse because of unmatched load) are plotted. We give energy dependence *vs* reverse temperature and (for convenience) *vs* gas density.

Typical behaviour of electrical current and reduced electric field *vs* time are given in Fig. 9.15. After applying a high voltage to the discharge system we observe electric field increase (at the time instant equal to 316 ns under the conditions of Fig. 9.15). 10 ns later, we observe strong peak of electrical current with duration of about 20 ns. Such data were obtained for all the points mentioned above. In the future, we assume to use them for the calculations of chemical kinetics in the discharge and nearest afterglow.

9.6 Approach to numerical modelling of plasma-assisted ignition in $\text{N}_2\text{O}:\text{H}_2:\text{O}_2:\text{Ar}$ mixture. Analysis of cross-sections and reactions

The difference in characteristic time between the discharge phase and ignition one allows a separate theoretical consideration of the production of atoms and radicals in the discharge and of ignition processes. The evolution in time of the density of all active particles in both phases is calculated on the basis of a numerical solution of the corresponding balance equations:

$$\frac{d[X_k]}{dt} = Q_k - R_k \quad (k = 1, \dots, K), \quad (9.2)$$

where $[X_k]$ is the molar concentration of particles of species k , Q_k and R_k are, respectively, the total rate of production and the total rate of decomposition of these particles. The energy conservation equation is simultaneously solved to follow temperature evolution in the ignition phase:

$$\frac{dT}{dt} = -\frac{1}{\rho c_p} \sum_{k=1}^K H_k(T) \frac{d[X_k]}{dt}, \quad (9.3)$$

where T is the temperature, ρ is the mass density, c_p is the mean specific heat capacity at constant pressure and H_k is the molar enthalpy of particles of species k .

The system of equations (9.2)–(9.3) is numerically solved in the zero-dimensional approximation using the STIFF code [50] in the discharge phase and the CHEMKIN code [84] in the ignition phase. Algorithms of these codes were specially developed to solve systems of stiff ordinary differential equations and are based on the Gear-type procedure

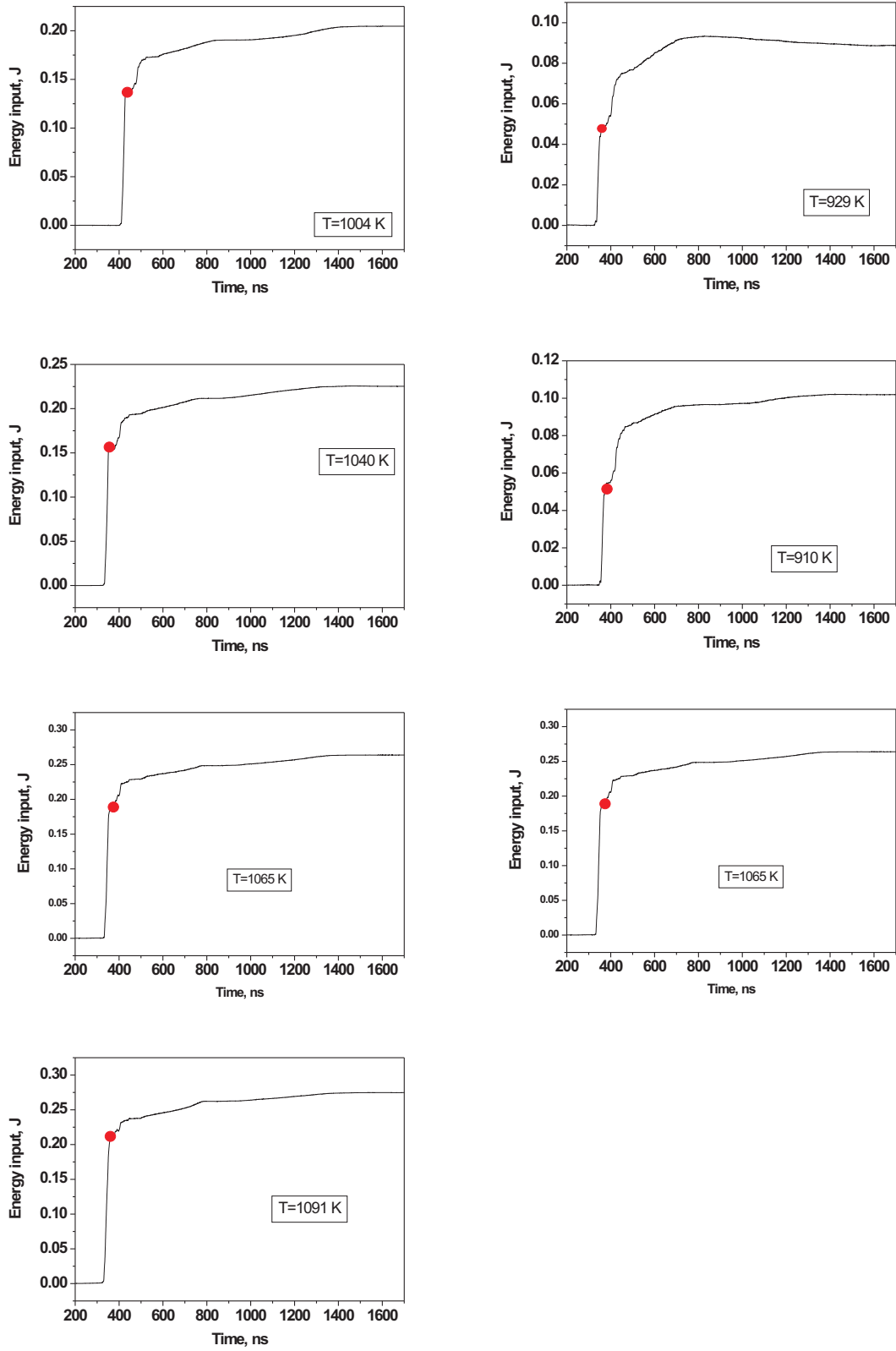


Figure 9.13: Energy input *vs* time in $\text{N}_2\text{O}:\text{H}_2:\text{O}_2:\text{Ar}$ mixture. Nanosecond discharge, time of the first pulse coming to the discharge section is indicated with a red circle.

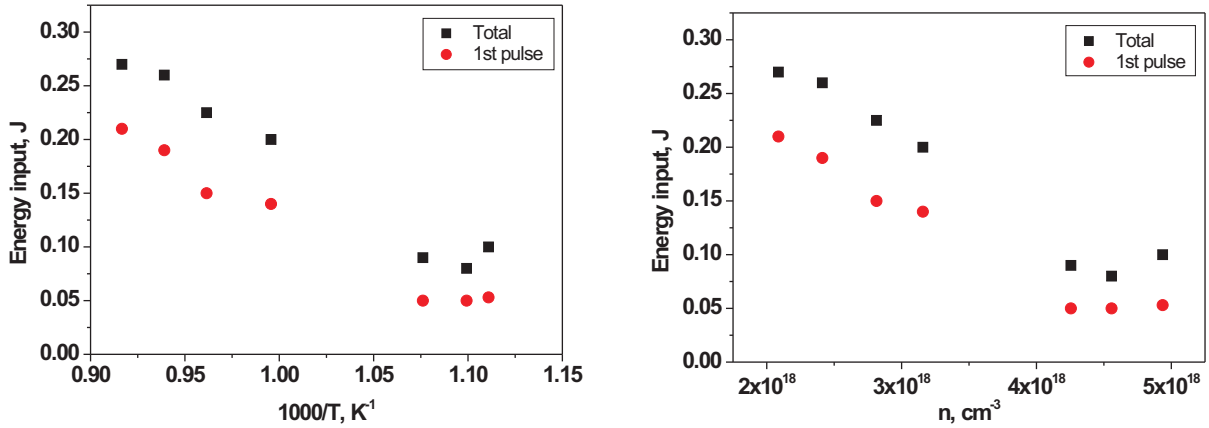


Figure 9.14: Energy input *vs* reverse temperature and *vs* gas density in $\text{N}_2\text{O}:\text{H}_2:\text{O}_2:\text{Ar}$ mixture.

[51] with adapted time step. In these codes, the input parameters are gas temperature, pressure and composition.

We neglect gas heating in the discharge phase and in its afterglow because, as it will be presented below, under the conditions considered, most of the discharge energy is deposited into excitation of electronic levels of atoms and molecules and into their ionization and dissociation. Moreover, the deposited energy is too low (a few mJ/cm^3) and, even with its total transformation into gas heating, the temperature increase would not exceed several tens of degrees, much less than the initial values of T .

Active particles are produced during the discharge phase due to electron impact dissociation, excitation, and ionization of atoms and molecules. The rate constants of these reactions depend on E/N and, consequently, vary in time. A special subroutine is added to the standard STIFF code to take into account the E/N -dependence of the rate constants. We take the function $E/N(t)$ from experimental measurements. Initial electron density will be taken as a parameter, and it is varied until we have a coincidence between calculated and measured dynamics of electrical current.

Ignition is modelled using the one-temperature Arrhenius mechanism proposed in [83]. Calculations are carried out at fixed gas pressure. Ignition delay time is defined as the interval between the instant at which active particles were injected and onset of the efficient production of OH radicals (or sharp temperature increase) in the ignition phase. Obtained ignition delay times is compared with experimental data.

In this code, we used self-consistent sets of electron collision cross sections for Ar [21], O_2 [17, 18]. For H_2 , cross-section set from the last version of BOLSIG+ code was used [22], and we need to check this set additionally. As a first stage of the calculations, we made analysis of the cross-sections for N_2O interactions with electrons available in the literature. Authors [85], analyzing the cross-sections of electron interaction with N_2O , indicate the following: “It is noteworthy that certain cross sections exhibit either a large discrepancy between the data given by different authors(dissociative attachment) or are not at all available in the literature (dissociative excitations leading to NO and N_2 products). Furthermore, let us underline that such a discrepancy persists in the case of the measured attachment coefficients where there is a deviation of about one order of magnitude between Teich [86] and Dutton et al [87]. However, ionization coefficients and the

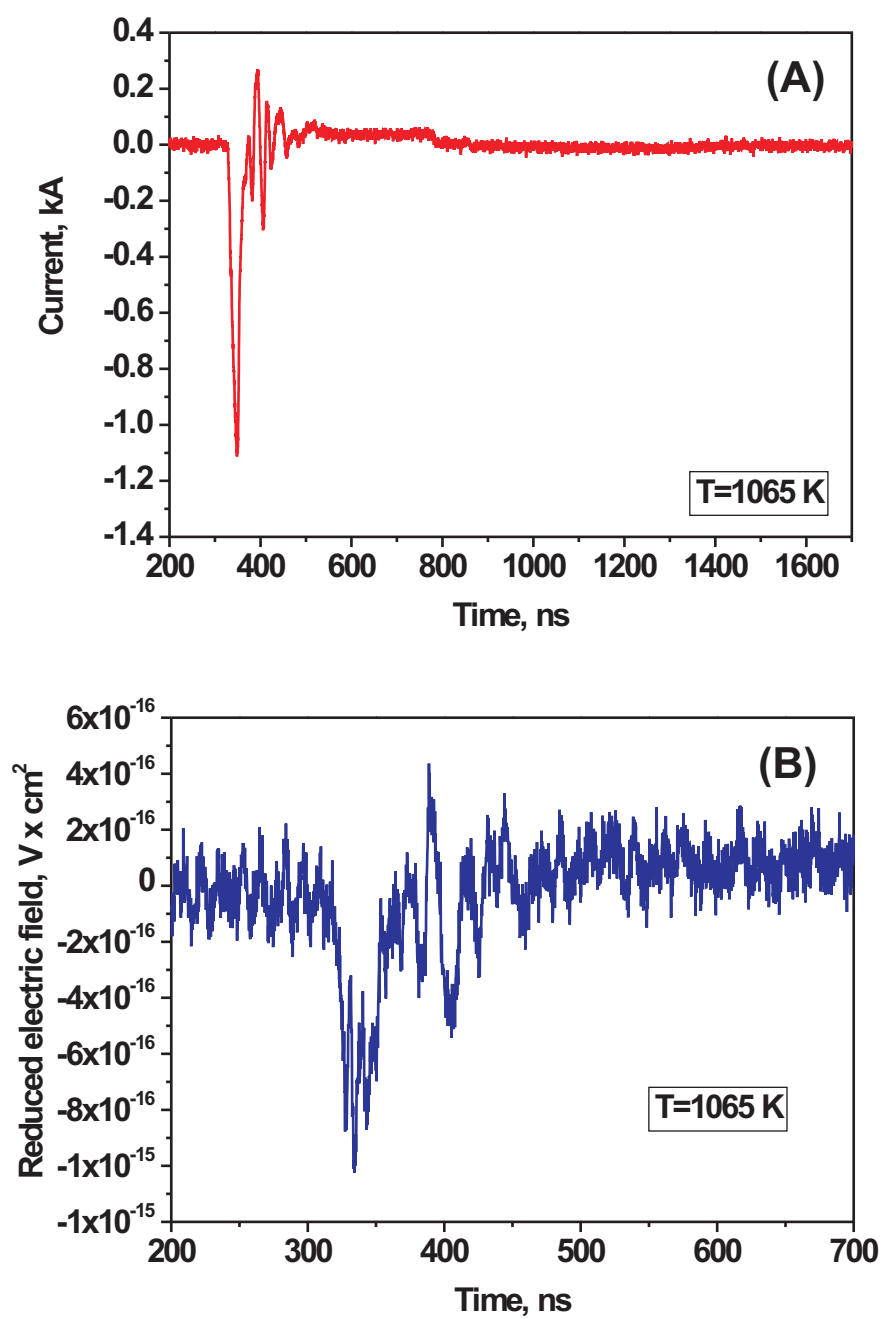


Figure 9.15: Typical behaviour of electrical current (A) and reduced electric field in $\text{N}_2\text{O}:\text{H}_2:\text{O}_2:\text{Ar}$ mixture.

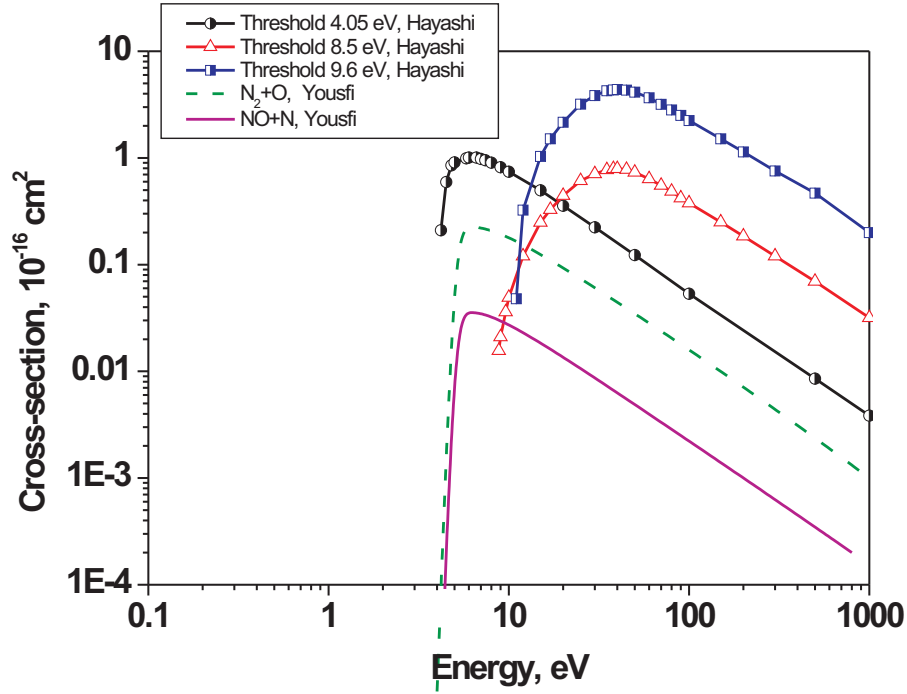


Figure 9.16: Excitation cross-sections for N_2O interaction with electrons. Dissociative excitation. “Hayashi”: [90], “Yousfi”: [85].

drift velocity of electrons in N_2O are better known and can therefore be used in the swarm unfolding method of cross section determination.” Finally, they take momentum transfer and ionization cross sections respectively from Hayashi and Niwa [89] and Rapp and Englander [88]. They also introduce dissociative excitation cross-sections with threshold equal to 4.05 eV, which correspond to the following processes:



Figure 9.16 illustrates the difference between cross-sections for the processes (I) and (II), and appropriate excitation cross-section taken from Hayashi set of cross-sections [90]. Two other cross-sections of electronic excitation of N_2O have thresholds 8.5 eV and 9.6 eV respectively.

It should be noted that cross-sections for electron impact dissociation given by the authors of [85] are significantly lower than corresponding cross-section of electronic excitation with a threshold of 4.5 eV given by [90]. This difference may change efficiency of dissociation process.

Another important point is a temperature dependence of attachment cross-section. Our experiments are carried out behind the reflected shock tube at relatively high initial temperatures. It is shown [91, 92] that below 4 eV strong dependence of cross-section of dissociative attachment upon gas temperature is observed. The scale of the effect is evident from the Fig. 9.17, where the cross-sections recommended by [90] (“Hayashi”), [85] (“Yousfi”) and [92] (“Chantry”) are given for the temperatures, respectively, 300 K, 300 K and 1040 K. With increase of a gas temperature, the dissociative attachment takes place without threshold, and the value of cross-section becomes comparable (or even higher) than gasdynamic cross-section. This influences significantly the energy branching

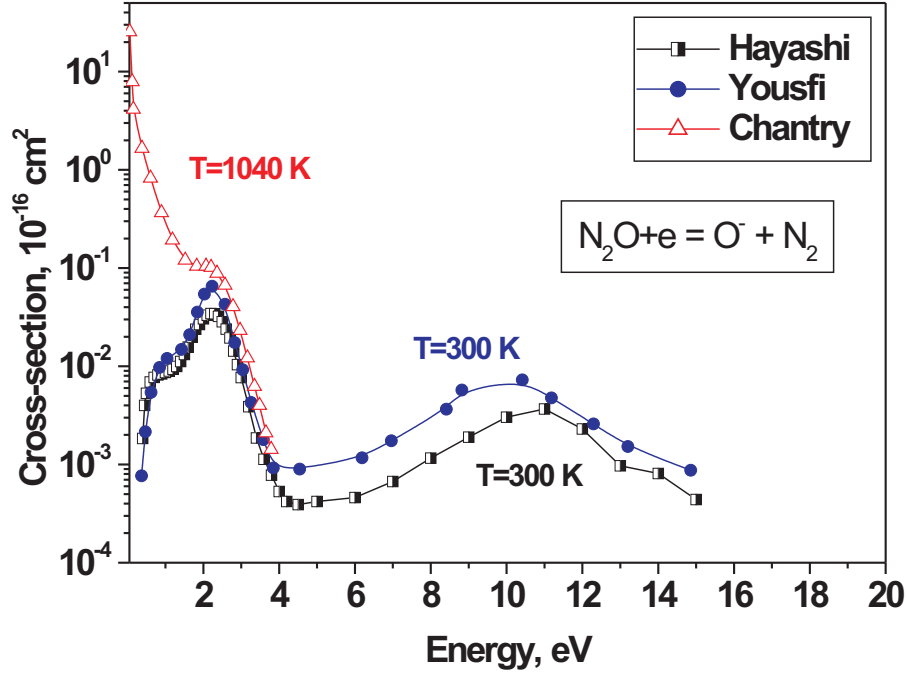


Figure 9.17: Cross-sections for N_2O interaction with electrons. Dissociative attachment. “Hayashi”: [90], “Yousfi”: [85], “Chantry”: [92].

at low values of reduced electric field, and this will be demonstrated below.

Three sets of cross-sections were chosen for more detailed analysis: (i) cross-sections given by Hayashi [90]; (ii) cross-sections given by Hayashi [90] with cross-section of N_2O excitation with 4.05 eV threshold replaced by two cross-sections of dissociation via excitation by electron impact proposed by Yousfi [85]; (iii) cross-sections given by Hayashi [90] with a cross-section for dissociative attachment for low energies (below 4 eV) taken from Chantry paper [92].

First, we calculated electron drift velocity for pure N_2O with two sets of cross-sections, (i) and (ii). The results are given by Fig. 9.18, (A). It is clearly seen that we obtain rather good correlation between experimental data given by Teich [86] and calculations using any set of cross-section. Ionization coefficient (α/N , where α is a first Townsend coefficient and N is a gas density) depends upon the set of cross-section (see Fig. 9.18, (B)), but for $E/N = 100$ Td (the highest value for our experimental conditions) we obtain values close to the measurements of Teich [86]. We believe that it is necessary to analyze α/N behaviour at higher electric fields (100-1000 Td), where the experimental data are available [86].

Let us note that in the case of drift velocity calculations for $\text{O}_2:\text{N}_2\text{O}:\text{H}_2:\text{Ar} = 0.3:1:3:5$ mixture (Fig. 9.19), “high-temperature” set of cross-sections (where we use low-energy part for cross-section of dissociative attachment [92]) changes drift velocity noticeably.

Energy branching in $\text{O}_2:\text{N}_2\text{O}:\text{H}_2:\text{Ar} = 0.3:1:3:5$ mixture has been analyzed for different sets of cross-sections. The details are given by Fig. 9.20.

Fractional power, δ , is determined as $\beta x_k N / (jE)$, where x_k is a part of component in the mixture, N is a gas density, jE is a discharge power (j is a current density, and E is an electric field), and $\beta = u_k k_k$ is an energy loss coefficient (u_k is a threshold of the

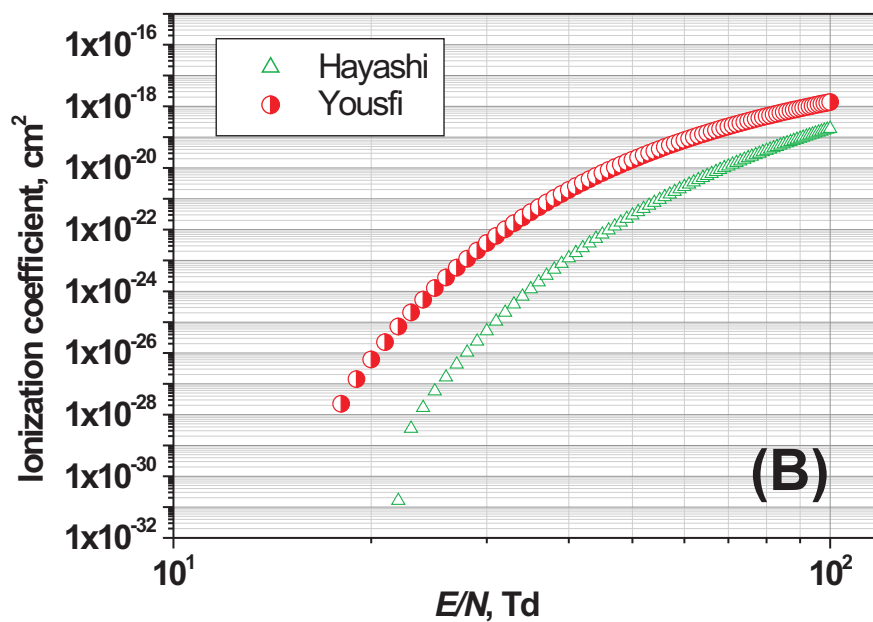
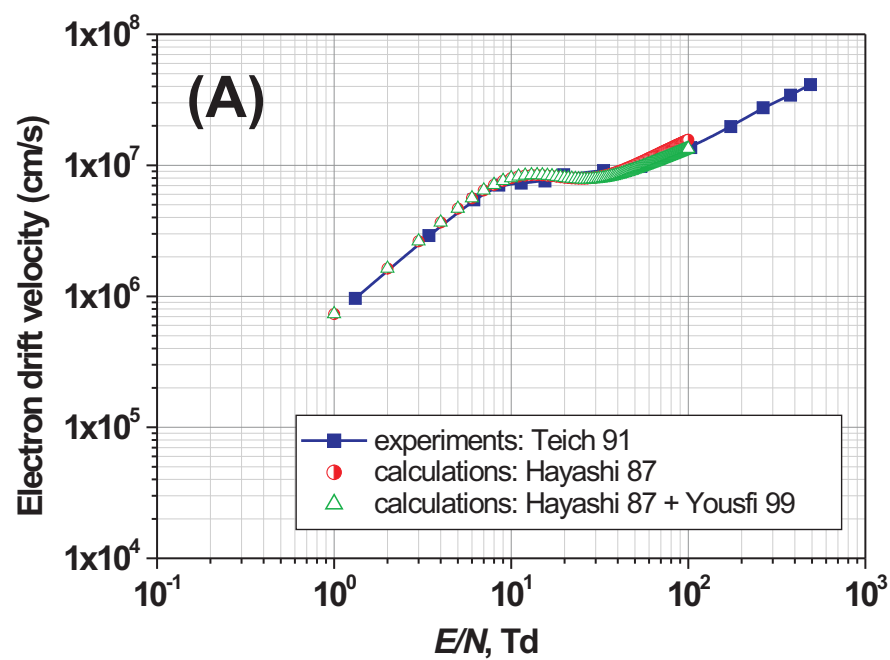


Figure 9.18: Pure N_2O . “Hayashi87”: [90], “Yousfi99”: [85], “Teich91”: [86]. (A): electron drift velocity as a function of reduced electric field (B): ionization coefficient as a function of reduced electric field.

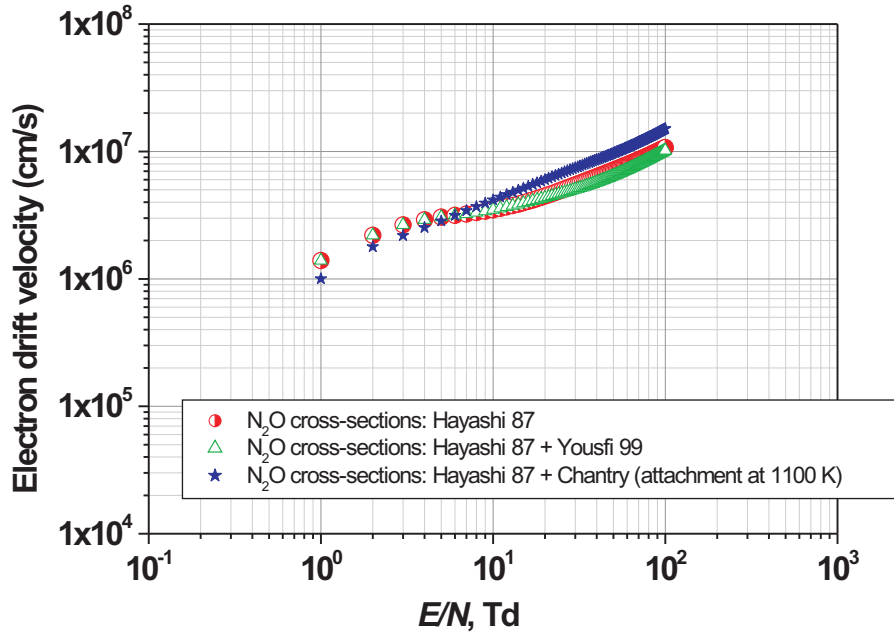


Figure 9.19: Electron drift velocity as a function of reduced electric field. $\text{O}_2:\text{N}_2\text{O}:\text{H}_2:\text{Ar} = 0.3:1:3:5$ mixture. “Hayashi87”: [90], “Yousfi99”: [85], “Teich91”: [86].

process and k_k is a rate constant of k^{th} process).

Let us describe the main peculiarities of the results obtained. It is clearly seen that for any set of cross-section the very important process is an electronic excitation of N_2O with a threshold equal to 4.05 eV, that is the excitation which leads to dissociation of N_2O molecule. The fractional power for this process may be as high as 50 % (case (A), first set of cross-sections). When we consider second set of cross-sections (with cross-sections of dissociation taken from [85]), the main parts of energy remains to be distributed in a similar way. It should be emphasized that reaction of dissociation to N_2 and O-atoms dominates comparing with the dissociation to NO and N-atoms. At high electric fields (55 Td and more) dissociation of high energy levels of hydrogen molecule (8.9 eV and higher) becomes to be a dominating process.

At low values of electric field, strong dependence of energy branching upon dissociative attachment cross-section is remarkable. When calculating energy branching with “high-temperature” cross-section of Chantry [92], we obtain significant increase of energy spent to attachment process. At low energies (10 Td and less) this fractional power exceeds unity, which can not be considered as reasonable value. This means that we need to provide additional numerical analysis to calculate energy branching at low reduced electric field values.

For all three cases ((A)–(C)) excitation of high energy levels of molecular oxygen (5.6 eV and higher) is noticeable. It increases with reduced electric field. At low electric fields, rotational excitation of hydrogen molecule is important. Ar excitation and ionization increases with electric field, but does not play significant role in energy distribution: part of energy which goes to Ar electronic excitation, does not exceed 10 %.

Finally, a set of reactions was proposed to model discharge and afterglow kinetics in $\text{O}_2:\text{N}_2\text{O}:\text{H}_2:\text{Ar}$. The set of reactions is given in Tables 9.3 and 9.4.

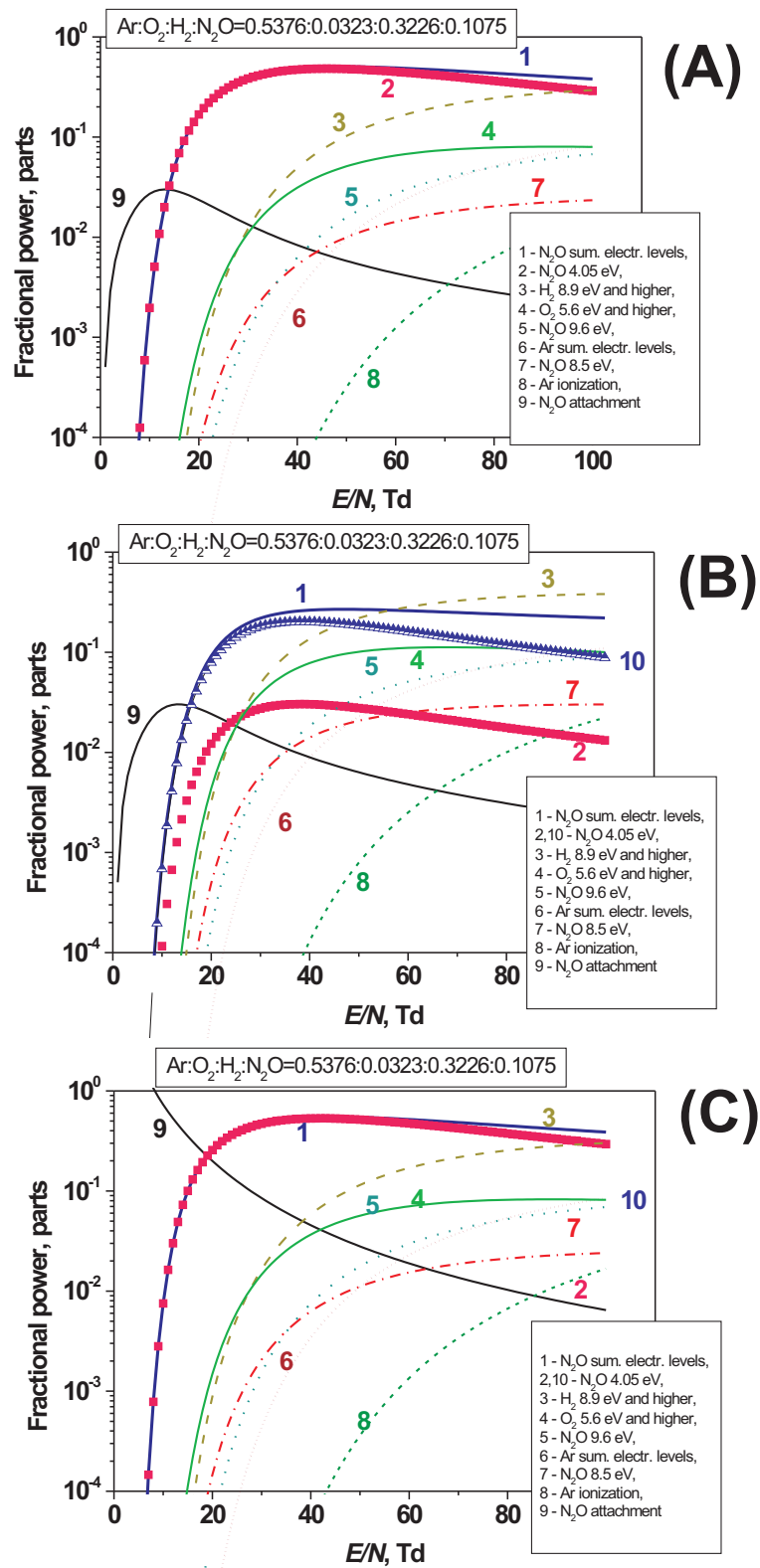


Figure 9.20: Energy branching in $\text{O}_2:\text{N}_2\text{O}:\text{H}_2:\text{Ar} = 0.3:1:3:5$ mixture. (A): first set of cross-sections (i); (B): second set of cross-sections (ii); (C): third set of cross-sections (iii).

Table 9.3: Ion–molecular reactions in Ar:H₂:O₂:N₂O mixture

N	Reaction	$k, \text{cm}^3/\text{s}$	Ref
1	$e + \text{Ar} \rightarrow \text{Ar}^+ + 2e$	$k = k(E/N)$	
2	$\text{Ar}^+ + \text{O}_2 \rightarrow \text{O}_2^+ + \text{Ar}$	$1.0 \cdot 10^{-10}$	[26]
3	$\text{Ar}^+ + \text{H}_2 \rightarrow \text{ArH}^+ + \text{H}$	$6.8 \cdot 10^{-10}$	[26]
4	$\text{ArH}^+ + \text{H}_2 \rightarrow \text{H}_3^+ + \text{Ar}$	$5.0 \cdot 10^{-10}$	[93]
5	$\text{Ar}^+ + \text{H}_2 \rightarrow \text{Ar} + \text{H}_2^+$	$3.0 \cdot 10^{-10}$	[93]
6	$e + \text{H}_2 \rightarrow \text{H}_2^+ + 2e$	$k = k(E/N)$	
7	$\text{H}_2^+ + \text{H}_2 \rightarrow \text{H}_3^+ + \text{H}$	$2.1 \cdot 10^{-9}$	[93]
8	$\text{H}_2^+ + \text{O}_2 \rightarrow \text{HO}_2^+ + \text{H}$	$1.9 \cdot 10^{-9}$	[93]
9	$\text{H}_3^+ + \text{O}_2 \rightarrow \text{HO}_2^+ + \text{H}_2$	$1.3 \cdot 10^{-10}$	[94]
10	$\text{HO}_2^+ + \text{H}_2 \rightarrow \text{H}_3^+ + \text{O}_2$	$1.4 \cdot 10^{-10}$	[94]
11	$\text{HO}_2^+ + \text{Ar} \rightarrow \text{ArH}^+ + \text{O}_2$	$1.9 \cdot 10^{-11}$	[95]
12	$\text{HO}_2^+ + \text{N}_2 \rightarrow \text{NH}_2^+ + \text{O}_2$	$8.0 \cdot 10^{-10}$	[93]
13	$\text{H}_2^+ + \text{N}_2 \rightarrow \text{NH}_2^+ + \text{N}$	$1.95 \cdot 10^{-9}$	[93, 96]
14	$\text{H}_3^+ + \text{N}_2 \rightarrow \text{NH}_2^+ + \text{H}$	$1.9 \cdot 10^{-9}$	[96]
15	$\text{H}_3^+ + \text{N}_2\text{O} \rightarrow \text{HN}_2\text{O}^+ + \text{H}_2$	$1.8 \cdot 10^{-9}$	[26, 93]
16	$\text{NH}_2^+ + \text{N}_2\text{O} \rightarrow \text{HN}_2\text{O}^+ + \text{NH}$	$7.9 \cdot 10^{-10}$	[26, 95]
17	$e + \text{O}_2 \rightarrow \text{O}_2^+ + 2e$	$k = k(E/N)$	
18	$\text{O}_2^+ + \text{H}_2 \rightarrow \text{H}_2\text{O}^+ + \text{O}$	$4.0 \cdot 10^{-11}$	[93]
19	$e + \text{N}_2\text{O} \rightarrow \text{N}_2\text{O}^+ + 2e$	$k = k(E/N)$	
20	$\text{O}_2^+ + e \rightarrow \text{O} + \text{O}(^1\text{D})$	$2.0 \cdot 10^{-7} \cdot (300/T_e)^{0.7}$	[97]
21	$\text{H}_2^+ + e \rightarrow \text{H} + \text{H}$	$3.0 \cdot 10^{-8} \cdot (300/T_e)^{0.5}$	[96]
22	$\text{H}_3^+ + e \rightarrow \text{H} + \text{H} + \text{H}$	$1.55 \cdot 10^{-7} \cdot (300/T_e)^{0.97}$	[96]
23	$\text{N}_2\text{O}^+ + e \rightarrow \text{N}_2(\text{A}^3\Sigma_u^+) + \text{O}(^1\text{D})$	$2.0 \cdot 10^{-7} \cdot (300/T_e)^{0.5}$	[27]
24	$\text{HN}_2^+ + e \rightarrow \text{H} + \text{N}_2(\text{A}^3\Sigma_u^+)$	$7.1 \cdot 10^{-7} \cdot (300/T_e)^{0.72}$	[96]
25	$\text{HO}_2^+ + e \rightarrow \text{H} + \text{O}_2$	$7.1 \cdot 10^{-7} \cdot (300/T_e)^{0.72}$	by analogy with (24)
26	$\text{HN}_2\text{O}^+ + e \rightarrow \text{H} + \text{N}_2\text{O}$	$7.1 \cdot 10^{-7} \cdot (300/T_e)^{0.72}$	by analogy with (24)

Table 9.4: Reactions of active species production in O₂:H₂:N₂O:Ar mixture

N	Reaction	k, cm ³ /s or cm ⁶ /s	Ref
1	$e + \text{Ar} \rightarrow 2e + \text{Ar}(^3\text{P}_0, ^3\text{P}_2)$	$k = k(E/N)$	
2	$\text{Ar}^* + \text{H}_2 \rightarrow \text{Ar} + \text{H} + \text{H}$	$7.0 \cdot 10^{-11}$	[98]
3	$\text{Ar}^* + \text{O}_2 \rightarrow \text{Ar} + \text{O}(^3\text{P}) + \text{O}(^3\text{P}, ^1\text{D})$	$2.3 \cdot 10^{-10}$	[98]
4	$\text{Ar}^* + \text{N}_2\text{O} \rightarrow \text{Ar} + \text{N}_2(\text{A}^3\Sigma_u^+) + \text{O}$	$4.5 \cdot 10^{-10}$	[98], *)
5	$e + \text{H}_2 \rightarrow e + \text{H} + \text{H}$	$k = k(E/N)$	
6	$e + \text{O}_2 \rightarrow e + \text{O}(^3\text{P}) + \text{O}(^3\text{P})$	$k = k(E/N)$	
7	$e + \text{O}_2 \rightarrow e + \text{O}(^3\text{P}) + \text{O}(^1\text{D})$	$k = k(E/N)$	
8	$\text{O}(^1\text{D}) + \text{O}_2 \rightarrow \text{O}(^3\text{P}) + \text{O}_2$	$3.2 \cdot 10^{-11} \cdot \exp(67/T)$	[99]
9	$\text{O}(^1\text{D}) + \text{H}_2 \rightarrow \text{H} + \text{OH}$	$1.1 \cdot 10^{-10}$	[99]
10	$\text{O}(^1\text{D}) + \text{N}_2\text{O} \rightarrow \text{NO} + \text{NO}$	$7.2 \cdot 10^{-11}$	[99]
11	$\text{O}(^1\text{D}) + \text{N}_2\text{O} \rightarrow \text{N}_2 + \text{O}_2$	$4.4 \cdot 10^{-11}$	[99]
12	$e + \text{N}_2\text{O} \rightarrow e + \text{N}_2 + \text{O}(^1\text{D})$	$k = k(E/N)$	*)
13	$e + \text{N}_2\text{O} \rightarrow e + \text{N}_2(\text{A}^3\Sigma_u^+) + \text{O}(^3\text{P})$	$k = k(E/N)$	*)
14	$\text{N}_2(\text{A}^3\Sigma_u^+) + \text{H}_2 \rightarrow \text{N}_2(v) + \text{H} + \text{H}$	$4.4 \cdot 10^{-10} \cdot \exp(-3500/T)$	[100]
15	$\text{N}_2(\text{A}^3\Sigma_u^+) + \text{O}_2 \rightarrow \text{N}_2(v) + 2 \cdot \text{O}(^3\text{P})$	$1.7 \cdot 10^{-12} \cdot (T/300)^{0.55}$	[100]
16	$\text{N}_2(\text{A}^3\Sigma_u^+) + \text{O}_2 \rightarrow \text{N}_2(v) + \text{O}_2$	$7.5 \cdot 10^{-13} \cdot (T/300)^{0.55}$	[100]
17	$\text{N}_2(\text{A}^3\Sigma_u^+) + \text{N}_2(\text{A}^3\Sigma_u^+) \rightarrow \text{N}_2(v) + \text{N}_2(\text{A}^3\Sigma_u^+)$	$3.0 \cdot 10^{-10}$	[100]
18	$\text{N}_2(\text{A}^3\Sigma_u^+) + \text{N}_2\text{O} \rightarrow 2 \cdot \text{N}_2(v) + \text{O}(^3\text{P}, ^1\text{D})$	$9.3 \cdot 10^{-12} \cdot \exp(-120/T)$	[100], *)

*) Products of reactions (4,12,13,18) with participation of N₂O molecules were determined on the basis of data on flash-photolysis of N₂O molecule and on the basis of N₂O potential energy curves [101].

9.7 Conclusions

A set of experiments have been carried out to analyze spatial distribution of laser radiation across the laser beam. 2D laser power measurements have been made for different laser energies. It was demonstrated that laser beam has Gaussian profile with a width equal to 6–7 cm on the half-height.

Taking into account the fact that we have some discrepancy in O(¹D) density determined from measured laser energy input into a gas and initial O(¹D) density necessary for numerical description of the shift of ignition delay time by laser flash-photolysis, we proposed and carried out the additional series of experiments which allows validation of method of O(¹D) determination in experiments on plasma assisted ignition initiated by flash-photolysis. The experiments were performed in N₂:O₂:N₂O=92:4:4 at ambient initial temperature $T = 295$ K and initial pressure $P = 1$ atm. Density of O(¹D)–atoms determined experimentally from the energy input. O(¹D)–atoms produced by ArF laser

radiation at 193 nm reacted with O_2 producing ozone. We calculated ozone density in assumption that quantum efficiency of flash-photolysis is equal to unity taking $O(^1D)$ density as an initial condition and we measured ozone density experimentally. Good coincidence between results of numerical modelling and experimental data has been demonstrated. This proves validity of $O(^1D)$ -density determination using measured value of energy input and quantum efficiency equal to unity.

Temporal behaviour of energy input, electric field and electric current has been measured and analyzed. It was shown that they are rather similar to obtained earlier for hydrocarbon:oxygen:argon mixture, but electric fields and current are lower because we kept energy input as low as obtained experimentally in experiments with laser flash-photolysis. These data are considered as initial conditions for numerical modelling of the discharge in $O_2:N_2O:H_2:Ar = 0.3:1:3:5$ mixture.

Ion-molecular reactions and reactions of active species production in $Ar:H_2:O_2:N_2O$ mixture were analyzed. The set of reactions to describe chemical transformation in the system due to the discharge action has been selected. Mechanism consisting of 26 ion-molecular reactions and 18 reactions of active species production has been proposed. Available cross-sections and energy branching in the discharge at different reduced electric fields have been preliminarily analyzed. Calculations of energy branching demonstrate that one of the most important processes in the discharge is N_2O dissociation via excitation of electronic levels with 4.05 eV threshold.

Chapter 10

Kinetics of Plasma-assisted Ignition in Methane–Air Mixture

10.1 Introduction

In Chapters 4 and 5, stoichiometric $C_nH_{2n+2}:O_2$ mixtures (10%) diluted with Ar (90%) were considered. From the practical standpoint, it is more interesting to study plasma assisted ignition in mixtures in which O_2 is replaced by air. In [35], the experimental approach used in [102]–[103] was extended to the study of CH_4 :air mixtures; however, based on the measured time-resolved discharge current and electric field, a numerical simulation of the experimental data obtained in [35] has not been carried out till now. The purpose of this study was to simulate numerically the ignition of the CH_4 :air mixtures under the conditions considered in [35] using the measured discharge current and electric field and to clarify the effect of N_2 addition on PAI in CH_4 -containing mixtures. In this work, we followed the computational approach suggested in [102]–[103] and extended the kinetic schemes to include the processes with N_2 affecting (i) the non-equilibrium electron energy distribution and average electron energy in the discharge, (ii) the rate coefficients and channels of production of active particles by the discharge and (iii) the ignition processes.

10.2 Experimental data on plasma-assisted ignition in CH_4 :air mixtures

We provide a brief survey of the main experimental results [35], which could be important for numerical simulation of PAI under the conditions considered.

10.2.1 Discharge characteristics

In [35], kinetics of ignition in a $CH_4:O_2:N_2:Ar = 1:4:15:80$ mixture was experimentally studied under the action of a high-voltage nanosecond discharge. The experiments were carried out behind a reflected shock wave at gas pressures of 0.3–2.4 atm and temperatures of 1100–2250 K. The emission from the discharge and the emission in the ignition phase were registered with a nanosecond ICCD camera under various experimental con-

ditions. Using emission spectroscopy the spatial uniformity of the discharge and ignition was investigated and ignition delay time was determined for various gas temperatures and pressures. In some cases, these measurements were accompanied by the measurements of discharge current and electric field waveforms with a nanosecond time resolution. It was shown that at low (~ 0.5 atm) pressures the discharge emission intensity was almost uniform and the discharge-induced combustion was also uniform. At high (1.5-2 atm) pressures, the nonuniformity of the discharge and combustion was observed. It was suggested in [35] that in this case the discharge developed as a corona near the high-voltage electrode and active particles favoring ignition were mainly produced in the electrode region.

The most important parameter governing the electron energy distribution and average electron energy in a given gaseous mixture is the reduced electric field, E/n , where n is the gas number density. Fig. 10.1 and 10.2 show, respectively, the typical evolution in time of the reduced electric field during the discharge and of the discharge current. High-voltage pulse was followed by two additional pulses induced due to a partial reflection of the high-voltage signal from the discharge cell and high-voltage generator. Time-resolved electric field and discharge current are required to calculate the electron impact rate coefficients for the production of active particles affecting PAI.

Fig. 10.3 shows the measured peak values of E/n versus the gas number density behind a reflected shock wave. It is more reasonable to estimate the efficiency of production of active particles using the values of E/n at the instant at which the discharge current peaks. These values are also given in Fig. 10.3; they decrease by half as the gas number density increases by a factor of ~ 3 ; that is, the average electron energy in the discharge at high pressures was lower than that in the discharge at low pressures.

Fig. 10.4 shows the typical temporal evolution of the specific (per one neutral particle) deposited energy, w , for various gas temperatures and pressures. The values of w were calculated in the same way as in paragraph 4.1.2. Here, it was assumed that the discharge plasma between the gauges was uniform. It follows from Fig. 10.4 that the energy is deposited in several high-voltage pulses, half the total energy being usually deposited in the first pulse. Fig. 10.5 shows the total (integrated over all high-voltage pulses) specific deposited energy as a function of pressure. The values of w in the discharge at low pressures are almost an order of magnitude higher than those in the discharge at high pressures. Consequently, under the conditions studied the discharge is expected to produce active species more efficiently at low pressures.

10.2.2 Ignition characteristics

Fig. 10.6 shows the evolution in time of the OH emission intensity measured in [35]. Here, the first peak of radiation signal was due to the radiation emitted in the discharge phase, whereas the second peak in this curve was due to the radiation in the ignition phase. Ignition delay time τ was determined as the interval between initiation of the discharge and the emission signal corresponding to ignition (see Fig. 10.6). It was possible to measure ignition delay time without discharge only at high pressures because at low (~ 0.5 atm) pressures autoignition delay time was comparable to or longer than the time of shock tube operation.

Tab. 10.1 presents the initial parameters measured behind the reflected shock wave,

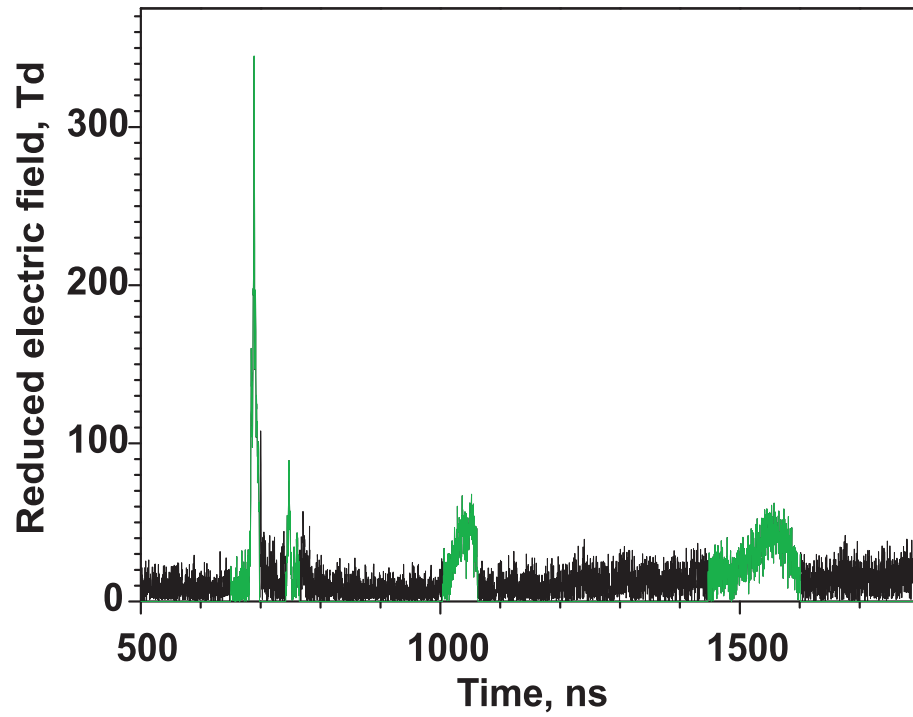


Figure 10.1: The temporal evolution of the reduced electric field for 1329 K and 0.45 atm. The green segments of the curve correspond to high-voltage pulses in which the discharge occurred and active species were produced ($1 \text{ Td} = 10^{-17} \text{ V cm}^2$).

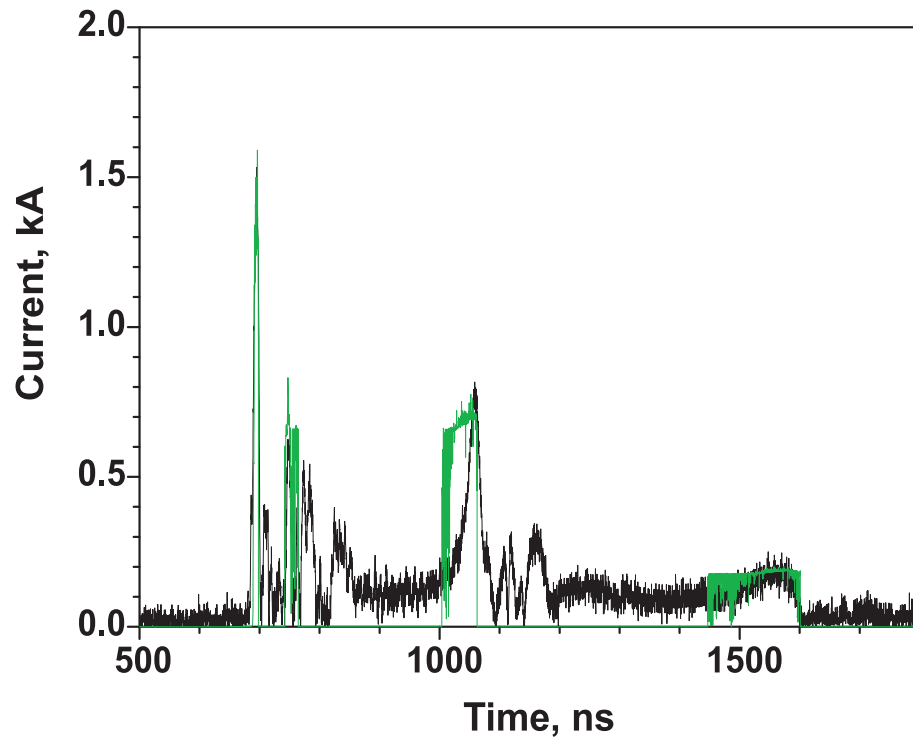


Figure 10.2: The temporal evolution of the discharge current for 1329 K and 0.45 atm. The black curve corresponds to the measurement and the green curve corresponds to the calculation.

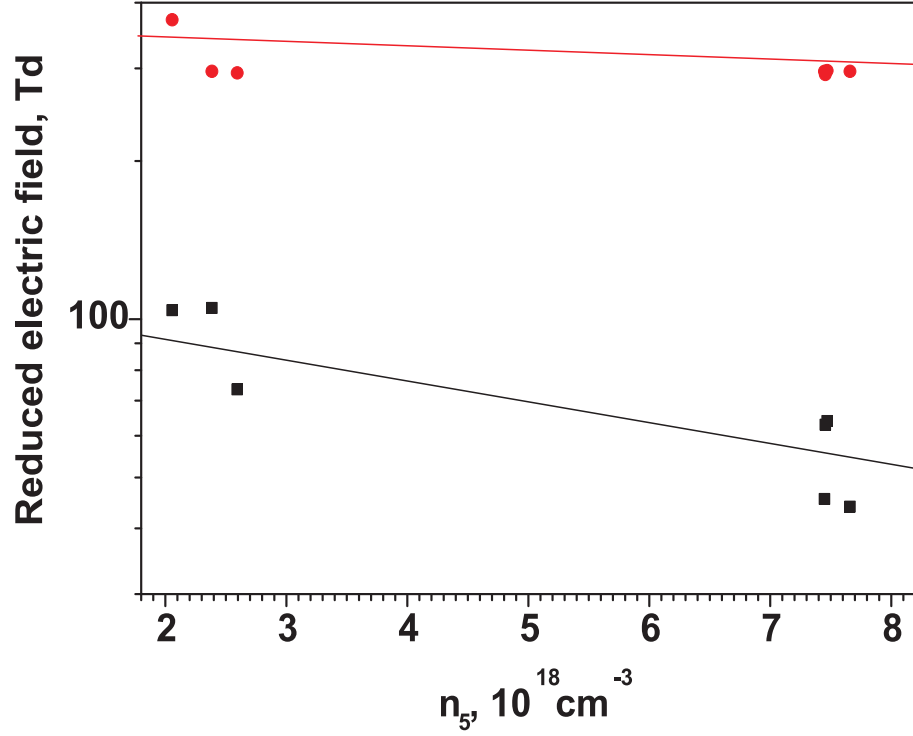


Figure 10.3: The measured peak values of the reduced electric field (red circles) and their values at the instant at which the discharge current peaks (black squares) as a function of the gas number density ($1 \text{ Td} = 10^{-17} \text{ V cm}^2$).

measured and calculated delay time for ignition by the discharge and calculated mole fractions of O, H and CH_3 , the dominant species of active particles produced in the discharge phase, for every experiment under consideration. Fig. 10.7 shows ignition delay time as a function of gas temperature for various gas pressures. According to the experiment [35], the effect of non-equilibrium plasma on ignition delay time was much more profound at low pressures.

Table 10.1: Initial gas parameters in a $\text{CH}_4:\text{O}_2:\text{N}_2:\text{Ar} = 1:4:15:80$ mixture behind the reflected shock wave, measured and calculated delay times for ignition by the discharge, calculated mole fractions of O, H, and CH_3 after the discharge, and calculated energy cost for production O atoms.

No	T_5, K	P_5, atm	$n_5, 10^{18} \text{ cm}^{-3}$	$\tau_{meas}, \mu\text{s}$	$\tau_{calc}, \mu\text{s}$	$[\text{O}]/n_5$	$[\text{H}]/n_5$	$[\text{CH}_3]/n_5$	$g(\text{O}), \text{eV}$
1	1329	0.45	2.45	376	559	2.35E-3	1.81E-4	5.76E-5	15.8
2	1285	0.46	2.59	440	661	2.99E-3	2.24E-4	7.37E-5	14.9
3	1233	0.35	2.06	259	559	4.26E-3	3.08E-4	1.05E-4	14.8
4	1798	1.85	7.46	104	42.7	4.74E-4	3.31E-5	1.14E-5	12.3
5	1649	1.70	7.47	159	87.4	5.47E-4	3.60E-5	1.29E-5	12.5
6	1580	1.67	7.66	254	130	5.99E-4	3.62E-5	1.35E-5	13.8
7	1576	1.62	7.45	240	128	6.24E-4	3.63E-5	1.40E-5	13.7

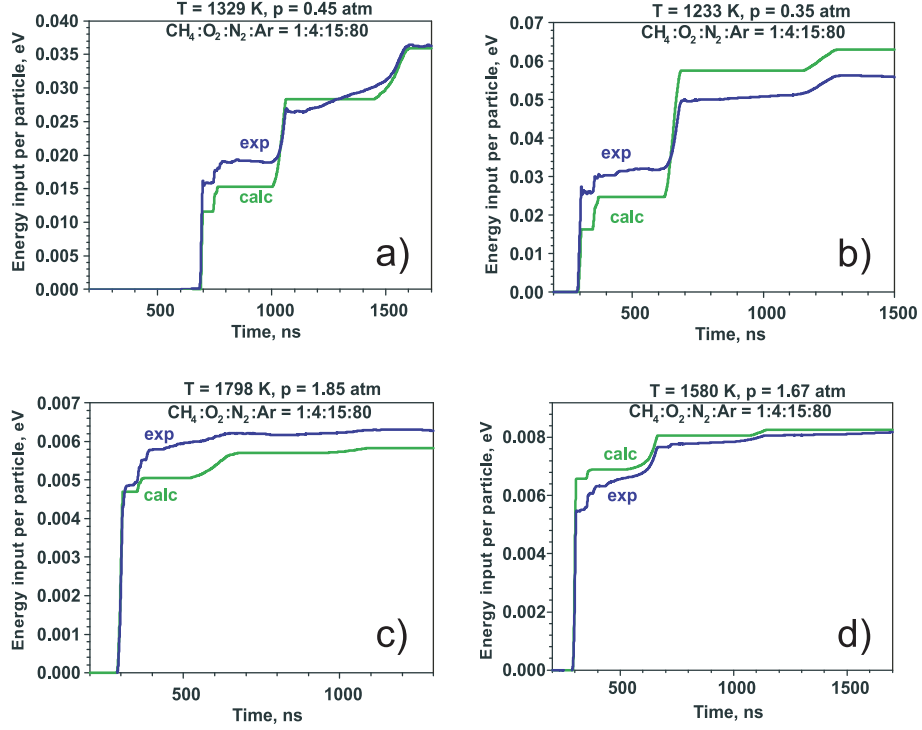


Figure 10.4: The temporal evolution of the specific deposited energy (per particle) in the discharge for various gas temperatures and pressures. Blue curves correspond to measurements and green curves correspond to calculations.

10.3 Numerical simulation of plasma-assisted ignition in CH_4 :air mixtures

This simulation of PAI in the CH_4 -containing mixture is based on our previous simulation [102, 38]. The main difference between them is that we have extended the kinetic models used in [102, 38] to take into account N_2 addition. This effect could be important for the production of active particles in the discharge and for chemical reactions in the ignition phase.

10.3.1 Kinetic model for discharge and near afterglow

Under the conditions considered, the discharge processes occurred on a nanosecond scale, whereas the ignition processes occurred on a microsecond scale. Therefore, we simulated the temporal evolution of densities of particles important for plasma-assisted ignition separately in the discharge phase and in the ignition phase. It was assumed that the effect of nonequilibrium discharge plasma is reduced to the accumulation of active particles that influence the ignition processes.

In the discharge phase, we simulated numerically the production of active particles in the gaseous mixture in a high electric field during the discharge and the conversion of the particles during the plasma decay in the near afterglow. Our kinetic model is similar to that used previously to simulate plasma-assisted ignition in $\text{CH}_4:\text{O}_2:\text{Ar}$ mixtures [38, 103], the main difference between these models being consideration of processes with

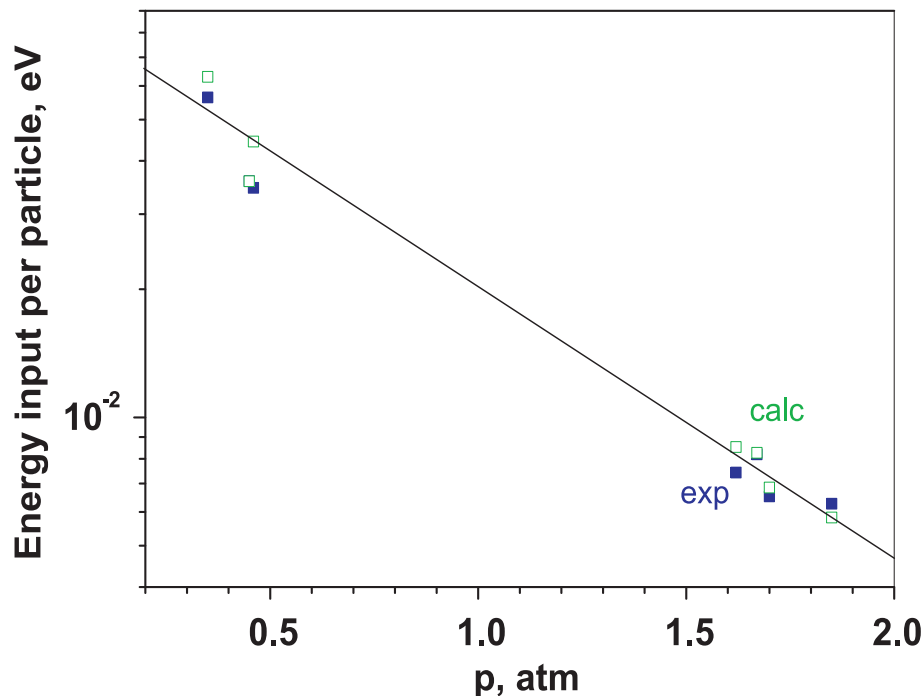


Figure 10.5: Total specific energy deposited per one neutral particle for all high-voltage pulses as a function of pressure.

N_2 molecules. The active particles under consideration were electronically excited O_2 and N_2 molecules, electronically excited Ar atoms, O atoms, N atoms, H atoms, hydrocarbon radicals, electrons and simple positive ions. The focus was on the mechanisms that could lead to dissociation of molecules. Therefore, we did not calculate the densities of vibrationally excited molecules and electronically excited states of O_2 , which have energy insufficient to dissociate molecules. Excitation of these states was taken into account only when solving the electron Boltzmann equation to determine the electron energy distribution, the mean electron energy and other electron parameters in the discharge.

The excitation of metastable Herzberg $O_2(c^1\Sigma_u^-)$, $O_2(C^3\Delta_u)$, and $O_2(A^3\Sigma_u^+)$ states was simulated by the excitation of one effective metastable state with an excitation energy of 4.5 eV (referred to as O_2^*), by analogy with [16]–[18]. The excitation of the electronic states of O_2 with higher excitation energy led to dissociation, and these processes were referred to as electron impact dissociation of O_2 . Excitation of electronic Ar states was also simulated by the excitation of one effective state (referred to as Ar^*), with the excitation rate being equal to the total rate of excitation of all excited Ar states. Here, there is no reason to consider excited Ar states in more detail, because little is known about the rates of their quenching in collisions with O_2 , N_2 and CH_4 to dissociate these molecules.

It was necessary to consider electronically excited states of N_2 in more detail because these states are efficiently quenched in collisions with O_2 to form O atoms. When calculating the densities of active species, we considered separately $N_2(A^3\Sigma_u^+)$, $N_2(B^3\Pi_g)$, $N_2(a'^1\Sigma_u^-)$, and $N_2(C^3\Pi_u)$ states. In some cases, other electronically excited states of N_2 were also considered by analogy with [104]. In the last case, the excitation of triplet $N_2(B^3\Pi_g)$, $N_2(B'^3\Sigma_u^-)$, and $N_2(W^3\Delta_u)$ states was simulated by the excitation of one effective state (referred to as $N_2(B)$) with the excitation rate being equal to the total

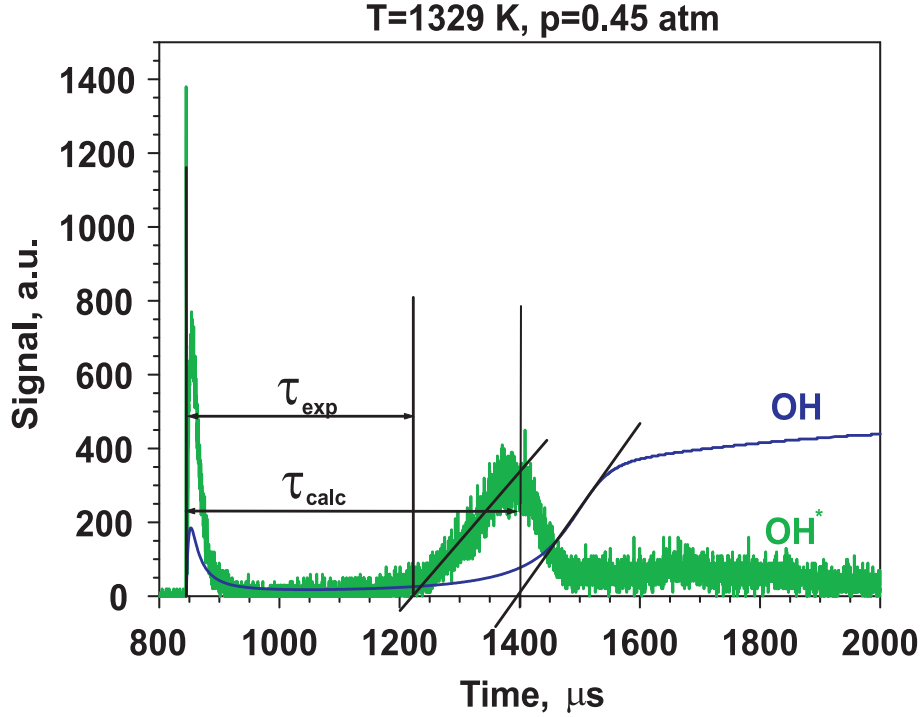


Figure 10.6: The temporal evolution of the measured OH* emission intensity (green curve) and the calculated evolution in time of the density of OH (blue curve) for 1329 K and 0.45 atm.

rate of excitation of all these N_2 states and with the quenching rates being equal to the quenching rates for $N_2(B^3\Pi_g)$ state. This assumption is reasonable because of an efficient energy transfer between these triplet states. For the same reason the excitation of singlet $N_2(a^1\Pi_g)$, $N_2(a'^1\Sigma_u^-)$, $N_2(a^1\Pi_g)$ and $N_2(w^1\Delta_u)$ states was simulated in [16] by the excitation of one effective state (referred to as $N_2(a)$) with the excitation rate being equal to the total rate of excitation of all these N_2 states and with the quenching rates being equal to the quenching rates for $N_2(a'^1\Sigma_u^-)$ state.

We neglected the formation of negative ions because their densities, as a rule, are much lower than electron density at high (>1000 K) gas temperatures (see, for instance, [105]). The formation of complex positive ions (Ar_2^+ , O_4^+ , N_4^+ , etc.) was not considered because the dissociation energies of complex ions are sufficiently low to decompose these particles at gas temperatures under study. At the end of plasma decay, only atoms and radicals were assumed to dominate the composition of active particles; the effect of long-lived excited particles on the ignition of the mixture was also neglected.

Tab. 10.2 shows the reactions considered in our kinetic model and their rate coefficients. We took into account electron impact dissociation, excitation and ionization of neutral particles, quenching of electronically excited particles, charge exchange in collisions between ions and neutral particles, and dissociative electron-ion recombination being the dominant mechanism of electron loss in the discharge afterglow under the conditions studied. The rate coefficients for reactions between heavy particles were taken from the literature. The only exceptions are reactions (R38) and (R51), for which we have failed to find rate coefficients. Therefore, they were estimated. The rate coefficient for reaction (R38) was assumed to be low and equal to the rate coefficient for the reaction $N_2(A^3\Sigma_u^+)$

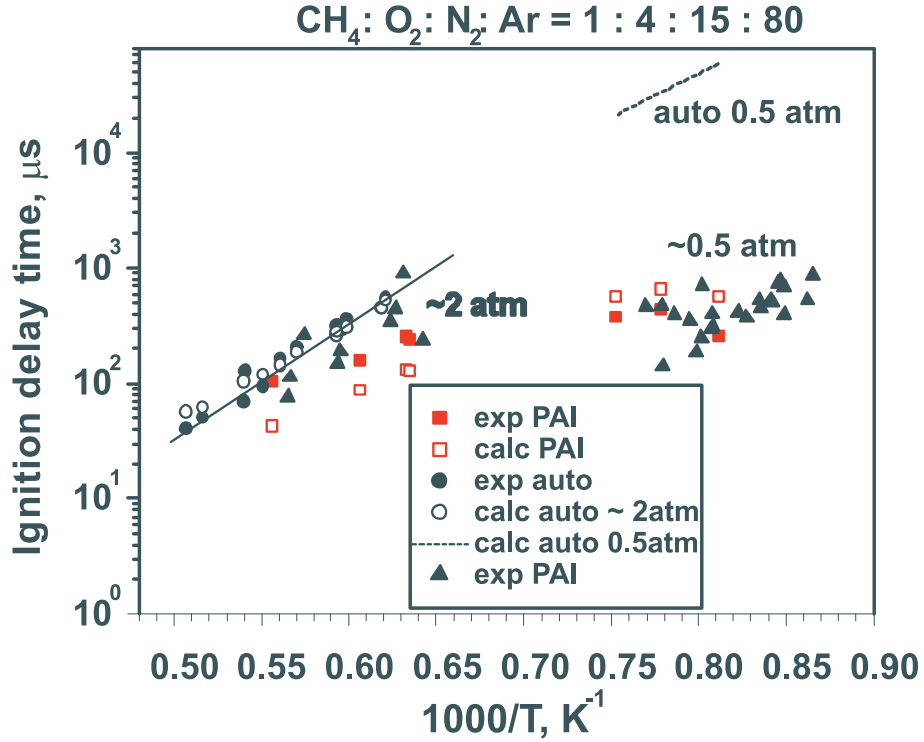


Figure 10.7: The delay time for autoignition (circles) and plasma-assisted ignition (squares and triangles) in a $\text{CH}_4:\text{O}_2:\text{N}_2:\text{Ar} = 1:4:15:80$ mixture as a function of gas temperature for various gas pressures. Closed symbols correspond to measurements and open symbols correspond to calculations. The solid curve is an approximation of the measured autoignition delay time and the dash curve corresponds to the calculated autoignition delay time at 0.5 atm. Red symbols correspond to the conditions under which time-resolved discharge current and electric field were measured during the discharge.

+ $\text{CH}_4 \rightarrow \text{products}$ (see [100]). Our calculations showed that reaction (R38) does not affect noticeably the results. The rate coefficient for reaction (R51) was similar to that used in [38]. It is worth noting that the magnitude of the rate coefficient for reaction (R51) could affect only the composition of positive ions and does not affect the density and composition of neutral active particles after the plasma decay. The scheme of ion-molecule reactions given in Tab. 10.2 is somewhat oversimplified. Additional calculations taking into account a more detailed scheme showed that the dominant positive ion in the discharge afterglow could be HCO^+ rather than O_2^+ , the ion species dominating according to the calculations based on the kinetic scheme from Tab. 10.2. However, the calculated density of neutral active particles is not sensitive to ion composition, and most of the calculations were carried out based on the reactions given in Tab. 10.2.

The density of vibrationally excited N_2 molecules participating in reaction (R25) was calculated under the assumption that the distribution of molecules over vibrational states is an equilibrium one with the temperature being equal to the gas temperature T . In this case, the fraction of N_2 molecules in the v -th vibrational state was expressed as $\delta v = (1 - z)z^v$, where $z = \exp(-\hbar\omega/T)$ and $\hbar\omega$ is the vibrational spacing of N_2 . Here, we neglected the effect of anharmonicity on excitation energies.

Table 10.2: The kinetic scheme of processes taken into account to simulate the production of atoms and radicals by gas discharge in CH₄:O₂:N₂:Ar mixture (T is in K)

Number	Reaction	Rate constant, cm ³ s ⁻¹	Reference
Electron impact dissociation			
R1	$e + O_2 \rightarrow e + O + O$	$f(E/n_5)$	see text
R2	$e + CH_4 \rightarrow e + CH_3 + H$	$f(E/n_5)$	see text
R3	$e + N_2 \rightarrow e + N + N$	$f(E/n_5)$	see text
Electron impact excitation			
R4	$e + O_2 \rightarrow e + O_2^*$	$f(E/n_5)$	see text
R5	$e + Ar \rightarrow e + Ar^*$	$f(E/n_5)$	see text
R6	$e + N_2 \rightarrow e + N_2(A^3\Sigma_u^+)$	$f(E/n_5)$	see text
R7	$e + N_2 \rightarrow e + N_2(B)$	$f(E/n_5)$	see text
N ₂ (B): N ₂ (B ³ Π _g), N ₂ (B ³ Σ _u ⁻), N ₂ (W ³ Δ _u)			
R8	$e + N_2 \rightarrow e + N_2(a)$	$f(E/n_5)$	see text
N ₂ (a): N ₂ (a ¹ Π _g), N ₂ (a ¹ Σ _u ⁻), N ₂ (w ¹ Δ _u)			
R9	$e + N_2 \rightarrow e + N_2(C^3\Pi_u)$	$f(E/n_5)$	see text
Electron impact ionization			
R10	$e + Ar \rightarrow 2e + Ar^+$	$f(E/n_5)$	see text
R11	$e + O_2 \rightarrow 2e + O_2^+$	$f(E/n_5)$	see text
R12	$e + CH_4 \rightarrow 2e + CH_4^+$	$f(E/n_5)$	see text
R13	$e + N_2 \rightarrow 2e + N_2^+$	$f(E/n_5)$	see text
Quenching of excited Ar			
R14	$Ar^* + O_2 \rightarrow Ar + 2O$	2×10^{-10}	[19]
R15	$Ar^* + CH_4 \rightarrow Ar + CH_2 + 2H$	3.3×10^{-10}	[23]–[25]
R16	$Ar^* + CH_4 \rightarrow Ar + CH + H + H_2$	5.8×10^{-11}	[23]–[25]
R17	$Ar^* + CH_4 \rightarrow Ar + CH_3 + H$	5.8×10^{-11}	[23]–[25]
R18	$Ar^* + CH_4 \rightarrow Ar + CH_2 + H_2$	5.8×10^{-11}	[23]–[25]
R19	$Ar^* + N_2 \rightarrow Ar + N_2(C^3\Pi_u)$	1.5×10^{-11}	[19]
R20	$Ar^* + N_2 \rightarrow Ar + N_2(B^3\Pi_g)$	1.5×10^{-11}	[19]
Quenching of excited N ₂			
R21	$N_2(A^3\Sigma_u^+) + O_2 \rightarrow N_2 + 2O$	1.7×10^{-12}	[[106, 107]]
R22	$N_2(A^3\Sigma_u^+) + O_2 \rightarrow N_2 + O_2(b^1\Sigma_g^+)$	7.5×10^{-13}	[[106, 107]]
R23	$N_2(A^3\Sigma_u^+) + N_2(A^3\Sigma_u^+) \rightarrow N_2 + N_2(B^3\Pi_g)$	7.7×10^{-11}	[108]
R24	$N_2(A^3\Sigma_u^+) + N_2(A^3\Sigma_u^+) \rightarrow N_2 + N_2(C^3\Pi_u)$	1.6×10^{-10}	[109]
R25	$N_2(A^3\Sigma_u^+) + N_2(v>4) \rightarrow N_2 + N_2(B^3\Pi_g)$	$10^{-10} \exp(-1500/T)$	[110]
R26	$N_2(A^3\Sigma_u^+) + O \rightarrow N_2 + O$	3×10^{-11}	[111]
R27	$N_2(B^3\Pi_g) + O_2 \rightarrow N_2 + 2O$	3×10^{-10}	[110]
R28	$N_2(B^3\Pi_g) + N_2 \rightarrow N_2(A^3\Sigma_u^+) + N_2$	1×10^{-11}	[110, 108]
R29	$N_2(a^1\Sigma_u^-) + O_2 \rightarrow N_2 + 2O$	2.8×10^{-11}	[112]
R30	$N_2(a^1\Sigma_u^-) + N_2 \rightarrow N_2 + N_2$	2×10^{-13}	[112]
R31	$N_2(C^3\Pi_u) + O_2 \rightarrow N_2 + 2O$	3×10^{-10}	[27]
R32	$N_2(C^3\Pi_u) + N_2 \rightarrow N_2(a^1\Sigma_u^-) + N_2$	1×10^{-11}	[27]
R33	$N_2(C^3\Pi_u) \rightarrow N_2(B^3\Pi_g) + \hbar\omega$	$3 \times 10^7 \text{ s}^{-1}$	[27]
R34	$N_2(A^3\Sigma_u^+) + CH_4 \rightarrow N_2 + CH_4$	3×10^{-15}	[100, 113]
R35	$N_2(B^3\Pi_g) + CH_4 \rightarrow N_2(A^3\Sigma_u^+) + CH_4$	2.85×10^{-10}	[113, 114]
R36	$N_2(B^3\Pi_g) + CH_4 \rightarrow N_2 + CH_4$	1.5×10^{-11}	[113, 114]
R37	$N_2(a^1\Sigma_u^-) + CH_4 \rightarrow N_2 + CH_4$	3×10^{-10}	[113, 114]
Quenching of excited O ₂			
R38	$O_2^* + CH_4 \rightarrow O_2 + \text{products}$	3×10^{-15}	estimate based on [100]
R39	$O_2^* + O_2 \rightarrow O_2(a^1\Delta_g) + O_2$	1.86×10^{-13}	[17]
R40	$O_2^* + O_2 \rightarrow O_2(b^1\Sigma_g^+) + O_2$	8.1×10^{-14}	[17]
R41	$O_2^* + O_2 \rightarrow O_2 + O_2$	2.3×10^{-14}	[17]
R42	$O_2^* + O \rightarrow O_2 + O$	5.0×10^{-12}	[17]
R43	$O_2^* + O \rightarrow O_2(a^1\Delta_g) + O$	2.7×10^{-12}	[17]
R44	$O_2^* + O \rightarrow O_2(b^1\Sigma_g^+) + O$	1.35×10^{-12}	[17]
Charge exchange			
R45	$Ar^+ + N_2 \rightarrow Ar + N_2^+$	5×10^{-11}	[26]
R46	$Ar^+ + CH_4 \rightarrow Ar + CH_3^+ + H$	1.1×10^{-9}	[26]
R47	$Ar^+ + CH_4 \rightarrow Ar + CH_2^+ + H_2$	2.3×10^{-10}	[26]
R48	$Ar^+ + O_2 \rightarrow Ar + O_2^+$	1×10^{-10}	[26]
R49	$N_2^+ + CH_4 \rightarrow N_2 + CH_3^+ + H$	1.3×10^{-9}	[26]
R50	$N_2^+ + O_2 \rightarrow N_2 + O_2^+$	$6 \times 10^{-11} (300/T)^{1/2}$	[27]
R51	$CH_4^+ + O_2 \rightarrow CH_4 + O_2^+$	5×10^{-10}	estimate [38]
Electron-ion recombination			
R52	$e + O_2^+ \rightarrow O + O$	$2 \times 10^{-7} (300/T)$	[27]

R53	$e + \text{CH}_4^+ \rightarrow \text{CH}_3 + \text{H}$	$1.7 \times 10^{-7} (300/T)^{1/2}$	[28, 29]
R54	$e + \text{CH}_4^+ \rightarrow \text{CH}_2 + 2\text{H}$	$1.7 \times 10^{-7} (300/T)^{1/2}$	[28, 29]
R55	$e + \text{CH}_3^+ \rightarrow \text{CH}_2 + \text{H}$	$3.5 \times 10^{-7} (300/T)^{1/2}$	[28, 29]
R56	$e + \text{CH}_2^+ \rightarrow \text{CH} + \text{H}$	$2.5 \times 10^{-7} (300/T)^{1/2}$	[28, 29]

The rate coefficients for electron impact dissociation (reactions (R1)-(R3)), for electron impact excitation (reactions (R4)-(R9)), and for electron impact ionization (reactions (R10)-(R13)) were calculated as a function of E/n_5 . We used the standard BOLSIG+ software [22] to solve the electron Boltzmann equation numerically in the classical two-term approximation [20] to determine the nonequilibrium electron energy distribution. In solving the Boltzmann equation, the input parameters were the reduced electric field E/n , gas temperature and gas composition. The electron distribution was not sensitive to gas temperature under the conditions considered. We considered only electron collisions with atoms and molecules of the dominant species in the gas mixture, O_2 , N_2 , CH_4 , and Ar. The effect of electron-electron and electron-ion collisions and collisions between electrons and new particles produced in the discharge was neglected because of the low density of these particles.

For electron collisions with O_2 , N_2 , CH_4 , and Ar, we used the self-consistent sets of cross sections, available in the literature, which allow good agreement between calculations and measurements of transport and rate coefficients in the pure gases. Fig. 10.8 show N_2 [22], which was used in our simulation. We took into account elastic scattering of electrons, rotational and vibrational excitation and dissociation of O_2 , N_2 and CH_4 and electronic excitation and ionization of O_2 , N_2 , CH_4 , and Ar. To estimate the effect of the uncertainty in electron cross sections on the calculated results, we made calculations with various sets of cross sections; in some cases, for Ar, the cross sections taken from [21] were replaced with those taken from [22], and for O_2 , the cross sections taken from [18] were replaced by those taken from [16]. It turned out that the calculated ignition delay time is insensitive to such replacements.

There is also some uncertainty in the electron impact dissociation cross section for CH_4 (see [115, 116]). Our calculations showed that this uncertainty is unimportant; indeed, halving the dissociation cross section used in this work led only to a 10% (or less) increase in ignition delay time.

Electron impact dissociation of N_2 occurs via the excitation of electronically excited N_2 states with high excitation energy followed by predissociation of these states [110]. We calculated the rate coefficient for this reaction (reaction (R3)) using the dissociation cross section [117].

10.3.2 Kinetic model for autoignition and plasma assisted ignition

The evolution in time of the density of all neutral active particles in the ignition phase was simulated on the basis of a numerical solution of the corresponding balance equations:

$$\frac{dX_k}{dt} = Q_k(T) - R_k(T), \quad (10.1)$$

where $[X_k]$ is the molar concentration of particles of the k-th species, T is the temperature, Q_k and R_k are, respectively, the total rate of production and the total rate of

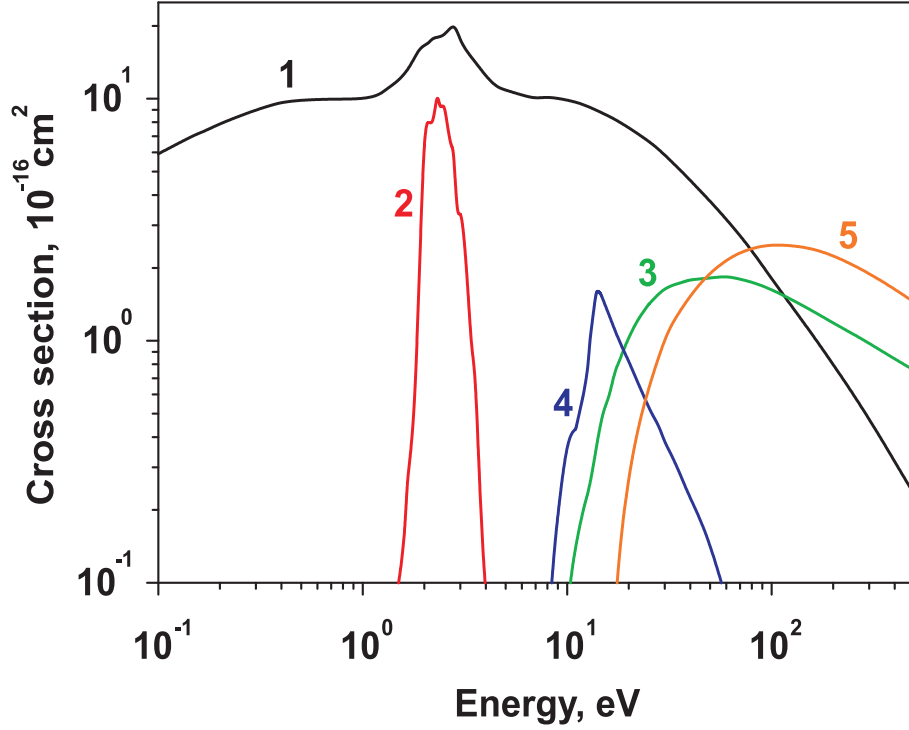


Figure 10.8: Electron collision cross sections for N_2 [22] as a function of electron energy: (1) momentum transfer in elastic collisions, (2) vibrational excitation, (3) excitation of the singlet electronic states, (4) excitation of the triplet electronic states, and (5) ionization.

decomposition of these particles. The energy conservation equation was simultaneously solved to follow temperature evolution in the ignition phase:

$$\frac{dT}{dt} = -\frac{1}{\rho c_p} \sum H_k(T) \frac{[X_k]}{dt}, \quad (10.2)$$

where ρ is the mass density, c_p is the mean specific heat capacity at constant pressure and H_k is the molar enthalpy of particles of the k -th species.

The system of equations (10.1) and (10.2) was numerically solved in the zero-dimensional approximation using the CHEMKIN code [84]. Algorithm of this code was developed to solve systems of stiff ordinary differential equations and is based on the Gear-type procedure [51] with an adapted time step. The input parameters were pressure and initial gas temperature and composition.

Most of the simulations of the ignition process were carried out using the kinetic mechanism suggested in [118]. The mechanism [118] includes 127 particle species and 1200 reactions. Some calculations were also made on the basis of the GRI-Mech 3.0 mechanism [119].

Calculations were carried out at fixed gas pressure. Ignition delay time was defined as the interval between the instant at which active particles were injected and the onset of the effective production of unexcited OH radicals in the ignition phase (see Fig. 10.6). Obtained ignition delay times were compared with the measurement carried out using the intensity of radiation from the excited OH ($A^2 \Sigma^+$) state. It was shown in [38] that the densities of the excited and unexcited OH radicals vary in time in a similar way and

that ignition delay time determined using the densities of the excited radicals differs by only several microseconds (i) from that determined using the densities of the ground-state radicals and (ii) from that determined using the calculated evolution of gas temperature. This difference is within the experimental error of the measurement of ignition delay time.

10.3.3 Calculated results for discharge processes

In discharges, the energy gained by electrons from external electric field is lost in collisions with neutral particles. Electron heating and the efficiency of electron impact excitation of various states are governed by the reduced electric field, E/n , (n is the gas number density) and by the composition of gaseous mixtures [30]. Let us compare electron characteristics in a $\text{CH}_4:\text{O}_2:\text{N}_2:\text{Ar} = 1:4:15:80$ mixture considered in this work and those in a $\text{CH}_4:\text{O}_2:\text{Ar} = 1:4:95$ mixture in which N_2 is replaced by Ar. Fig. 10.9 shows the calculated mean electron energy in these mixtures versus E/n . The calculation was carried out using a numerical solution of the Boltzmann equation.

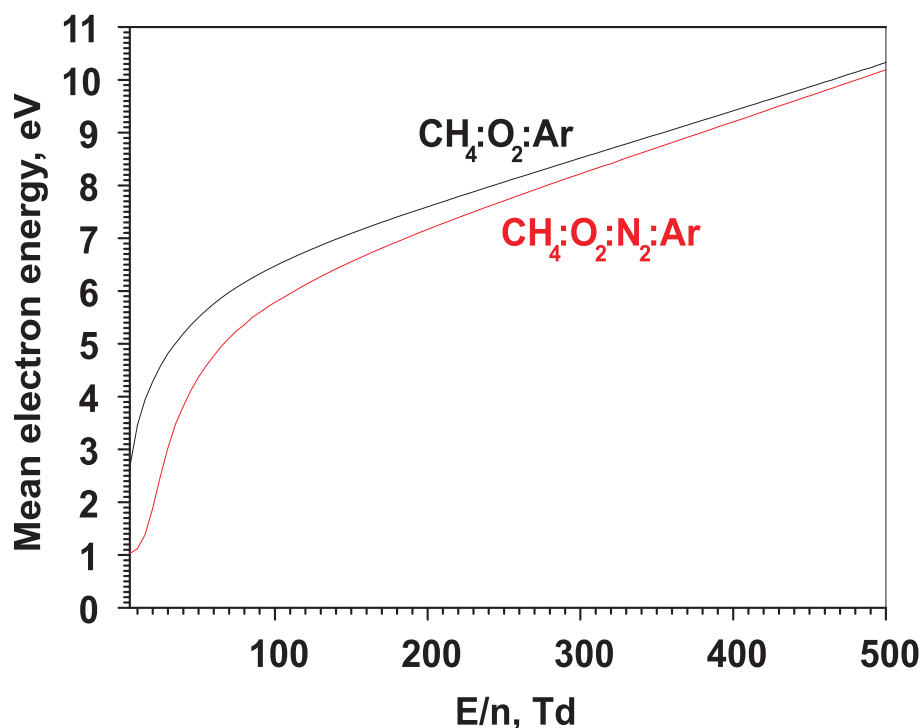


Figure 10.9: Mean electron energy in $\text{CH}_4:\text{O}_2:\text{N}_2:\text{Ar} = 1:4:15:80$ and $\text{CH}_4:\text{O}_2:\text{Ar} = 1:4:95$ mixtures as a function of reduced electric field ($1 \text{ Td} = 10^{-17} \text{ V cm}^2$).

The addition of N_2 leads to a noticeable decrease in the mean electron energy for all values of E/n . This is explained in the following way. As opposed to Ar, electrons efficiently lose their energy to excite vibrational states of N_2 . In addition, the cross sections for electron impact excitation of electronic states of N_2 are noticeably higher than the cross sections for electron impact excitation of electronic states of Ar and the excitation energy thresholds for N_2 are lower than those for Ar (see Fig. 4.8 and 10.8). As a result, in the N_2 -containing mixture, at a given value of E/n , the efficiency of production of active

particles by electron impact is expected to differ noticeably from that of production of active species in the absence of N_2 .

To demonstrate the effect of N_2 addition on the production of active species, we calculated the fractional power transferred by electrons to neutral particles through various collisional mechanisms. Fig. 10.10 shows the calculated fractional power calculated in the $CH_4:O_2:N_2:Ar$ and $CH_4:O_2:Ar$ mixtures versus reduced electric field. It is worth noting that the results shown in Fig. 10.10(b) for a $CH_4:O_2:Ar = 1:4:95$ mixture are very similar to the results obtained in [38] for a $CH_4:O_2:Ar = 3.3:6.7:90$ mixture. It is most interesting to consider the effect on the production of O atoms, the active species playing the most important role in ignition of a stoichiometric $CH_4:O_2:Ar$ mixture by a high-voltage nanosecond discharge [102, 38]. Because of lower mean electron energies in the N_2 -containing mixture at given values of E/n , the production of O atoms peaks at higher values of E/n when adding N_2 ; this value of E/n is around 65 Td in the $CH_4:O_2:N_2:Ar$ mixture and 30 Td in the $CH_4:O_2:Ar$ mixture. What is more important, the peak value of the power transferred to electron impact O_2 dissociation decreases from 56 to 17 % when N_2 is added. This could lead to a much less efficient ignition by the discharge. However, a major portion of power (up to 27 %) is spent on excitation of the electronic excited $N_2(a'^1\Sigma_u^-)$, $N_2(A^3\Sigma_u^+)$, $N_2(B^3\Pi_g)$ and $N_2(C^3\Pi_u)$ states, which are efficiently quenched by O_2 to produce O atoms (see reactions (R21), (R27), (R29), and (R31) in Tab. 10.2).

The peak values of the reduced electric field under the conditions considered in the experiment [35] are given in Fig. 10.3. To estimate the efficiency of the discharge, it is more appropriate to use the values of E/n at the instant at which the current peaks. Indeed, this instant corresponds also to peak values of the deposited power $W(t)$ [38] and consequently to the most efficient production of active particles. It follows from Fig. 10.3 that the discharge has its strongest effect for the reduced electric fields in the range 70–100 Td at low pressures and in the range 45–65 Td at high pressures. Here, according to Fig. 10.10(a), the composition of active particles should be dominated by O atoms and excited electronic states of N_2 , which can be quenched by O_2 to form O atoms. At low values of E/n , vibrationally excited N_2 molecules are also produced. But, these excited molecules are useless to plasma-assisted ignition. At high values of E/n , a noticeable amount of electronically excited Ar is produced.

These atoms can also be quenched by O_2 to form O atoms (reaction (R14) in Tab. 10.2) and by CH_4 to form H atoms and radicals (reactions (R15)–(R18) in Tab. 10.2). However, this channel of production of active species is less efficient because the energy required to produce one excited Ar atom is more than the dissociation energy of O_2 by a factor of 2–3 and hence the amount of excited Ar atoms is expected to be lower than the amount of O atom produced in direct electron impact dissociation of O_2 and via quenching of electronically excited N_2 states with much lower excitation energies than the excitation energies of Ar.

To simulate the evolution in time of the densities of active particles in a high electric field during the discharge, we solved the balance equations numerically using the E/n -dependent electron rate coefficients. Temporal evolution of the electric field was taken from the measurements [35]. At the beginning of the first pulse of applied voltage (in the discharge front), there was generally a very short and high overshoot of the applied voltage that could not be experimentally resolved. During the corresponding peak of the electric field in the discharge gap, a noticeable amount of charged particles was produced,

whereas the production of neutral active particles was negligible. To take into account the production of electrons and ions in this phase, we considered the initial electron density at the beginning of the main pulses of applied voltage to be an adjusted parameter. This parameter was determined when the evolution in time of the discharge current was calculated and adjusted to corresponding measured data. It is also difficult to predict initial electron density at the beginning of the following pulses because between the pulses the plasma decays with the rate, which depends on ion composition and is unknown in our case. To overcome this difficulty, we also considered initial electron density at the beginning of the following pulses to be a parameter, which was adjusted in a similar way.

As an example, Fig. 10.2 compares the temporal evolution of the calculated discharge current and that of the measured current under the same conditions. The calculations were based on the temporal evolution of the electric field shown in Fig. 10.1. The discharge current was determined using the calculated values of electron density and electron drift velocity calculated from the Boltzmann equation as a function of E/n_5 . The method used allowed good agreement between the measured and calculated currents to be obtained. Good agreement was also obtained between the calculated and measured values of specific deposited energy (see Fig. 10.4 and 10.5).

Fig. 10.11 and 10.12 show the evolution in time of the mole fractions of active species in the discharge afterglow, respectively, at low and high pressures, whereas the mole fractions of O, H, and CH₃ at the end of the afterglow are given in Tab. 10.1. Here we took into account dissociation of O₂ via quenching of N₂($A^3\Sigma_u^+$), N₂($B^3\Pi_g$), N₂($a'^1\Sigma_u^-$), and N₂($C^3\Pi_u$) states and neglected dissociation of O₂ via quenching of N₂($B'^3\Sigma_u^-$), N₂($W^3\Delta_u$), N₂($a^1\Pi_g$), and N₂($w^1\Delta_u$) states. At all pressures the dominant active species is O atoms.

Their mole fraction is almost an order of magnitude higher than the mole fractions of other species. (It should be noted that O atoms also dominated in a CH₄:O₂:Ar=3.3:6.7:90 mixture after the discharge [38]; however, in the absence of N₂, the fraction of O was comparable with the fractions of H and CH₃.) The fractions of all excited and charged particles decrease with time after the discharge, whereas the fractions of O and of other atoms and radicals increase in time. The reason is that in the afterglow electrons and positive ions recombine fast to produce atoms and excited particles are generally quenched on a nanosecond scale to produce atoms and radicals (see Tab. 10.2). In our kinetic model, in the end, charged and excited particles were excluded from the consideration and the gas mixture was assumed to consist of initial neutral species and atoms and radicals produced during the discharge and in its afterglow. The densities of atoms and radicals were used further as input parameters to simulate ignition.

From Fig. 10.11 and 10.12, the fractions of active species produced by the discharge at low pressures are an order of magnitude higher than those produced by the discharge at high pressures. This is associated with higher specific energies deposited per one particle in the discharge at low pressures (see Fig. 10.4 and 10.5). Fig. 10.13 shows the mole fractions of atoms and radicals produced by the discharge versus the gas number density behind the reflected shock wave, n_5 . Here, an increase in n_5 from 2×10^{18} to 8×10^{18} cm⁻³ leads to a decrease in the mole fraction of O atoms from 3×10^{-3} to 5×10^{-4} . This means that the absolute density of O atoms produced by the discharge decreases by a factor of 1.5 as the pressure increases from ~ 0.5 to ~ 2 atm. The densities of other atoms and radicals behave in a similar way. It should be noted that the discharge characteristics and production of active species are not sensitive to gas temperature [38].

In the simulation, we neglected gas heating during the discharge and in its afterglow. To estimate an increase in gas temperature in this phase, we carried out additional calculations. According to Fig. 10.3 and 10.10(a), most of the energy deposited by the discharge is lost to excite electronic and vibrational states of N_2 and to dissociate O_2 . In our case, vibrationally excited N_2 molecules has no time to transfer the excitation energy into gas heating because the rates of VT processes are too low. It is known (see, for instance, [104]) that around 30 % of the energy spent in high-voltage discharges in air on excitation of electronic states and dissociation of N_2 and O_2 is fast (for a time of $\sim 1 \mu s$) transferred to gas heating. Based on this statement, we calculated gas heating in the discharge and in its afterglow under the conditions considered. It turned out that in this case the gas temperature increased only by 50 K, the value comparable with the error of temperature measurement in the experiment under study.

10.3.4 Calculated results for autoignition and plasma assisted ignition

We calculated autoignition delay time under the conditions of the experiment [35]. Fig. 10.7 compares the calculated results obtained using the kinetic scheme [118] and autoignition delay times measured in [35] at ~ 2 atm. There is good agreement between the calculations and measurements. Autoignition delay time was not measured in [35] at low (~ 0.5 atm) pressures because this time was longer than the time of operation of the shock tube used. To show the effect of gas discharge at low pressures, in a similar way we calculated autoignition delay time also at 0.5 atm. It is seen from Fig. 10.7 that at low pressures the delay time after the discharge is two orders of magnitude shorter than the calculated autoignition delay time; that is, the effect of non-equilibrium plasma on ignition is profound.

Fig. 10.14 compares the autoignition delay time calculated on the basis of the kinetic scheme [118] and on the basis of the kinetic scheme [119], the gas parameters being the same and corresponding to the measurements [35]. The difference between these calculated results does not exceed 30 %. The calculations using the data [118] agree somewhat better with the experiment and in the following we used only this kinetic scheme to study plasma assisted ignition.

It is interesting to compare autoignition delay times in $CH_4:O_2:N_2:Ar = 1:4:15:80$ and $CH_4:O_2:Ar = 1:4:95$ mixtures. We carried out these calculations and obtained the same results. The replacement of N_2 by Ar does not affect autoignition process and consequently the role of N_2 in autoignition is negligible.

We simulated plasma-assisted ignition for gas parameters corresponding to the measurements [35] and using time-resolved measurements of the electric field and current in the discharge phase. Fig. 10.6 shows the evolution in time of the calculated density of unexcited OH radical, which agrees well with the evolution of the emission intensity for excited OH radicals.

Fig. 10.7 compares the ignition delay times calculated from the evolution of the density of OH with measured ignition delay times. The effect of non-equilibrium plasma is most profound at low (~ 0.5 atm) pressures at which the injection of atoms and radicals produced by the discharge leads to a two-orders-of-magnitude decrease in the ignition delay time with respect to autoignition, the calculated ignition delay time after the dis-

charge being in good agreement with the observations. At high pressures, the effect of the discharge on ignition delay time does not exceed 100%. In this case, the difference between calculated and measured ignition delay times after the discharge could reach up to 100%, much higher than that at low pressures. The possible reason for this difference may be associated with a non-uniformity of the discharge development registered in [35] at high pressures. Our zero-dimensional computational model of the discharge and ignition processes seems to be less appropriate in this case. The reason that the effect of the discharge on ignition delay is less profound at high pressures is related with lower specific energy deposited per one particle and consequently with lower fraction of active particles produced by the discharge.

To clarify the effect of N_2 addition on ignition delay time after the discharge, we carried out additional calculations for a $CH_4:O_2:Ar = 1:4:95$ mixtures and for a $CH_4:O_2:N_2:Ar = 1:4:15:80$ mixture when quenching of excited N_2 molecules by O_2 to form O atoms (reactions (R21), (R27), (R29), and (R31) in Tab. 10.2) was neglected. Fig. 10.15 shows the obtained results, which are more profound at low pressures when the mole fraction of active species is higher. Here, the effect of N_2 addition on the electron energy distribution and on the rates of electron impact production of active species in the discharge manifests itself when comparing ignition delay time for the $CH_4:O_2:Ar$ mixture and those for the $CH_4:O_2:N_2:Ar$ mixture, the formation of O atoms via quenching of electronically excited N_2 molecules being excluded. In this case, the addition of N_2 leads to an order-of-magnitude increase in ignition delay time. Taking into account the production of O atoms via the electronically excited N_2 molecules leads to a decrease in ignition delay time by a factor of 3-4. As a result, the transition for the $CH_4:O_2:Ar$ mixture to the $CH_4:O_2:N_2:Ar$ mixture leads only to an increase in ignition delay time after the discharge by a factor of ~ 3 . Here, when considering the formation of O atoms via excited N_2 molecules, we took into account only the $N_2(A^3\Sigma_u^+)$, $N_2(B^3\Pi_g)$, $N_2(a'^1\Sigma_u^-)$, and $N_2(C^3\Pi_u)$ states. In [104], it was suggested that dissociation of O_2 can occur also via the quenching of $N_2(B'^3\Sigma_u^-)$, $N_2(W^3\Delta_u)$, $N_2(a^1\Pi_g)$ and $N_2(w^1\Delta_u)$ states. We also carried out calculation considering these states. It follows from Fig. 10.15 that in this case agreement between the measurements and calculations for 0.5 atm is much better.

Fig. 10.16(a) and 10.16(b) show the evolution in time of the mole fractions for the main components in the N_2 -containing mixture during autoignition and plasma-assisted ignition, respectively. The curves shown in these figures are similar to those calculated in [38] for autoignition and ignition by the discharge in the absence of N_2 . By analogy with autoignition of $CH_4:O_2:Ar$ mixtures, in the induction phase of autoignition, the composition of radicals and atoms is dominated by CH_3 . Here, the fractions of H_2O , H_2 , and CO increase gradually, whereas the fractions of O, H, and OH remain one to two orders of magnitude lower and become important only after 1 ms, at the point of ignition. In the case of plasma-assisted ignition, the excess of O and, to a smaller degree, of H at the beginning of the ignition phase leads to an essential change in fuel composition already after 1 μs , when the fractions of H_2O , H_2 , and CO become comparable to the initial fractions of the injected atoms and radicals. A number of intermediate components (CH_2O , etc.) are important in the induction phase of plasma-assisted combustion. The gas temperature remains practically constant in the induction phase of autoignition and increases gradually after the discharge. Here, by analogy with the plasma-assisted ignition processes in $CH_4:O_2:Ar$ mixtures (see [38]), the production of atoms and radicals by the

discharge leads to a fast initiation of chain reactions due to shortening of the time of chain formation. The role of N_2 in the ignition processes turns out to be negligible.

Our calculations showed that under the conditions studied the dominant active species produced by the discharge is O atoms (see Fig. 10.11– 10.13). It is interesting to determine the conditions under which the production of O atoms by a non-equilibrium plasma is most efficient. For this purpose, we calculated the energy cost of production of O atoms, w_O , for various reduced electric fields E/n . The energy cost was defined as the ratio between the power deposited per unit volume in a discharge maintained at an electric field E , jE , and the rate of production of O atoms; in the simplest case when O atoms are produced by electron impact dissociation of O_2 this rate is equal to $2k_1n_e[O_2]$, where k_1 is the rate constant of reaction (R1), n_e is the electron density and $[O_2]$ is the density of O_2 . Taking into account that the current density is $j = en_e w_e$ (w_e is the electron drift velocity), we have

$$w_0 = \frac{w_e \frac{eE}{n}}{2k_1\delta_{O_2}}, \quad (10.3)$$

where $\delta_{O_2} = [O_2]/n$ is the mole fraction of O_2 in a mixture. When O atoms are also produced via quenching of electronically excited N_2 molecules in collisions with O_2 (reactions (R21), (R27), (R29) and (R31)) and via quenching of excited Ar atoms (reaction (R14)), equation (10.3) should be extended to

$$w_O = \frac{w_e \frac{eE}{n}}{2k_1\delta_{O_2} + 2\delta_{N_2}(k_6p_A + k_7p_B + k_8p_a + k_9p_C) + 2\delta_{Ar}k_5p_{Ar*}}, \quad (10.4)$$

where $\delta_{N_2} = [N_2]/n$ is the mole fraction of N_2 , $\delta_{Ar} = [Ar]/n$ is the mole fraction of Ar, k_6 , k_7 , k_8 , k_9 and k_5 are, respectively, the rate constants for reactions (R6), (R7), (R8), (R9) and (R5), p_A , p_B , p_a and p_C are, respectively, the probabilities that the $N_2(A^3\Sigma_u^+)$, $N_2(B)$, $N_2(a)$ and $N_2(C^3\Pi_u)$ states are quenched to dissociate O_2 and p_{Ar*} is the probabilities that the Ar^* state is quenched to dissociate O_2 .

Based on (10.4), we calculated the energy cost w_O (i) using a numerical calculation of the electron Boltzmann equation to determine the electron drift velocity and electron impact rate coefficients and (ii) obtaining the probabilities p_A , p_B , p_a , p_C and p_{Ar*} on the basis of the quenching rate coefficients from Tab. 10.2. Fig. 10.17 shows the calculated values of w_O in the $CH_4:O_2:N_2:Ar$ and $CH_4:O_2:Ar$ mixtures as a function of the reduced electric field. The calculations were carried out taking into account the production of O atoms due to direct electron impact dissociation of O_2 and due to quenching of electronically excited N_2 and Ar states by O_2 molecules. To show the effect of electronically excited N_2 states, the calculations were also made neglecting the formation of O in collisions between the excited N_2 states and O_2 . In our calculations, the least energy costs are obtained at the reduced electric fields at which electron impact dissociation of O_2 and electron impact excitation of the $N_2(A^3\Sigma_u^+)$, $N_2(B)$, $N_2(a)$ and $N_2(C^3\Pi_u)$ states occur (see Fig. 10.10). In the mixture with N_2 this occurs at 85-100 Td and, in the absence of N_2 , the mean electron energy is higher and w_O reaches its minimum value at 50 Td. We have $(w_O)_{min} = 7$ eV in the $CH_4:O_2:N_2:Ar$ mixture and $(w_O)_{min} = 6.3$ eV in the $CH_4:O_2:Ar$ mixture. At lower values of E/n the production of O is not efficient because of energy loss to the excitation of vibrational states and electronically excited states with low excitation energies whereas at higher E/n energy is spent on ionization. This energy could be useful for O production in dissociative electron-ion recombination (see reaction

(R52)); however, we did not consider this in the results shown in Fig. 10.17 since the ionization energy is much higher than the dissociation energy of O_2 and consequently this channel of O formation is not very efficient.

It follows from Fig. 10.3 that, in the experiment [35], the discharge occurred at the values of E/n at which the production of O atoms is efficient. Tab. 10.2 shows the values of w_O obtained under the conditions of the experiment [35]; these values were calculated as the ratio between the total energy input per one neutral particle (see Fig. 10.4 and 10.5) and the mole fraction of O atoms produced by the discharge (see Tab. 10.2 and Fig. 10.11(b) and 10.12(b)). The obtained energy costs w_O are twice as large as $(w_O)_{min}$ given in figure 18 (see the solid blue curve). This difference is associated with the fact that, during the discharge, the reduced electric field varied in time and could be higher and lower than that corresponding to $(w_O)_{min}$.

Comparison of the results presented in Fig. 10.17 for the $CH_4:O_2:N_2:Ar$ and $CH_4:O_2:Ar$ mixtures shows that, when neglecting the formation of O atoms in collisions between electronically excited N_2 molecules and O_2 , the energy cost of O production is noticeably higher in the N_2 -containing mixture. The difference is much greater at low reduced electric fields at which vibrational states of N_2 are efficiently excited. However, when taking into account dissociation of O_2 due to quenching of the electronically excited N_2 states, the difference between the energy costs for the mixtures under consideration becomes negligible at high (>80 Td) reduced electric fields.

It should be noted that the importance of the production of O atoms via the collisional quenching of electronically excited N_2 states by O_2 in air discharges was mentioned in [120, 104]. This mechanism of dissociation of O_2 was considered in [121, 72] when studying plasma assisted ignition and combustion in hydrocarbon-containing mixtures.

Thus, it may be concluded that, in N_2 -containing mixtures, O atoms are efficiently produced both due to direct electron impact dissociation of O_2 and due to electron impact excitation of N_2 states followed by their quenching in collisions with O_2 molecules. These mechanisms are important to plasma-assisted ignition of CH_4 -containing mixtures under the conditions studied.

10.4 Conclusions

A kinetic scheme was developed to describe the production of active particles (charged particles, excited particles, atoms and radicals) in a high-voltage nanosecond discharge in $CH_4:O_2:N_2:Ar$ mixtures. This scheme was used to calculate the evolution in time of active particles produced in a $CH_4:O_2:N_2:Ar = 1:4:15:80$ mixture in the discharge phase and in the near afterglow under the conditions of the experiment [12]. The study was made for gas temperatures in the range 1200 – 1800 K and gas pressures in the range 0.35 – 1.9 atm. The calculations were carried out on the basis of a numerical solution of the balance equations with the rate coefficients calculated using time-resolved measurements of discharge current and electric field.

The calculated results were compared with those obtained under similar conditions for a $CH_4:O_2:Ar = 1:4:95$ mixture. It was shown that the addition of N_2 leads (i) to a decrease in the mean electron energy for the same values of the reduced electric field and (ii) to a several times decrease in the fractional power transferred to direct electron impact dissociation of O_2 to form O atoms, the most important active species for ignition

in hydrocarbon-containing mixtures. This is associated with an efficient electron impact excitation of vibrational and electronic states of N_2 .

The calculations showed that, in the N_2 -containing mixture, O atoms are efficiently produced not only due to electron impact dissociation of O_2 , but due to electron impact excitation of electronically excited N_2 states followed by their quenching in collisions with O_2 . As a result, at the end of the discharge afterglow, the mole fraction of O atoms turns out to be an order of magnitude higher than the mole fractions of other active species. The fractions of O atoms and of other active species were higher in the discharge at lower pressures at which the specific energy deposited per one neutral particle in the discharge phase was higher.

The densities of active particles produced by the discharge were used as initial parameters for simulation of the ignition processes on the basis of a numerical solution of the corresponding balance equations and energy conservation equation. Ignition delay time was determined from the calculated results with and without the discharge. Good agreement was obtained between the calculated ignition delay times and experimental data.

It was shown that the effect of non-equilibrium plasma is most profound at low pressures at which the injection of atoms and radicals produced by the discharge leads to an order-of-magnitude decrease in the ignition delay time with respect to autoignition. At high pressures, the effect of the discharge on ignition delay time does not exceed 100

The analysis of simulation results showed that the effect of N_2 addition during plasma-assisted ignition of CH_4 -containing mixtures is reduced to a change in the densities of active species produced by the discharge due to a decrease in the mean electron energy in the discharge phase and to an additional production of O atoms via electronically excited N_2 molecules, whereas the direct effect of N_2 on ignition processes is negligible.

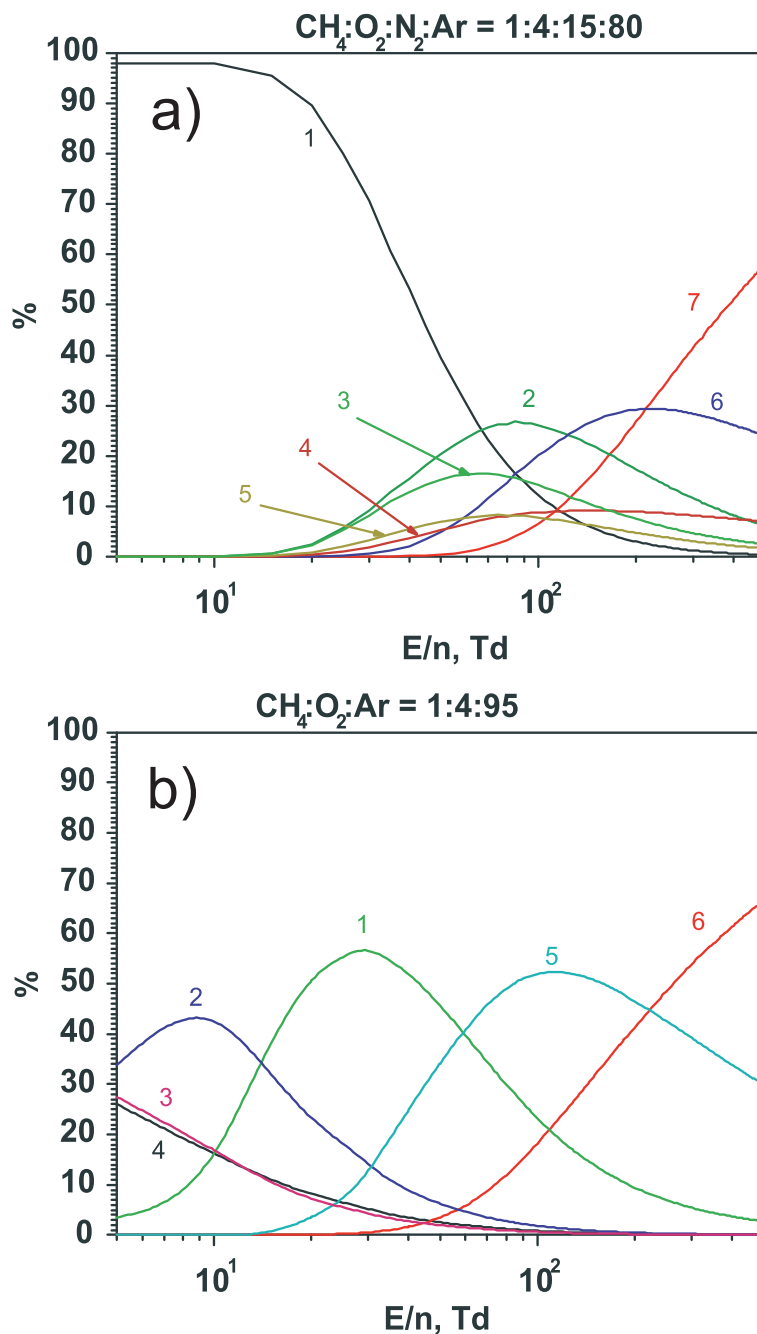


Figure 10.10: Fractional power transferred in (a) $\text{CH}_4:\text{O}_2:\text{N}_2:\text{Ar} = 1:4:15:80$ and (b) $\text{CH}_4:\text{O}_2:\text{Ar} = 1:4:95$ mixtures from electrons to neutral particles as a function of reduced electric field ($1 \text{ Td} = 10^{-17} \text{ V cm}^2$). The $\text{CH}_4:\text{O}_2:\text{N}_2:\text{Ar}$ mixture: (1) vibrational excitation of N_2 , (2) excitation of the $\text{N}_2(A^3\Sigma_u^+)$, $\text{N}_2(B^3\Pi_g)$, $\text{N}_2(a'^1\Sigma_u^-)$, and $\text{N}_2(C^3\Pi_u)$ states, (3) dissociation of O_2 , (4) excitation of other singlet N_2 states, (5) excitation of other triplet N_2 states, (6) excitation of Ar^* states, and (7) total ionization. The $\text{CH}_4:\text{O}_2:\text{Ar}$ mixture: (1) dissociation of O_2 , (2) excitation of the O_2 state with $\Delta E = 4.5 \text{ eV}$, (3) excitation of $\text{O}_2(a^1\Delta_g)$ and $\text{O}_2(b^1\Sigma_g^+)$ states, (4) vibrational excitation of O_2 , (5) excitation of Ar^* states, and (6) total ionization.

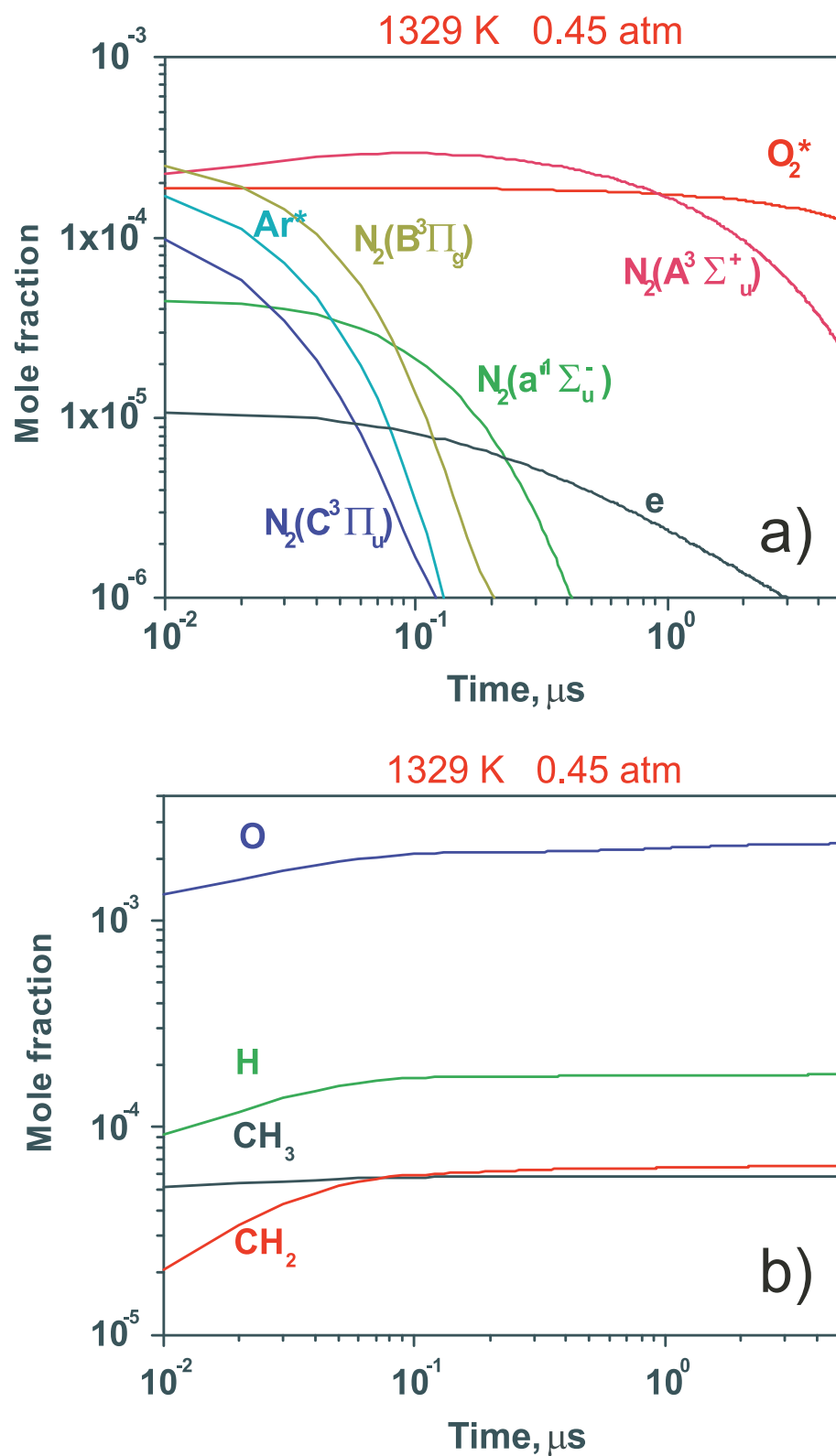


Figure 10.11: The evolution in time of the mole fractions for (a) electrons and excited particles and (b) atoms and radicals in the discharge afterglow in the $\text{CH}_4:\text{O}_2:\text{N}_2:\text{Ar}$ mixture at 1329 K and 0.45 atm.

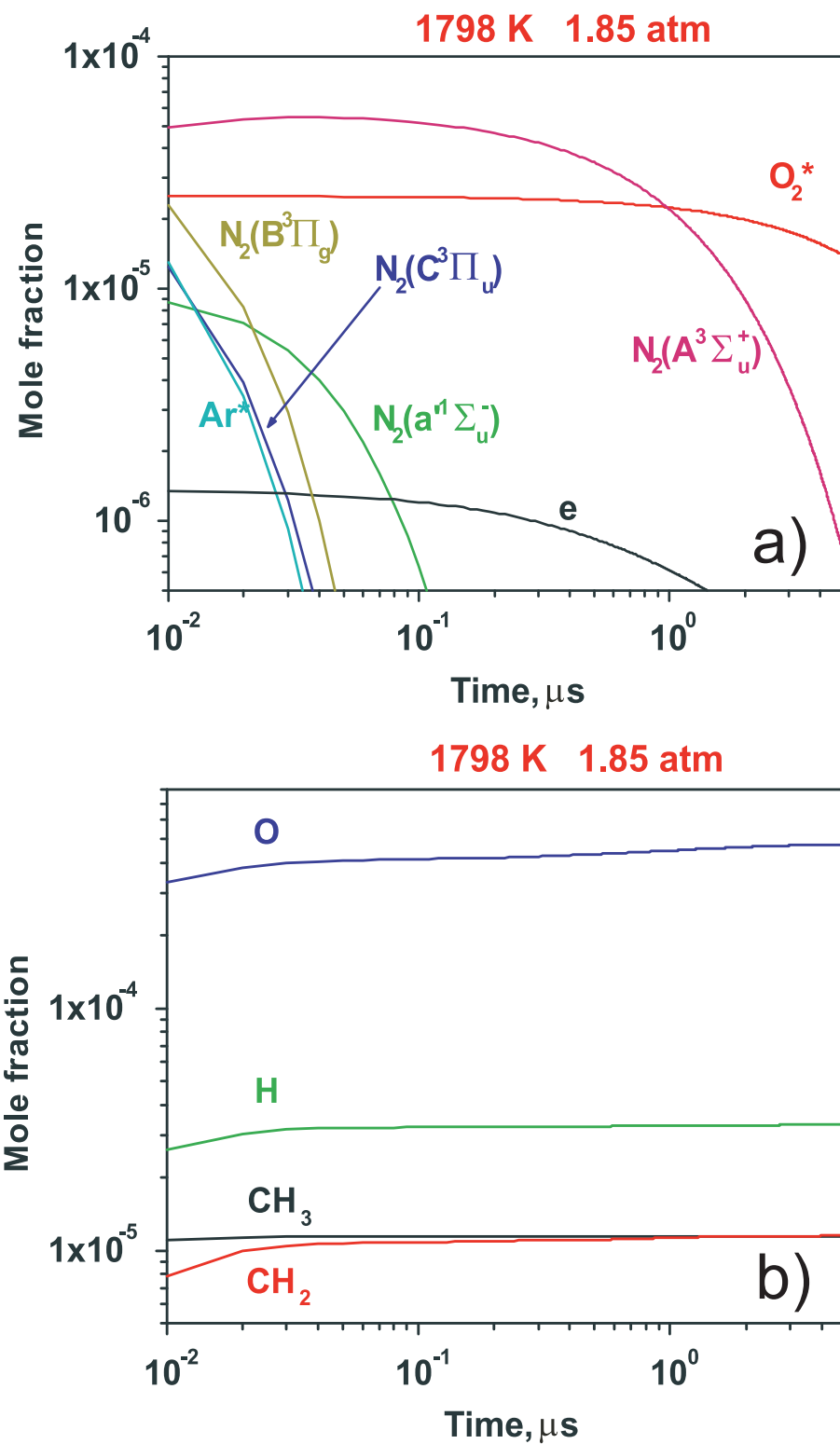


Figure 10.12: The evolution in time of the mole fractions for (a) electrons and excited particles and (b) atoms and radicals in the discharge afterglow in the $\text{CH}_4:\text{O}_2:\text{N}_2:\text{Ar}$ mixture at 1798 K and 1.85 atm.

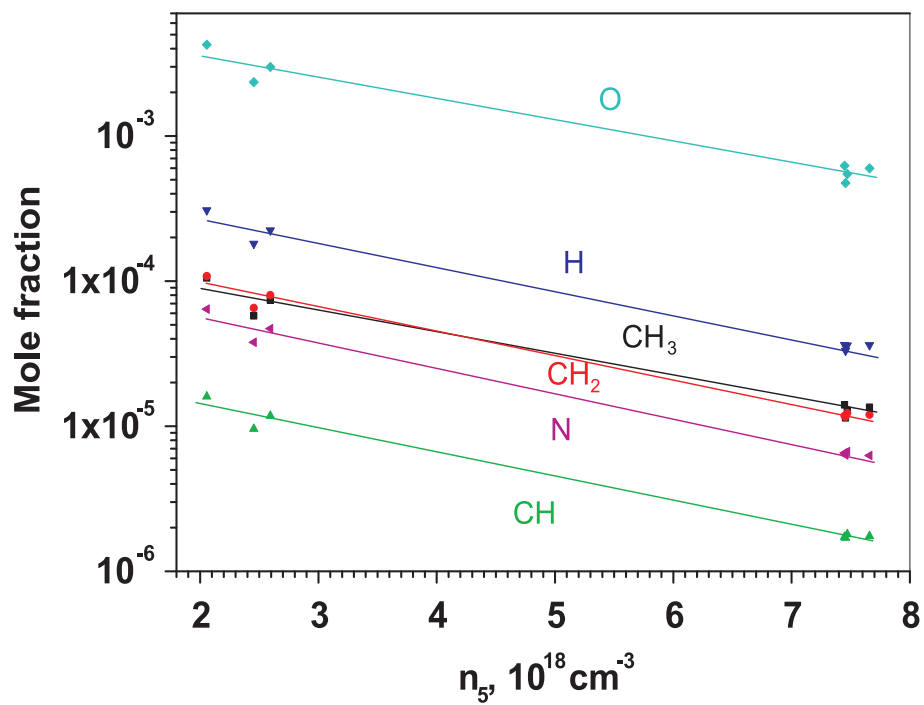


Figure 10.13: The calculated mole fractions of atoms and radicals produced by the discharge in the $\text{CH}_4:\text{O}_2:\text{N}_2:\text{Ar}$ mixture as a function of n_5 .

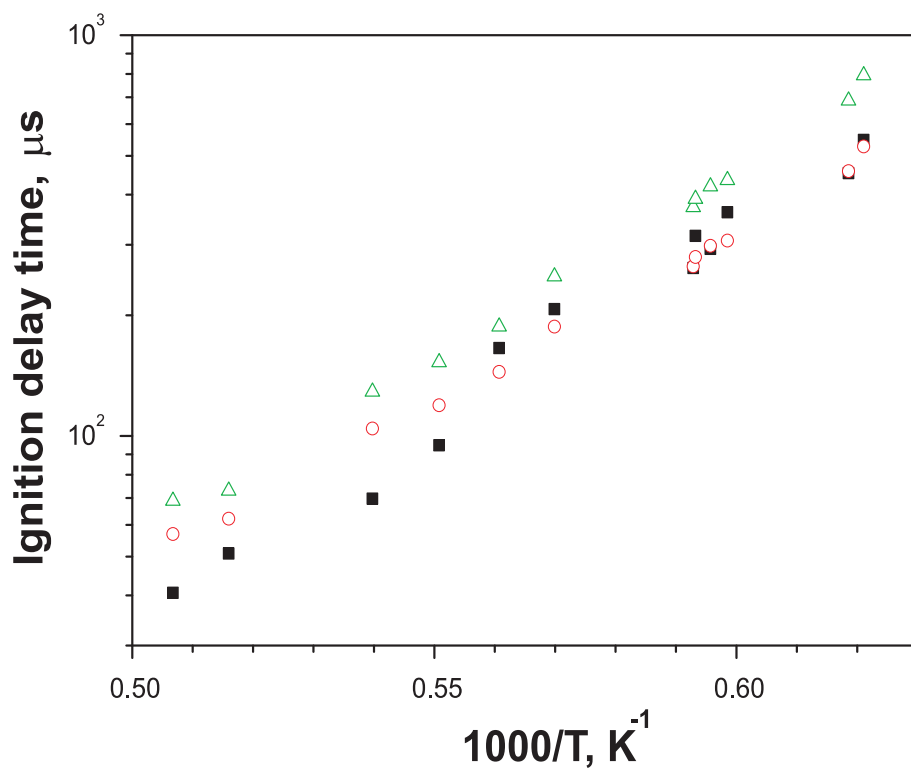


Figure 10.14: The autoignition delay time in the $\text{CH}_4:\text{O}_2:\text{N}_2:\text{Ar}$ mixture as a function of temperature. Closed symbols correspond to measurements and open circles and triangles correspond, respectively, to calculations using kinetic schemes from [118] and [119].

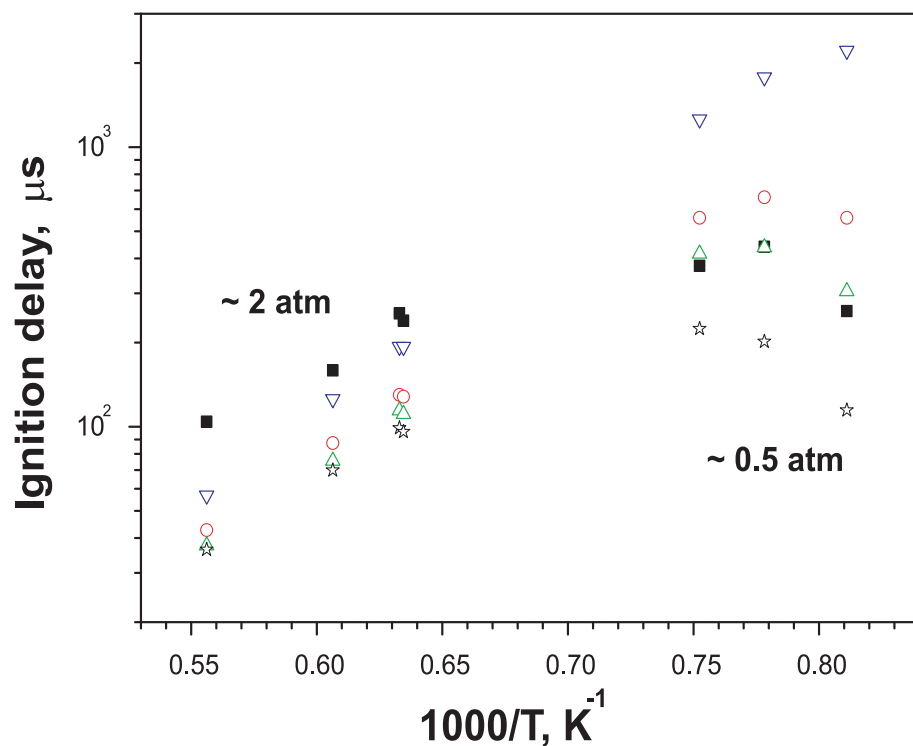


Figure 10.15: The delay time for ignition by the discharge in the $\text{CH}_4\text{:O}_2\text{:N}_2\text{:Ar}$ mixture as a function of temperature. Closed squares correspond to measurements, open circles correspond to calculations taking into account the formation of O via the $\text{N}_2(a')$, $\text{N}_2(A)$, $\text{N}_2(B)$ and $\text{N}_2(C)$ states, open triangles correspond to calculations taking into account the formation of O via the $\text{N}_2(a')$, $\text{N}_2(A)$, $\text{N}_2(B)$, $\text{N}_2(C)$, $\text{N}_2(B')$, $\text{N}_2(W)$, $\text{N}_2(a)$ and $\text{N}_2(w)$ states, open inverse triangles correspond to calculations neglecting the formation of O via excited N_2 states, and open stars correspond to calculations for a $\text{CH}_4\text{:O}_2\text{:Ar} = 1\text{:}4\text{:}95$ mixture.

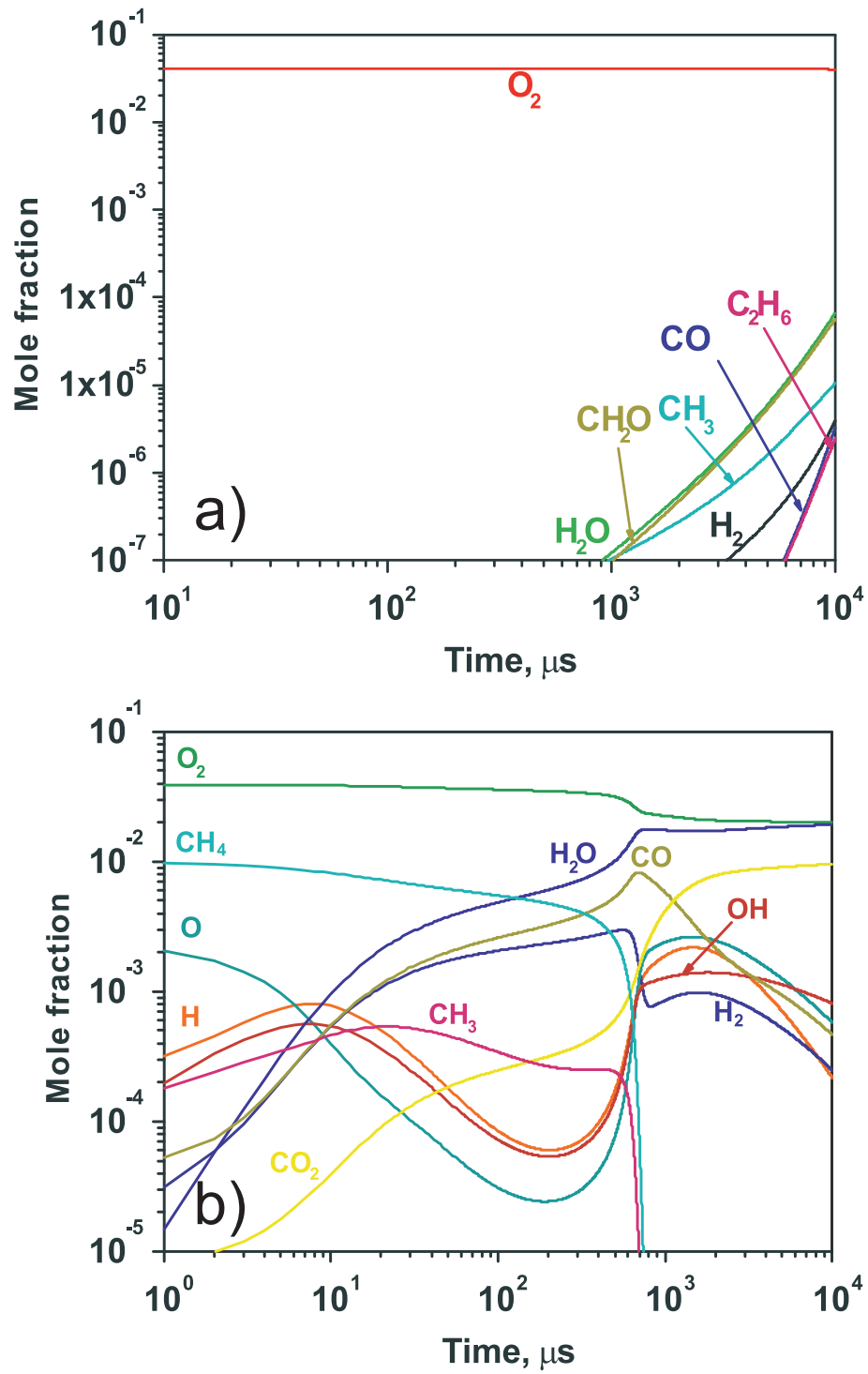


Figure 10.16: The evolution in time of the mole fractions of the main components for (a) autoignition and (b) ignition by the discharge for 1329 K and 0.45 atm. In plasma-assisted ignition, time is reckoned from the instant at which active particles are injected into the mixture.

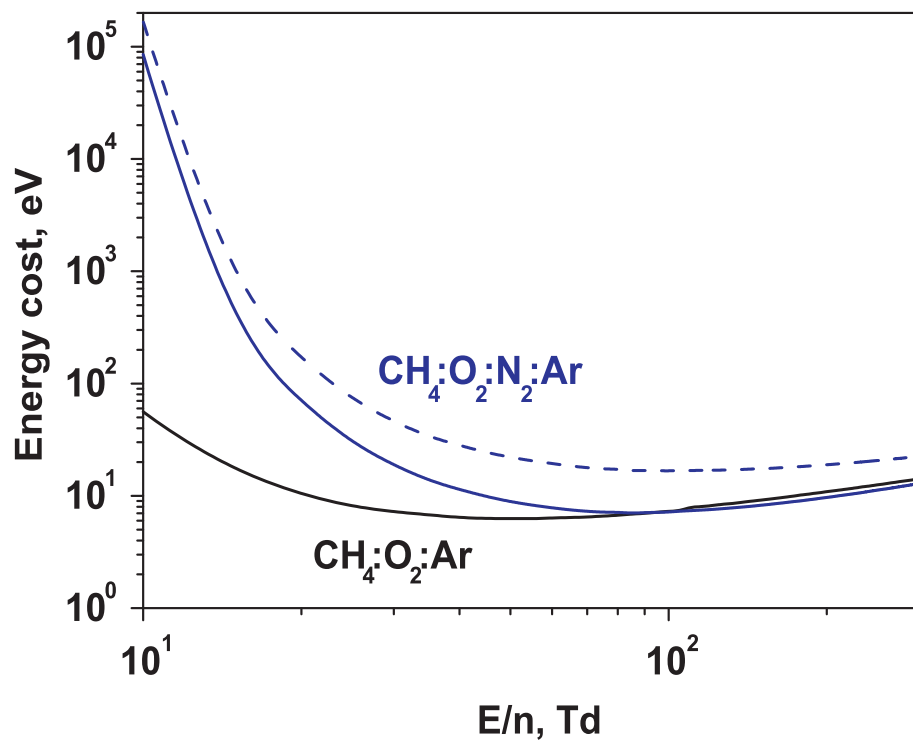


Figure 10.17: The energy cost for production of O atoms in $\text{CH}_4:\text{O}_2:\text{N}_2:\text{Ar} = 1:4:15:80$ and $\text{CH}_4:\text{O}_2:\text{Ar} = 1:4:95$ mixtures as a function of reduced electric field. The solid curves correspond to the calculations taking into account direct electron impact dissociation of O_2 and formation of O atoms via quenching of the electronically excited Ar and N_2 states; the dash curve corresponds to the calculations taking into account direct electron impact dissociation of O_2 and formation of O atoms via quenching of the electronically excited Ar states and neglecting formation of O atoms via quenching of the excited N_2 states.

Chapter 11

Ignition by Nanosecond DBD and Nanosecond Spark Discharge

11.1 Introduction

At the present time the study of ignition by nonequilibrium low-temperature plasma is an actual problem. Previously, it was shown in [38, 102] that the ignition delay time in hydrocarbon-oxygen mixtures could be shortened by the plasma of a homogeneous nanosecond high-voltage discharge at relatively low (< 1 atm) pressures in comparison with autoignition. For many applications (internal-combustion engines, etc.), it would be interesting to broaden the pressure range of plasma-assisted ignition to several atmospheres and tens of atmospheres. Thus, the next step is to extrapolate the results obtained for nanosecond-discharge ignition to higher pressures.

In several papers it was shown that the efficiency of plasma as an ignitor strongly depends on reduced electric field. In the paper [38] authors said that 30–90 Td is the most effective range for ignition in the system considered. In this range, production of O and H atoms by the nanosecond high-voltage discharge is very high. The presence of O and H atoms in a reacting system efficiently stimulates ignition, because these atoms take part in the main chain-branching reactions. Conclusions of work [38] about discharge ignition effectiveness could be extrapolated to higher pressure range. In this case, electric field in the discharge have to be increased in order to keep reduced electric field in the required range.

One of the types of the discharge in which high electric fields are realised is a sliding dielectric barrier discharge (sliding DBD). Under standard conditions, the reduced electric field in a sliding nanosecond DBD [122] can reach 700–900 Td. Besides high electric field, this type of the discharge can be characterized by the ability to cover large areas quasi-uniformly. Therefore, combustible mixtures could be ignited instantly in large volumes. This feature of sliding nanosecond DBD is valuable for ignition applications.

In this chapter, experimental setup peculiarities and preliminary results of experiments concerning ignition of a combustible mixture by a sliding nanosecond DBD are presented. Ignition parameters are compared between a nanosecond spark discharge and sliding nanosecond DBD.

11.2 Experimental setup

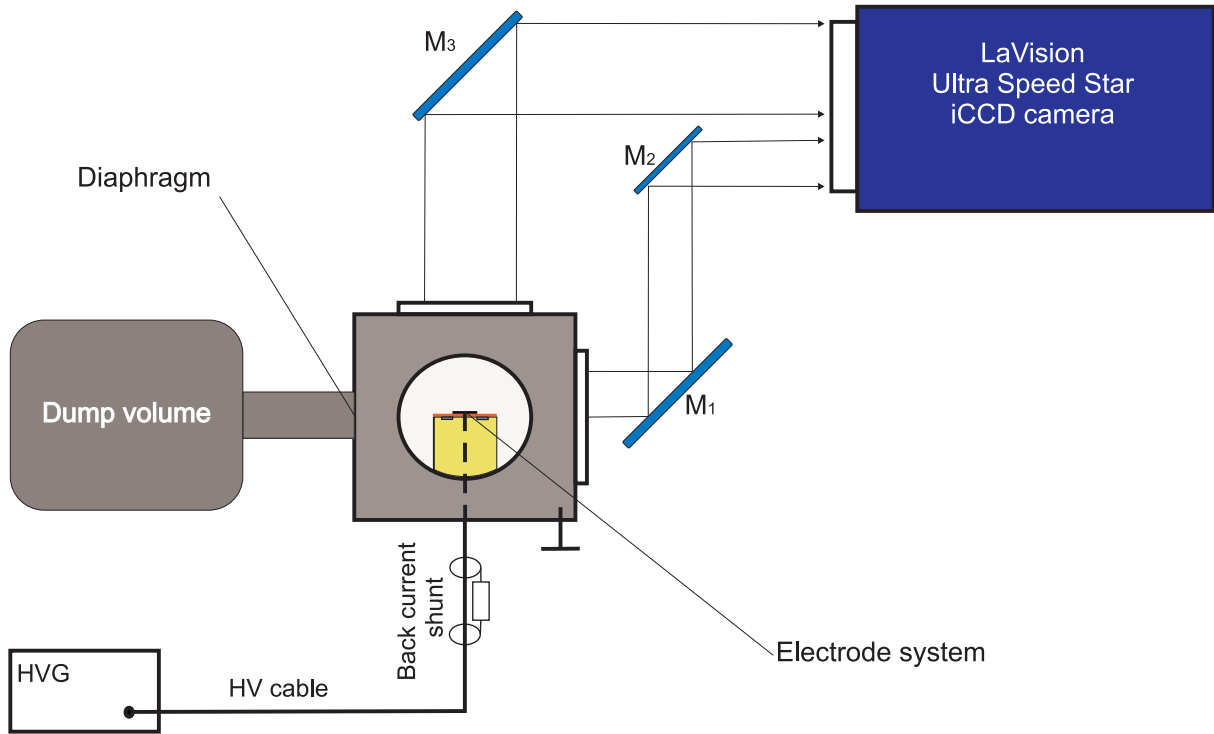


Figure 11.1: Scheme of experimental setup. HVG is the high-voltage generator; M_1 , M_2 , and M_3 are the optical mirrors

One pulse of the same nanosecond high-voltage generator was used both for a nanosecond spark discharge and a sliding nanosecond DBD. The pulse duration was 25 ns at half-height. The voltage rise time was 5 ns and the amplitude was up to 15 kV in the cable. High-voltage pulse parameters were measured by the back-current shunt soldered in the middle of the voltage-supplying cable, which was 26 m in length (130 ns for pulse propagation). Tectronix TDS 3054 with 500 MHz bandwidth was used for pulse detection. Typical oscillogram of the back-current shunt signal is shown in Fig. 11.2. It is seen that there are 13 rereflections, which follow a nanosecond 12 kV pulse of negative polarity. Positive peaks are reflections from the discharge unit and negative peaks are reflections from the generator.

Typical configuration of the electrodes for the sliding DBD is shown in Fig. 11.3. The metal plate above the dielectric layer is a high-voltage electrode and grounded electrode is installed adjacent to it just under the dielectric layer. In this work, the high-voltage electrode was a thin metal disc (see Fig. 11.3(a)) 20 mm in diameter placed on a dielectric layer (polyvinylchloride (PVC)) in alignment with the cylindrical dielectric (teflon) body of electrode assembly. The high-voltage electrode was supplied with a voltage pulse through a metal rod in the center of the cylindrical electrode assembly. One tip of the rod was attached to the supplying cable central core. A metal tube of 20 mm inner diameter and 5 mm thickness served as a grounded electrode. It was mounted into a special cavity in alignment with the electrode assembly and its upper surface was covered with

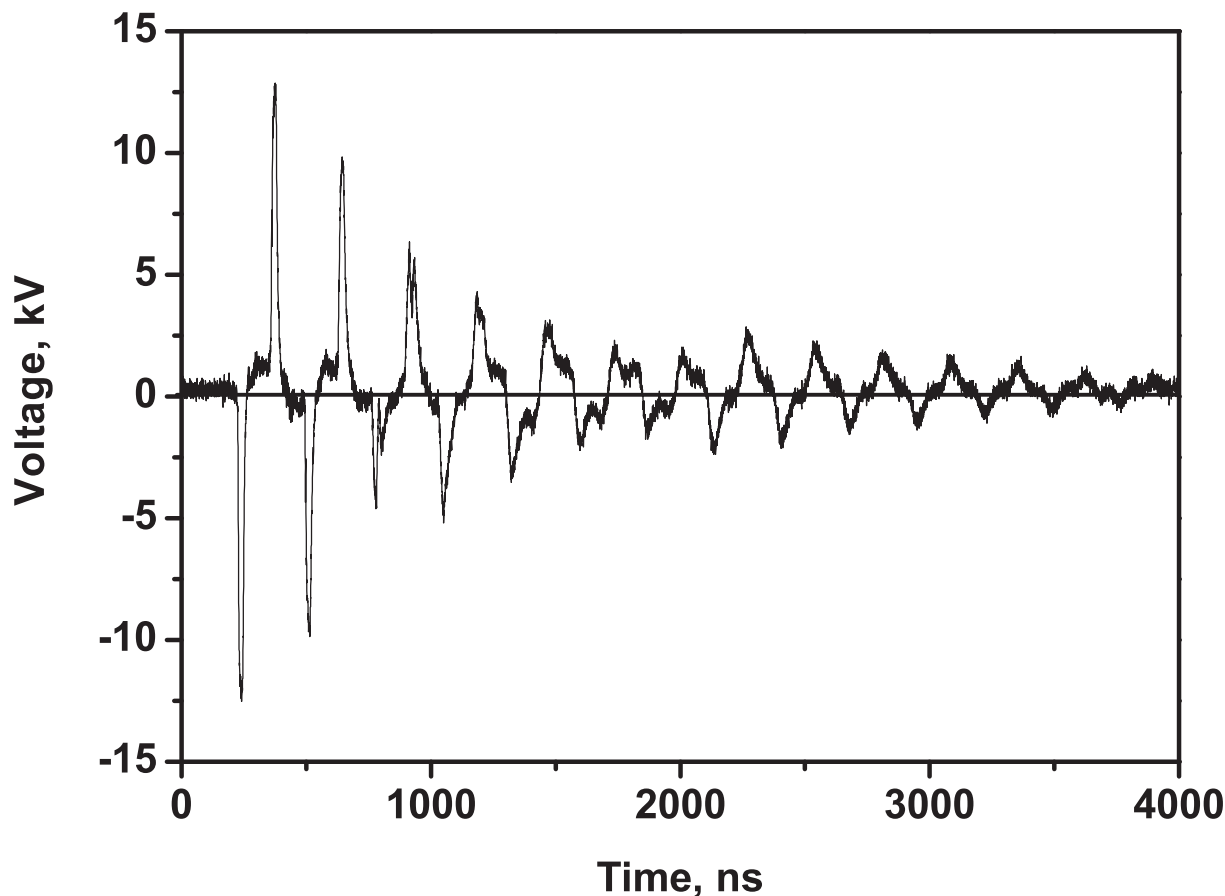


Figure 11.2: Oscillogram of back-current shunt signal. A nanosecond 12 kV pulse of negative polarity and its rereflections from the discharge unit and the generator. The experiment was carried out in a $\text{C}_2\text{H}_6:\text{O}_2 = 2:7$ mixture at room temperature and 1 atm.

a PVC layer. In spark ignition experiments, the electrodes were two metal rods 6 mm in diameter (see Fig. 11.3(b)). One of the rods was a high-voltage supplier and another was grounded. Two screws of 3 mm diameter with pin tips pointed to each other were driven in high-voltage and grounded rods. The discharge gap between the pin tips was 2 mm.

The electrode assembly in both types of experiments was placed in the steel cubic chamber with thick walls (see Fig. 11.1). The chamber could be evacuated down to 10^{-2} Torr before experiment run. Then, the chamber was filled with a premixed $\text{C}_2\text{H}_6:\text{O}_2 = 2:7$ stoichiometric mixture by the gas supply system. In order to make pressure release after ignition, the diaphragm section was installed in one of sidewalls of the chamber. Dacron diaphragm could carry 3 atm. Time was enough to achieve such pressure and to observe early stages of ignition. After the diaphragm break, exhaust gases went out to the dump volume.

To perform optical measurements and observations, the cubic chamber had three thick quartz optical windows, each 50 mm in diameter. Two windows were on the opposite sidewalls and one was on the roof above the electrode assembly. A system of three mirrors was mounted in order to perform instant imaging of flame propagation from top view and side view (see Fig. 11.1). The LaVision Ultra Speed Star ICCD was used for

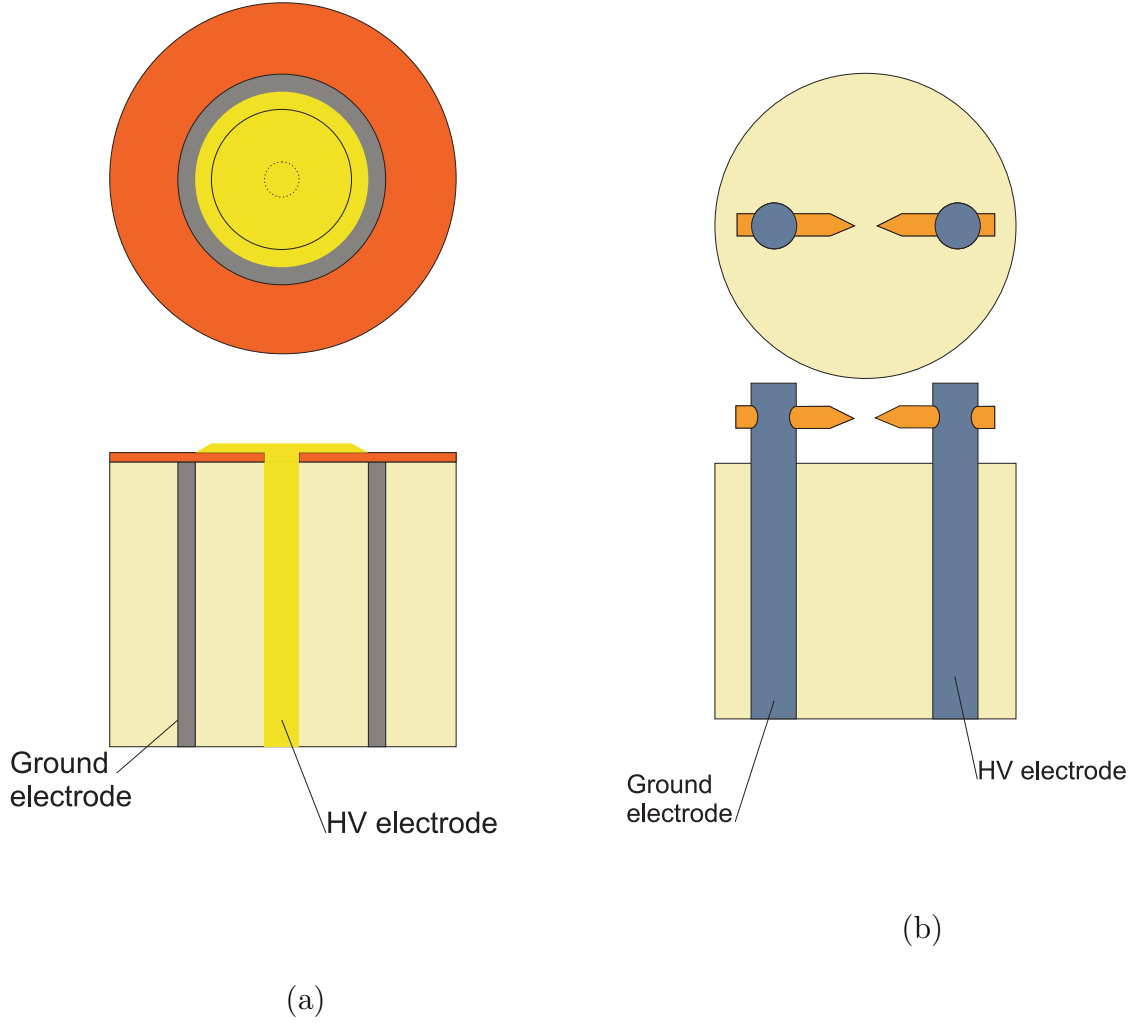


Figure 11.3: Electrode assembly in case of ignition by (a) sliding nanosecond DBD and (b) nanosecond spark.

high-speed photography. This camera allows to take 16 photos with a minimal exposure time of $0.5 \mu\text{s}$ and a minimal time of $1 \mu\text{s}$ between frames. All 16 exposures and frames were manually adjustable.

11.3 Results and discussion

In the case of the sliding DBD, one can divide the ignition process into four stages: (i) discharge development (see Fig. 11.4 (a), (a')), (ii) induction delay, (iii) development of flame fronts with petal-like structure (see Fig. 11.4 (b), (b'), (c), (c')) and (iv) ignition of the whole volume (see Fig. 11.4 (d), (d')) with rapid pressure increase. In the case of the nanosecond spark ignition, the same four stages can be observed with the only difference in the third stage; here, the flame front was spherical during all the time of flame propagation from the discharge point to the walls of the chamber and had no complex structure (see Fig. 11.5).

From high-speed camera photographs with 500 ns exposure time, we estimated the

combustion volume and found the temporal evolution of inflammation volume in the cases of nanosecond spark ignition and sliding nanosecond DBD ignition (see Fig. 11.6). It is easily seen that the sliding DBD gives approximately twice the inflammation volume at the later part of the flame propagation stage of ignition.

11.4 Conclusions

A stoichiometric $\text{C}_2\text{H}_6:\text{O}_2 = 2:7$ mixture was ignited in a closed chamber by a sliding nanosecond dielectric barrier discharge at room temperature and 1 atm. Single pulse of the high voltage generator with a total energy of 110 mJ was applied. Induction delay time, inflammation volume and flame propagation were investigated. We compared these parameters in the cases of the sliding nanosecond DBD ignition and ignition by nanosecond spark in a "pin-to-pin" geometry. It was shown that the sliding DBD gives approximately twice the inflammation volume at the same time after discharge initiation. We can conclude that the sliding nanosecond DBD looks promising as an ignitor.

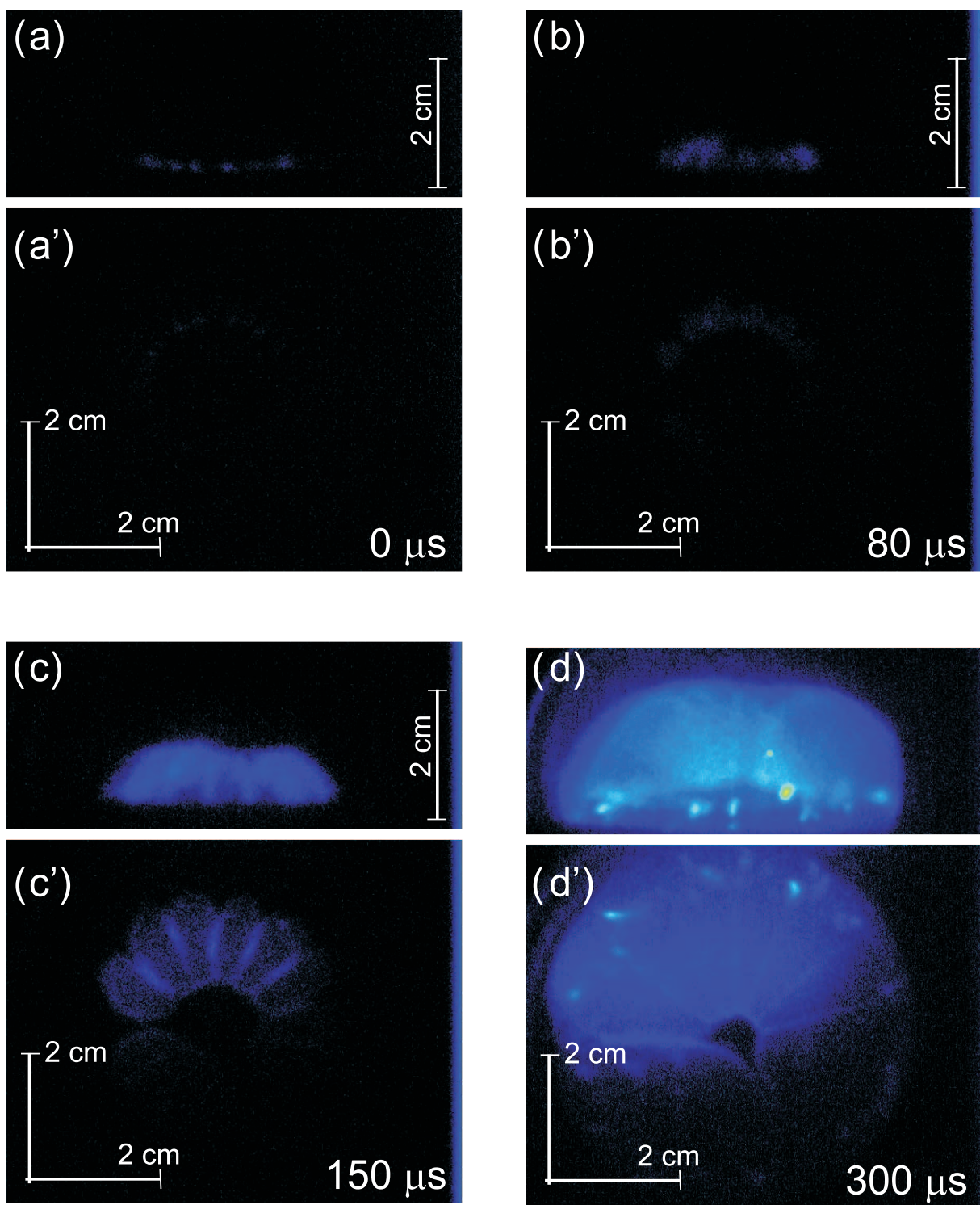


Figure 11.4: High-speed camera photographs with 500 ns exposure. (a), (a') sliding nanosecond DBD; (b), (b'), (c), (c'), (d), (d') subsequent flame propagation. Accented letter - top view, other - side view. $\text{C}_2\text{H}_6:\text{O}_2 = 2:7$ at room temperature and 1 atm pressure.

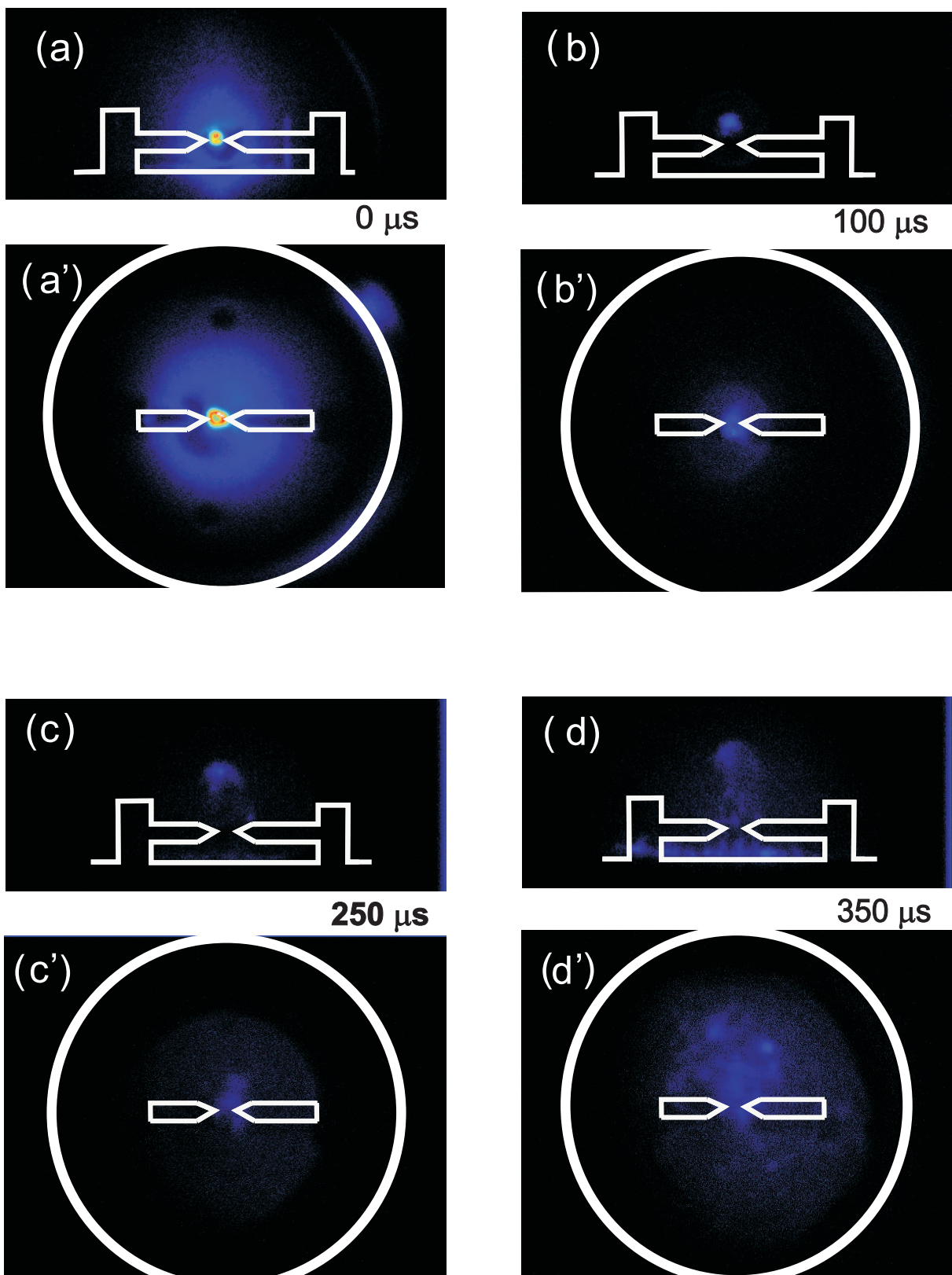


Figure 11.5: High-speed camera photographs with 500 ns exposure. (a), (a') nanosecond spark; (b), (b'), (c), (c'), (d), (d') subsequent flame propagation. Accented letter - top view, other - side view. $\text{C}_2\text{H}_6:\text{O}_2 = 2:7$ at room temperature and 1 atm pressure.

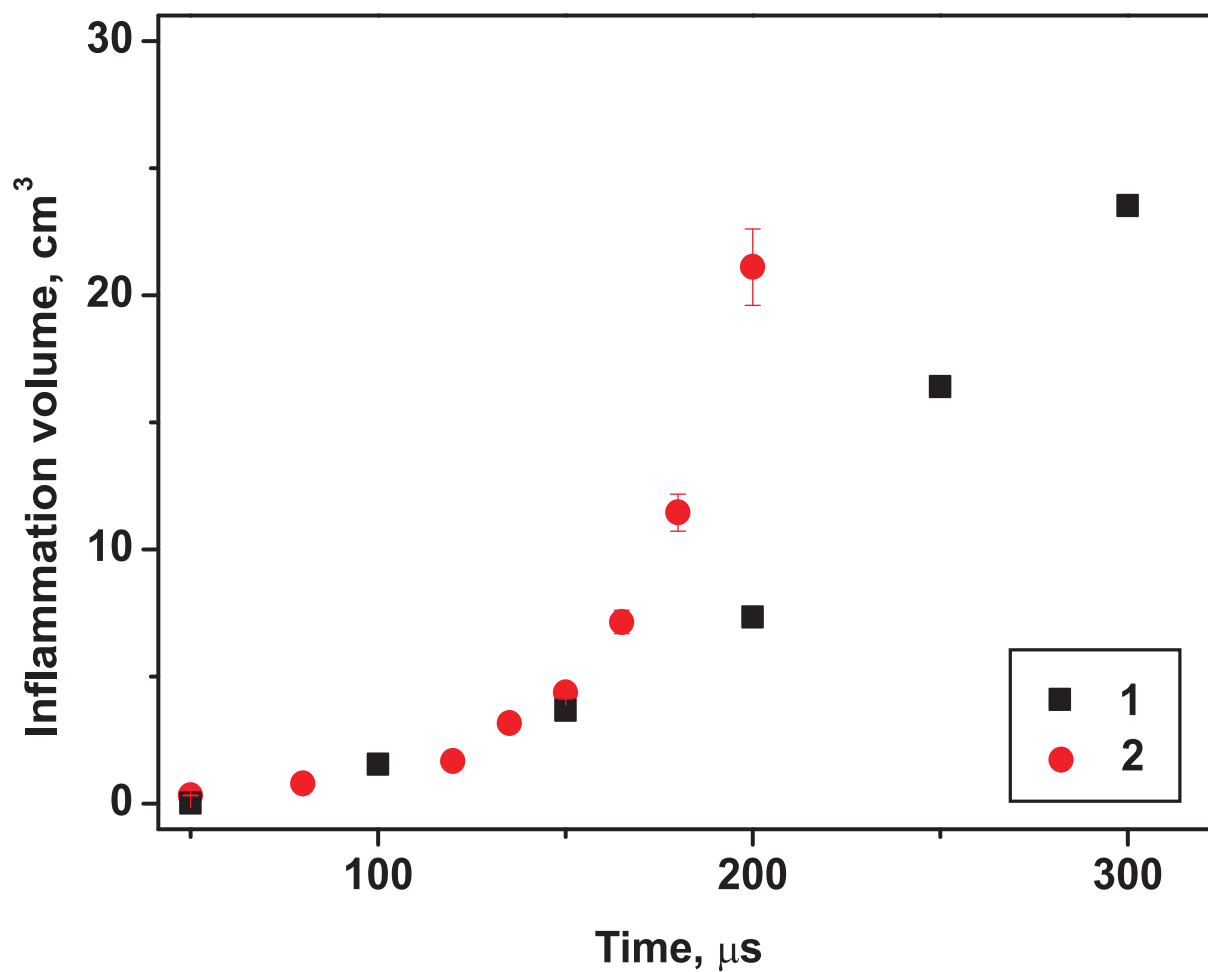


Figure 11.6: The evolution in time of the inflammation volume in the case of 1 — nanosecond spark ignition and 2 — sliding nanosecond DBD ignition. $\text{C}_2\text{H}_6:\text{O}_2 = 2:7$ at room temperature and 1 atm pressure.

Chapter 12

Summary

We have made an experimental and numerical study of the ignition of CH_4 – to C_5H_{12} –containing mixtures under the action of a high–voltage nanosecond discharge at elevated temperatures and showed that its initiation leads to a noticeable decrease in gas temperatures at which the mixtures are ignited and to an order of magnitude decrease in ignition delay time. Comparison of the data obtained and data available in the literature has been made.

Based on measured time–resolved electric field in the discharge, deposited energy and discharge current were calculated for stoichiometric mixtures $\text{C}_n\text{H}_{2n+2}:\text{O}_2$ (10 %) diluted with Ar (90 %) and good agreement with the measurements was obtained for various initial gas temperatures and pressures. Development of the nanosecond discharge in these mixtures have been analyzed and energy branching and densities of active species produced by the discharge were calculated. The densities of these species were taken as initial data for high–temperature calculations of ignition using standard combustion kinetic mechanisms.

A good agreement was obtained between the ignition delay times calculated on the basis of an one–temperature, Arrhenius, chemical kinetics and experimentally measured ones. We conclude that to explain our observations, there is no need to use any additional mechanism suggested to favour the ignition processes, such as chemical reactions with excited or charged particles. It follows from the analysis of the calculated results that, at temperatures near the ignition threshold and at electric fields such that most of the electron energy is spent in the discharge to excite electronic levels of neutral particles and to ionize them, the main mechanism of the effect of gas discharge on the ignition of stoichiometric hydrocarbon–oxygen mixtures is the electron impact dissociation of O_2 molecules in the discharge phase; this leads to an essential increase in the density of atoms and radicals at the beginning of ignition. As a result, the stage of chain activation is significantly shortened.

Detailed kinetics of intermediates in the ignition phase after the discharge has been simulated. Species and techniques were selected to control plasma decay and plasma assisted ignition in the discharge afterglow and in the ignition phase. Capabilities of absorption spectroscopy in UV and IR regions of spectra, of microwave interferometry, and of fast streak imaging have been analyzed. Preliminary results proving the possibility to study experimentally temporal dynamics of key species in ignition processes after the discharge have been obtained.

Possible gas heating in the discharge was overestimated for different mixtures and possible decrease in ignition delay time due to this additional heating has been calculated. It was shown that this effect is not sufficient to explain the measured data; that is, the nonequilibrium nature of plasma assisted ignition was proved under the conditions studied. Efficiency of production of O atoms, dominant active species, by the high-voltage nanosecond discharge in different mixtures has been analyzed. It was demonstrated that, in the wide range of parameters, we obtain that the energy required to produce one O-atom in the discharge is 4–8 eV/atom, close to the theoretical minimal values for these mixtures.

Detailed kinetics of intermediates during ignition after the discharge has been simulated. Species and techniques were selected to control different phases of plasma assisted ignition.

The UV laser absorption technique has been adjusted to measure OH density in single-shot experiments for plasma assisted ignition. The experiments were carried out in the shock tube combined with the discharge section. To obtain absolute values of the density of OH radicals, calibration procedure has been proposed and realized. The procedure was based on the autoignition experiments. For these experiments, temporal evolution of OH density have been calculated. The calculated results were compared with experimental data for the same initial pressures and temperatures under assumption that the distribution of OH density is uniform along the axis of measurements. Finally, the absorption coefficient has been determined under the conditions of the experiments.

Behavior of OH density during plasma assisted ignition has been investigated. We received that the evolution in time of OH density is in good correlation with OH* emission behaviour. Here, OH* emission and time derivative of OH density peak simultaneously. Good agreement was obtained between the ignition delay times calculated on the basis of the temporal evolution of OH absorption and on the basis of the temporal evolution of OH* emission.

A set of experiments have been carried out to analyze spatial distribution of laser radiation across the laser beam. 2D laser power measurements have been made for different laser energies. It was demonstrated that laser beam has Gaussian profile with a width of 6–7 cm on half-height.

To separate the effects of various active species, ignition delay was experimentally studied for N₂O-containing mixtures (i) in the autoignition regime, (ii) by the nanosecond discharge and (iii) by laser flash-photolysis (ArF laser). Pronounced decrease in ignition delay time was obtained both for laser flash-photolysis and for plasma assisted ignition. There have been some discrepancy in the O(¹D) density determined from measured laser energy input into a gas and initial O(¹D) density necessary for the numerical description of the shift of ignition delay time by laser flash-photolysis. Therefore, we proposed and carried out an additional series of experiments to validate the method of O(¹D) determination in experiments with flash-photolysis. The experiments were performed in a N₂:O₂:N₂O=92:4:4 mixture at initial room temperature and atmospheric pressure. Density of O(¹D) atoms was determined from measured energy input. Here, O(¹D) atoms produced by ArF laser radiation at 193 nm reacted with O₂ to produce ozone. We calculated ozone density under assumption that the quantum efficiency of flash-photolysis is equal to unity and measured ozone density. Good agreement between the calculated results and experimental data has been obtained. This proves validity of O(¹D) density

determination using measured values of energy input and a quantum efficiency of unity.

Temporal behavior of energy input, electric field and electric current has been measured and analyzed in the discharge developing in N_2O -containing mixtures. It was shown that these characteristics are similar to those obtained previously for hydrocarbon:oxygen:argon mixtures. However, electric fields and discharge currents are lower because we kept energy input as low as possible in experiments with laser flash-photolysis. The obtained data could be considered as input data for numerical modelling of the discharge in the N_2O -containing mixtures.

Ion-molecular reactions and reactions of active species production in $\text{Ar:H}_2\text{:O}_2\text{:N}_2\text{O}$ mixture were analyzed. The set of reactions to describe chemical transformation in the system due to the discharge action has been selected. Available cross-sections and energy branching in the discharge at different reduced electric fields have been preliminary analyzed and mechanisms for production of active species in the discharge have been determined.

A kinetic scheme was developed to describe the production of active particles (charged particles, excited particles, atoms and radicals) in a high-voltage nanosecond discharge and plasma assisted ignition in $\text{CH}_4\text{:O}_2\text{:N}_2\text{:Ar}$ mixtures. This scheme was used to calculate ignition delay times in a $\text{CH}_4\text{:O}_2\text{:N}_2\text{:Ar} = 1:4:15:80$ mixture under the conditions of the experiment [12]. Good agreement was obtained between the calculated ignition delay times and available experimental data, which show an order of magnitude decrease in ignition delay due to the discharge plasma.

Analysis of the calculated results showed that the presence of N_2 in gas mixtures leads (i) to a decrease in the mean electron energy in the discharge for the same values of the reduced electric field and (ii) to a several times decrease in the fractional power transferred to direct electron impact dissociation of O_2 to form O atoms, the most important active species for ignition in hydrocarbon-containing mixtures. This is associated with an efficient electron impact excitation of vibrational and electronic states of N_2 .

The calculations showed that, in N_2 -containing mixtures, O atoms are efficiently produced not only due to electron impact dissociation of O_2 , but due to electron impact excitation of electronically excited N_2 states followed by their quenching in collisions with O_2 as well.

A stoichiometric $\text{C}_2\text{H}_6\text{:O}_2 = 2:7$ mixture was ignited in a closed chamber by a sliding nanosecond dielectric barrier discharge at room temperature and 1 atm. Single pulse of the high voltage generator with a total energy of 110 mJ was applied. Induction delay time, inflammation volume and flame propagation were investigated. A comparison of these parameters was made in the cases of the sliding nanosecond DBD ignition and ignition by nanosecond spark in a "pin-to-pin" geometry. It was shown that the sliding DBD gives approximately twice the inflammation volume at the same time after discharge initiation. We can conclude that the sliding nanosecond DBD looks promising as an ignitor.

Bibliography

- [1] Starikovskaia S M 2006 Plasma assisted ignition and combustion *J.Phys.D: Appl. Phys.* **39** R265—R299
- [2] Warnatz J, Maas U and Dibble R W 2001 *Combustion. Physical and chemical fundamentals, modeling and simulations, wxperiments, pollutant Formation*. (Springer Publ.)
- [3] Emmaluel N M, Knorre D G 1974 *Lectures on chemical kinetics*. (Moscow: Vusshaia Shkola) (*In Russian*)
- [4] Maas U and Warnatz J 1988 Ignition process in hydrogen–oxygen mixtures *Comb. and Flame* **74** 53–69
- [5] Semenov N N 1958 *Concerning some problems of chemical kinetics and chemical reactivity (free radicals and chain reactions)*. (Moscow: USSR Academy of Science Publ.) (*In Russian*)
- [6] Semenov N N 1958 *Some problems of chemical kinetics and reactivity*. (Pergamon Press, 1958.)
- [7] Dubovitsky F 1935 *Acta Physicochim. URSS* **2** 361
- [8] Nalbandjan A 1934 *Acta Physicochim. URSS* **1** 305
- [9] Gorchakov G, Lavrov F 1934 Influence of electric discharge on the region of spontaneous ignition in the mixture $2\text{H}_2\text{--O}_2$ *Acta Physicochim. URSS* **1** 139—44
- [10] MacLeana H L and Lave L B 2003 Evaluating automobile fuel/propulsion system technologies *Progress in Energy and Combustion Science* **29** (2003) 1--69
- [11] Polak L S, Ovsyannikov A A, Slovetskii D I and Vurzel' F B 1975 *Theoretical and applied plasmachemistry* (Moscow: Nauka) (*In Russian*)
- [12] Raizer Yu P 1991 *Gas discharge physics* (New York: Springer)
- [13] EOARD/CRDF Project # RP0-1349-MO-02. 2007. Final Report.
- [14] K.A. Bhaskaran and P. Roth, *Progress in Energy ang Combust. Science* **28** (2002) 151–192.
- [15] V.P. Glushko (Ed.), *Thermodynamical properties of individual species*, Moscow: Nauka, 1978.

- [16] Eliasson B and Kogelschatz U 1986 Basic data for modeling of electric discharge in gases: oxygen Report KLR-86-11C (Report Brown Boveri Forschungszentrum CH-5405 Baden)
- [17] O V Braginskiy, A N Vasilieva, K S Klopovskiy, A S Kovalev, D V Lopaev, O V Proshina, T V Rakhimova and A T Rakhimov 2005 Singlet oxygen generation in O₂ flow excited by RF discharge: I. Homogeneous discharge mode: α -mode, J. Phys. D: Appl. Phys. 38, 3609—3625
- [18] A.A. Ionin, I.V. Kochetov, A.P. Napartovich, N.N. Yuryshev, J. Phys. D: Appl. Phys. 40 (2007) 25—61.
- [19] Delcroix J L, Ferreira C M and Ricard A 1976 Metastable atoms and molecules in ionized gases, In: Principles of laser plasma, G Bekefi (Ed.), New York: Wiley, pp176-244
- [20] Shkarofsky I P, Johnston T W and Bachinski M P 1966 The particle kinetics of plasmas. Addison-Wesley (Reading, MA)
- [21] K Tachibana 1989 Excitation of the 1s₅, 1s₄, 1s₃, and 1s₂ levels of argon by low-energy electrons, Phys. Rev. A 34, 1007-1015
- [22] G J M Hagelaar and L C Pitchford 2005 Solving the Boltzmann equation to obtain electron transport coefficients and rate coefficients for fluid models, Plasma Sources Sci. Technol. 14 722—733
- [23] Velazco J E, Kolts J H , Setser D W, 1975 J.Chem.Phys. 62, 1996.
- [24] B M Smirnov 1982 Excited atoms, Moscow: Energoizdat (in Russian)
- [25] Balamuta J, Golde M F, Mole A M 1985 Product distribution in the reactions of excited noble gas with halogen-containing compounds, J. Chem. Phys. 82, 3169-3178.
- [26] McEwan M J and Phillips L F 1975 Chemistry of the atmosphere (Edward Arnold)
- [27] I A Kossyi, A Yu Kostinsky, A A Matveyev, V P Silakov 1992 Kinetic scheme of the non-equilibrium discharge in nitrogen-oxygen mixtures, Plasma Sources Sci. Technol. 1 207-220
- [28] J B A Mitchell 1990 The dissociative recombination of molecular ions, Phys. Reports 186 215-248
- [29] D R Bates 1986 Products of dissociative recombination of polyatomic ions, Astrophys. J. 306 L45-L47 [16t]
- [30] Raizer Yu P 1991 *Gas discharge physics* (Berlin, New York: Springer)
- [31] Petersen E L, Davidson D F, Hanson R K 1999 Kinetic modelling of shock-induced ignition in low-dilution CH₄/O₂ mixtures at high pressures and intermediate temperatures *Comb. and Flame* **117** 272—290.

- [32] Frenklach M, Wang H, Goldenberg M, Smith G P, Golden D M, Bowman C T, Hanson R K, Gardiner W C, and Lissianski V 1995 GRI Topical Report No. GRI-95/0058
- [33] Alkam M K, Pai V M, Butler P B, and French N B 1993 University of Iowa Report No SAND89-8009
- [34] Smith G P, Luque J, Park C, Jeffries J B, Crosley D R 2002 Low pressure flame determinations of rate constants for OH(A) and CH(A) chemiluminescence *Combust. Flame* **131** 59—69
- [35] Starikovskaia S M, Kukaev E N, Kuksin A Yu, Nudnova M M and Starikovskii A Yu 2004 Analysis of the spatial uniformity of the combustion of a gaseous mixture initiated by a nanosecond discharge. *Comb. and Flame* **139** 177–87
- [36] Bozhenkov S A, Starikovskaia S M, Starikovskii A Yu 2003 Nanosecond gas discharge ignition of H₂ – and CH₄ – containing mixtures. *Comb. and Flame* **133** 133–146
- [37] Lou G, Bao A, Nishihara M, Keshav S, Utkin Y G and Adamovich I V Ignition of premixed hydrocarbon–air flows by repetitively pulsed, nanosecond pulse duration introduction plasma *41st AIAA Aerospace Sciences Meeting and Exhibit* (Reno, Nevada, USA, 9—12 January 2003) AIAA-2006-1215
- [38] Kosarev I N, Aleksandrov N L, Kindysheva S V, Starikovskaia S M, Starikovskii A Yu 2008 Kinetics of ignition of saturated hydrocarbons by nonequilibrium plasma: CH₄-containing mixtures. *Comb. and Flame*, 154 (2008) 569—586.
- [39] Curran H J, Gaffuri P, Pitz W J, Westbrook C K 1998 *Comb. and Flame* **114** 149—77
- [40] Morgan W L 2000 Electron collision data for plasma chemistry modelling *Adv. At. Mol. Opt. Physics* **43** 79—110
- [41] Janev R K and Reiter D 2004 Collision processes of C_{2,3}H_y and C_{2,3}H_y⁺ hydrocarbons with electrons and protons *Phys. Plasmas* **11** 780—829
- [42] Jiao C Q, DeJoseph C A and Garscadden A 2007 Electron impact ionization and ion reactions in *n*-butane *J. Phys. D: Appl. Phys.* **40** 409—414
- [43] Rodrigues J M, Agneray A, Jaffrezic X, Bellenoue M, Labuda S, Leys C, Chernukho A P, Migoun A N, Cenian A, Savel'ev A M, Titova N S and Starik A M 2007 Evolution of charged species in propane/air flames: mass-spectrometric analysis and modelling *Plasma Sources Sci. Technol.* **16** 161—172
- [44] Burcat A, Lifshitz A, Scheller K 1971, Shock tube investigation of comparative ignition delay times for C₁-C₅ alkanes, *Comb. and Flame* **16** 1971
- [45] M Hayashi 1987 Electron collision cross-sections for molecules determined from beam and swarm data, In: Swarm studies and inelastic electron-molecule collisions, L.C. Pitchford, B.V. McCoy, A. Chutjian and S. Trajmar (Eds.), Springer Verlag (New York) pp 167-187

- [46] Warnatz J. Chemistry of high temperature combustion of alkanes up to octane. XXth Symp. (International) on Combustion, The Combustion Institute, 1984. Plenary lecture, pp. 845–856.
- [47] Praxmarer C, Hansel A, Lindinger W and Herman Z 1998 *J. Chem. Phys.* **109** 4246–52
- [48] Lissianski V V, Zamansky V M, Gardiner W C Jr, Gas-phase combustion chemistry, Springer-Verlag, Ed. Gardiner W C Jr, New York, 2000
- [49] Heghes C I, 2006, C₁–C₄ Hydrocarbon Oxidation Mechanism, PhD Thesis, Heidelberg, Scientific supervisor Prof. Warnatz J. 119 p.
- [50] Forsythe J.E., Malcolm M.A., Moler C.B. 1977 *Computer methods for mathematical calculations* (Prentice-Hall, Englewood Cliffs, NJ)
- [51] Gear C W 1971 *Comm.of the ACM*, **14**(3) 176—179
- [52] Zhukov V.P., Sechenov V.A., Starikovskii A.Yu. 2005 *Kinetics and Catalysis* **40**(3) 344—353
- [53] Kosarev I.N., Kindysheva S.V., Aleksandrov N.L., Starikovskaia S.M., Starikovskii A.Yu., 45-th AIAA Aerospace Sciences Meeting and Exhibit, 2007, Reno, Nevada, USA, 3—7 January, paper AIAA-2007-1386
- [54] Hidaka Y., Higashihara T., Ninomiya N., Oshita H., Kawano H. 1993 *J. Phys. Chem.* **97** 10977—10983
- [55] http://www.uviterno.com/file/pdf/Spektrum_Hg.pdf
- [56] http://en.wikipedia.org/wiki/Deuterium_arc_lamp, according with (to) data of <http://www.oceanoptics.com>
- [57] <http://www.astrosurf.com/buil/us/spe2/hresol4.htm>
- [58] S.M. Starikovskaia, N.B. Anikin, S.V. Pancheshnyi, D.V. Zatsypin and A.Yu. Starikovskii 2001 *Plasma Sources Sci. Technol.* **10** 344—355
- [59] Heald M.A. and Wharton C.B. 1965 *Plasma diagnostics with microwaves* (NY: Wiley) p. 139
- [60] I.V. Adamovich, W.R. Lempert, J.W. Rich, and M. Samimy, Experimental studies of high-speed flow control and ignition by nonequilibrium plasmas, XIX European Sectional Conference on Atomic and Molecular Physics of Ionized Gases (ESCAMPIG), 14-20 July 2008, Granada, Spain, Invited lecture.
- [61] G.D. Stancu, M. Janda, F. Kaddouri, T. Spence, C. Harb, D.A. Lacoste, C.O. Laux, Study of nanosecond repetitively pulsed discharges in atmospheric air or nitrogen by advance laser techniques, XIX European Sectional Conference on Atomic and Molecular Physics of Ionized Gases (ESCAMPIG), 14-20 July 2008, Granada, Spain, Invited lecture.

- [62] A.A. Radtsyg, B.M. Smirnov, Handbook on atomic and molecular physics, M.: Energoatomizdat Publ., 1980.
- [63] Handbook “Tables of physical values”, Energoatomizdat, 1991, p.408.
- [64] A.M. Prokhorov, Handbook on lasers, V. 2, M.: Sovetskoe Radio Publ., 1978, 400 p.
- [65] LIBASE, <http://www.sri.com/psd/lifbase>
- [66] V.L Kasyutich, Eur.Phys.J D33, 29—33 (2005).
- [67] B. Shirinzadeh, D.M. Bakalyar, C.C. Wang, J. Chem. Phys., 82 2877 (1985).
- [68] S.B. Leonov, D.A. Yarantsev, A.P. Napartovich, and I.V. Kochetov, IEEE Trans. Plasma Sci. 34 (2006) 2514-2525.
- [69] A. Klimov, V. Bitiurin, I. Moralev, B. Tolkunov, A. Nikitin, A. Velichko and I. Biler, 44th AIAA Aerospace Sciences Meeting and Exhibit, AIAA-2006-617.
- [70] N.B. Anikin, E.I. Mintoussov, S.V. Pancheshnyi, D.V. Roupasov, V.E. Sych, A.Yu. Starikovskii, 41st AIAA Aerospace Sciences Meeting and Exhibit, (Reno, Nevada, USA, 9-12 January 2003) AIAA-2003-1053.
- [71] G. Pilla, D. Galley, D.A. Lacoste, F. Lacas, D. Veynante, and C.O. Laux, IEEE Trans. on Plasma Science 34 (2006) 2471-2477.
- [72] N. Chintala, A. Bao, G. Lou, I.V. Adamovich. Comb. and Flame 144 (2006) 744-756.
- [73] G.V. Naidis, J. Phys. D: Appl. Phys. 40 (2007) 4525-4531.
- [74] N.A. Popov, High Temp. 45 (2007) 261-279.
- [75] A.M. Starik, N.S. Titova, L.V. Bezgin and V.I. Kopchenov, J. Phys. D: Appl. Phys. 41 No 12 (21 June 2008) 125210.
- [76] A.P. Napartovich, I.V. Kochetov, S.B. Leonov, High Temperature Teplophysics 43 (2005) 677-684.
- [77] I.V. Kochetov, A.P. Napartovich, S.B. Leonov, High Energy Chemistry 40 (2006) 98-104.
- [78] S.B. Leonov, D.A. Yarantsev, A.P. Napartovich, and I.V. Kochetov, Plasma Sci. Technol. 9 (2007) 760-765.
- [79] Plasma Assisted Combustion. EOARD/CRDF Project N RP0-1349-MO-02, 2nd Quarter.
- [80] Plasma Assisted Combustion. EOARD/CRDF Project N RP0-1349-MO-02, 7th Quarter.
- [81] Plasma Assisted Combustion. EOARD/CRDF Project N RP0-1349-MO-02, 8th Quarter.

- [82] Plasma Assisted Combustion. EOARD/CRDF Project N RP0-1349-MO-02, 11th Quarter.
- [83] I.N. Kosarev, S.M. Starikovskaia, A.Yu. Starikovskii, Comb. and Flame 151 (2007) 61-73.
- [84] R.J. Kee, J.A. Miller, T.H. Jefferson, Report No. SAND 80-8003 (1980), Sandia National Laboratory, Livermore, CA
- [85] L. Date, K. Radouane, B. Despax, M. Yousfi, H. Caquineau and A. Hennad, J. Phys. D: Appl. Phys. 32 (1999) 1478-1488.
- [86] T.H. Teich, 1991, Int. Conf. on Plasma Ion. Gases XX 5442, ed. V. Palleshi and M. Vaselli (Pisa: Istituto di Fisica).
- [87] J. Dutton, J.W. Gallagher, E.C. Beaty and L.C. Pitchford, J. Phys. Chem. Ref. Data 22 (1982) 203.
- [88] D. Rapp and P. Englander-Golden, J. Chem. Phys. 43 (1965) 1464.
- [89] M. Hayashi and A. Niwa, Gaseous Dielectrics V (1987) ed. L.G. Christophorou and D.W. Bouldin (New York: Pergamon) p.27.
- [90] M. Hayashi, personal communication to the JILA Atomic Collisions Data Center, 1987
- [91] P.J. Chantry, J. Chem. Phys. 51 (1969) 3380-3384.
- [92] P.J. Chantry, J. Chem. Phys. 51 (1969) 3369-3379.
- [93] L.I. Virin, R.V. Jagatsapnyan, G.V. Karachevtsev, V.K. Potapov, V.L. Talroze, Ion-molecular reactions in gas phase, Moscow, Nauka Publ., 1979. 548 p.
- [94] P.F. Fennelly, R.S. Hemsworth, H.I. Schiff, D.K. Bohme, J. Chem. Phys. 59 (1973) 6405.
- [95] B.M. Smirnov, Complex ions. Moscow, Nauka publ., 1983.
- [96] E. Tatarova E., F.M. Dias, B. Gordiets, C.M. Ferreira, Plasma Sources Sci. Technol. 14(2005) 19-31.
- [97] A.V. Eletskii, B.M. Smirnov, Physics—Uspekhi, 136 (1982) 25.
- [98] L.G. Piper, J.E. Velazco, D.W. Setser, J. Chem. Phys. 59 (1973) 3323-3340.
- [99] D.L. Baulch, R.A. Cox, R.F. Hampson, J.A. Kerr, J. Phys. Chem. Ref. Data. 13(1984) 1259.
- [100] J.T. Herron, J. Phys. Chem. Ref. Data 28(1999) 1453-1483.
- [101] A.M. Pravilov, Photoprocess in molecular gases. Moscow, Energoatomizdat Publishing, 1992, 352 p.

- [102] I.N. Kosarev, N.L. Aleksandrov, S.V. Kindysheva, S.M. Starikovskaia, A.Yu. Starikovskii, *J. Phys. D: Appl. Phys.* 41 (2008) 032002 (6pp).
- [103] I.N. Kosarev, N.L. Aleksandrov, S.V. Kindysheva, S.M. Starikovskaia, A.Yu. Starikovskii, *Combust. Flame* 156 (2009) 221—233.
- [104] N.A. Popov, *Fiz. Plazmy* 27 (2001) 940—949.
- [105] N.L. Aleksandrov, S.V. Kindysheva, I.N. Kosarev, A.Yu. Starikovskii, *J. Phys. D: Appl. Phys.* 41 (2008) 215207 (9pp).
- [106] M.P. Iannuzzi, J.B. Jeffries, F. Kaufman, *Chem. Phys. Lett.* 87 (1982) 570.
- [107] A.R. DeSousa, M. Touzeau, M. Petitdidier, *Chem. Phys. Lett.* 121 (1985) 423.
- [108] L.G. Piper, *J. Chem. Phys.* 88 (1988) 6911.
- [109] L.G. Piper, *J. Chem. Phys.* 88 (1988) 231.
- [110] D.I. Slovetskii, *Mechanisms of Chemical Reactions in Nonequilibrium Plasmas*, Nauka, Moscow, 1980 (in Russian).
- [111] L.G. Piper, G.E. Caledonia, J.P. Kennealy, *J. Chem. Phys.* 75 (1981) 2847.
- [112] L.G. Piper, *J. Chem. Phys.* 87 (1987) 1625.
- [113] C.D. Pintassilgo, J. Loureiro, G. Cernogora, M. Touzeau, *Plasma Sources Sci. Technol.* 8 (1999) 463—478.
- [114] L.G. Piper, *J. Chem. Phys.* 97 (1992) 270.
- [115] H.F. Winters, *J. Chem. Phys.* 63 (1975) 3462—3466.
- [116] S. Motlagh, J.H. Moore, *J. Chem. Phys.* 109 (1998) 432—438.
- [117] P.C. Cosby, *J. Chem. Phys.* 98 (1993) 9544—9553.
- [118] A.A. Konnov, *Proceedings of the Combustion Institute*, Vol. 28, The Combustion Institute, Pittsburg, 2000, p. 317.
- [119] www.me.berkeley.edu/gri-mech.
- [120] N.L. Aleksandrov, A.M. Konchakov, *Pis'ma Zh. Tekh. Fiz.* 16, #6 (1990) 4—7.
- [121] E.I. Mintoussov, S.V. Pancheshnyi, A.Yu. Starikovskii, AIAA2004-1013, 42nd AIAA Aerospace Sciences Meeting and Exhibit, Reno, Nevada (2004).
- [122] D.V. Roupasov, A.A. Nikipelov, M.M. Nudnova, A.Yu. Starikovskii, 2009 Flow separation control by plasma actuator with pulsed nanosecond periodic discharge. *AIAA Journal* Vol. 47, No 1, pp. 168-185.

List of Figures

3.1	Limits of explosion for hydrogen–oxygen mixture (according to [4]).	11
3.2	Extension of explosion limits of $\text{H}_2\text{:O}_2$ mixture under the action of a discharge. Different curves correspond to different current in a primary electric circuit (according to [9]).	13
3.3	Rate constants for reactions responsible for autoignition, and for dissociation by electron impact at electric field values equal to 100 Td and 200 Td (horizontal lines).	14
4.1	Scheme of the experimental setup: DC, discharge cell; A, cross-section of measurement; EP, end plate; HPC, high pressure cell; HVG, high voltage generator; ShT, shock tube; PD, photodiodes; PMT, photomultiplier; CG, capacitive gauge; MCG, magnetic current gauge. The insert gives the discharge cell on an enlarged scale.	17
4.2	Typical signals on a nanosecond scale from (1) the capacitive gauge No 1 (see Figure 4.1), (2) capacitive gauge No 2 and (3) magnetic current gauge. The gas parameters are $T_5=1275$ K, $P_5 = 0.68$ bar and $n_5 = 3.9 \times 10^{18} \text{ cm}^{-3}$. The voltage amplitude is 175 kV.	19
4.3	The temporal evolution of (a) the reduced electric field E/n and (b) discharge current for 1450 K and 1.2 bar. The red curves correspond to measurements, the blue curve in Fig. 4.3(a) corresponds to an approximation of the experimental data and the dash curve in Fig. 4.3(b) corresponds to calculations. $1 \text{ Td} = 10^{-17} \text{ V cm}^2$	19
4.4	The peak values of the reduced electric field (closed symbols) and their values at the instant at which the discharge current peaks (open symbols) as a function of the gas number density. Series <i>I</i> and <i>II</i> correspond to measurements at different values of T_5 , the values of n_5 being the same. Solid lines correspond to approximations of the experimental data.	21
4.5	The typical temporal evolution of the specific deposited energy for various gas temperatures and pressures. Solid curves correspond to measurements and dash curves correspond to calculations.	22
4.6	Typical behaviour of synchronized signals from (1)–(2) schlieren gauges, (3) photomultiplier, and (4) IR detector on a microsecond scale for (a) autoignition and (b) ignition by the discharge. Distance between the schlieren gauges is 226 mm. Amplitude of voltage pulse is $U=-115$ kV.	23

4.7	Ignition delay time in a stoichiometric $\text{CH}_4\text{:O}_2$ mixture (10 %) diluted with Ar (90%) as a function of temperature for autoignition and (I)–(II) ignition with discharge. Closed symbols correspond to measurements and open symbols correspond to calculations. Solid curves approximate experimental data.	23
4.8	Electron collision cross-sections for (a) CH_4 , (b) O_2 , and (c) Ar. CH_4 : (1) momentum transfer, (2)–(3) vibrational excitation, (4) electronical dissociation, and (5) ionization. O_2 : (1) momentum transfer, (2) vibrational excitation, (3) excitation of $a^1\Delta_g$ electronical state, (4) excitation of $b^1\Sigma_g$ electronical state, (5) excitation of electronical state with $\Delta E = 4.5$ eV, (6) excitation of electronical state with $\Delta E = 6$ eV, (7) excitation of electronical state with $\Delta E = 8.4$ eV, and (8) ionization. Ar: (1) momentum transfer, (2) excitation of $1s_5$ electronical state, (3) excitation of $1s_4$ electronical state, (4) excitation of $1s_2$ electronical state, (5) excitation of other allowed electronical states, (6) excitation of other forbidden electronical states, and (7) ionization.	27
4.9	Fractional power transferred by the electrons to the neutral particles in (1) elastic collisions, (2) vibrational excitation of CH_4 and O_2 , (3) excitation of Ar^* , (4) dissociation of CH_4 , (5) excitation of O_2 ($a^1\Delta_g$) and O_2 ($b^1\Sigma_g^+$), (6) excitation of O_2^* ($\Delta E = 4.5$ eV state), (7) dissociation of O_2 and (8) ionization as a function of E/n for $\text{CH}_4\text{:O}_2\text{:Ar}=1\text{:}2\text{:}27$ mixture.	27
4.10	Densities of active particles produced in a $\text{CH}_4\text{:O}_2\text{:Ar}=1\text{:}2\text{:}27$ mixture for $P_5 = 1.1$ bar, $T_5 = 1500$ K as a function of E/n	28
4.11	The evolution in time of the measured and calculated deposited power(in arb. units) . The curves correspond to the same conditions as those in Fig. 4.3. For comparison, the temporal evolution of E/n (blue curve in Fig. 4.3(a)) and of I (dash curve in Fig. 4.3) are also given.	29
4.12	The evolution in time of mole fractions for (a) charged end excited particles and (b) atoms and radicals generated in the discharge. The curves correspond to the same conditions as those in Fig. 4.3.	30
4.13	The evolution in time of the rates for production of various active species during the discharge. The curves correspond to the same conditions as those in Fig. 4.3.	30
4.14	Initial data for high-temperature chemistry: densities of atoms and radicals produced by nanosecond discharge. Series I and II correspond to measurements at different values of T_5 , the values of n_5 being the same. . .	31
4.15	Sensitivity of the ignition delay time to the changes in density of atomic oxygen: (1) $[\text{O}]$ is 30 % higher than initial one; (2) $[\text{O}]$ is 30 % lower than initial one; (3) $[\text{O}]$ at every point is equal to the $[\text{O}]$ in the point with the highest temperature.	33
4.16	The evolution in time of the rates for the chemical reactions for (a) autoignition, and (b) ignition by pulsed discharge.	33
4.17	Results of sensitivity analysis for the autoignition and ignition by the discharge.	34
4.18	Induction delay time for the specific deposited energy 14 mJ/cm^3 as a function of reduced electric field.	35

5.1	Typical signals on a nanosecond scale from (1) the capacitive gauge No 1 (see Figure 4.1), (2) capacitive gauge No 2 and (3) magnetic current gauge in the C_2H_6 -containing mixture. The gas parameters are $T_5=1318$ K and $P_5 = 0.6$ bar. The voltage amplitude is 110 kV on the high-voltage electrode.	38
5.2	Parameters of the experiments for C_2H_6 -containing mixture: (a): dependence of gas temperature behind the reflected shock wave (T_5) upon the gas density (n_5); (b) dependence of volumetric energy input upon gas density, role of the first pulse and re-reflections is indicated; (c) maximal value of electrical current for different gas densities; (d) amplitude of high-voltage pulse on the high-voltage electrode at different gas densities	39
5.3	Parameters of the experiments for C_3H_8 -containing mixture: (a): dependence of gas temperature behind the reflected shock wave (T_5) upon the gas density (n_5); (b) dependence of volumetric energy input upon gas density, role of the first pulse and re-reflections is indicated; (c) maximal value of electrical current for different gas densities; (d) amplitude of high-voltage pulse on the high-voltage electrode at different gas densities	40
5.4	Parameters of the experiments for C_4H_{10} -containing mixture: (a): dependence of gas temperature behind the reflected shock wave (T_5) upon the gas density (n_5); (b) dependence of volumetric energy input upon gas density, role of the first pulse and re-reflections is indicated; (c) maximal value of electrical current for different gas densities; (d) amplitude of high-voltage pulse on the high-voltage electrode at different gas densities	41
5.5	Parameters of the experiments for C_5H_{12} -containing mixture: (a): dependence of gas temperature behind the reflected shock wave (T_5) upon the gas density (n_5); (b) dependence of volumetric energy input upon gas density, role of the first pulse and re-reflections is indicated; (c) maximal value of electrical current for different gas densities; (d) amplitude of high-voltage pulse on the high-voltage electrode at different gas densities	43
5.6	The values of the reduced electric field at the instant at which the discharge current peaks as a function of the gas number density. Solid lines are approximations of the experimental data.	45
5.7	The typical temporal evolution of the specific deposited energy for various gas temperatures, pressures and gas mixture composition. Solid curves correspond to measurements and dash curves correspond to calculations. . .	45
5.8	The total specific deposited energy for various gas mixtures as a function of gas density. Solid lines are approximations of the experimental data. . .	46
5.9	The delay time for autoignition and PAI in the $C_2H_6:O_2:Ar$ mixture as a function of temperature for autoignition and ignition with the discharge. Closed symbols correspond to measurements and open symbols correspond to calculations.	47
5.10	The delay time for autoignition and PAI in the $C_3H_8:O_2:Ar$ mixture as a function of temperature for autoignition and ignition with the discharge. Closed symbols correspond to measurements and open symbols correspond to calculations.	48

5.11	The delay time for autoignition and PAI in the $C_4H_{10}:O_2:Ar$ mixture as a function of temperature for autoignition and ignition with the discharge. Closed symbols correspond to measurements and open symbols correspond to calculations.	48
5.12	The delay time for autoignition and PAI in the $C_5H_{12}:O_2:Ar$ mixture as a function of temperature for autoignition and ignition with the discharge. Closed symbols correspond to measurements and open symbols correspond to calculations.	49
5.13	Electron collision cross-sections for C_2H_6 [45]: (1) momentum transfer, (2) vibrational excitation with a threshold of 0.168 eV, (3) vibrational excitation with a threshold of 0.371 eV, (4) electronical excitation with a threshold of 7.53 eV, (5) electronical excitation with a threshold of 10.12 eV, and (6) ionization.	49
5.14	Densities of active particles produced in (a) $C_2H_6:O_2:Ar=2:7:81$ and (b) $C_5H_{12}:O_2:Ar=1:8:81$ mixtures as a function of E/n . The specific deposited energy is (a) 23 and (b) 19 mJ/cm ³ . Solid curves correspond to calculation taking into account reaction (R13) and dashed curves correspond to calculation neglecting this reaction.	50
5.15	The evolution in time of mole fractions for different species generated in the discharge. for C_2H_6 -containing mixture. $T_5=1275$ K, $P_5=0.7$ bar. . . .	52
5.16	The evolution in time of the rates for production of various active species during the discharge for C_2H_6 -containing mixture. $T_5=1275$ K, $P_5=0.7$ bar. . . .	52
5.17	The calculated mole fractions of O, H and C_nH_{2n+1} produced by the discharge in the gas mixtures under consideration as a function of n_5	53
5.18	The ignition delay time in ethane containing mixtures for two different artificial ways of C_2H_6 destruction by the discharge.	54
5.19	The evolution in time of the mole fractions of main components for autoignition (a) and ignition after the discharge (b) in $C_2H_6:O_2:Ar$ mixture. $T_5 = 1318$ K, $P_5 = 0.60$ bar.	55
5.20	The evolution in time of the mole fractions of main components for autoignition (a) and ignition after the discharge (b) in $C_5H_{12}:O_2:Ar$ mixture. $T_5 = 1309$ K, $P_5 = 0.58$ bar.	56
5.21	The results of the sensitivity analysis for autoignition and ignition by the discharge. (a) $C_2H_6:O_2:Ar$ mixture, and (b) $C_5H_{12}:O_2:Ar$ mixture.	56
5.22	The ignition delay time for the C_nH_{2n+2} -containing mixtures versus the number of C atoms in C_nH_{2n+2} molecule. Closed points correspond to measurements, and open points correspond to calculations. The initial temperature was between 1430 and 1450 K and the pressure was between 0.4 and 0.5 atm.	57
5.23	The parameters used in the experiments for the C_nH_{2n+2} -containing mixtures versus the number of C atoms in C_nH_{2n+2} molecule. (a): gas number density; (b): gas temperature.	58
5.24	The ignition delay time for the C_nH_{2n+2} -containing mixtures versus the number of C atoms in C_nH_{2n+2} molecule. Comparison of autoignition and ignition assisted by nonequilibrium plasma of high-voltage nanosecond discharge.	59

6.1	Scheme of streak-camera operation	62
6.2	Scheme of experimental setup	63
6.3	(a) spectrum, (b) streak-image of mercury lamp; (b) spectrum of mercury lamp taken from the literature [55]	64
6.4	(a) spectrum, (b) streak-image of deuterium lamp, and (c) spectrum of deuterium lamp taken from the literature [56]	65
6.5	(a) spectrum, (b) streak-image of neon lamp, and (c) spectrum of neon lamp taken from the literature [57]	66
6.6	Calibration curve for the streak-camera images	67
6.7	Streak images of (a) autoignition, (b) plasma assisted ignition, and (c) discharge in a cold gas, with decreased sensitivity of a streak-camera. (C ₃ H ₈ :O ₂):Ar=10:90 stoichiometric mixture	67
6.8	Two lines presented in streak spectra at high temperatures (see explanations in the text)	68
6.9	Emission spectra for the nanosecond high-voltage discharge in air and (C ₃ H ₈ :O ₂):Ar=10:90 stoichiometric mixture	69
6.10	Comparison of the emission spectra of the nanosecond high-voltage discharge and of autoignition in a (C ₃ H ₈ :O ₂):Ar=10:90 stoichiometric mixture	69
6.11	Comparison of the emission spectra of the autoignition and plasma-assisted ignition in a (C ₃ H ₈ :O ₂):Ar=10:90 stoichiometric mixture	70
6.12	Comparison of temporal behavior of CH emission for autoignition (red line) and plasma-assisted ignition (blue line) in a (C ₃ H ₈ :O ₂):Ar=10:90 stoichiometric mixture	71
6.13	A schematic diagram of microwave interferometer	72
6.14	Data from (a) microwave interferometer; (b) microwave interferometer correlated with OH* emission at 306 nm at the conditions of plasma assisted ignition	72
6.15	Experimental setup for OH density measurements. G5-54: synchro generator, DG: delay generator, MR: monochromator, PMT: photomultiplier, HVG: high voltage generator, FL: forming line, Sch: schlieren system detectors, LPC: low pressure chamber, HPC: high pressure chamber	73
6.16	Oscillogrammes of the experiments of OH measurements. "Sch1", "Sch2", "Sch3" are the signals from Schlieren detectors, "Emiss" is OH emission at 306 nm, "Ref" is a laser emission, "Abs" is an absorption signal, "OH" is the preliminary data for OH density.	74
7.1	Pure nitrogen. Typical signals on a sub-microsecond scale from (C1) the capacitive gauge, (TD) back current shunt and (Ch1, Ch2) signals from two channels of microwave interferometer. The voltage amplitude is 11 kV in the cable, pulse duration is 25 ns, rise time is 5 ns, repetitive frequency is 40 Hz.	78
7.2	Pure oxygen. Typical signals on a sub-microsecond scale from (C1) the capacitive gauge, (TD) back current shunt and (Ch1, Ch2) signals from two channels of microwave interferometer. The voltage amplitude is 11 kV in the cable, pulse duration is 25 ns, rise time is 5 ns, repetitive frequency is 40 Hz.	78

7.3	Pure argon. Typical signals on a sub-microsecond scale from (C1) the capacitive gauge, (TD) back current shunt and (Ch1, Ch2) signals from two channels of microwave interferometer. The voltage amplitude is 11 kV in the cable, pulse duration is 25 ns, rise time is 5 ns, repetitive frequency is 40 Hz.	79
7.4	Electron density obtained from data of the Figures 7.1–7.3. (a): Nitrogen, P=6 Torr; (b) Oxygen, P=6 Torr; (c) argon, P=6 Torr. The voltage amplitude is 11 kV in the cable, pulse duration is 25 ns, rise time is 5 ns, repetitive frequency is 40 Hz.	80
7.5	Fractional power transferred in different mixtures from electrons to neutral particles (energy branching).	81
7.6	Calculated ignition delay time for different gas heating. Initial conditions (pressure P_5 and temperature T_5) correspond to those in the $C_2H_6:O_2:Ar$ mixture. See detailed explanations in the text.	82
7.7	$CH_4:O_2:Ar$ mixture. (a): specific deposited energy during the first pulse of nanosecond generator (hollow symbols) and total specific deposited energy (filled symbols); (b): energy efficiency of O-atoms production in the first pulse and in total during all the reflections of high-voltage pulse.	83
7.8	$C_2H_6:O_2:Ar$ mixture. (a): specific deposited energy during the first pulse of nanosecond generator (hollow symbols) and total specific deposited energy (filled symbols); (b): energy efficiency of O-atoms production in the first pulse and in total during all the reflections of high-voltage pulse.	83
7.9	$C_3H_8:O_2:Ar$ mixture. (a): specific deposited energy during the first pulse of nanosecond generator (hollow symbols) and total specific deposited energy (filled symbols); (b): energy efficiency of O-atoms production in the first pulse and in total during all the reflections of high-voltage pulse.	84
7.10	$C_4H_{10}:O_2:Ar$ mixture. (a): specific deposited energy during the first pulse of nanosecond generator (hollow symbols) and total specific deposited energy (filled symbols); (b): energy efficiency of O-atoms production in the first pulse and in total during all the reflections of high-voltage pulse. . . .	84
7.11	$C_5H_{12}:O_2:Ar$ mixture. (a): specific deposited energy during the first pulse of nanosecond generator (hollow symbols) and total specific deposited energy (filled symbols); (b): energy efficiency of O-atoms production in the first pulse and in total during all the reflections of high-voltage pulse. . . .	85
7.12	Analysis of energy consumption, (a): total specific deposited energy for different hydrocarbon-containing mixtures; (b): total O-atoms density; (c) Energy consumption for one O-atom formation for different hydrocarbons; (d) average values of O-atom formation energy cost for different hydrocarbon-containing mixtures.	86
8.1	The evolution in time of the mole fractions of main components for plasma assisted ignition (a) in the $C_3H_8:O_2:Ar$ mixture at $T_5 = 1350$ K and $P_5 = 0.6$ bar; (b) in the $C_4H_{10}:O_2:Ar$ mixture at $T_5 = 1350$ K and $P_5 = 0.6$ bar The gas temperature evolution is represented by the thick red line.	90

8.2	Experimental setup and absorption diagnostic scheme. HVG: high-voltage generator, MDR+PMT: monochromator and photomultiplier, SG: synchro-generator, PW: power supply, Sch1, Sch2, Sch3: Schlieren-systems.	92
8.3	Scheme of the dye flow system of cw laser. 1:gear-type pump, 2: dampener-filter-heat exchanger, 3: by-pass valve for the actuating pressure adjustment, 4: auxiliary dampener, 5: quartz nozzle, 6: downcomer, 7: reservoir, 8: rotary mini-pump (hydro-starter), 9: pressure gauge. The dye flow system is powered by 380 VAC, 50 Hz, 3-phases.	93
8.4	Scheme of the AMETIST dye cw laser (Tekhnoscan, Novosibirsk, Russia) and photo of the laser.	93
8.5	Output laser power <i>vs</i> anode Ar^+ laser current.	94
8.6	Photo of the external part of dye laser cavity (doubling system)	95
8.7	Schematic view of the cross-section of the discharge cell (the last section of the shock tube).	96
8.8	Scheme of optical part of AMETIST-03 dye laser.	97
8.9	Scheme of stability regions of a laser cavity.	98
8.10	Experimentally measured OH emission spectrum (blue curve) and numerically simulated OH emission spectra (black curves) with different spectral resolution.	99
8.11	Scheme of laser beam transmission through Fabry-Perot etalon.	101
8.12	Overlapping of laser line and OH absorption.	102
8.13	$\text{H}_2\text{:O}_2$ stoichiometric mixture diluted with Ar (90 %). Initial parameters of the experiments: pressure and temperature behind the reflected shock wave.	103
8.14	$\text{H}_2\text{:O}_2$ stoichiometric mixture diluted with Ar (90 %). Experimental oscillogramms for autoignition regimes (to be continued). Sch1, Sch2, Sch3: signals from Schlieren systems, Emiss: signal from photomultiplier, $\lambda=306$ nm, Ref: reference laser signal at 307 nm, Abs: absorption of laser radiation at 307 nm.	104
8.15	$\text{H}_2\text{:O}_2$ stoichiometric mixture diluted with Ar (90 %). Experimental oscillogramms for autoignition regimes.	105
8.16	$\text{H}_2\text{:O}_2$ stoichiometric mixture diluted with Ar (90 %). Experimental oscillogramms for plasma assisted ignition (to be continued). Sch1, Sch2, Sch3: signals from Schlieren systems, Emiss: signal from photomultiplier, $\lambda=306$ nm, Ref: reference laser signal at 307 nm, Abs: absorption of laser radiation at 307 nm.	106
8.17	$\text{H}_2\text{:O}_2$ stoichiometric mixture diluted with Ar (90 %). Experimental oscillogramms for plasma assisted ignition.	107
8.18	$\text{H}_2\text{:O}_2$ stoichiometric mixture diluted with Ar (90 %). Calculated OH density upon time for different experimental regimes (to be continued).	108
8.19	$\text{H}_2\text{:O}_2$ stoichiometric mixture diluted with Ar (90 %). Calculated OH density upon time for different experimental regimes.	108
8.20	Coefficient k obtained from comparison of experimentally obtained $[\text{OH}](t)$ dependence and calculations for the same initial conditions.	109
8.21	$\text{H}_2\text{:O}_2$ stoichiometric mixture diluted with Ar (90 %). Plasma assisted ignition. Measured OH density upon time for different experimental regimes (to be continued).	110

8.22	H ₂ :O ₂ stoichiometric mixture diluted with Ar (90 %). Plasma assisted ignition. Measured OH density upon time for different experimental regimes.	111
8.23	Ignition delay time for H ₂ :O ₂ :Ar mixture with CO ₂ additions. Comparison of ignition delay time determined using OH* emission and OH absorption profiles.	111
9.1	Idea of the experiments on comparison of the efficiency of laser flash-photolysis and nanosecond discharge in their efficiency to initiate combustion.	115
9.2	Ignition delay time vs temperature. Comparison of autoignition, ignition by flash-photolysis and by the discharge.	115
9.3	Initial parameters of oxygen-containing gas mixture: relationship between gas density, temperature, and pressure. (a) comparison of initial parameters for the discharge and for autoignition; (b) gas density <i>vs</i> temperature for experiments in the discharge.	116
9.4	Energy input in experiments with flash-photolysis and with the discharge.	116
9.5	Decrease of the ignition delay time. Comparison of autoignition and laser flash-photolysis. Experiments 5 mm apart from the end plate.	118
9.6	Sensitivity analysis of the numerical scheme for different mixtures. Autoignition and laser flash-photolysis.	119
9.7	Distribution of O(¹ D)-atoms density due to nonuniformity of the laser beam. Schematic view of a laser spot and 2D image of emission intensity are given on the right hand side. Laser energy in the cross-section of inlet window is equal to 120 mJ.	121
9.8	2D images of laser emission intensity at $\lambda = 193$ nm. Laser energy in the cross-section of inlet window is equal to 120 mJ (upper row) and to 24 mJ (lower row).	122
9.9	Scheme of experimental setup for O ₃ density measurements by absorption of UV-emission at $\lambda = 250$ nm (upper part of the Figure). Shape of absorption coefficient for O ₃ molecule (lower plot).	123
9.10	Spectrum of DDS-30 deuterium lamp (upper plot). Typical oscillogram of the emission at 250 nm. The emission trace is given by a red curve. Green curve corresponds to smoothed signal, and blue curve represents the results of calculations (lower plot).	124
9.11	Calculated kinetic curves of ozone for N ₂ :O ₂ :N ₂ O=92:4:4 mixture. Kinetic mechanism (reactions (N1)-(N4)) is given in the Table 9.1, different initial pressures and O(¹ D) densities are considered.	125
9.12	Comparison of calculated and measured values of ozone density for different initial densities of O(¹ D). N ₂ :O ₂ :N ₂ O=92:4:4 mixture, $T = 295$ K, $P = 1$ atm.	125
9.13	Energy input <i>vs</i> time in N ₂ O:H ₂ :O ₂ :Ar mixture. Nanosecond discharge, time of the first pulse coming to the discharge section is indicated with a red circle.	128
9.14	Energy input <i>vs</i> reverse temperature and <i>vs</i> gas density in N ₂ O:H ₂ :O ₂ :Ar mixture.	129
9.15	Typical behaviour of electrical current (A) and reduced electric field in N ₂ O:H ₂ :O ₂ :Ar mixture.	130

9.16	Excitation cross-sections for N_2O interaction with electrons. Dissociative excitation. “Hayashi”: [90], “Yousfi”: [85].	131
9.17	Cross-sections for N_2O interaction with electrons. Dissociative attachment. “Hayashi”: [90], “Yousfi”: [85], “Chantry”: [92].	132
9.18	Pure N_2O . “Hayashi87”: [90], “Yousfi99”: [85], “Teich91”: [86]. (A): electron drift velocity as a function of reduced electric field(B): ionization coefficient as a function of reduced electric field.	133
9.19	Electron drift velocity as a function of reduced electric field. $\text{O}_2:\text{N}_2\text{O}:\text{H}_2:\text{Ar} = 0.3:1:3:5$ mixture. “Hayashi87”: [90], “Yousfi99”: [85], “Teich91”: [86]. .	134
9.20	Energy branching in $\text{O}_2:\text{N}_2\text{O}:\text{H}_2:\text{Ar} = 0.3:1:3:5$ mixture. (A): first set of cross-sections (i); (B): second set of cross-sections (ii); (C): third set of cross-sections (iii).	135
10.1	The temporal evolution of the reduced electric field for 1329 K and 0.45 atm. The green segments of the curve correspond to high-voltage pulses in which the discharge occurred and active species were produced ($1 \text{ Td} = 10^{-17} \text{ V cm}^2$).	141
10.2	The temporal evolution of the discharge current for 1329 K and 0.45 atm. The black curve corresponds to the measurement and the green curve corresponds to the calculation.	141
10.3	The measured peak values of the reduced electric field (red circles) and their values at the instant at which the discharge current peaks (black squares) as a function of the gas number density ($1 \text{ Td} = 10^{-17} \text{ V cm}^2$).	142
10.4	The temporal evolution of the specific deposited energy (per particle) in the discharge for various gas temperatures and pressures. Blue curves correspond to measurements and green curves correspond to calculations. . . .	143
10.5	Total specific energy deposited per one neutral particle for all high-voltage pulses as a function of pressure.	144
10.6	The temporal evolution of the measured OH^* emission intensity (green curve) and the calculated evolution in time of the density of OH (blue curve) for 1329 K and 0.45 atm.	145
10.7	The delay time for autoignition (circles) and plasma-assisted ignition (squares and triangles) in a $\text{CH}_4:\text{O}_2:\text{N}_2:\text{Ar} = 1:4:15:80$ mixture as a function of gas temperature for various gas pressures. Closed symbols correspond to measurements and open symbols correspond to calculations. The solid curve is an approximation of the measured autoignition delay time and the dash curve corresponds to the calculated autoignition delay time at 0.5 atm. Red symbols correspond to the conditions under which time-resolved discharge current and electric field were measured during the discharge.	146
10.8	Electron collision cross sections for N_2 [22] as a function of electron energy: (1) momentum transfer in elastic collisions, (2) vibrational excitation, (3) excitation of the singlet electronic states, (4) excitation of the triplet electronic states, and (5) ionization.	149
10.9	Mean electron energy in $\text{CH}_4:\text{O}_2:\text{N}_2:\text{Ar} = 1:4:15:80$ and $\text{CH}_4:\text{O}_2:\text{Ar} = 1:4:95$ mixtures as a function of reduced electric field ($1 \text{ Td} = 10^{-17} \text{ V cm}^2$). . . .	150

10.10	Fractional power transferred in (a) $\text{CH}_4:\text{O}_2:\text{N}_2:\text{Ar} = 1:4:15:80$ and (b) $\text{CH}_4:\text{O}_2:\text{Ar} = 1:4:95$ mixtures from electrons to neutral particles as a function of reduced electric field ($1 \text{ Td} = 10^{-17} \text{ V cm}^2$). The $\text{CH}_4:\text{O}_2:\text{N}_2:\text{Ar}$ mixture: (1) vibrational excitation of N_2 , (2) excitation of the $\text{N}_2(A^3\Sigma_u^+)$, $\text{N}_2(B^3\Pi_g)$, $\text{N}_2(a'^1\Sigma_u^-)$, and $\text{N}_2(C^3\Pi_u)$ states, (3) dissociation of O_2 , (4) excitation of other singlet N_2 states, (5) excitation of other triplet N_2 states, (6) excitation of Ar^* states, and (7) total ionization. The $\text{CH}_4:\text{O}_2:\text{Ar}$ mixture: (1) dissociation of O_2 , (2) excitation of the O_2 state with $\Delta E = 4.5 \text{ eV}$, (3) excitation of $\text{O}_2(a^1\Delta_g)$ and $\text{O}_2(b^1\Sigma_g^+)$ states, (4) vibrational excitation of O_2 , (5) excitation of Ar^* states, and (6) total ionization.	158
10.11	The evolution in time of the mole fractions for (a) electrons and excited particles and (b) atoms and radicals in the discharge afterglow in the $\text{CH}_4:\text{O}_2:\text{N}_2:\text{Ar}$ mixture at 1329 K and 0.45 atm.	159
10.12	The evolution in time of the mole fractions for (a) electrons and excited particles and (b) atoms and radicals in the discharge afterglow in the $\text{CH}_4:\text{O}_2:\text{N}_2:\text{Ar}$ mixture at 1798 K and 1.85 atm.	160
10.13	The calculated mole fractions of atoms and radicals produced by the discharge in the $\text{CH}_4:\text{O}_2:\text{N}_2:\text{Ar}$ mixture as a function of n_5	161
10.14	The autoignition delay time in the $\text{CH}_4:\text{O}_2:\text{N}_2:\text{Ar}$ mixture as a function of temperature. Closed symbols correspond to measurements and open circles and triangles correspond, respectively, to calculations using kinetic schemes from [118] and [119].	161
10.15	The delay time for ignition by the discharge in the $\text{CH}_4:\text{O}_2:\text{N}_2:\text{Ar}$ mixture as a function of temperature. Closed squares correspond to measurements, open circles correspond to calculations taking into account the formation of O via the $\text{N}_2(a')$, $\text{N}_2(A)$, $\text{N}_2(B)$ and $\text{N}_2(C)$ states, open triangles correspond to calculations taking into account the formation of O via the $\text{N}_2(a')$, $\text{N}_2(A)$, $\text{N}_2(B)$, $\text{N}_2(C)$, $\text{N}_2(B')$, $\text{N}_2(W)$, $\text{N}_2(a)$ and $\text{N}_2(w)$ states, open inverse triangles correspond to calculations neglecting the formation of O via excited N_2 states, and open stars correspond to calculations for a $\text{CH}_4:\text{O}_2:\text{Ar} = 1:4:95$ mixture.	162
10.16	The evolution in time of the mole fractions of the main components for (a) autoignition and (b) ignition by the discharge for 1329 K and 0.45 atm. In plasma-assisted ignition, time is reckoned from the instant at which active particles are injected into the mixture.	163
10.17	The energy cost for production of O atoms in $\text{CH}_4:\text{O}_2:\text{N}_2:\text{Ar} = 1:4:15:80$ and $\text{CH}_4:\text{O}_2:\text{Ar} = 1:4:95$ mixtures as a function of reduced electric field. The solid curves correspond to the calculations taking into account direct electron impact dissociation of O_2 and formation of O atoms via quenching of the electronically excited Ar and N_2 states; the dash curve corresponds to the calculations taking into account direct electron impact dissociation of O_2 and formation of O atoms via quenching of the electronically excited Ar states and neglecting formation of O atoms via quenching of the excited N_2 states.	164

11.1	Scheme of experimental setup. HVG is the high-voltage generator; M_1 , M_2 , and M_3 are the optical mirrors	166
11.2	Oscillogram of back-current shunt signal. A nanosecond 12 kV pulse of negative polarity and its rereflections from the discharge unit and the generator. The experiment was carried out in a $C_2H_6:O_2 = 2:7$ mixture at room temperature and 1 atm.	167
11.3	Electrode assembly in case of ignition by (a) sliding nanosecond DBD and (b) nanosecond spark.	168
11.4	High-speed camera photographs with 500 ns exposure. (a), (a') sliding nanosecond DBD; (b), (b'), (c), (c'), (d), (d') subsequent flame propagation. Accented letter - top view, other - side view. $C_2H_6:O_2 = 2:7$ at room temperature and 1 atm pressure.	170
11.5	High-speed camera photographs with 500 ns exposure. (a), (a') nanosecond spark; (b), (b'), (c), (c'), (d), (d') subsequent flame propagation. Accented letter - top view, other - side view. $C_2H_6:O_2 = 2:7$ at room temperature and 1 atm pressure.	171
11.6	The evolution in time of the inflammation volume in the case of 1 — nanosecond spark ignition and 2 — sliding nanosecond DBD ignition. $C_2H_6:O_2 = 2:7$ at room temperature and 1 atm pressure.	172